



Mbomson, Ifeoma Grace (2016) *Mid-infrared photonic sensors based on metamaterial structures*. PhD thesis.

<http://theses.gla.ac.uk/7462/>

Copyright and moral rights for this work are retained by the author

A copy can be downloaded for personal non-commercial research or study, without prior permission or charge

This work cannot be reproduced or quoted extensively from without first obtaining permission in writing from the author

The content must not be changed in any way or sold commercially in any format or medium without the formal permission of the author

When referring to this work, full bibliographic details including the author, title, awarding institution and date of the thesis must be given

Glasgow Theses Service

<http://theses.gla.ac.uk/>

theses@gl.a.ac.uk



**University  
of Glasgow**

**Mid-Infrared Photonic Sensors  
Based On  
Metamaterial Structures**

**Ifeoma Grace Mbomson**

**B. Eng., M.Sc.**

**A thesis for the degree of  
Doctor of Philosophy (Ph.D.),  
Submitted to the School of Engineering,  
University of Glasgow**

**© I.G Mbomson, January 2016**

# ABSTRACT

In this work three different metallic metamaterials (MMs) structures such as asymmetric split ring resonators (A-SRRs), dipole and split H-shaped (ASHs) structures that support plasmonic resonances have been developed. The aim of the work involves the optimization of photonic sensor based on plasmonic resonances and surface enhanced infrared absorption (SEIRA) from the MM structures. The MMs structures were designed to tune their plasmonic resonance peaks in the mid-infrared region. The plasmonic resonance peaks produced are highly dependent on the structural dimension and polarisation of the electromagnetic (EM) source. The ASH structure particularly has the ability to produce the plasmonic resonance peak with dual polarisation of the EM source. The double resonance peaks produced due to the asymmetric nature of the structures were optimized by varying the fundamental parameters of the design. These peaks occur due to hybridization of the individual elements of the MMs structure. The presence of a dip known as a trapped mode in between the double plasmonic peaks helps to narrow the resonances. A periodicity greater than twice the length and diameter of the metallic structure was applied to produce narrow resonances for the designed MMs. A nanoscale gap in each structure that broadens the trapped mode to narrow the plasmonic resonances was also used. A thickness of 100 nm gold was used to experimentally produce a high quality factor of 18 in the mid-infrared region. The optimised plasmonic resonance peaks was used for detection of an analyte, 17 $\beta$ -estradiol. 17 $\beta$ -estradiol is mostly responsible for the development of human sex organs and can be found naturally in the environment through human excreta. SEIRA was the method applied to the analysis of the analyte. The work is important in the monitoring of human biology and in water treatment. Applying this method to the developed nano-engineered structures, enhancement factors of  $10^5$  and a sensitivity of 2791 nm/RIU was obtained. With this high sensitivity a figure of merit (FOM) of 9 was also achieved from the sensors. The experiments were verified using numerical simulations where the vibrational resonances of the C-H stretch from 17 $\beta$ -estradiol were modelled. Lastly, A-SRRs and ASH on waveguides were also designed and evaluated. These patterns are to be use as basis for future work.

# CONTENTS

<b>Title</b>	<b>i</b>
<b>Abstract</b>	<b>ii</b>
<b>Contents</b>	<b>iii</b>
<b>List of figures</b>	<b>vi</b>
<b>List of Tables</b>	<b>xiv</b>
<b>Acknowledgements</b>	<b>xv</b>
<b>Publications</b>	<b>xvi</b>
<b>Chapter 1 INTRODUCTION</b>	<b>1</b>
1.1 Introduction	1
1.2 Motivation and Contribution	4
1.3 Structure of the Thesis	5
1.4 References	7
<b>Chapter 2 METAMATERIAL CONCEPT</b>	<b>9</b>
2.1 Introduction	9
2.2 Metamaterials	10
2.3 Plasmonics	21
2.4 Photonic sensors based on metamaterial	22
2.5 Discussions and Conclusion	28
2.6 References	29

<b>Chapter 3 Modelling and Simulation</b>	<b>35</b>
3.1 Introduction	35
3.2 Modelling	36
3.3 Simulations Setup	37
3.4 Asymmetric split ring resonators (A-SRRs)	40
3.5 Dipole structures	56
3.6 Asymmetric split H-shape (ASHs)	58
3.7 Discussions and Conclusion	65
3.8 References	67
<b>Chapter 4 Fabrication of Metamaterial Devices</b>	<b>72</b>
4.1 Introduction	72
4.2 Fabrication technique	72
4.2.1 CAD design and Substrate preparation	74
4.2.2 Electron beam Lithography	76
4.2.3 Pattern development	79
4.2.4 Metallization	79
4.3 Fabrication on Fused Silica (SiO <sub>2</sub> )	80
4.4 Discussion and Conclusion	88
4.5 References	90
<b>Chapter 5 Experimental Results</b>	<b>92</b>
5.1 Introduction	92
5.2 Measurement Setup	93
5.3 Asymmetric split ring resonators (A-SRRs)	97
5.4 Dipole structures	110

5.5 Asymmetric Split H-shape structure	112
5.6 Discussions and conclusion	115
5.7 References	119
<b>Chapter 6 Detection of 17<math>\beta</math>-Estradiol</b>	<b>122</b>
6.1 Introduction	122
6.2 Sensing technique	123
6.3 Modelling and Simulation	124
6.4 Experimental Process	129
6.5 Experiment and Simulation results	130
6.6 Discussions and conclusion	145
6.7 References	147
<b>Chapter 7 Future Work and Conclusions</b>	<b>151</b>
7.1 Future work	151
7.2 Conclusion	160
7.3 References	163
<b>Appendices</b>	<b>165</b>
A Modelling	165
B FDTD simulations	166
C 17 $\beta$ -estradiol experiment and simulation	168
D Lumerical mode calculation	181
E References	183

# LIST OF FIGURES

## Chapter 2

<b>Figure 2.1:</b> Illustration of electromagnetic spectrum.....	11
<b>Figure 2.2:</b> Three dimensional MM structures with arc radii, R- r, angle, $\theta^0$ , thickness, t, arm lengths, gap and slit.....	12
<b>Figure 2.3:</b> Sketch of A-SRR structure: Four orientations of the A-SRR studied with respect to the E, H and k vectors of the incidence EM field with double gaps between the two asymmetric arcs.....	13
<b>Figure 2.4:</b> Sketch illustrating the analogy between a simple conventional inductive-capacitive (LC) circuits design .....	15
<b>Figure 2.5:</b> Transmission spectral from FDTD simulation of A-SRR metamaterial.....	17
<b>Figure 2.6:</b> Reflectance spectra of <b>TE</b> polarized for a split ring resonator .....	18
<b>Figure 2.7:</b> E-field polarisation plots for the designed MM device components.....	19
<b>Figure 2.8:</b> Reflectance spectra of <b>TE</b> polarized for asymmetric (A-SRR).....	20
<b>Figure 2.9:</b> Exponential decay of field into two different materials.....	21
<b>Figure 2.10:</b> Block diagram of a photonic sensor showing excitation of resonances from EM radiation on arrays of A-SRRs structure and then with analyte which produces a shift to longer wavelengths of electromagnetic (EM) spectrum.....	23
<b>Figure 2.11:</b> Water vapour and carbon dioxide bands in the infrared spectrum.....	24
<b>Figure 2.12:</b> Common molecular resonances in the IR from spectroscopic methods in organic chemistry by Williams and Fleming .....	25
<b>Figure 2.13:</b> Schematic diagram of broad and narrow resonances with respect to wavelength position ( $\lambda_p$ ) and showing the Full width half maximum (FWHM) of a resonance.....	26

### Chapter 3

<b>Figure 3.1:</b> Image of Perspective view for the three dimensional simulations setup.....	37
<b>Figure 3.2:</b> Image of asymmetric Split Ring Resonators, A-SRR with equal angles ( $\theta = g$ ) but two unequal arcs ( $L_1$ and $L_2$ ), $w$ is the width of the arcs and $t$ is the thickness of the pattern.....	34
<b>Figure 3.3:</b> Schematic diagram showing two concentric asymmetric arcs for the A-SRRs metamaterial.....	41
<b>Figure 3.4:</b> Reflectance spectra for arcs length difference (shown as percentage) using Lumerical simulations to show the double plasmonic resonance peaks from the asymmetric arcs with direction of E-field.....	43
<b>Figure 3.5:</b> FDTD Lumerical simulations of various nanoscale gaps with the double resonance peaks corresponding to the large and small arcs length.....	44
<b>Figure 3.6:</b> E- field strength and transmission plots for the A-SRRs at nanoscale gap.....	45
<b>Figure 3.7:</b> Reflectance plots from FDTD simulation for different arcs width ( $w$ ) and the schematic diagrams of the A-SRR.....	47
<b>Figure 3.8:</b> Schematic diagram of A-SRRs Au pattern on a fused silica substrate showing the periodicity ( $a_{xy}$ ).....	49
<b>Figure 3.9:</b> (a) Graph to compare periodicity and magnitude of reflectance peak (b) FDTD numerical simulation of 100 nm Au thick for 1 $\mu$ m diameter of A-SRRs radius at different periodicity (c) Reflectance peak for periodic array of 2.4 $\mu$ m.....	50
<b>Figure 3.10:</b> Reflectance spectra from the FDTD numerical simulation of 0.48 $\mu$ m radius of A-SRRs for 10 nm to 70 nm Au thicknesses showing double plasmonic peaks with defects at 2.2 $\mu$ m from grating order due to periodic boundary conditions.....	52
<b>Figure 3.11:</b> Reflectance plots for A-SRR thickness comparison.....	53
<b>Figure 3.12:</b> Zoomed image of the resonance peak shorter wavelength from the simulation of 100 nm Au thickness.....	54
<b>Figure 3.13:</b> Comparing gold thickness for the 960 nm diameter A-SRRs pattern.....	55

<b>Figure 3.14:</b> Arrays of asymmetric dipole structures on fused silica substrate.....	56
<b>Figure 3.15:</b> Reflectance spectra of 100 nm Au thick for dipole with asymmetric arm's length of (1.1 and 0.9) $\mu\text{m}$ at different periodicity.....	57
<b>Figure 3.16:</b> Schematic diagram of ASHs Au pattern on a fused silica substrate showing an array of split-H structures.....	58
<b>Figure 3.17:</b> FDTD numerical simulation of 100 nm Au thick for (a) plasmonic resonance peaks tune within (2 to 7) $\mu\text{m}$ by varying the asymmetric arm's length of ASHs structure (b) comparison of the resonance peak position of the large arm.....	60
<b>Figure 3.18:</b> Reflectance spectra from the Lumerical simulations ASHs periodicity (b) Periodic of 2 $\mu\text{m}$ for asymmetric dipole and ASH structures.....	61
<b>Figure 3.19:</b> Schematic diagram showing the directions of the wave on the ASH.....	63
<b>Figure 3.20:</b> (a) Reflectance spectra for dual the polarization of source on that produce plasmonic resonance (b) Electric field plots for ASH (c) Transverse electric (TE) along asymmetric cross bar of ASH, inset.....	64
<b>Chapter 4</b>	
<b>Figure 4.1:</b> Flow chart of fabrication process for electron beam lithography writing.....	74
<b>Figure 4.2:</b> Arrays of metallic metamaterial (A-SRRs and ASHs) pattern designed.....	75
<b>Figure 4.3:</b> Flow chart of the fundamental systems of electron beam lithography, VB6 in the JWNC.....	78
<b>Figure 4.4:</b> Flow chart (clockwise) of fabrication process on a fused silica substrate and resist spinning for metallic metamaterial patterns.....	81
<b>Figure 4.5:</b> Fabrications on fused silica (a) Scanning electronic microscopic (SEM) image of A-SRRs arrays showing irregular arcs due to inadequate design resolution (b) optical microscope image of A-SRRs arrays showing a high density of structure (c) Properly design SEM image of A-SRRs, with less dense and smooth arcs.....	82

<b>Figure 4.6:</b> SEM image of different periodicity (a) of A-SRRs arrays fabricated on fused silica.....	82
<b>Figure 4.7:</b> Fabrication of two different gaps (parallel and wedge) between the asymmetric arcs.....	83
<b>Figure 4.8:</b> Variation of the nanoscale gap between the asymmetric arcs (a) 175 nm (b) 145 nm (c) 115 nm (d) 85 nm (e) 55 nm.....	84
<b>Figure 4.9:</b> SEM image of A-SRRs arrays on a different substrates silicon.....	84
<b>Figure 4.10:</b> SEM image of the dipole structure at different gap (g) (a) Single dipole $g = 400$ nm (b) $s = 200$ nm (c) $s = 450$ nm (b) $s = 650$ nm.....	85
<b>Figure 4.11:</b> SEM image of (a) symmetric and (b) asymmetric ASHs showing the gap (g) and space (s) in the structure.....	86
<b>Figure 4.12:</b> SEM image of ASHs at different slit (s) between arms with cross (a) $s = 50$ nm (b) $s = 150$ nm (c) $s = 250$ nm (d) $s = 350$ nm.....	87

## Chapter 5

<b>Figure 5.1:</b> Pictorial image of the measurement setup.....	93
<b>Figure 5.2:</b> FTIR measurement on fused silica using (a) the fused silica sample and (b) gold mirror for background measurement which show the atmospheric interference and spectra from the silica substrate at points pointed with red markers.....	94
<b>Figure 5.3:</b> Schematic image of an optical beam-path showing both reflectance and transmittance path [2].....	96
<b>Figure 5.4:</b> Reflectance spectra in mid-infrared for E-field polarizations showing the trapped mode separating the double plasmonic peaks of A-SRRs, and vibrational spectrum from fused silica at $9.1 \mu\text{m}$ (a) FTIR measurement with $\text{H}_2\text{O}$ vapour ripples at $2.85 \mu\text{m}$ (b) Simulation with grating order defects.....	98

<b>Figure 5.5:</b> Reflectance spectra of double plasmonic peaks from A-SRR for the asymmetric arcs variation percentage (a) FTIR measurements (b) Lumerical Simulation.....	100
<b>Figure 5.6</b> Energy diagrams that describe A-SRR plasmonic hybridization from the large and small arcs.....	101
<b>Figure 5.7:</b> Reflectance spectra of 0.96 $\mu\text{m}$ A-SRR diameters showing the double and single plasmonic peaks from A-SRR and different arcs (large) length (a) FTIR measurements showing measurement artefacts at 2.5 $\mu\text{m}$ (b) Lumerical simulations.....	103
<b>Figure 5.8:</b> Reflectance plots of 0.96 $\mu\text{m}$ A-SRR diameters showing the double and single plasmonic peaks from A-SRR and different arcs (small) length (a) FTIR measurements (b) Lumerical simulations.....	104
<b>Figure 5.9:</b> Reflectance spectra showing double plasmonic peaks from A-SRR for the periodicity variation (a) FTIR measurements with water vapour ripples at 2.85 and $\text{CO}_2$ at 4.2 (b) Lumerical Simulation with grating order defects due to periodic boundary condition corresponding to the varied periods.....	106
<b>Figure 5.10:</b> FTIR measurement of A-SRRs with parallel and wedge arc that form gap....	108
<b>Figure 5.11:</b> FTIR measurement (a) for the variations of two equal nanoscale gaps between asymmetric arcs of A-SRRs (b) Gap of 145nm showing peak with the highest Q (c) comparison of the resonance peaks shift due to gap.....	109
<b>Figure 5.12:</b> Reflectance spectra for dipole structure at different gap (g) between the asymmetric arms (a) FTIR measurements (b) Lumerical simulations.....	111
<b>Figure 5.13:</b> FTIR measurement for reflectance spectra showing plasmonic resonance peak of (a) symmetric split H-shape (b) asymmetric split H-shape.....	113
<b>Figure 5.14:</b> FTIR measurement of ASH at different periodicity.....	114
<b>Figure 5.15:</b> Matching reflectance from experiment and simulation for asymmetric structure of metallic metamaterial.....	115
<b>Figure 5.16:</b> Reflectance spectra from experiment and simulation for hybridized resonance of A-SRR structure (a) A-SRR and Large arm (b) A-SRR and small arm.....	116
<b>Figure 5.17:</b> Reflectance resonance peak that produced the highest Q factor from the experimental results.....	167

## Chapter 6

- Figure 6.1:** Molecular structure of 17 $\beta$ -estradiol.....122
- Figure 6.2:** Systematic diagram of 3D arrays of molecular formula of 17 $\beta$ -estradiol on an asymmetric split H-shape metamaterial.....124
- Figure 6.3:** Refractive index and absorption coefficient of the analyte E2 with a Fano type resonance of the C-H bond at (a) 3.42  $\mu\text{m}$  (b) 3.49  $\mu\text{m}$ .....126
- Figure 6.4:** Fano type resonance plots for different refractive indexes (a)  $n = 1$ (b)  $n = 1.2$  (c)  $n = 1.4$  (d)  $n = 1.6$ .....127
- Figure 6.5:** Comparison of the resonance magnitude for the indexes.....128
- Figure 6.6:** Atomic force microscopy (AFM) for fine surface measurement of the 17 $\beta$ -estradiol spun silicon substrate, the scanning height was set from 0 nm to 200 nm.....129
- Figure 6.7:** Reflectance spectra measurements from two different fused silica samples using FTIR (a) 1  $\mu\text{m}$  thickness of sample, normalised on gold mirror (b) 1  $\mu\text{m}$  thickness of sample, normalised on fused silica substrate (c) 0.5  $\mu\text{m}$  thickness of sample, normalised on fused silica substrate.....130
- Figure 6.8:** Experimental measurements for the sensing work using FTIR apparatus (a) reflectance spectra from fused silica substrate, A-SRR and E2 (b) reflectance resonance peaks of A-SRRs with E2 (c) Vibrational resonance of C-H on substrate (d) Vibrational resonance of C-H on A-SRRs.....132
- Figure 6.9** Vertically offset plots of reflectance spectra of the red-shifted resonance peaks due to refractive index change in the ASH surroundings (a) FTIR measurements for different molarity; ripples from H<sub>2</sub>O vapour at 2.8  $\mu\text{m}$ , C-H vibrational resonance bond stretch from 3.31 $\mu\text{m}$  to 3.55 $\mu\text{m}$  and CO<sub>2</sub> at 4.2  $\mu\text{m}$  (b) Lumerical simulations for different thickness...134
- Figure 6.10:** FTIR reflectance spectra of the red-shifted resonance peaks due to refractive index change in the ASH surroundings for the four different molarity in  $\mu\text{mole/ ml}$  (a)0.37 (b) 3.7(c) 36 (d) 334; ripples from H<sub>2</sub>O vapor at 2.8  $\mu\text{m}$ , C-H vibrational resonance bond stretch from 3.31 $\mu\text{m}$  to 3.55 $\mu\text{m}$  and CO<sub>2</sub> at 4.2  $\mu\text{m}$ .....136

<b>Figure 6.11:</b> Absolute magnitude of the E-field from the design simulated for x-y axis with E-field parallel to arms of ASH for the resonance peak at wavelength 3.31 $\mu\text{m}$ .....	139
<b>Figure 6.12:</b> FTIR reflectance spectra of the enhanced C-H bond stretching from 3.31 $\mu\text{m}$ to 3.55 $\mu\text{m}$ vibrational resonance peaks by the ASH plasmon resonances zoomed plots.....	140
<b>Figure 6.13:</b> FTIR measurements for reflectance spectra showing the redshift in the resonance peaks from an initial wavelength of (a) 3.23 $\mu\text{m}$ for SSHs and (b) 3.05 $\mu\text{m}$ and 3.57 $\mu\text{m}$ for two peaks of ASHs. Other spectral features are water vapour at 2.85 $\mu\text{m}$ , CO <sub>2</sub> at 4.20 $\mu\text{m}$ and the C-H resonance stretch at 3.31 $\mu\text{m}$ . Note: Small dip on the blue plot of (a) is due to fabrication errors from the symmetric structure.....	142
<b>Figure 6.14:</b> Simulations results (a) Reflectance plots for 200 nm thickness of E2 at various indexes (b) Matching results of experiment and simulation for reflectance molecular resonances of the E2 (c) simulations of the red-shift in the position of the resonance peaks for E2 thickness of (10, 100, 200, & 400) nm (d) Comparison of sensitivity of the ASH due to refractive index changes and thickness of E2.....	144
<b>Figure 6.15:</b> FTIR measurement and simulation reflectance spectra from A-SRRs and E2.....	145

## Chapter 7

<b>Figure 7.1:</b> Schematic diagram of Silicon-on-Insulator sample.....	152
<b>Figure 7.2:</b> Sketch of gold A-SRRs on a waveguide of silicon-on insulator (SOI) substrate.....	153
<b>Figure 7.3:</b> SEM images of (a) Global markers with cross (b) Misaligned A-SRRs on waveguide (c) Aligned A-SRRs on waveguide.....	155
<b>Figure 7.4:</b> Dimension of waveguide width (y-axis), effective index, loss and modal field plots for electric component.....	156
<b>Figure 7.5:</b> Transmittance spectra showing plasmonic peaks from waveguide with A-SRRs and no resonance from waveguide without A-SRRs with design inset.....	158

**Figure 7.6:** (a) 3-D schematic diagram of split H-shaped structure on SOI (b) Reflectance spectra showing double plasmonic peaks from ASH simulation for a normal incidence source.....159

**Appendix**

**Figure 1:** Transmission spectra plots and  $E_x$ -field plots from more symmetric to less symmetric A-SRRs.....166

**Figure 2:** Transmission spectra and z-components of the E-field plots from the two peaks.....167

**Figure 3:** Schematic diagram for volume of (150 by 150 by 0.2)  $\mu\text{m}$  E2 measured.....171

**Figure 4:** Reflectance spectra from simulation of 200 nm E2 thicknesses on (a) Fused silica substrate (b) ASHs structure (c) Plain gold.....177

**Figure 5:** Schematic diagram for volume of (2 by 2 by 0.2)  $\mu\text{m}$  E2 measured.....178

**Figure 6:** Screen shot of Lumerical solution mode source showing the (a) mode field (b) material properties.....182

# LIST OF TABLES

<b>Table 3.1:</b> Variation of the arcs length.....	42
<b>Table 3.2:</b> Comparison of Average Q-factor for the reflectance plots of figure 3.7.....	47
<b>Table 3.3:</b> Comparing periodicity of A-SRRs with magnitude of reflectance.....	49
<b>Table 3.4:</b> Comparing gold thickness for the 960 nm diameter A-SRRs pattern.....	55
<b>Table 5.1a:</b> Table for the large arcs length.....	102
<b>Table 5.1b:</b> Table for the small arcs length.....	104
<b>Table 6.1:</b> Values for $E_f$ and sensitivity for the four experiments.....	146
<b>Table A:</b> The tabulated values are obtained from measurements .....	176
<b>Table B:</b> Reflectance from simulations of 200 nm on fused silica, ASH and gold.....	178

# ACKNOWLEDGEMENTS

To God is the glory for His amazing grace that followed me all through my studies.

Firstly, I would like to thank Dr Nigel Johnson for his intellectual guidance, unrelenting support and inspiring words during my PhD years. I am very happy and lucky to have him as my research supervisor. I am very thankful and fortunate to have Prof Richard De La Rue in our research group, who always shares his fascinating knowledge and experience. Prof is a power house of research knowledge. I am very grateful to Prof Scott McMeekin and Dr Graham Sharp for their initial directions that make me confident in the numerical simulations and experiments, respectively. I am also thankful to all Dr Johnsons' research team for their contributions towards the success of this work especially Dr Basudev Lahiri.

The last three years of my education have undoubtedly been the busiest time in my study life but enjoyable. The overwhelming friendship of my office mates, catholic chaplaincy brethren, colleagues both inside and outside the School of Engineering has been the key to my happiness during the research work. Special thanks to Adam, Peter and Harry for helping me to proof read some of my chapters. I am very grateful to my entire office mate for making the environment comfortable and peaceful place to study, where all are willing to help.

Secondly, the fabrication part of this work would not have been possible without the technical staff of James Watt Nanofabrication Centre (JWNC) for their directions in fabricating some of the devices. I am also thankful to my fellow PhD students and staff of Electronics and Nanoscale Engineering who may have assisted me with my research at one time or another.

Finally, I am very pleased to the sponsor of my PhD project J. J. Mbomson Education Foundation. I am also grateful to my sibilings: Tessy, Nduka, Justin, Justina, Henry, Dominic and Nwamaka for their inevitable support and love. All I am, and all I have achieved, I owe to my parents, Ichie Justin Nwafor and Grace Amaechi Mbomson.

Ifeoma Mbomson

January, 2016

# PUBLICATIONS

1. I. G. Mbomson, B. Lahiri, S. G. McMeekin, R. M. De La Rue, and N. P. Johnson,, “Gold asymmetric split ring resonators (A-SRRs) for nano sensing of estradiol,” Proc. SPIE Vol. 9125, Brussels, Belgium, 02 May 2014.
2. Johnson, N. P., Lahiri, B., Sharp, G. J., Mbomson, I. G., De La Rue, R. M., and McMeekin, S. G. (2014) Nano-plasmonic sensors from asymmetric split-ring resonators (A-SRRs) [invited]. In: SPIE Photonics Europe, Brussels, Belgium, 14-17 April 2014.
3. Johnson, N. P., Sharp, G. J., Khan, S. I., Mbomson, I., McMeekin, S. G., Lahiri, B., and De La Rue, R. M. (2014) Progress in metamaterial fishnet formed by nanoimprint lithography and asymmetric split ring resonators (A-SRRs) for sensing. In: 2014 16th International Conference on Transparent Optical Networks (ICTON), Graz, Austria, 6-10 Jul 2014.
4. Richard M. De La Rue; Ifeoma G. Mbomson; Saima I. Khan; Graham J. Sharp; Basudev Lahiri; Nigel P. Johnson; Henrique Vilhena; Scott G. McMeekin, “Molecular bond Fano resonances in organic thin films enhanced by (A)SRR arrays,” Proc. SPIE Vol. 9162, San Diego, USA, 29 September 2014.
5. I. G. Mbomson, S. G. McMeekin, R. M. De La Rue, and N. P. Johnson, “Matching plasmon resonances to the C=C and C-H bonds in estradiol,” Proc. SPIE Vol. 9340, San Francisco, USA, 11 March 2015.
6. I. G. Mbomson, S. G. McMeekin, R. M. De La Rue, and N. P. Johnson, “The effect of geometry on the quality factor of resonance peaks in asymmetric nano-antennas at mid-infrared wavelengths,” Proc. SPIE Vol. 9502, Prague, Czech Republic , 05 May 2015.
7. I. G. Mbomson, S. G. McMeekin, R. M. De La Rue, and N. P. Johnson, “Novel Metamaterial Structures for Sensing Applications,” Proc. Metamaterials, Oxford, 7-12 September 2015.
8. Ili F. Mohamad Ali Nasri, Ifeoma G. Mbomson, Richard M. De La Rue, Nigel P. Johnson, “Varying the periodicity to achieve high quality factor on asymmetrical H-Shaped resonators,” Proc. SPIE Brussels, Belgium, 18 April 2016.

# CHAPTER 1

## INTRODUCTION

### 1.1 Introduction

The etymology of the word photonic comes from Greek “photos” meaning light. Photonic devices are rooted in light generation and interaction with matter. The interactive phenomenon between light and matter has been under continuous development for example the discovery of quadratic the electro-optic effect (QEC) by John Kerr in 1875 and then establishment of fundamental theory of laser by Albert Einstein in 1917. Photonics applications have become inescapable in all areas of everyday life, for example: in telecommunication, security, measurements, imaging, medicine, agriculture and biology.

The technological development of photonics towards their wider range of applications brought an era of the device enhancement. Among the targeted features of the new era photonics which is analogous to electronics are low cost, robust, compact, portable devices and high performance. Most optoelectronic devices already have these features and have been utilised in many equipment for example in digital cameras, plasma screens, and blue DVD ray players etc. Currently, researchers are advancing into topics such as optical fibres, photonic crystals and metamaterial in photonics to thoroughly investigate and fabricate various structures and materials with engineered optical properties. Following the advancement and employing much of the technology developed in the photonics industries, metamaterials may contribute a large part of the revolution in the optoelectronics in the coming years. The topic of metamaterials has shown great potential in tuning resonances to desired spectral region and that opens up a wider promising field for the development of photonic sensors.

Victor Veselago, in 1968 was the first to theoretically describe materials that exhibited reversed physical characteristics [1]. This theory was practically developed to left-handed metamaterials by Pendry [2], a material that permits an electromagnetic wave to transport energy in the opposite direction to its phase velocity. Hence, materials that do not adhere to the right-hand rule or are not accessible in naturally occurring material were introduced [2]. More generally, there has been a continuous development of materials with sub-wavelength structures which have led to the concept of metamaterial based photonic sensors.

The general idea of a metamaterial based sensor can be traced back to the work in references [3-5] where a planar array of resonant metallic structures can be applied to realization of a simple sensor system. They proposed that a periodic array of metallic resonator structures can be sensitive to its immediate environment. Over the years many researchers in the field have continuously improved this idea, introducing various new methods of producing high sensitive as well as high figure of merit (FOM) metamaterial devices. The current stage this technological revolution focuses on is development of metamaterial without metals.

Metals have been the traditional material choice for designing metamaterial structures. A wide range of single and double shaped structures for example nanowires [6], chiral structures [7], dipoles [8] and different shapes resembling alphabetical characters have been explored in patterning the metallic metamaterials (MMs). The use of these satisfies the high demands of MMs components application that cover the visible, infrared and microwave region of electromagnetic spectrum. References [9-13] suggested the importance of using materials other than metals minimise losses in MM devices. Even metals with the highest conductivities metals such as gold, silver and copper have significant losses.

Recent improvements in metamaterials involve various designed structures particularly investigating materials that reduce losses. Following the demonstrations of high quality factor MM components at microwave, visible and near infrared of electromagnetic spectrum [14-18], there has been a considerable progress in the modelling and fabrication of all-dielectric [19-21] metamaterial for higher quality components in mid-infrared. Thus a high figure of merit (FOM) defined by the shift in resonance divided by the full width at half

maximum of the resonance peak is made possible in mid-infrared by the all-dielectric structures which are free from losses due to metals as well exhibiting the ability to sustain Fano-resonances [19]. The generic metamaterial approach of using metal still plays important role in enhancing the sensitivity of MMs based sensors which may not be achievable in all-dielectric structures.

Advances in technology also play an essential role in the development of MMs. The invention of metamaterial based sensors was an important milestone in solving the sensing problems in some fields such as in medicine [22], chemistry [23] and biology [24-25]. They also provide an overview of the basic principles and prospects for the application of metamaterial based on photonic sensors for human welfare generally. The current work on photonic sensors devices has now become focused on the possibility of developing optoelectronics components, where the device could be monitored and controlled using the tuning ability of MMs structures to the targeted EM signals. MMs based photonic sensors operating in a passive manner have been reported by some authors [26-27] with significant losses. These are mainly resistive losses through metal [13] which are frequency dependent.

The MMs structure has been developed as a promising platform for plasmonic sensors as have proven with their ability of high signal enhancement factor in sensing applications even in mid-infrared region [28-29]. MM structures such as A-SRRs and dipoles as presented in [4, 8] have since been undergone some adjustments, re-engineering and optimisation to improve on the original design. Extensive investigations have been performed on the gap and periodicity or density of the MM structures [8]. Corresponding simulations and optimisation techniques have been used to improve the metamaterial based photonic sensors. A-SRRs on waveguides and Split H-shaped metamaterials are possible approaches towards producing a high quality and sensitive biochemical sensor device.

## 1.2 Motivation and Contribution

Metamaterials are now commonly found in everyday life for example mobile phone antenna. The field is growing because metamaterial devices open up a wide platform for development and applications. Applying photonic technological concepts in the field of biology has been the key motivation for this project. This thesis describes the numerical simulations of the MM designs and the nano-fabrication of the metamaterial devices such as A-SRRs, dipole, split H-shaped, A-SRRs on waveguide and antenna structures. The goal of the research is to design different types of structures and determine the MM devices that produce a more sensitive and higher quality sensor. The step by step procedures followed through to reproduction of the fabricated nano-devices was imitated from processes established by other James Watt Nanofabrication centre (JWNC) clean room users. Continuous reproduction and reliable fabrication of the devices has always been a big challenge due to frequent updates in the JWNC facilities used.

The major contribution of my work has been the production of what I believe to be very high Q-factor devices produced from lossy MM structures in mid-infrared region. This was achieved firstly with the existing structure A-SRRs and secondly by introducing a new structure split asymmetric H-shaped (ASH) metamaterial. A-SRRs on waveguide were also realised in different ways, by design and fabrication of the structure on silicon on insulator (SOI) sample. Micro antenna structures are also fabricated on indium phosphide sample. Lastly the MM structures designed were experimentally used to detect presence of  $17\beta$ -estradiol. The author also numerically modelled a near-perfect match to the experimental result for the  $17\beta$ -estradiol molecular resonance using the Drude model.

There are new approaches developed by the author for the numerical simulation of the design such as investigating how the periodicity and gap length affect the Q-factor for a good FOM MMs device. In the fabrication process the resist thickness, exposure and development recipe was modified to suit metallization of the developed patterns. The novel split H-shaped structure utilises the two main polarisations and produce a higher sensitivity when compared with the other MM devices such as dipoles.

## 1.3 Structure of the Thesis

The thesis is composed of seven chapters:

- Chapter 1: Introduction

This introduces the thesis, providing context, motivation and contributions.

- Chapter 2: Metamaterial Concepts

The concept of metamaterial and photonic sensors is briefly explained here. This background is necessary to understand the design and challenges associated with the operating principle of photonic sensors based upon metamaterials. Also basic concepts of propagating EM signal into metamaterial structures are presented.

- Chapter 3: Modelling and Simulation

This chapter introduces the background to design of the metamaterial devices such as A-SRRS, dipole and split asymmetric H-shaped. There is a breakdown of what can be considered a numerical simulation that employs the finite difference time domain (FDTD) and a brief summary of the software package, Lumerical use for the modelling and simulations. The work presented in chapter three provides motivation and base for the proposed fabrication procedures presented in the next chapter.

- Chapter 4: Fabrication of Metamaterial Devices

Explains the fabrication processes used and the author highlights the main features in the computer aided design (CAD) tools, pattern writing using Electron-Beam Lithography (EBL), development of the patterns, metallization and etching techniques, during the fabrication of various devices presented in the modelling chapter. Details of the recipes used to fabricate metamaterial devices and the results achieved. Also included are notes of the major problems and suggestions towards updating the processes. This explanation is followed by analysis of Fourier Transform Infrared measurements (FTIR) in comparison to simulation results to understand the effects of fabrication tolerance.

- Chapter 5: Experimental Results

Explores a collection of different experimental results from the fabricated metamaterial devices presented in the chapter four. An explanation of the FTIR apparatus used is included. Special attention is given to the metamaterial devices such as A-SRRs and ASHs which were the main structures optimised for the high sensitivity purpose of this work.

- Chapter 6: Detection of 17 $\beta$ -Estradiol

Presents simulation and experimental results relating to the previous work of A-SRRs, SSHs and ASHs discussed in this thesis. This chapter starts by describing the modelling environment used, and validating the environment as well as the numerical models in use. The sensing experimentation of 17 $\beta$ -estradiol is then evaluated, including comparison of the sensitivity for different metamaterial structures. Results from ASHs structure with brief analysis and suggestions for further work were included.

- Chapter 7: Future work and Conclusions

Future works performed during the project period are presented in this chapter. Possible future work and suggestions on how to improve the metamaterial designed devices presented in this thesis are discussed. This chapter also concludes the work based on metallic metamaterial presented in this thesis. The strengths, and weaknesses of the work are summarised, and extent to which the original research motivation has been achieved is highlighted. Reasons for not presenting the measurement results of the fabricated A-SRRs on waveguide are briefly explained.

## 1.4 References

2. V. G. Veselago, "The electrodynamics of substances with simultaneously negative values of permittivity and permeability," *Soviet Physics Uspekhi*, 10, 509-514, 1968.
3. J. B. Pendry, A. J. Holden, D. J. Robbins, and W. J. Stewart, "Magnetism from Conductors and Enhanced Nonlinear Phenomena," *IEEE transactions on microwave theory and techniques*, 47, 2075-2084, 1999.
4. C. Debus and P.H. Bolivar, "Frequency selective surfaces for high sensitivity terahertz sensing," *Appl. Phys. Lett.* 91, 184102, 2007.
5. B. Lahiri, A. Z. Khokhar, R. M. De La Rue, S. G. McMeekin, and N. P. Johnson, "Asymmetric split ring resonators for optical sensing of organic materials," *Optics Express*, 17, 1107-1115, 2009.
6. L. La Spada, F. Bilotti, and L. Vegni, "Metamaterial-based sensor design working in infrared frequency range," *Progress In Electromagnetics Research B*, 34, 205–223, 2011.
7. J. Yao, Z. Liu, Y. Liu, Y. Wang, C. Sun, G. Bartal, A. M. Stacy, and X. Zhang, "Optical Negative Refraction in Bulk Metamaterials of Nanowires," *Science* 321, 2008.
8. B. Wang, J. Zhou, T. Koschny, M. Kafesaki, and C. M. Soukoulis, "Chiral metamaterials: simulations and experiments," *Journal of Optics A Pure and Applied Optics* 11, 2009.
9. I. Sersic, M. Frimmer, E. Verhagen, and A. F. Koenderink, "Electric and Magnetic Dipole Coupling in Near-Infrared Split-Ring Metamaterial Arrays," *Phys. Rev. Lett.* 103, 213902, 2009.
10. Z. Jacob, L. V. Alekseyev, and E. E. Narimanov, "*Optical Hyperlens*: Far-field imaging beyond the diffraction limit," *Opt. Express* 14, 8247, 2006.
11. M. G. Blaber, M. D. Arnold, and M. J. Ford, "Designing materials for plasmonic systems," *J. Phys. Cond. Mat.* 21, 144211, 2009.
12. P.R. West, S. Ishii, G.V. Naik, N.K. Emani, V.M. Shalaev, and A. Boltasseva, "Searching for better plasmonic materials," *Laser & Photonics Reviews* 4, 795–808, 2010.
13. N. Engheta, "Taming Light at the Nanoscale," *Physics World*, 23, 31-34, 2010.
14. A. Boltasseva, and H. A. Atwater, *Science* 331, 6015, 2011.
15. I. A. I. Al-Naib, C. Jansen, and M. Koch, *Appl. Phys. Lett.* 94, 153505, 2009.
16. J. Shu, W. Gao, K. Reichel, D. Nickel, J. Dominguez, I. Brener, D. M. Mittleman, and Q. Xu, *Opt. Soc.* 22, 3748-3753, 2014.

17. V. G. Kravets, F. Schedin, and A. N. Grigorenko, *PhysRevLett*, 101, 087403, 2008.
18. Y. Moritake, Y. Kanamoria, and K. Hane, *Proc. SPIE*. 9371, Photonic and Phononic Properties of Engineered Nanostructures 5, 2078784, 2014.
19. J. Breeze, M. Oxborrow, N. M. Alford, *Appl. Phys. Lett.* 99, 113515, 20011.
20. J. Zhang, K. F. MacDonald, and N. I. Zheludev, *Opt. Soc. Am.* 39, 4883-4886, 2014.
21. Wu, C., N. Arju, G. Kelp, J. A. Fan, J. Dominguez, E. Gonzales, E. Tutuc, I. Brener, and G. Shvets, *Nature Communications* 5, 3892, 2014.
22. Y. Yang, I. I. Kravchenko, D. P. Briggs, and J. Valentine, *Nature Communications* 5, 6753, 2014.
23. La Spada, L., F. Bilotti, and L. Vegni, "Metamaterial biosensor for cancer detection," *IEEE Sensors*, 627–630, 2011.
24. C. Drexler, T. V. Shishkanova, C. Lange, S. N. Danilov, D. Weiss, S. D. Ganichev, and Vladimir M. Mirsky, "Terahertz split-ring metamaterials as transducers for chemical sensors based on conducting polymers: a feasibility study with sensing of acidic and basic gases using polyaniline chemosensitive layer," Springer-Verlag Wien, 1007, 2014.
25. S. J. Park, J. T. Hong, S. J. Choi, H. S. Kim, W. K. Park, S. T. Han, J. Y. Park, S. Lee, D. S. Kim, and Y. H. Ahn, "Detection of microorganisms using terahertz metamaterials," *Scientific Reports* 4, 4988, 2014.
26. I. G. Mbomson, B. Lahiri, S. G. McMeekin, R. M. De La Rue, and N. P. Johnson, "Gold asymmetric split ring resonators (A-SRRs) for nano sensing of estradiol," *Proc. SPIE*. 9125, 91251O, 2014.
27. B. Lahiri, R. Dylewicz, R. M. De La Rue, and N. P. Johnson, "Impact of titanium adhesion layers on the response of arrays of metallic split-ring resonators (SRRs)," *Optics Express* 18, 11202-11208, 2010.
28. V. A. Fedotov, M. Rose, S. L. Prosvirnin, N. Papasimakis, and N. I. Zheludev, *PhysRevLett*, 99, 147401, 2007.
29. Pryce, I. M., Kelaita, Y. A., Aydin, K., and Atwater, H. A., "Compliant Metamaterials for Resonantly Enhanced Infrared Absorption Spectroscopy and Refractive Index Sensing," *Nano Lett.* 5, 8167-8174, 2011.
30. CK. Chen, MH. Chang, HT. Wu, YC. Lee, and TJ. Yen, "Enhanced vibrational spectroscopy, intracellular refractive indexing for label-free biosensing and bioimaging by multiband plasmonic-antenna array," *Biosens Bioelectron.*, 60, 343-350, 2014.

# CHAPTER 2

## METAMATERIAL CONCEPTS

### 2.1 Introduction

Metamaterials are arrays of repeated substances that derive their characteristics from the structures and not from the material composition. Naturally, material fundamental parameters such as magnetic permeability ( $\mu$ ) and electrical permittivity ( $\epsilon$ ) determine the material response to electromagnetic radiation but metamaterials exhibit their electromagnetic properties beyond the various materials found in nature [1]. Thus, metamaterials are associated with negative  $\mu$  and  $\epsilon$  parameters over a band of wavelengths with the ability to tune resonances to desired areas of the EM spectrum through the structural size and geometry. However, it should be noted that neither negative  $\mu$  nor  $\epsilon$  are necessary to define a metamaterial. The defining feature of a metamaterial is that the structural elements are sub-wavelength and that their arrangements determine the metamaterial properties.

Since the publication of the first literature proposing the existence of material with negative properties [2], many researchers have reported their findings [3-5]. The theory of the metamaterials is covered extensively in these papers [3-5]. Based on the concept of determining metamaterial properties through the structural arrangement, the fundamental theory of metamaterial was used to re-engineer and design different types of MM structures. These structures enable realisation of highly sensitive MM based sensors.

This chapter is divided into two sections, the background of metamaterials and illustration of how they are applied in this project. A-SRRs metamaterial is used as the guiding structure for re-engineering and designing of other MM structures presented in this thesis.

The basic concepts of metamaterials: such as negative  $\mu$  and  $\epsilon$  material properties, resonance tuning in the EM spectrum which depends on the geometrical parameters of various sub-wavelength scale MM structures, periodicity and gap between elements of different devices are introduced in the first section. In the second section, the operational concepts of plasmonics sensors based on MM were explained. Analysis on the technological application of the devices is also presented.

## **2.2 Metamaterials**

The artificial materials, metamaterials are associated with the fact that light propagates in a completely different way. This is when  $\mu$  and  $\epsilon$  are both negative. The study of these types of material structures has rapidly advanced both in theory and experiment since 1999 when Smith et al. [1] and Pendry [4] demonstrated how to make this metamaterial.

In the exponential growth of publications in the subject of metamaterial particularly the traditional MM structures, split ring resonators [6] are most common structure. The MM structures application based on photonic sensors devices has reached a level of sophistication along with other mechanical or electronic sensor devices in existence. These devices have shown higher enhancement factor and sensitivities [7-8] than the recent all-dielectric metamaterials [9-12] which have been used to reduce losses, particularly in mid-infrared region.

Over the years of MM structural developments, authors in this field of study have mostly worked in three EM spectral regions: microwave [13], infrared [7] and visible [14] which were determined by the dimension of the structures.

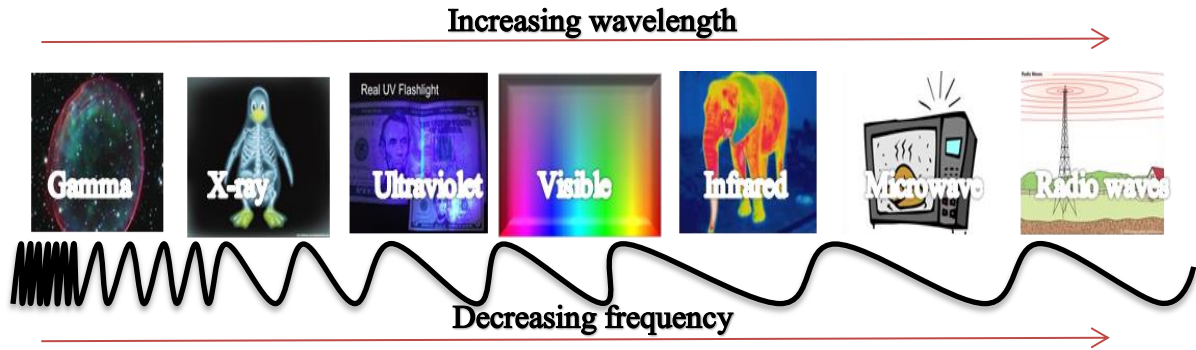


*Figure 2.1: Illustration of electromagnetic spectrum*

The MM structures presented in this work are designed to tune the plasmonic resonances in infrared region of the EM spectrum as shown in figure 2.1. The structures shown in figures 2.2 (a) and (b) are scaled such that their fundamental tuning elements which comprises of arcs of radius,  $R$  is (0.3 to 0.5)  $\mu\text{m}$  and the arms lengths,  $L$  is (0.9 to 1.5)  $\mu\text{m}$  produce resonance peaks in mid-infrared region. Arrays of gold A-SRRs patterns as shown in figure 2.2 (c) are modelled on a three dimensional (3D) in-plane ( $x, y, z$ ) of a fused silica substrate. The figure also shows a normal incidence radiation on the plane of MM structures. In EM wave the electric field ( $E$ ) and magnetic field ( $H$ ) are orthogonal to each other and also to the direction of propagation constant ( $k$ ) as shown in figure 2.2c. The propagation constant measures changes in the amplitude of EM wave as it propagates in a given direction; in this work it is in  $z$ -direction. The resonance peaks produced from MM structures behave differently at the different orientations which show a total dependence of the resonance on the structural orientation and radiation polarization [15-17].

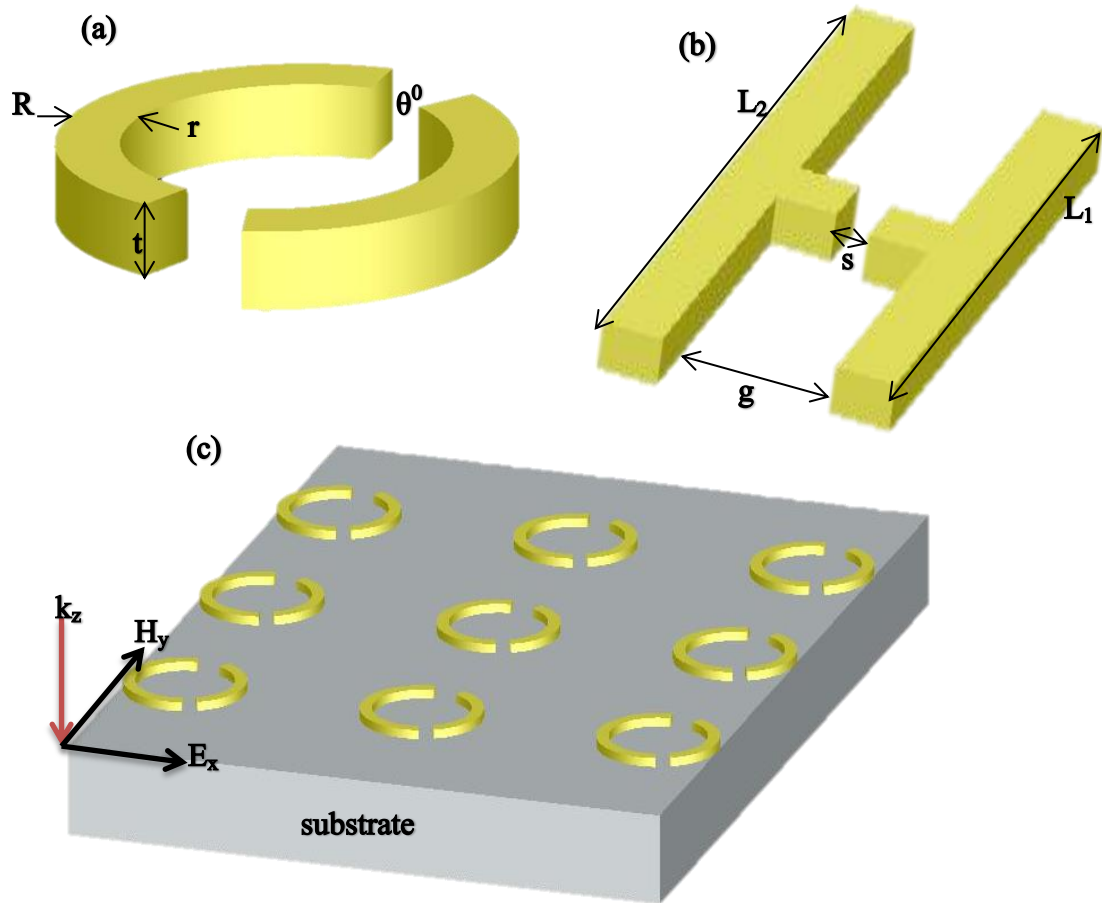


**Figure 2.2** Three dimensional MM structures with arc radii,  $R$ -  $r$ , angle,  $\theta^0$ , thickness,  $t$ , arm lengths,  $L_1$  and  $L_2$ , gap,  $g$ , slit,  $s$ : (a) A-SRR (b) ASH (c) Schematic of a three dimensional A-SRRs arrays on a fused silica substrate.

The description of the metamaterial is based on the fundamental equation (2.1) derived from electromagnetic plane wave equations. From the equations electric, magnetic and wave vectors form a left-handed metamaterial if  $\mu < 0$  and  $\epsilon < 0$  while the right-handed vector will be the case if the material properties are greater than zero. Details of this equation are stated in reference [2]:

$$[kE] = \frac{\omega}{c} \mu H ; \quad (2.1)$$

$$[kH] = - \frac{\omega}{c} \epsilon E ,$$

Where  $k$ ,  $E$  and  $H$  represent the wave vectors of the incident wave, electric field and magnetic field respectively and  $\omega$  is the frequency of an EM plane wave. The dielectric constant  $\epsilon$  and the magnetic permeability constant  $\mu$  are the fundamental properties of material which determines the EM wave propagation.

The metallic metamaterial structures such as A-SRR pattern design is based on a particular orientation derived from different orientations [1, 18] with respect to electric and magnetic fields ( $E$  and  $H$ ) and the direction of propagation constant as shown in figure 2.3.

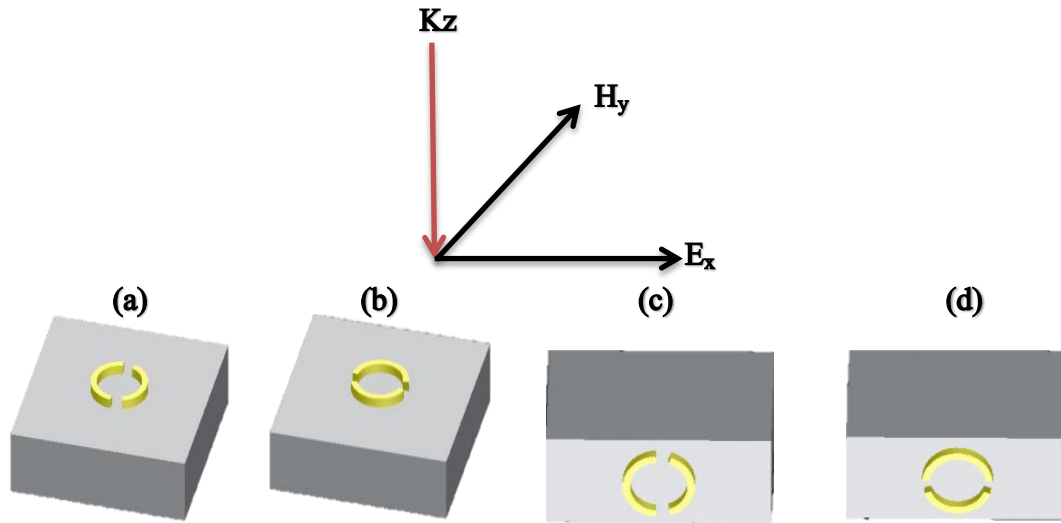


**Figure 2.3:** Sketch of A-SRR structure: Four orientations of the A-SRR studied with respect to the  $E$ ,  $H$  and  $k$  vectors of the incidence EM field with double gaps between the two asymmetric arcs.

Four distinct orientations as shown in figure 2.3 demonstrate a normally incidence EM wave to a substrate of an asymmetric split ring. References [1, 18] suggest that when the direction

of  $H$  is parallel to the A-SRR plane, figures 2.3(a & b) there is no coupling to produce magnetic resonance. Figures 2.3 (a and c) show electric field,  $E_x$  coupling across the gap which can produce magnetic resonance generated from circulating current while figure 2.3b is product of electric resonance which generates the plasmonic resonance. The excitation of the electric (plasmonic) resonances from A-SRR is produced along the arc length for electric field propagating along the arcs as shown in figures 2.3(b and d). These orientations are as a complementary to the work of the stated references, as also applied in the design of the MM structures for numerical simulation and experiment of this work. In this work, the resonance produced from simulation and experiment is based on the described orientations of the A-SRR of figure 2.3b.

An illustrative model is shown to reveal the concept of the MM design. From the illustrations on how the simulations and experiments design were performed in this work, the wave vector ( $k$ ) propagates perpendicular to the electric and magnetic plane. The gap between the two asymmetric arcs is analogous to the capacitance in inductor-capacitor (LC) circuit. The operating principle of metamaterial structures can be described by using the basic idea of materials science and engineering. Most of the established theories used in studying the topic are LC (inductor-capacitor) circuit resonance and electromagnetism in physics can be applied in the design and orientation of MM structures to match the EM wave polarization.

The magnetic resonance which arises from an LC circuit occurs when the incident EM wave is normally on A-SRR plane and the electric field of the incident source is coupled through to the capacitance [15]. The conventional LC circuit as shown in figure 2.4 (a) is used either for signal generation or filtering out a signal at a particular wavelength from a broad band signal.

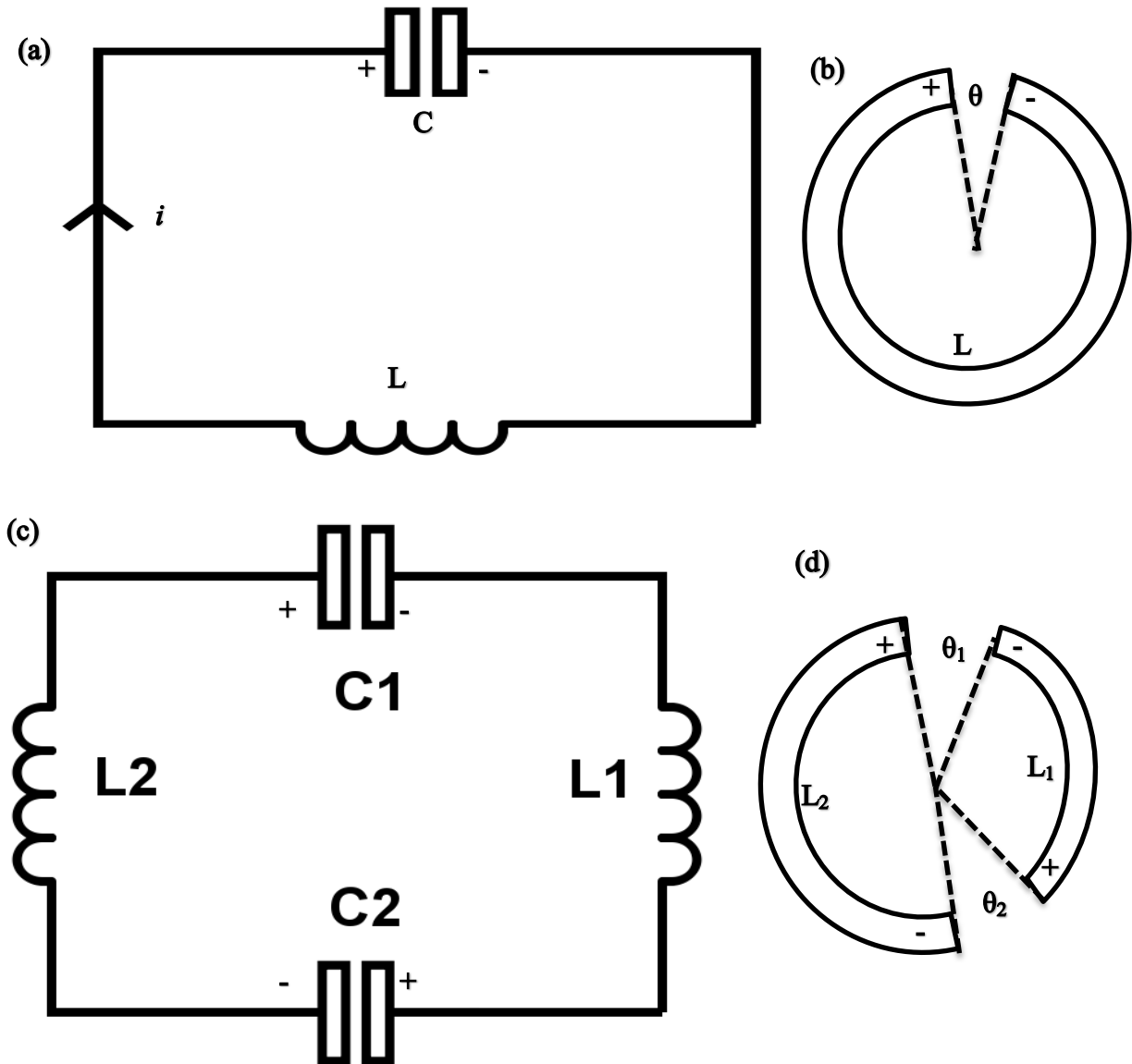


**Figure 2.4:** Sketch illustrating the analogy between a simple conventional inductive-capacitive (LC) circuits design (a), where (c) consist of two capacitors ( $C_1$  and  $C_2$ ), two inductances ( $L_1$  and  $L_2$ ) while (b) & (d) show the single and the double split ring resonators, arc width ( $L_1$  and  $L_2$ ) and gap or angle ( $\theta_1$  and  $\theta_2$ ) between the two asymmetric arcs.

In this present work, the resonances produce from EM wave normally incident on MMs such as SRR reveals the fundamental theory of LC resonance generator. Here, the incident EM wave can couple to LC resonance as shown with the simplified LC circuits of figures 2.4(a &

c) for the A-SRR metamaterial. For figures 2.4(b & d) the gap and the arc length represent the capacitance and inductance of the LC circuit respectively. The incident wave is able to couple to produce resonance if either of the following criteria is certified: E-field vector of the incident light has a component normal to the plates of the capacitor, or H-field vector of incident light has a component normal to the plane of the coil [19]. These metamaterials phenomenon produces a magnetic resonance reflectance peak and dip for transmittance within EM spectra. Works [20-21] on numerical calculations for a finite length of MM have been performed. For a finite geometric MM such as arc of a homogenous material, the complex reflection and transmission coefficients are related to the impedance  $z$  and refractive index  $n$  associated with resonant frequency/wavelength. The permittivity  $\mathcal{E}$  and permeability  $\mu$  of a finite MM are obtained from the fundamental material properties [22];

$$n = \sqrt{\varepsilon\mu} \quad \text{and} \quad z = \sqrt{\frac{\mu}{\varepsilon}} \quad (2.2)$$

For the transmission coefficients, the transfer-matrix method was previously used by Pendry et al to calculate the EM field through photonic band-gaps [23-24] while here finite-difference time-domain (FDTD) method is used for the MM structures. FDTD being a time domain method was used to provide simulation results at wide range of wavelengths with a single simulation.

Drude model [25] was applied in the method to describe the dispersive nature of the metallic (gold) material. According to the model, the dielectric function of free electrons,  $\mathcal{E} = \mathcal{E}_{real} + i\mathcal{E}_{imaginary}$  can be expressed in the following equations [26]:

$$\mathcal{E}_{real} = \varepsilon_{\infty} - \frac{\omega_p^2}{\omega^2 + \tau^2} \quad (2.3)$$

$$\mathcal{E}_{img} = \frac{\omega_p^2 \tau}{\omega(\omega^2 + \tau^2)} \quad (2.4)$$

Where  $\omega_p = \sqrt{\frac{ne^2}{m\varepsilon_0}}$  and  $\omega = 2\pi f$

The definition of the expressions is as follows:  $\epsilon_\infty$  is the dielectric electric constant at infinite frequency,  $\tau$  is the reciprocal relaxation time, and  $\omega_p$  is the plasma frequency which involves  $m$ , mass of free electrons.

The model was applied to produce simulations of the transmission plots as shown in figure 2.5. The spectral plot is a product of mid-infrared source incident on the plane of gold patterned A-SRR structures. The modelling of asymmetric patterns produces the resonance peaks from the effective material properties based on the equations of dielectric constant. The absorption was calculated by the expression;  $\text{Absorption} = 1 - R - \text{abs}(T)$ , where  $R$  is the reflectance and  $\text{abs}(T)$  is the absolute transmission value. A full description of how the simulation was performed is included in chapter three of this work.

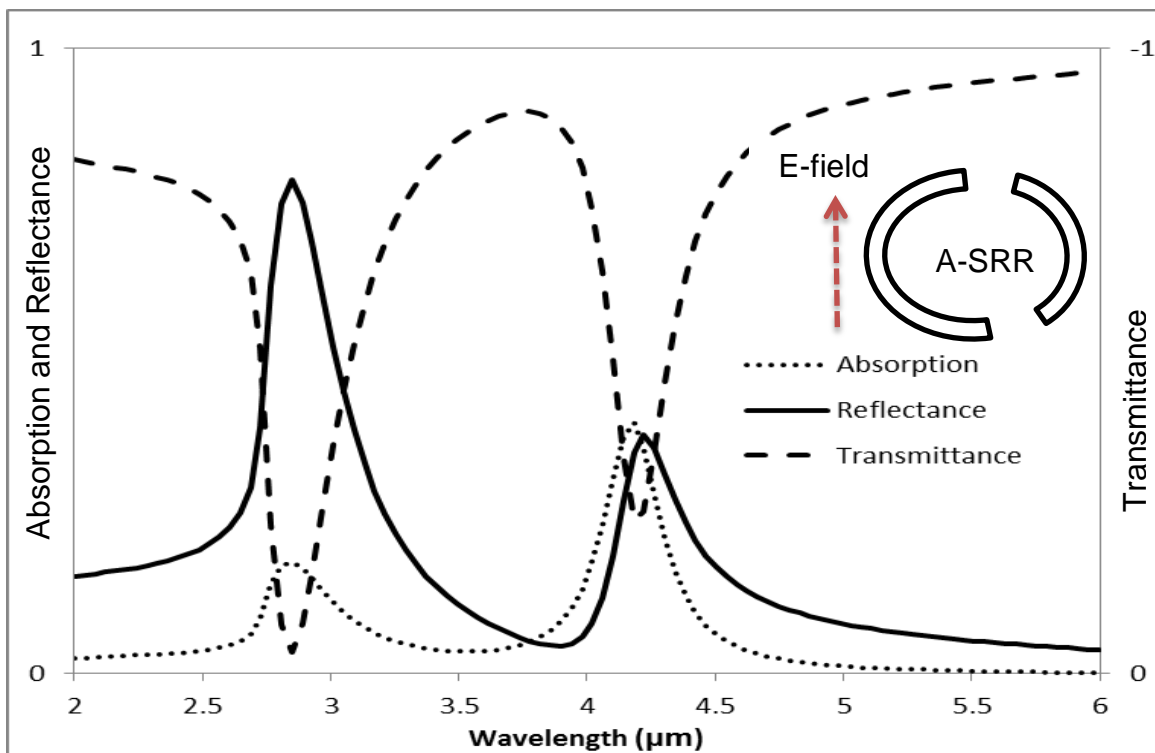


**Figure 2.5:** Transmittance, reflectance and absorption spectra from FDTD simulation showing polarisation of E-field parallel to the A-SRR (inset) arcs.

The polarization of the EM wave is crucial because there are well defined fields at the incident source. Thus the description of the electric and magnetic fields component are

included in order to determine the polarisation properties. The polarization properties of the field are determined from the amplitude of the MM components such as the x, y and z components. A three dimensional (x, y, z) split ring resonator is designed with FDTD software, Lumerical to produce a resonance peak when E-field is parallel to the arcs, as shown in figure 2.6. The figure also shows a resonance peak resulting from the fused silica substrate at both polarisation of E-field parallel to the arcs and across the gap.

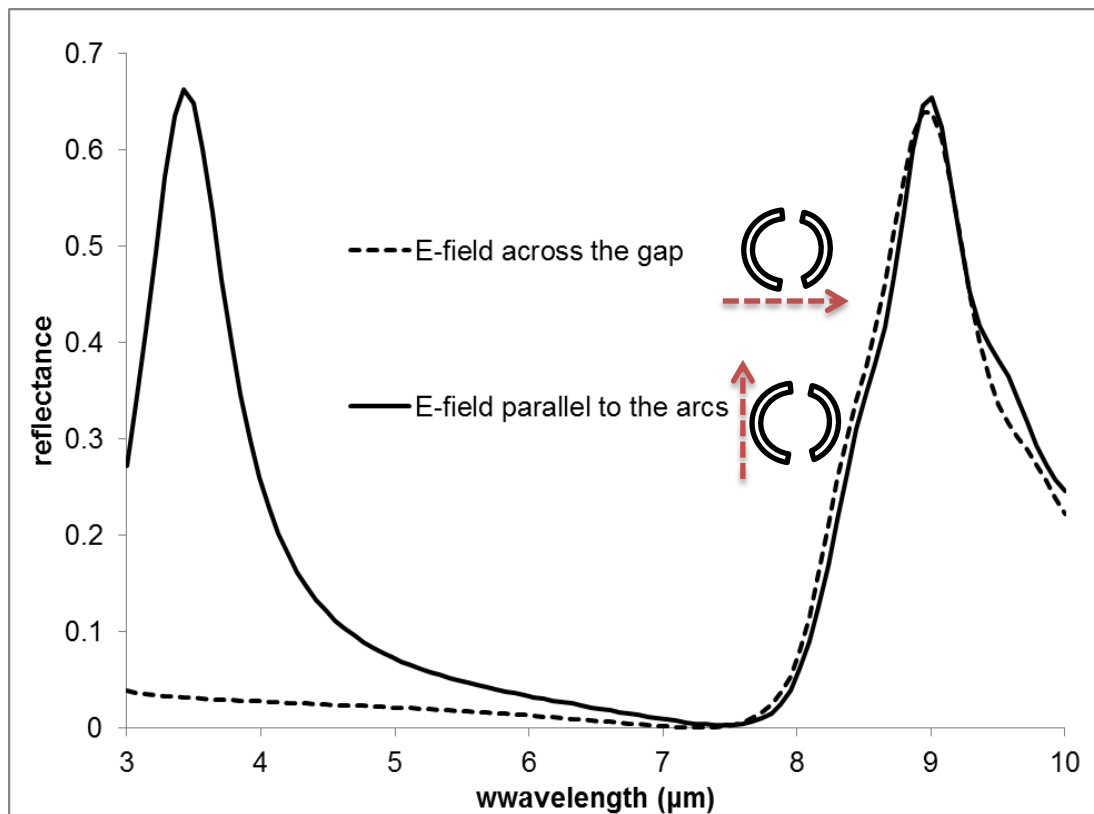


**Figure 2.6:** Reflectance spectra of E-field polarisation for asymmetric a split ring resonator (SRR).

The reflectance spectra plots for the two different polarisation of the E-field with respect to the designed MM structure was tuned to produced plasmonics resonance peak at 3.42  $\mu\text{m}$  while the peak from the fused silica occurs at 9.0  $\mu\text{m}$  as shown in figure 2.6. Figure 2.7 shows examples of electric field plots at a particular wavelength (3.4 and 9.0)  $\mu\text{m}$  position for the three components from reflectance monitor of Lumerical. From the spectral plots the

polarization of E-field across the gap results to zero plasmonics resonance but magnetic (LC) resonance was produce which demonstrated the coupling of the current across the gap.

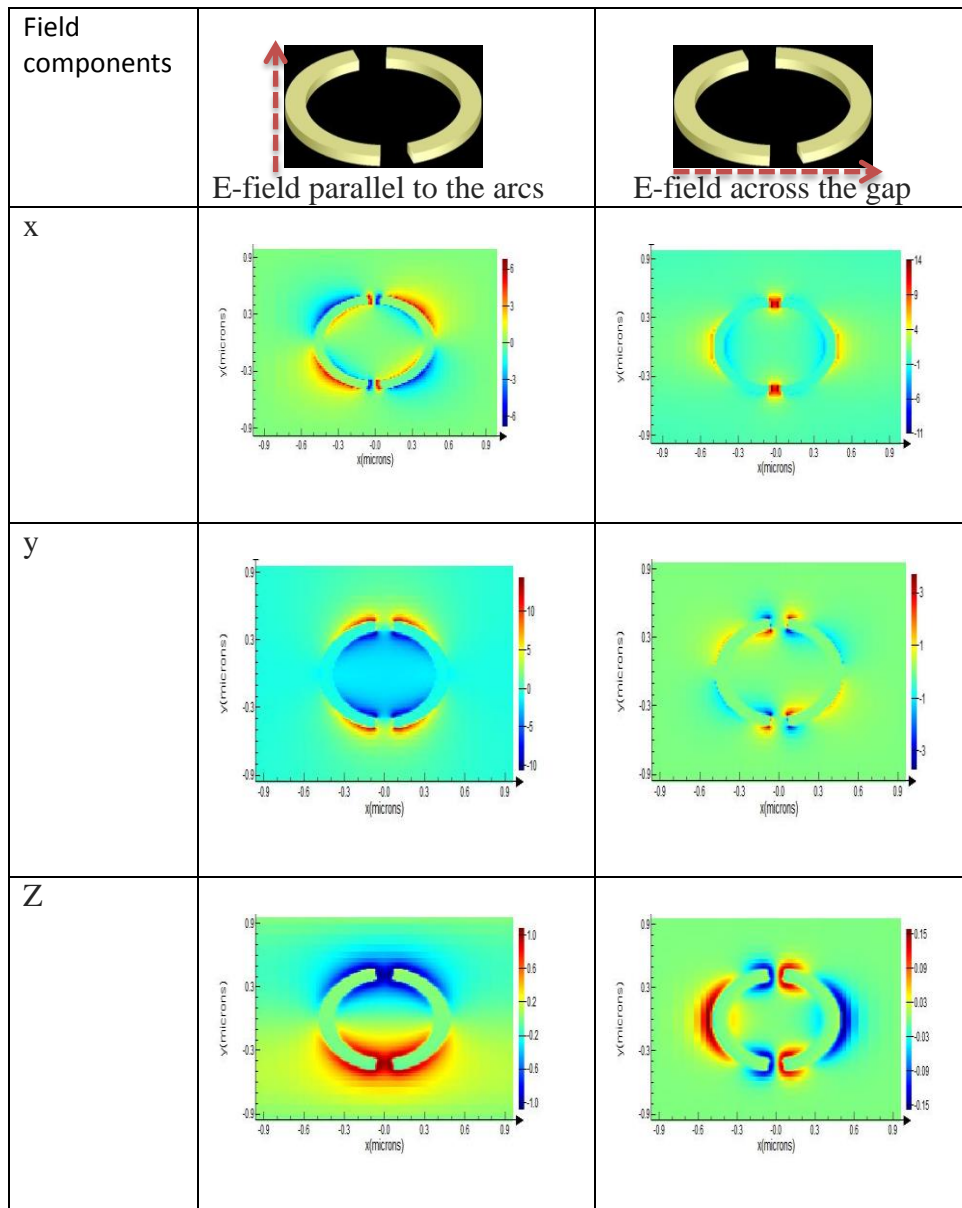


**Figure 2.7:** E-field polarisation plots for the designed MM device components.

The red and blue colours in the field plots indicate the maximum and minimum E-field which corresponds to the magnitude of the spectra plots of figure 2.6. Here the two colours red and blue are also used to explain the electric charges of the device. The E-field plots for the three components showed greater field strength values on the colour bars from plasmonics resonance at  $3.42 \mu\text{m}$  than the LC resonance at  $9.0 \mu\text{m}$ . Thus, the E-field at this particular polarization with respect to the designed split ring resonator produces the required resonance

peak. The second and third column of figure 2.7 showed the field plots produced when the E-field is parallel and across the gaps respectively for a split ring resonator. The corresponding wavelengths of the E-field are 3.42  $\mu\text{m}$  for the second column and 9.0  $\mu\text{m}$  for the third column of the figure.

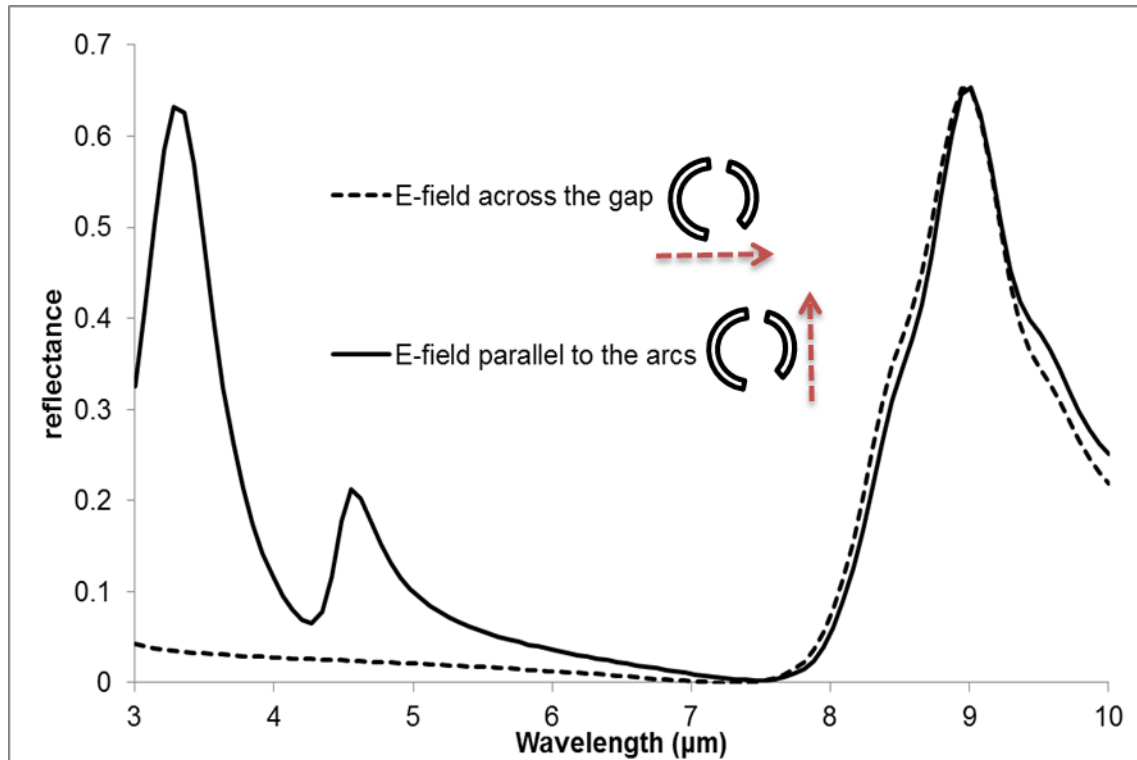


**Figure 2.8:** Reflectance spectra of E-field polarisation for asymmetric split ring resonators (A-SRR).

Again, the design for asymmetric split ring resonator (A-SRR) using similar polarisation of E-field produces the plasmonics at the expected tuned wavelength position and resonances peak from fused silica as shown in figure 2.8. The A-SRR produced a second resonance peak at 4.6  $\mu\text{m}$  due to asymmetric nature of the MM structure. This research is concentrated on the asymmetric MM structure which produces double resonance peaks. Understanding and manipulating the described E-field parallel to the arcs helps in production of an optimized reflectance resonance peaks for the sensors based on MM applications. It has been shown

here that E-field at polarization parallel to the electric conductor, gold (inductor in case of LC circuit) produces the plasmonic resonances.

## 2.3 Plasmonics

Plasmonics is analogy to electronics using plasmons. In physics, a plasmon is the quantum of the collective excitation of free electrons in solids. Plasmonic nanoparticles are particles whose electron density can couple with electromagnetic (EM) radiation of wavelengths that are larger than the particle due to the nature of the dielectric-metal interface between the medium and the particles. The theory of plasmonics is dated as far back as 1950's when some researchers Ritchie, Kretschmann and Otto [27-29] published their findings from light incident on dielectric and metal interfaces. Figure 2.9 shows that surface plasmonic can exist at interface between a metal ( $\epsilon < 0$ ) and a dielectric medium ( $\epsilon > 0$ ).

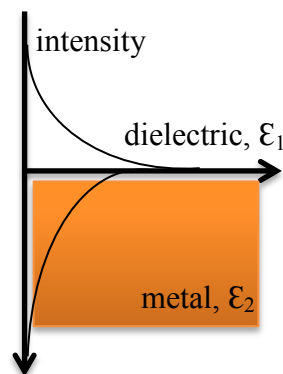


*Figure 2.9: Exponential decay of field into two different materials*

The illustration composed of EM wave in the dielectric medium and oscillating electron plasma in the metal where both modes have an exponentially decaying evanescent character. Over the years, many photonic sensing systems which comprises of a thin film metal and a bulk dielectrics have been developed utilizing the sensitivity of surface plasmonic resonance (SPR) to the changes in the system surrounding environment [30]. The SPR occur as a result of a resonant interaction between an illuminating EM wave and a collective electron density

oscillation of the free electrons of the conductor. These phenomena can take various forms ranging from freely propagating electron density waves along metal surfaces to localised electron oscillations on metal nanoparticles. Their unique characteristics enable a wide range of applications such as manipulation at the nanoscale, detection of biological analyte at a single molecule level and enhancement of molecular resonances [7-8, 31-34].

## **2.4 Photonic sensors based on metamaterial**

The use of metamaterial as a sensor device is of great interest in many fields such as medicine, environmental, bio-chemistry, then security and defence. Photonic sensors based on plasmonic resonances of metamaterial were numerically modelled several years ago (2005) by A. Ishimaru et al [35]. The reference illustrated the use of a sharp resonance peak in the reflection coefficient to analyse material characteristics and determine metamaterial features. In this work, the developed MM device that produces plasmonic resonance can be classified as photonic sensors. Photonics is generally described as science of light (photon). The photon manipulation can occur following different criteria such as light generation, transmission, amplification, modulation and sensing. These criteria are mostly used to define the photonics application in some research areas. The photonic sensor based on the developed MM structures has been used in sensing a chemical analyte in mid-infrared region. Photonic sensing technology is increasingly used in early-detection and monitoring systems for structural flaws, security threats and biological hazards [36]. The technology provides a comprehensive review of an exciting and fast evolving field, focusing on the development of cutting-edge various applications in a wide range of areas from biochemical detection to environmental monitoring.

The concept of analysing and exploring the use of metamaterial to produce surface plasmonic resonance subsequently follow the idea of using a white-light source to generate a large range of resonating wavelengths [37]. Thus, describing how to determine the sensed material from measured resonance spectrum through the transmission spectra intensity. Recently, many articles have been published on sensors utilizing the resonances produce from metamaterial

device across the EM spectrum [7, 38-40]. The plasmonic resonance resulting from the traditional metamaterial, devices have been widely and commonly used as the basis for photonic sensors.

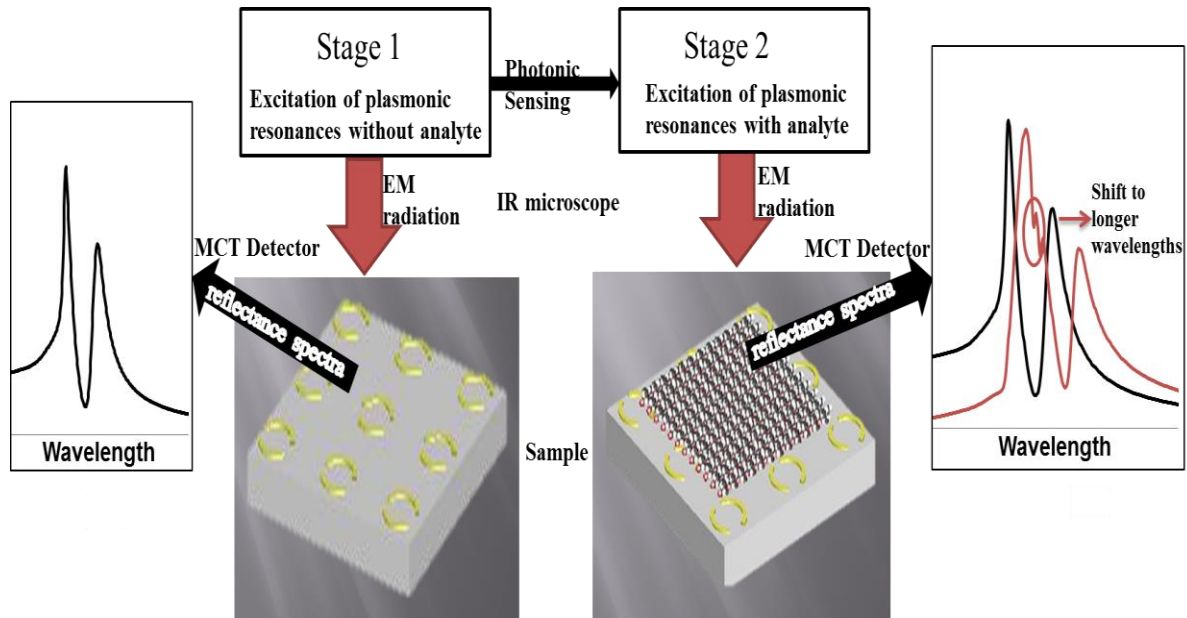


**Figure 2.10:** Block diagram of a photonic sensor showing infrared (IR) excitation of resonances from EM radiation on arrays of A-SRRs structure and then with analyte which produces a shift to longer wavelengths of electromagnetic (EM) spectrum.

Figure 2.10 shows the block diagram of a photonic sensor. Mercury cadmium telluride (MCT) is an infrared detector used for the measurements. In stage I of the diagram, there is a coupling of EM source through a dielectric (air) normally into arrays of A-SRRs structures. Reflectance spectra produced from the excitation of arrays asymmetric structure are usually a double plasmonic resonance peaks as shown in the figure. Presence of analyte in stage 2 replaced the initial refractive index of air surrounding the sensors. In this case, the introduced analyte in the sensors surroundings has a higher refractive index than air thereby shifting the resonance peaks to longer wavelength of the EM spectrum. The sensitivity of photonic sensors depends on the resonance peak shift. Again, the sensor enhances other molecular resonances present in the targeted wavelength region of EM spectrum. An example of a photonic sensor that closely relate the sensor used in this work is a biosensor. A biosensor is an analytical device that employs biological material for a specific interaction with an

analyte. Different types of biosensors such as screen-printed carbon electrochemistry (SPCE) [41], gas chromatography-mass spectrometry (GC-MS) [42], gold electrode surface via under-potential deposition (UDP) [43] and aptamer-based optical fibre [44, 45] which may not be characterise with change in the refractive index that leads to shift in the resonance peak have been used to detect the  $17\beta$ -estradiol analyte. In this work,  $17\beta$ -estradiol is the chemical material analysed with the developed photonic sensors. The technological advantages of using plasmonic resonances for sensing this analyte have also been compared and presented in these references [46-48].

There has been a continuous optimization and development of new structures in order to obtain high sensitivity and enhanced performances of the sensors at microwave, terahertz and infrared spectral region. This research is focused on sensing at mid-infrared with the MM devices. Figure 2.11 show the spectral features of water vapour ( $H_2O$ ) and carbon dioxide ( $CO_2$ ) in the region of operation [49-50].

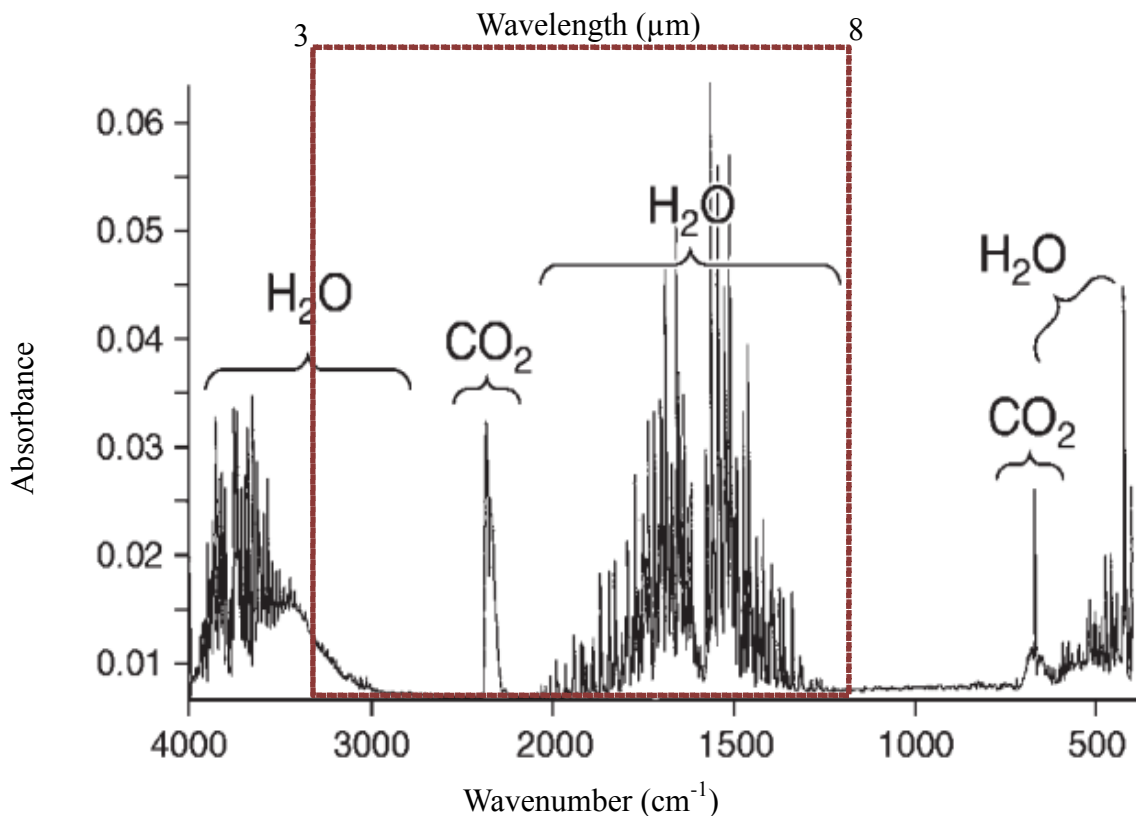


**Figure 2.11:** Water vapour and carbon dioxide bands in the infrared spectrum [50].

These features are present in all the experimental measurement results of this work. The present work uses reflectance spectra of Fourier transform infrared spectroscopy (FTIR) for the measurements. The detection target for the resonance peaks here is designed for a chemical analyte which exhibit vibrational resonances of different molecular bonds as shown in figure 2.12 [51].

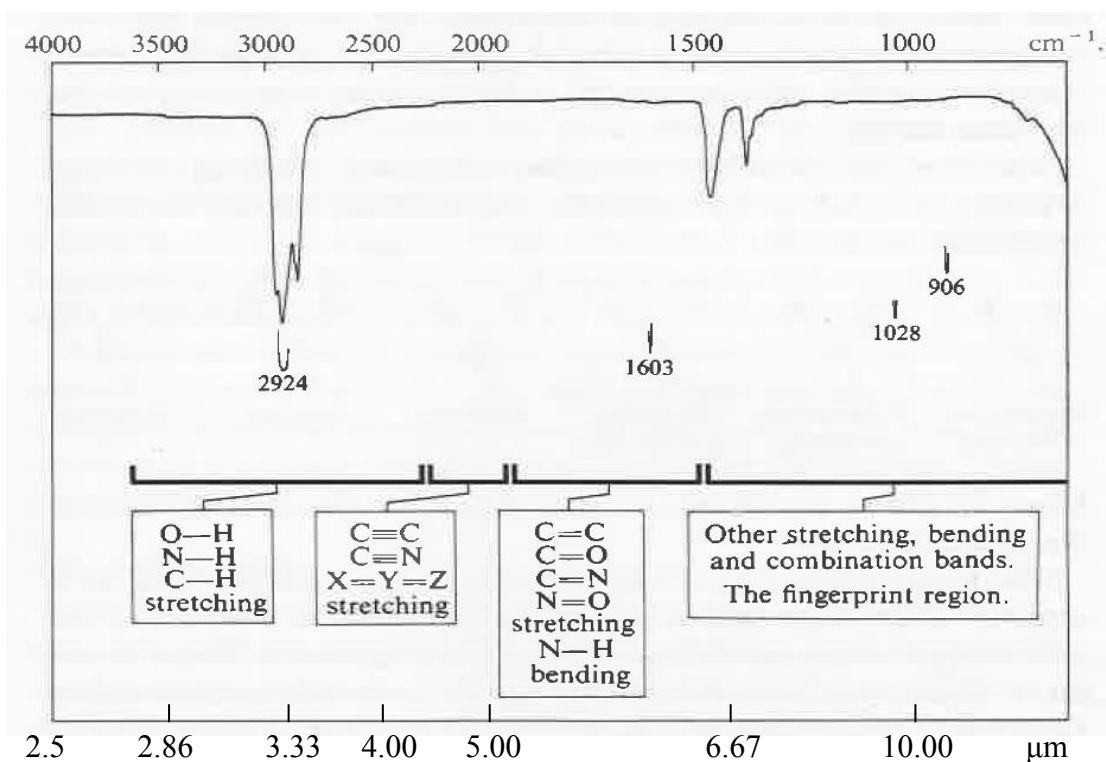


**Figure 2.12:** Common molecular resonances in the IR from spectroscopic methods in organic chemistry by Williams and Fleming [51].

Specifically, the analyte detected here is  $17\beta$ -estradiol which exhibits C-H and C=C vibrational resonances between 3  $\mu\text{m}$  to 8  $\mu\text{m}$  wavelength [52-53] and the C-H is analysed in chapter 6 of this work. The vibrational resonance from these bonds is the guide for the design of MM symmetric and asymmetric structural devices presented here.

## **Functionalization**

Increasing interest for protein biochip in the field of biomedical applications has been focused on surface activation and subsequent functionalization approaches for immobilization of various biological molecules. Different functionalization approaches that use covalent and non-covalent chemistry with emphasis on the chemical specification of protein attachment and on retention of protein function have been presented [54]. Examples of these approaches include wet chemical treatment, plasma treatment, radiation and photo-grafting or through fabrication of integrated biochip and micro-fluidic channel [54-59]. Over the years, surface of sensors based on metallic metamaterial is usually treated using the listed strategies to form a specific reactive functional group for immobilization of protein. References [59-61] have used different types of material such as polydimethylsiloxane (PDMS) and thiols to make the attachment or functionalize biomolecules to surface of nanostructures used for sensing application. Thiols are the sulphur analogue of alcohols and it has a specific attraction to biomolecules while PDMS which belong to a group of polymeric organosilicon compounds is commonly used for flow delivery in microfluidics chips of a biosensor device.

A specialize functionalization approach as explained above may not be employed to all photonic sensing applications. This approach distinguishes the photonic sensing application of this work with a typical biosensor device. A biosensor employs biological material for immobilization or a specific interaction with an analyte. The analyte 17 $\beta$ -estradiol used in this work was dissolved in ethanol before depositing the mixture on to MM device surface. The solvent ethanol was allowed to evaporate before proceeding to measurement as explained in chapter six.

## **Figure of Merit (FOM)**

Figure of merit is a numerical expression used to characterize the efficiency or performance of sensor devices. This can be defined as the ratio of sensitivity (S) divided by full width half maximum (FWHM) of a resonance and it is expressed as [62]:  $S/ \text{FWHM}$ . This parameter allows the efficiency of nanostructures to be compared against one another when use as a sensor, irrespective of the dimensions or shape of the structure. The sensitivity of a sensor is ratio of a wavelength shift ( $\Delta\lambda$ ) to change in refractive index ( $\Delta n$ ). FOM is known to be a

key parameter of sensor devices and it is determined by the sensitivity with which very small wavelength changes can be measured. Sharpness of a resonance peak is also supported by this parameter. Production of a narrow line width of plasmonic resonances or sharp resonances increases the FOM of sensor devices [63-65]. This criterion relates the FOM of devices to another important parameter of sensor devices known as quality factor.

Quality factor (Q-factor) is a dimensionless parameter that describes how under-damped a resonator can be and it characterizes the resonator's bandwidth relative to its centre wavelength.

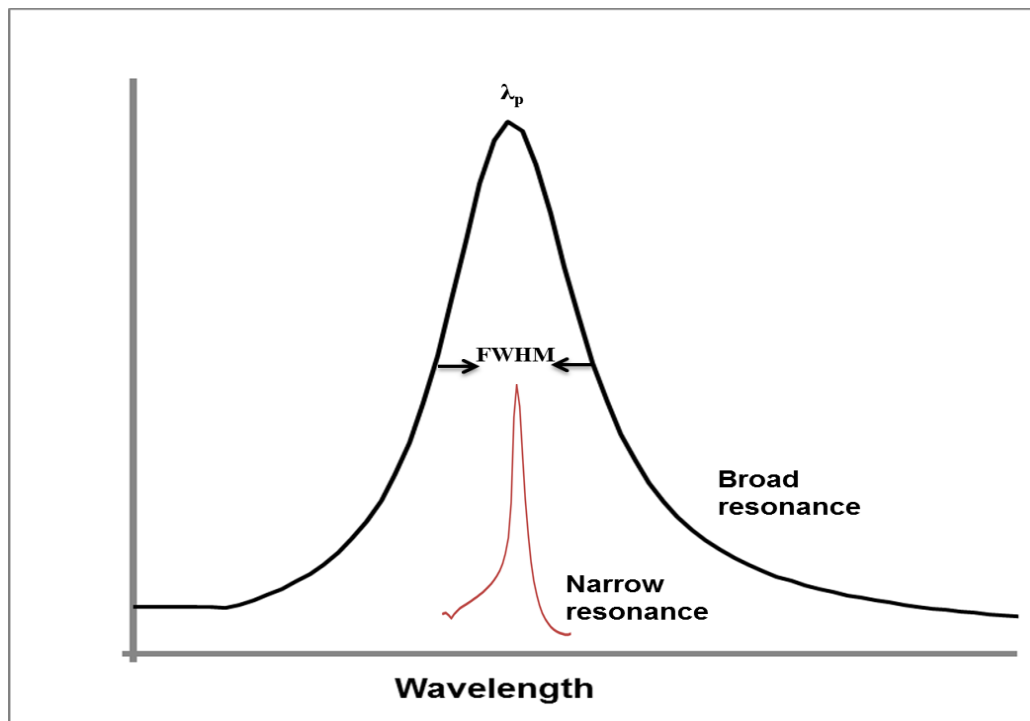


**Figure 2.13:** Schematic diagram of broad and narrow resonances with respect to wavelength position ( $\lambda_p$ ) and showing the Full width half maximum (FWHM) of a resonance.

Q-factor of plasmonic resonance is a measure of the goodness or quality of the device. A higher value of Q-factor corresponds to a narrow bandwidth of the resonance which is desirable in many applications. This factor supports the efficiency of sensor devices as explained with FOM. Figure 2.13 shows a schematic diagram of a broad and narrow resonance from which expression;  $\lambda_p / \text{FWHM}$  for Q-factor can be derived. This is the

expression employed in this work to calculate the Q-factor of the different metallic metamaterial developed. Effects from radiation or material losses which can result to low quality factor of a metamaterial devices have been presented [66-67]. Again, reference 67] stated that loss in metal which is the common fundamental material of the metamaterial device varies along the regions of electromagnetic spectrum. This effect leads to wide variation of Q-factor values achieve from MM structures at different regions of the EM spectrum.

## **2.5 Discussions and Conclusion**

This chapter has attempted to provide the main concepts of metamaterial for this research. It has also sought to introduce a few main parameters used to produce transmission spectral specifically reflectance and the characteristics of material structures used in the course of the work. As the aim of this project, is focused more on numerical simulation and experimental work. This is based on designing and optimising MM structures that will produce sharp spectral resonances. Production of a narrow line width of plasmonic resonances or sharp resonances increases the FOM of sensor devices. Sensors based on metallic metamaterial are the basis of this work; the operating principal of the device was described, demonstrating how the plasmonic resonance peaks produced from E-field parallel to conductor (metal) can be used as a photonic sensors.

## 2.6 References

1. D. R. Smith, W. J. Padilla, D. C. Vier, R. Shelby, S. C. Nemat-Nasser, N. Kroll, S. Schultz, "A composite medium with simultaneous negative permittivity and permeability," *Phys. Rev. Lett.* 84, 4184–4187, 2000.
2. V. G. Veselago, "The electrodynamics of substances with simultaneously negative values of permittivity and permeability," *Soviet Physics Uspekhi*, 10, 509-514, 1968.
3. R. A. Shelby, D. R. Smith, S. Shultz, and S. C. Nemat-Nasser, "Microwave transmission through a two-dimensional, isotropic, left-handed metamaterial" *Applied Physics Letters* 78, 2001.
4. J. B. Pendry, "Negative refraction," *Contemporary Physics* 45, 191-202, 2004.
5. K. B. Alici, and E. Özbay, "Radiation properties of a split ring resonator and monopole composite," *phys. stat. sol.* 4, 1192–1196, 2007.
6. A. Boltasseva, and H. A. Atwater, *Science* 331, 290-291, 2011.
7. I. M. Pryce, Y. A. Kelaita, K. Aydin, and A. Atwater, "Compliant Metamaterials for Resonantly Enhanced Infrared Absorption Spectroscopy and Refractive Index Sensing," *Nano Lett.* 5, 8167-8174, 2011.
8. C. K. Chen, M. H. Chang, H. T. Wu, Y. C. Lee, and T. J. Yen, "Enhanced vibrational spectroscopy, intracellular refractive indexing for label-free biosensing and bioimaging by multiband plasmonic-antenna array," *Biosens Bioelectron.* 60, 343-350, 2014.
9. J. A. Schuller, R. Zia, T. Taubner, and M. L. Brongersma, "Dielectric metamaterials based on electric and magnetic resonances of silicon carbide particles," *Phys. Rev. Lett.* 99,107401, 2007.
10. J. C. Ginn, I. Brener, D. W. Peters, J. R. Wendt, J. O. Stevens, P. F. Hines, L. I. Basilio, L. K. Warne, J. F. Ihlefeld, P. G. Clem, and M. B. Sinclair, "Realizing optical magnetism from dielectric metamaterials," *Phys. Rev. Lett.* 108, 097402, 2012.
11. P. Moitra, Y. Yang, Z. Anderson, I. I. Kravchenko, D. P. Briggs, and J. Valentine, "Realization of an all-dielectric zero-index optical metamaterial," *Nat. Photonics* 7, 791–795, 2013.

12. C. Wu, N. Arju, G. Kelp, J. A. Fan, J. Dominguez, E. Gonzales, E. Tutuc, I. Brener, and G. Shvets, "Spectrally selective chiral silicon metasurfaces based on infrared Fano resonances," *Nature Communication* 5, 3892, 2014.
13. S. J. Park, J. T. Hong, S. J. Choi, H. S. Kim, W. K. Park, S. T. Han, J. Y. Park, S. Lee, D. S. Kim, and Y. H. Ahn, "Detection of microorganisms using terahertz metamaterials," *Scientific Reports* 4, 4988, 2014.
14. Z. Liu, X. Xia, Y. Sun, H. Yang, R. Chen, B. Liu, B. Quan, J. Li, and C. Gu, "Visible transmission response of nanoscale complementary metamaterials for sensing applications," *Nanotechnology* 23, 275503, 2012.
15. S. Linden, C. Enkrich, M. Wegener, J. Zhou, T. Koschny, and C. M. Soukoulis, "Characterisation at infrared wavelengths of metamaterials formed by thin-film metallic split-ring resonator arrays on silicon," *Science* 306, 1351-1353, 2004.
16. N.P. Johnson, A.Z. Khokhar, H.M.H. Chong, R.M. De La Rue and S. McMeekin, "Characterisation at infrared wavelengths of metamaterials formed by thin-film metallic split-ring resonator arrays on silicon," *Electron. Lett.* 42, 1117–1119, 2006.
17. V. M. Shalaev, "Optical negative index metamaterials," *Nature Photonics* 1, 41–48, 2007.
18. N. Katsarakis, T. Koschny, and M. Kafesaki, "Electric coupling to the magnetic resonance of split ring resonators," *Applied Physics Letters* 84, 2943-2945, 2004.
19. D. R. Smith, and S. Schultz, "Determination of effective permittivity and permeability of metamaterials from reflection and transmission coefficients," *Physical Review* 65, 195104, 2002.
20. P. Marko~s, I. Rousochatzakis, and C. M. Soukoulis, "Transmission Losses in Left-handed Materials," *Phys. Rev. E* 66, 045601, 2002.
21. P. Marko~s, and C. M. Soukoulis, "Transmission properties and effective electromagnetic parameters of double negative metamaterials," *Optics Express* 11, 649, 2003.
22. T. Koschny, P. Marko~s, D. R. Smith, and C. M. Soukoulis, "Resonant and anti-resonant frequency dependence of the effective parameters of metamaterials," *Phys. Rev.* 68, 065602, 2004.
23. J. B. Pendry and A. MacKinnon, "Calculation of photon dispersion relations," *Phys. Rev. Lett.* 69, 2772, 1992.
24. J. B. Pendry, "Photonic Band Structures," *J. Mod. Opt.* 41, 209-229, 1994.
25. M. Born and E. Wolf, "The Principles of Optics," Pergamon, Oxford, 1964.

26. H. Y. Li, S. M. Zhou, J. Li, Y. L. Chen, S. Y. Wang, Z. C. Shen, L. Y. Chen, H. Liu, and X. X. Zhang, "Analysis of the Drude model in metallic films," *Applied Optics* 40, 6307-6311, 2001.
27. R. H. Ritchie, "Plasma losses by fast electrons in thin films," *Physical Review*, 106:874, 1957.
28. E. Kretschmann and H. Reather, "Radiative decay of nonradiative surface plasmon excited by light," *Z. Naturf*, 23A:2135, 1968.
29. A. Otto, "Excitation of nonradiative surface plasma waves in silver by the method of frustrated total reflection," *Z. Phys.*, 216:398, 1968.
30. R. C. Jorgenson and S. S. Yee, "A fiber-optic chemical sensor based on surface plasmon resonance," *Sensors and Actuators* 8, 12, 213-220, 1993.
31. W. Kubo and S. Fujikawa, "Au Double Nanopillars with Nanogap for Plasmonic Sensor," *Nano Lett.*, 11, 8-15, 2011.
32. D.R. Ward, N.K. Grady, C.S. Levin, N.J. Halas, Y. Wu, P. Nordlander and D. Natelson, "Electromigrated nanoscale gaps for surface-enhanced Raman spectroscopy," *Nano Lett.*, 7, 1396-1400, 2007.
33. H. Aouani, H. Šípová, M. Rahmani, M. Navarro-Cia, K. Hegnerová, J. Homola, M. Hong and S. A. Maier, "Ultrasensitive Broadband Probing of Molecular Vibrational Modes with Multifrequency Optical Antennas," *Nano Lett.*, 7, 669-675, 2013.
34. S. Lal, N. K. Grady, J. Kundu, C. S. Levin, J. B. Lassiter and N. J. Halas, "Tailoring plasmonic substrates for surface enhanced spectroscopies," *Chem. Soc. Rev.* 37, 898-911, 2008.
35. A. Ishimaru, S. Jaruwatanadilok, and Y. Kuga, "Generalized surface plasmon resonance sensors using metamaterials and negative index materials," *Progress In Electromagnetics Research, PIER* 51, 139-152, 2005.
36. P. Adam, M. Piliarik, H. Sipova, T. Springer, M. Vala, and J. Homola "Photonic Sensing: Principles and Applications for Safety and Security Monitoring," First Edition, 45, 2012.
37. R. C. Jorgenson and S. S. Yee, "A fiber-optic chemical sensor based on surface plasmon resonance," *Sensors and Actuators B* 12, 213-220, 1993.
38. L. La Spada, F. Bilotti, and L. Vegni, "Metamaterial-based sensor design working in infrared frequency range," *Progress In Electromagnetics Research* 34, 205-223, 2011.

39. B. Lahiri, S. G. McMeekin, R. M. De La Rue, and N. P. Johnson, “Enhanced Fano resonance of organic material films deposited on arrays of asymmetric split-ring resonators (A-SRRs),” *Optics Express* 21, 9343-9352, 2013.
40. S. J. Park, J. T. Hong, S. J. Choi, H. S. Kim, W. K. Park, S. T. Han, J. Y. Park, S. Lee, D. S. Kim, and Y. H. Ahn, “Detection of microorganisms using terahertz metamaterials,” *Scientific Reports* 4, 4988, 2014.
41. R. M. Pemberton, T. T. Mottram and J. P. Hart, “Development of a screen-printed carbon electrochemical immunosensor for picomolar concentrations of estradiol in human serum extracts,” *J. Biochem. Biophys. Methods*, 63, 201–212, 2005.
42. P-T. Katalin, B. Darius and P. Laszlo, “Simultaneous Measurement of  $17\beta$ -Estradiol,  $17\alpha$ -Estradiol and Estrone by GC–Isotope Dilution MS–MS,” *Chromatographia.*, 71, 311–315, 2010.
43. X.Q. Liu, X. H. Wang, J. M. Zhang, H. Q. Feng, X. H. Liu and D. K. Y. Wong, “Detection of estradiol at an electrochemical immunosensor with a Cu UPD vertical bar DTBP-Protein G scaffold,” *Biosens Bioelectron*, 35, 56-62, 2012.
44. N. Yildirim, F. Long, C. Gao, M. He, H-Cg. Shi and A. Z. Gu, “Aptamer-Based Optical Biosensor For Rapid and Sensitive Detection of  $17\beta$ -Estradiol In Water Samples,” *Environ. Sci. Technol.*, 46, 3288–3294, 2012.
45. J. Liu, W. Bai, S. Niu, C. Zhu, S. Yang and A. Chen, “Highly sensitive colorimetric detection of  $17\beta$ -estradiol using split DNA aptamers immobilized on unmodified gold nanoparticles,” *Scientific Reports* , 4, 7571, 2014.
46. Q. Zhang, Y. Wang, A. Mateescu, K. Sergelen, A. Kibrom, U. Jonas, T. Wei and J. Dostalek, “Biosensor based on hydrogel optical waveguide spectroscopy for the detection of  $17\beta$ -estradiol,” *Talanta*, 104, 149-154, 2013.
47. M. Miyashita, T. Shimada, H. Miyagawa, M. Akamatsu, “Surface plasmon resonance-based immunoassay for  $17\beta$ -estradiol and its application to the measurement of estrogen receptor-binding activity,” *Anal. Bioanal. Chem.*, 381,667–673, 2005.
48. W-W. Zhang, Y-C. Chen, Z-F. Luo, J-Y. Wang and D-Y. Ma, “Analysis of  $17\beta$ -estradiol from sewage in coastal marine environment by surface plasmon resonance technique,” *Chem. Res. Chin.*, 404–407, 2007.
49. C. N. Banwell, and E. M. McCash, “Fundamentals of Molecular Spectroscopy” 4th edition, 1994.

50. Kauffman, J. M., "Water in the atmosphere," *Journal of Chemical Education* 81, 1229–1230, 2004.
51. Williams, D.H., and Flemming, I., "Spectroscopic methods in organic chemistry," Second edition, 40, 1973.
52. I. G. Mbomson, S. McMeekin, Basudev Lahiri, R. De La Rue, and N. P. Johnson, "Gold asymmetric split ring resonators (A-SRRs) for nano sensing of estradiol," *Proc. SPIE 9125, Metamaterials IX*, 91251O, 2014.
53. I. G. Mbomson, S. McMeekin, R. De La Rue, and N. P. Johnson, "Matching plasmon resonances to the C=C and C-H bonds in estradiol," *Proc. SPIE 9340, Plasmonics in Biology and Medicine XII*, 93400G, 2015.
54. P. Jonkheijm, D. Weinrich, H. Schröder, C. M. Niemeyer and H. Waldmann, "Chemical strategies for generating protein biochips," *Angew. Chem. Int. Ed* 47, 9618-9647, 2008.
55. J. P. Lafleur, R. Kwapiszewski, T. G. Jensen and J. P. Kutter, "Rapid photochemical surface patterning of proteins in thiol-ene based microfluidic devices," *Analyst* 138, 845–849, 2013.
56. S. Hosseini, F. Ibrahim, I. Djordjevic and L. H. Koole, "Recent advances in surface functionalization techniques on polymethacrylate materials for optical biosensor applications," *Analyst* 139, 2933-2943, 2014.
57. J. M. Goddard and J. H. Hotchkiss, "Polymer surface modification for the attachment o bioactive compounds," *Prog. Polym. Sci.*, 32, 698–725, 2007.
58. R. H. Liu, J. Yang, R. Lenig, J. Bonanno, and P. Grodzinski, "Self-Contained, Fully Integrated Biochip for Sample Preparation, Polymerase Chain Reaction Amplification, and DNA Microarray Detection," *Anal. Chem.*, 76, 1824–1831, 2004.
59. G. S. Fiorini and D. T. Chiu, "Disposable microfluidic devices: fabrication, function, and application," *BioTechniques*, 38, 429-446, 2005.
60. J. Paul, M. Richard and N. P. Johnson, "Gold asymmetric-split ring resonators (A-SRRs) for proteins sensing," *Proc. SPIE 9883, Metamaterials X*, 98831C, 2016.
61. S. Lin , Y. Tsai , C. Chen , C. Lin , and C. Chen, "Two-Step Functionalization of Neutral and Positively Charged Thiols onto Citrate-Stabilized Au Nanoparticles," *J. Phys. Chem. B*, 108, 2134–2139, 2004.

62. L. J. Sherry, S. H. Chang, G. C. Schatz and R. P. Van Duyne, "Localized Surface Plasmon Resonance Spectroscopy of Single Silver Nanocubes," *Nano Lett.*, 5, 2034-2038, 2005.
63. L. J. Sherry, R. Jin, C. A. Mirkin, G. C. Schatz and R. P. V. Duyne, "Localized Surface Plasmon Resonance Spectroscopy of Single Silver Triangular Nanoprisms," *Nano Lett.*, 6, 2060-2065, 2006.
64. P. Offermans, M. C. Schaafsma, S. R. K. Rodriguez, Y. Zhang, M. Crego-Calama, S. H. Brongersma and J. G. Rivas, "Universal Scaling of the Figure of Merit of Plasmonic Sensors," *ACS Nano*, 5, 5151-5157, 2011.
65. A. V. Kabashin, P. Evans, S. Pastkovsky, W. Hendren, G. A. Wurtz, R. Atkinson, R. Pollard, V. A. Podolskiy and A. V. Zayats, "Plasmonic nanorod metamaterials for biosensing," *Nature Materials*, 8, 867-871, 2009.
66. T. Hao, C.J. Stevens and D.J. Edwards, "Optimisation of metamaterials by Q factor," *Electronics Letters*, 41, 11, 2005.
67. V. A. Fedotov, M. Rose, S.L. Prosvirnin, N. Papasimakis and N. I. Zheludev, "Sharp trapped-mode resonances in planar metamaterials with a broken structural symmetry," *Phys Rev Lett.*, 99, 147401, 2007.

# Chapter 3

## Modelling and Simulation

### 3.1 Introduction

Planar metallic metamaterial (MM) or metasurfaces consist of various structures such as chiral shapes [1], bowties [2], multi-frequency optical antennas [3] and several different shapes resembling alphabetic characters [4-6]. The individual geometries of a component have a direct effect on the operational characteristics of the device as a whole, and result to compromises made in order to optimise the structures.

The MM devices designed for both single and double reflectance resonance peaks were restricted to the TE polarization of the EM wave source parallel to the length of the metallic device elements. The reflectance resonance is produced from asymmetric elements of MM structure which correspond to double resonance peaks. The MM structures made with gold have a square periodic array designed on fused silica substrates. The periodicity of the different structures requires optimisation to increase the quality factor (Q) and amplitude of the resonances.

Three dimensional finite difference time domain (FDTD) numerical simulations were used to optimise the key dimensional parameters of the MM structures, such as the gap between two concentric arcs of an A-SRR, the length of dipole arms and periodicity. The Drude model proposed by Paul Drude in 1900 which explains the optical properties of material mostly metals was employed to model the gold patterns of this work [7-8].

In this chapter the method used for simulation is briefly described. The MM structures designed are described in detail, with the optimisation of the parameters, starting with the width ( $w$ ) of the arc and arm, gap ( $g$ ) between two elements of the structures and periodicity ( $a$ ). These are the key structural parameters for the MMs designed in this work. Three designed MM devices are presented, the asymmetric split ring resonators (A-SRR), dipole structures and asymmetric split H-shape. The last section includes discussions and conclusions of this chapter.

### **3.2 Modelling**

The metallic metamaterial structures were modelled and optimized using finite different time domain (FDTD) method. This is a time domain method which can cover a wide wavelength range with a single simulation run. Determination of optimal properties is obtained by applying electromagnetic laws to material properties. The relations of material properties and application of electromagnetic fields are primarily contained in Maxwell equations [9]. These are a set of partial differential equations which describe how electric and magnetic fields are generated and altered by each other and by charges and currents. The equations introduce the electric ( $E$ ) and magnetic ( $H$ ) field vectors which are generally material and time dependent.

The differential formulation of the equation calculates the fields in complicated situations of source where the time evolution of the fields is due to the partial derivatives of the fields with respect to time. When the differential equations of Maxwell are examined, it can be observed that the change in the field in time derivatives is dependent on the other field across space. This is the basic of FDTD time stepping relation [10] results which shows the updated value of the E-field in time is dependent on the stored value of the E-field and numerical curl of the local distribution of the H-field in space. Similarly, that the updated value of the H-field in time is dependent on the stored value of the H-field and numerical curl of the local distribution of the E in space. Adapting and repeating the E and H fields' output results in a time processing form with material data analogues to the electromagnetic waves propagation in a numerical grid stored in computer memory [10]. This describes the three different dimensions of FDTD method as applied in the simulations software used in this work.

### 3.3 Simulations Setup

The structures were simulated using FDTD method based on the commercial software package, Lumerical. Lumerical software can perform simulations in both two and three dimensional structures. In this work, three (x, y and z) dimensional numerical computation for simulation as shown in figure 3.1 was used. This type of simulation requires more memory and can take a longer time but it ensures more accuracy in the results.

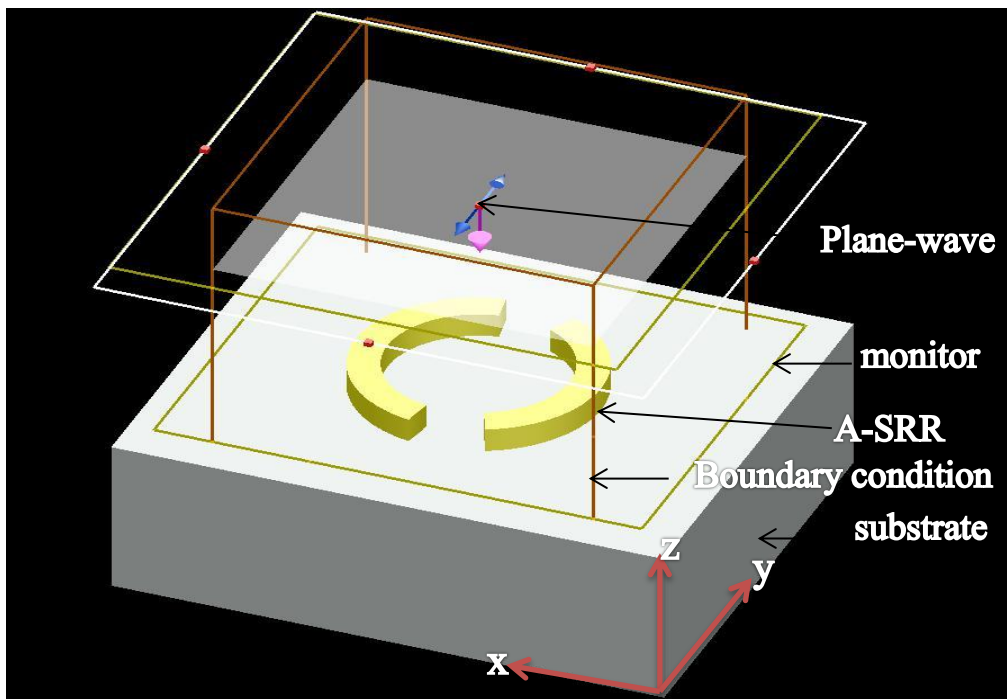


*Figure 3.1: Image of Perspective view for the three dimensional simulations setup.*

The software package requires several items to set up the simulation tools [11] a representation is shown in figure 3.1. These tools enable correct running of the numerical simulation. The following section describes the basic computation tools and how the design was built up to perform the simulations used in this work.

➤ **Material model ( $n, k$ )**

This section describes how FDTD solution can accurately model different sets of material over a wide wavelength range. The refractive index of different material used has been defined for broadband simulations. Here, materials used in the MM structures and the substrate design comprises of both the real and imaginary valued refractive index which has a complex value,  $(n + ik)$  while the background index is taken as refractive index of the air or vacuum (equal to 1).

The index distribution for various materials can be added in the software from the data material files by importing lists of  $n$  and  $k$  data as a function of wavelength. A broadband wavelength between  $2 \mu\text{m}$  to  $8 \mu\text{m}$  is used for the Au pattern using Drude model from references [8-9, 11] and attached in appendix A1. For the fused silica substrate the optical dispersion was considered by using data from reference [11]. This results to changes in material data of Lumerical to fit the corresponding transmission spectrum from the experimental work.

➤ **Boundary Conditions**

The boundary conditions (BCs) the orange coloured box shown in figure 3.2 are applied to the simulation of both finite and periodic MM structures are supported by FDTD numerical method. For the finite structure, a perfectly matched layer (PML) BC which absorb EM waves incident upon the design as was applied in the  $z$ -direction. The PML was applied in  $Z$ -direction which corresponds to the direction of the propagating source. PML uses an absorbing layer especially designed to absorb the EM waves without reflection [12]. The substrate structure is completely extended through the PML boundary condition region because the PML perform best in such conditions [13]. For this application the PML is placed at distance of half a wavelength from the broadband source. Periodic BCs were applied along the  $x$  and  $y$ -axis of the design to account for the periodic arrays of MM devices. In Lumerical for periodic structures it is necessary to have the FDTD mesh set to  $d_{xy} = a/N$ , where  $a$  is the period and  $N$  is an integer. This guarantees a perfectly periodic FDTD mesh.

➤ ***Electromagnetic plane wave source***

There are different types of source available in the FDTD software such as dipole, beam, waveguide mode, total-field scattered-field and plane wave. Plane wave sources shown in white colour in figure 3.1 are used to inject laterally-uniform EM wave and for the three dimensional simulations the source propagates along the plane. The source is used for the design since it can be injected at different angles of polarization. Using Lumerical, the setting for the source angle is usually set at  $90^0$  i.e. perpendicular to the designed plane (substrate). This allows the normally incident EM to produce E-field parallel to the length of metallic element of all the design structure presented here.

➤ ***Software detectors***

The following types of monitors are available in the Lumerical: (a) Frequency-domain field monitors that collect the field profile in the frequency domain which is converted to wavelength from the simulation results across some spatial area of the simulation. The field and power monitor snaps to the nearest mesh cell to minimize the interpolation required which lead to more accurate spectra. Here the field and power monitor in the yellow rectangular box shown in figure 3.1 collect the transmittance and reflectance spectra depending on the placement position. The monitor is a reflectance monitor when it is place behind the source while it serves as transmittance monitor when it is opposite the source. The field profile monitors are identical to the power but mostly used to plot the electric and magnetic field strength plots. The field value for the plot is related to the strength of the incident source. (b) Time-domain monitors provide the time-domain information for field components during simulation. The monitor consists of plane, line and point types to capture data at different regions within the FDTD simulation. (c) Movie monitors are used to capture the desired field component over the region spanned by the monitor for the duration of the simulation. This monitor is only available in the 2-D for the software and among other monitors stated this requires more memory and slows the simulation speed.

### 3.4 Asymmetric split ring resonators (A-SRRs)

The A-SRR structure is formed by breaking a circular ring in an asymmetric form to create gaps between the two arcs from the angular separations. This structure is presented here as a 3D pattern, where the radius of the ring is at the x and y-plane, the height of the ring is on the z- direction.

The design of A-SRRs as conventional metallic metamaterial structures, as reported in the related publications, require the formation of a nanoscale gap which together with sharp edges, form hot spots that produce large electric fields [14-19]. The enhancement of the electric field emerging from the hot spots has been stated to greatly exceed the strength of the incident field which improves the detection ability of MM based sensors [17-19]. In this work, the asymmetric arcs dimensions have been designed for nanoscale gaps produced from the two angles ( $\theta^0 = g$ ) as shown in figure 3.2.

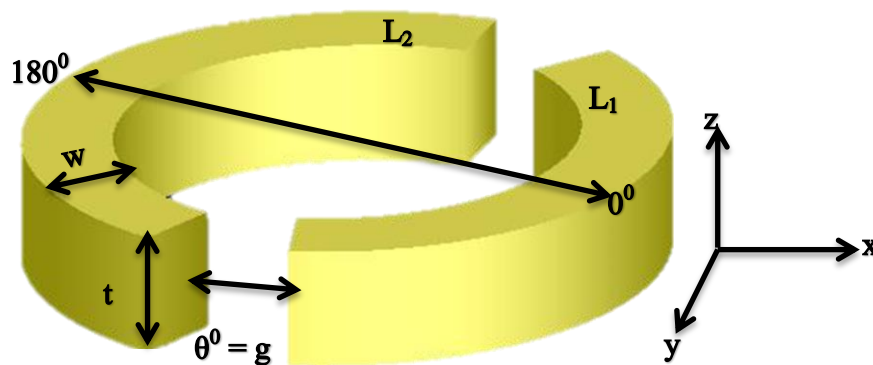


**Figure 3.2:** Image of asymmetric Split Ring Resonators, A-SRR with equal angles ( $\theta^0 = g$ ) but two unequal arcs ( $L_1$  and  $L_2$ ),  $w$  is the width of the arcs and  $t$  is the thickness of the pattern. The x, y and z-axes show the 3D orientation of the A-SRR.

#### Effect of variation of the arcs length

Using A-SRRs metallic metamaterial shown in figure 3.2 which follows work by Lahiri et al [5], these serve as a guideline to development of new MM structures that have nanoscale gap

with the aim of achieving an optimised MM structure of high sensitivity. Previous work [5] has concentrated on A-SRRs with angles ( $\theta$ ) ranging from  $10^0$  to  $50^0$  which corresponds with 105 nm to 524 nm gaps for a ring radius of  $0.6 \mu\text{m}$ . This design is to tune the reflectance resonance peaks to the targeted sensing wavelength band. In this present, work the sensing region is at shorter wavelength than the previous work and the gaps are much smaller. The gap and arc length are calculated from the circle geometry.

Simulations were performed for different arcs length to evaluate the effect of the degree of asymmetry on the amplitude of plasmonic resonance peaks. The E-field strength of the double resonances produced by the A-SRRs depends on the differences in the length between the two concentric asymmetric arcs as shown figure 3.3.

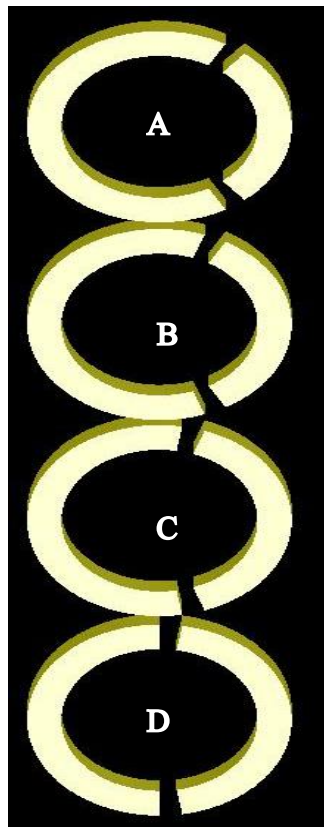


**Figure 3.3:** Schematic diagram showing two concentric asymmetric arcs for the A-SRRs metamaterial with different degree of asymmetry between the arcs.

The extent of asymmetry is defined by the degree of the arc lengths and given in percentages. This is the difference between the arcs calculated in percentage. Figure 3.3 shows the differences in the arcs from (A) being a 25% more asymmetric structure to (D) 9% less

asymmetric structure. The two equal gaps of 168 nm ( $20^\circ$ ) were kept constant while varying the length of the arcs as shown in the figure. Table 3.1 contains the asymmetric length of the A-SRR structure in micrometres calculated from the arcs length in degrees as shown in column 2 and 3. The percentage differences between the two arcs of the A-SRR structures were tabulated in column 4 of the table. The tabulated arcs lengths in  $\mu\text{m}$  are calculated from geometry of a circle (i.e. arc length =  $2\pi r\theta / 360^\circ$ ).

**Table 3.1:** Variation of the arcs length

A-SRR diagram	Large arc ( $\mu\text{m} / \text{degree}$ )	Small arc ( $\mu\text{m} / \text{degree}$ )	Arc length variation in percentage (%)
A	1.67 / $200^\circ$	1.00 / $120^\circ$	25
B	1.59 / $190^\circ$	1.09 / $130^\circ$	19
C	1.55 / $185^\circ$	1.17 / $140^\circ$	14
D	1.51 / $180^\circ$	1.25 / $150^\circ$	9

Simulations of the modelled A-SRR with an outer and inner radius of  $0.48 \mu\text{m}$  and  $0.38 \mu\text{m}$  were performed for the different arcs length as tabulated in table 3.1. The left hand arcs were reduced from  $200^\circ$  to  $180^\circ$  i.e. ( $1.67$  to  $1.51$ )  $\mu\text{m}$  and the right hand arc increased from  $120^\circ$  to  $150^\circ$  i.e. ( $1.00$  to  $1.25$ )  $\mu\text{m}$  as shown in figure 3.3. From the simulations double resonance peaks at short and long wavelengths correspond to the small and large arcs respectively for the A-SRRs as shown in figure 3.4. The spectral plots are data extracted from the reflectance monitor corresponding to field and power monitor of Lumerical.

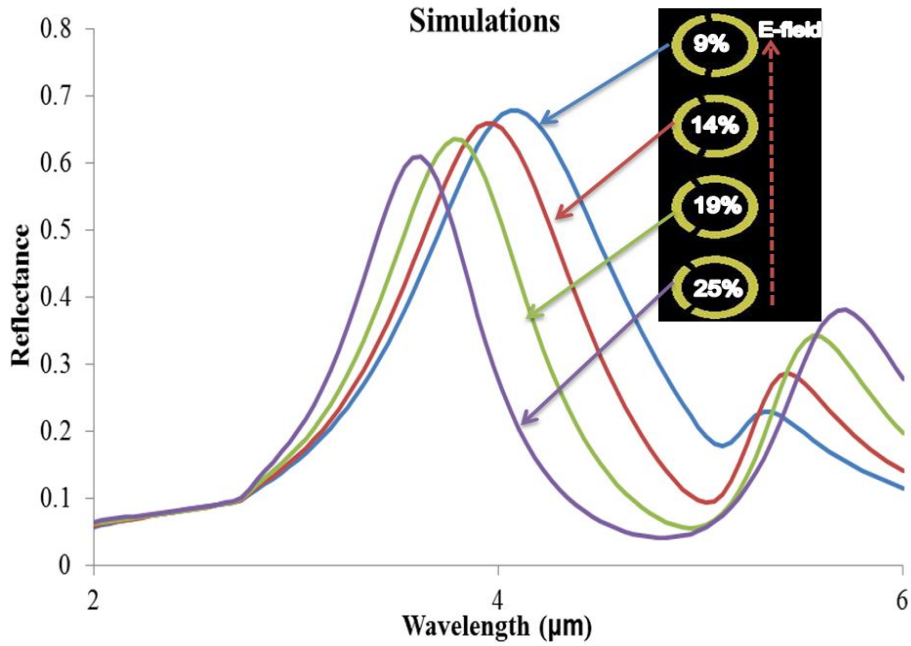


**Figure 3.4:** Reflectance spectra of plasmonic resonance peaks from numerical simulations of arcs length variation; inset of A-SRRs percentage differences between the asymmetric arcs with polarised E-field.

Figure 3.4 shows increment in the reflectance magnitude for the plasmonic resonance peaks at shorter and longer wavelengths as the small and large arcs (inset A-SRRs) increases, respectively. The increment in the reflectivity is attributed to presence of high gold used for the design A-SRRs which will result to reduction in the reflectivity as the arcs decreases. There is also a blue-shift (shift to shorter wavelength EM spectrum) in the plasmonic resonance peaks as both arcs are being reduced due, shown in figure 3.4.

The reflectance spectra show less coupling between the double peaks for the more asymmetric A-SRR i.e. purple plot of 25%. The red plot i.e. 14% show the best coupling for the design variation having the well-developed dip called trapped mode [20]. In this work the trapped mode is the dip that appears between the double plasmonic resonances of asymmetric structure. The reflectance spectra show the more asymmetric arcs introduce a broader trapped mode. Ding et al has previously studied the coupling ability of two concentric asymmetric rings between visible and near infrared [21]. A repeat of the reference simulation is included in the appendix B at visible and near-infrared region. By evaluating the reflectance spectra with the qualitative properties of the structure with previously reported theory at microwave

region [22-23], the author proposes there is need to achieve an optimum variation of the arcs length for resonance coupling. This will support the use of the plasmonic resonances developed from the asymmetric structure in sensing applications.

### **Effect of variation of the gaps**

There are various gap comparisons in this section which help to characterise the A-SRRs metamaterial for high quality and E-field enhancement. The enhancement E-field increases the intensity of molecular resonances and it is related to high positions of field strength. The comparison was achieved by modelling the arcs length of (1.59 by 1.09, 1.68 by 1.17, 1.72 by 1.21 and 1.74 by 1.24)  $\mu\text{m}$  for 0.48  $\mu\text{m}$  A-SRRs radius, which corresponds to the structural gaps of (168, 84, 42 and 21) nm respectively. The thickness used in this design is 50 nm. FDTD numerical simulations were performed using Lumerical and reflectance spectra were produced as shown in the figure 3.5.

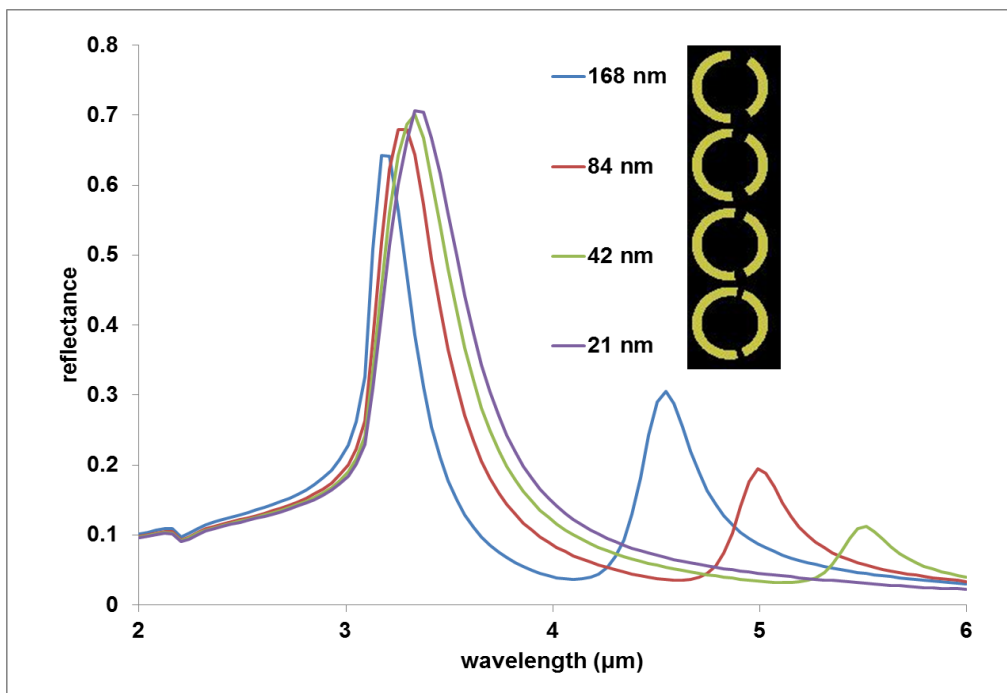


*Figure 3.5: FDTD Lumerical simulations of various nanoscale gaps with the double resonance peaks corresponding to the large and small arcs length.*

The data collected with the field and power monitor produced double resonance peaks with the modelling of a 168 nm gap which is compared with 21 nm gap.

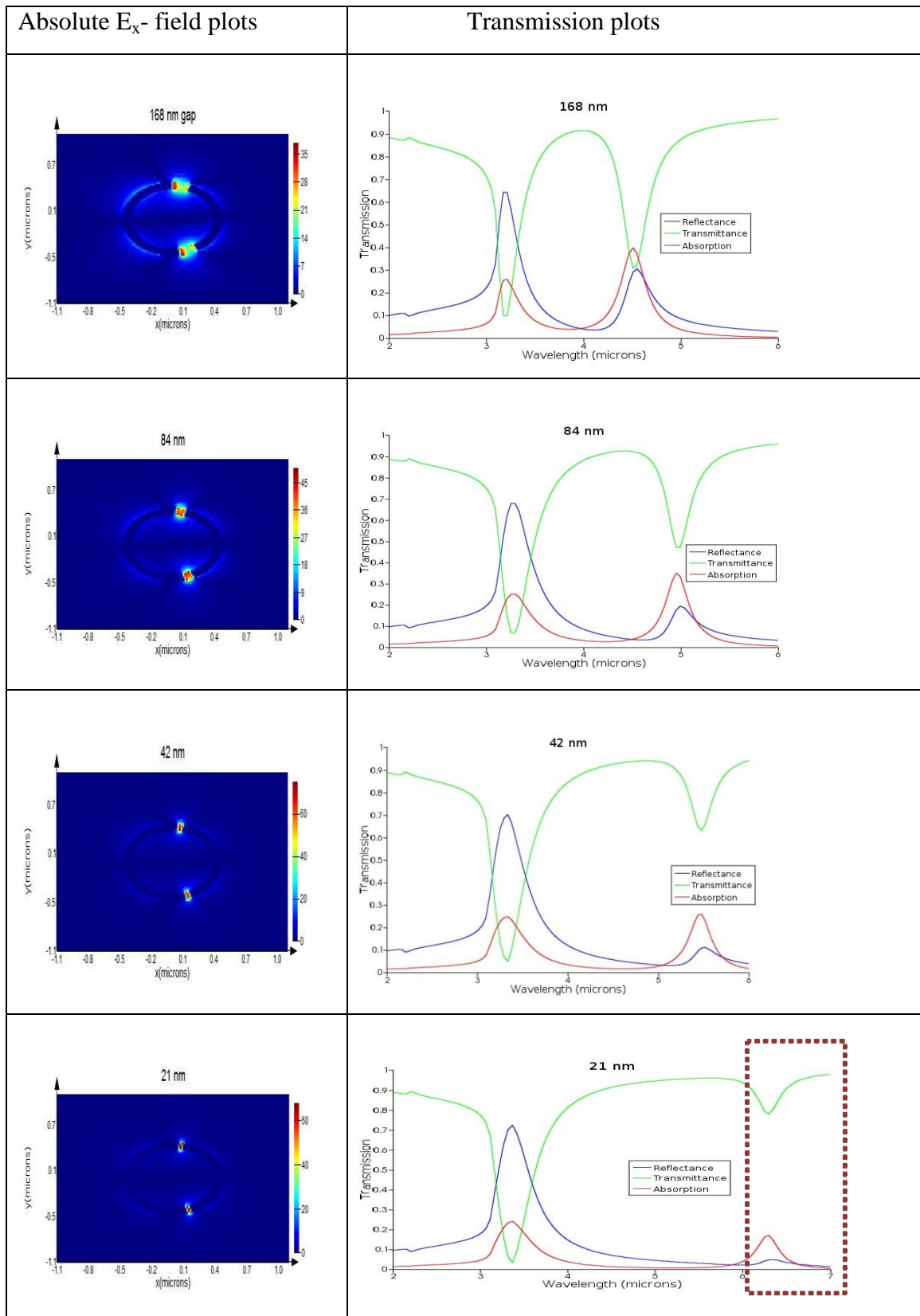


**Figure 3.6:**  $E$ -field strength and transmission plots for the A-SRRs at nanoscale gap

The positions of the peaks are affected by the length of the arcs as discussed earlier in this chapter. Variations of the arcs length of the asymmetric resonators tend to tune the resonance peaks accordingly. The absolute x-component of E-field plot in the first column shows increase in the E-field as the gap is being reduced from 168 nm to 42 nm. For this design a nanoscale gap of approximate value of 42 nm (i.e.  $\theta = 5^\circ$ ) is the optimum gap length for the A-SRRs structure. At that gap length the E-field gives the maximum strength as shown in the third row of figure 3.6. The E-field is reduced from the gap length of 21 nm as shown in figure 3.6. The colour bars on the right of each plot describe the magnitude of E-field from dark blue representing the minimum and red the maximum E-field.

The E-field was plotted at the position of the shorter wavelengths of resonance peak to show the effect of reduction in gap from (168, 84, 42 and 21) nm. The second column includes the transmittance, reflectance and absorption spectra. The absorption was calculated from the data collected with the field and power monitor using the expression:  $\text{absorption} = 1 - R - \text{abs}(T)$ . Where R is the reflectance,  $\text{abs}(T)$  is the absolute value of transmission. The resonance peaks correspond to the large and small arc at long and short wavelength respectively. The peaks are red-shifted due to increase in arc length as stated earlier and the trapped modes are broadened with smaller gap. This shifted the second peak of the plot (21 nm) to wavelength beyond the targeted region as highlighted with red dotted box.

### **Variation of the arc width**

The effect of the arc width on the optimization of the resonance peak was also investigated and is shown in figure 3.7. An outer radius of the ring was still maintained as 0.48  $\mu\text{m}$  while the inner radius was varied from (0.43, 0.38, 0.33 and 0.28)  $\mu\text{m}$  which produced the arc width of (50, 100, 150 and 200) nm. This was modelled at a constant gap of 168 nm and thickness of 50 nm. The resonance peaks at short and long wavelength are being modified by this variation as demonstrated.

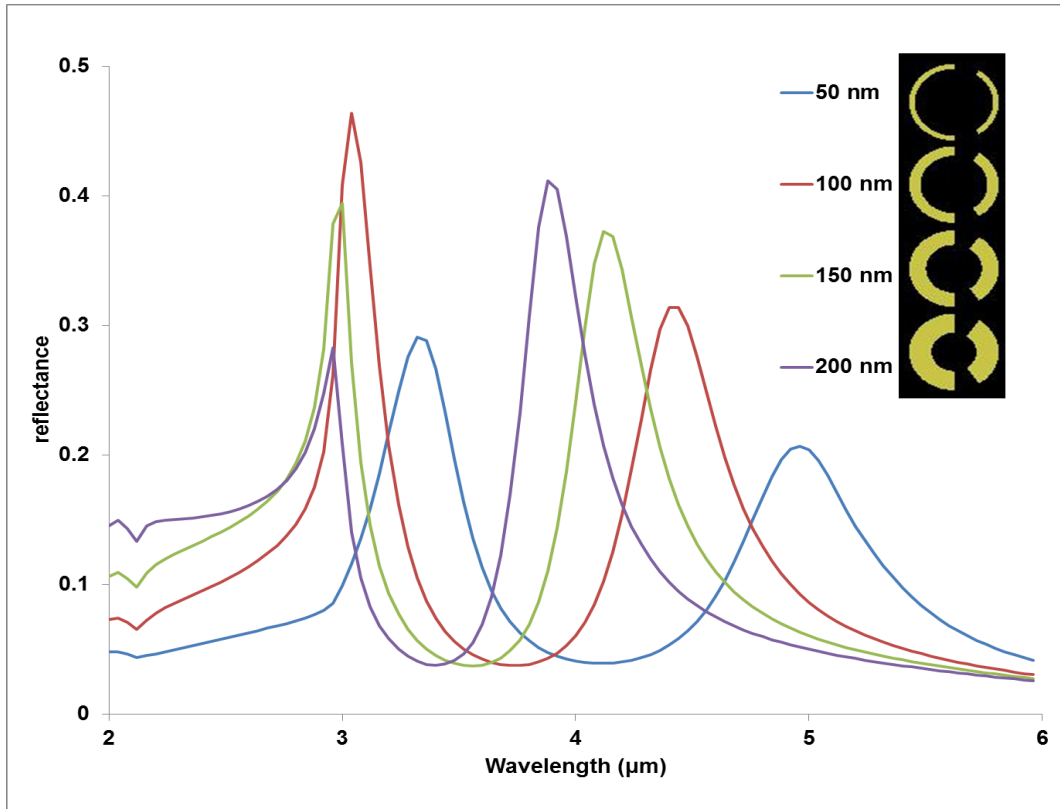


**Figure 3.7:** Reflectance plots from FDTD simulation for different arcs width ( $w$ ) and the schematic diagrams of the A-SRR.

The peaks at shorter wavelengths were narrowed at wider arc widths. The reflectance magnitude is reduced at shorter wavelength as the width is widened from (100 to 200) nm. Resonance peaks at longer wavelength are narrowed also but the strength is increased at wider width. From this study, an optimum design is produced through the well-developed trapped mode between the resonance peaks. The variation shows that A-SRR design with width of 100 nm produces well defined plasmonic resonance peaks at shorter and longer wavelengths compared to others as shown in figure 3.7. Quality factor of the plasmonic resonances were calculated using the expression:  $Q = \lambda_p / \Delta\lambda$  as included in table 3.2.

**Table 3.2:** Comparison of Average  $Q$ -factor for the reflectance plots of figure 3.7

Arc width (nm)	$\lambda_p$ Shorter/longer ( $\mu\text{m}$ )	$\Delta\lambda$ Shorter/longer ( $\mu\text{m}$ )	Average $Q$ -factor
50	3.32 / 4.96	0.36 / 0.56	9.04
100	3.04 / 4.44	0.24 / 0.48	10.96
150	3.00 / 4.12	0.20 / 0.40	12.65
200	2.96 / 3.88	0.40 / 0.36	9.09

The plasmonic resonance peaks ( $\lambda_p$ ) at the shorter and longer wavelengths of the reflectance spectra are in the second column while the full width half maximum (FWHM) represented with  $\Delta\lambda$  are in the third column of table 3.2. Q-factor of the  $\lambda_p$  at the shorter and longer wavelengths was averaged as tabulated in the fourth column of the table. Other features of the A-SRR were evaluated using width of 100 nm to design the structure.

### **Periodicity Variation**

The quality factor of the metallic metamaterial geometrical arrangement imposes constraints on the accuracy with which A-SRRs arrays must be model and as well fabricated. Material losses can result in low Q due to the real part of the dielectric permittivity that determines the optical performance of the device. The materials used for the design can be classified on the basis of two important parameters that determine the optical features of the conducting materials. These parameters are the concentration and mobility carriers as it has been reported that the carrier concentration needs to be high enough to provide a negative real permittivity and that lower mobility carriers leads to a higher material losses [24]. Permittivity in general is a function of frequency. The complex permittivity ( $\mathcal{E} = Re + Im$ ) of the Au (pattern) and SiO<sub>2</sub> (substrate) materials was used for investigation of the optimum periodicity (a). The periodicity of the structure illustrated in figure 3.8.

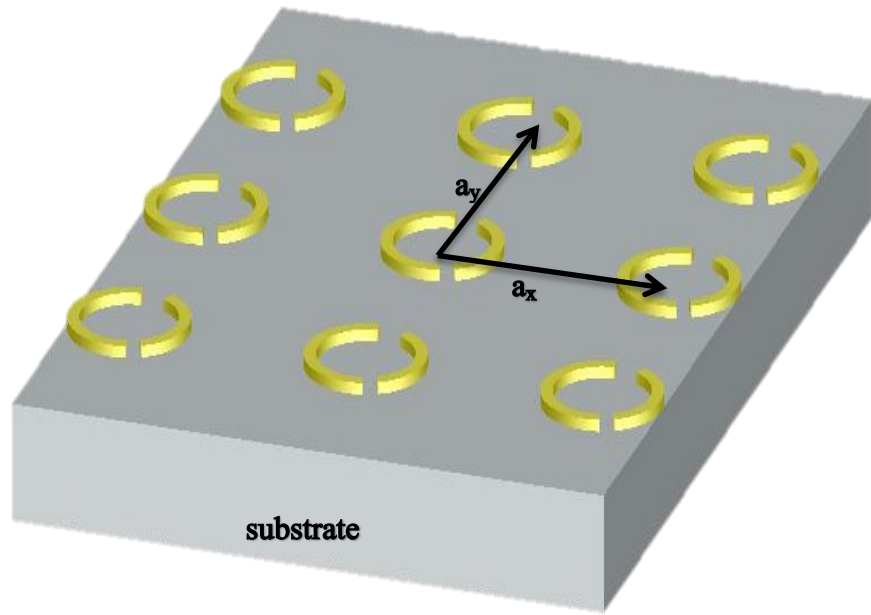


**Figure 3.8:** Schematic diagram of A-SRRs Au pattern on a fused silica substrate showing the periodicity ( $a_{xy}$ ).

For a given periodic arrangement of the A-SRRs array, the scattered fields can add in phase at a specific wavelengths corresponding to the resonance peaks (modes). This is because the currents in both sections of an asymmetrically split ring oscillate in phase [20] but excitation of one of the sections dominates the other as shown in plots of figure 3.9. Researchers [25-30] have previously proposed that plasmonic resonance from structures such as A-SRRs or dipoles requires an optimum periodicity to produce high-Q factors. In this work the periodicity of the A-SRRs arrays was varied and the effect on the reflectance resonance peaks was observed.

**Table 3.3:** Comparing periodicity for 1  $\mu\text{m}$  diameter A-SRRs with magnitude of reflectance

Periodicity ( $\mu\text{m}$ )	1	1.4	1.8	2	2.2	2.4	2.6	2.8	3.0
Reflectance amplitude	0.84	0.56	0.4	0.34	0.29	0.26	0.23	0.21	0.19

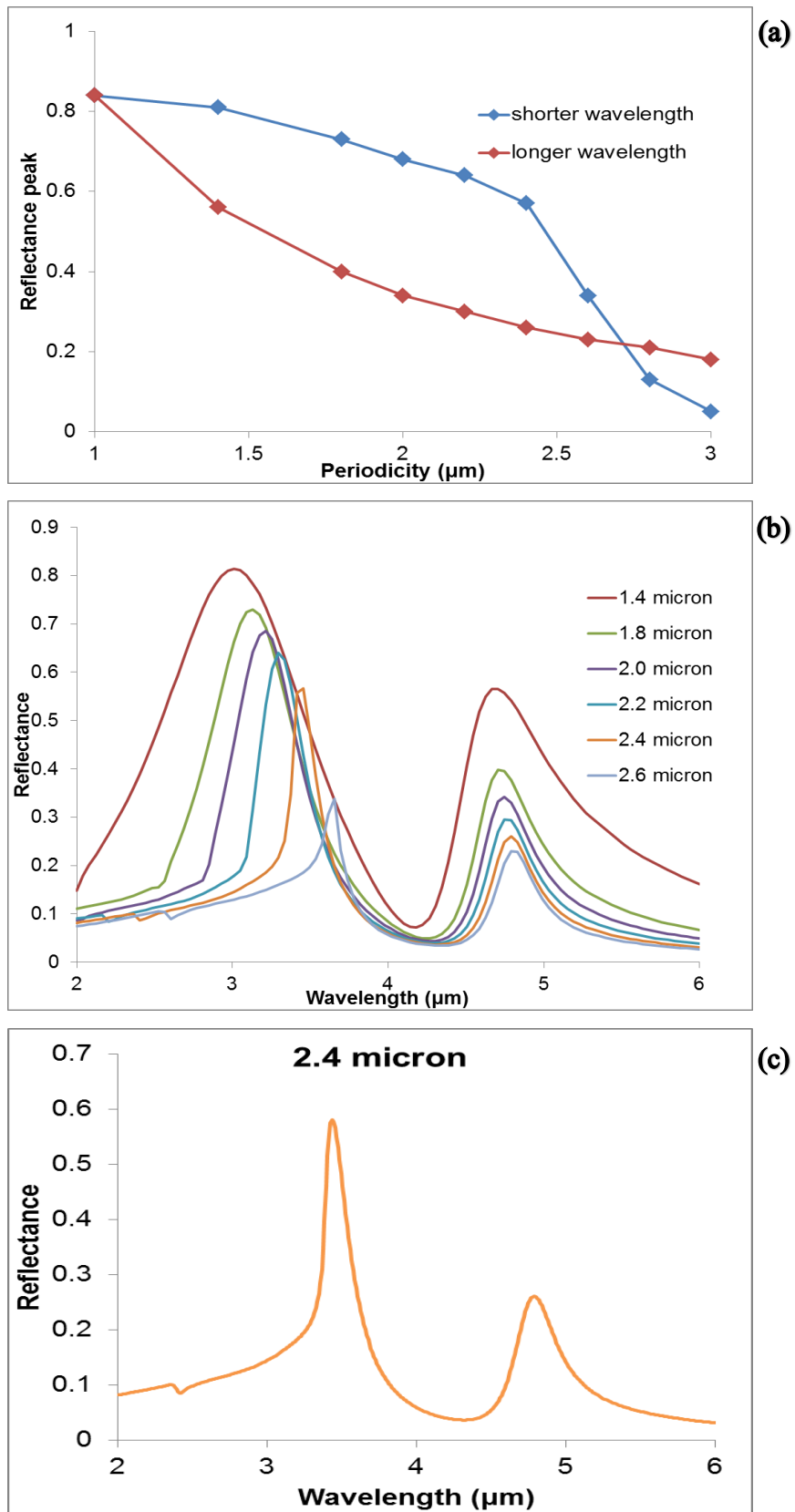


**Figure 3.9:** (a) Periodicity versus magnitude of reflectance peaks (b) FDTD numerical simulation of 100 nm Au thick for 1  $\mu\text{m}$  diameter of A-SRRs radius at different periodicity (c) Reflectance spectra for periodic array of 2.4  $\mu\text{m}$ .

The periodicity ( $a_{xy}$ ) was increased from diameter size of 1  $\mu\text{m}$  of the modelled A-SRRs to three times the diameter (i.e. 3  $\mu\text{m}$ ). Efforts have been concentrated on optimizing the metamaterial geometries and design to improve and control the resonance peaks line-widths [25]. The resonance peaks as stated in the paper and demonstrated in figure 3.9 is controlled by the dimensions and periodicity of the design. For this modelling, Palik material data [9] was used. The dielectric substrates ( $\text{SiO}_2$ ) which contributes to the radiation losses together with ohmic losses that come from the Au pattern through the periodicity arrangement are evaluated. The resonance peaks are broadened with an increasing reflectance magnitude as the periodicity is reduced as shown in table 3.3 and figure 3.9(a-b). The blue shifts as shown by the resonance peaks of figure 3.9 are in agreement with references [25, 31-32] and this occur at reduced periodicity. The periodicity of 2.4  $\mu\text{m}$  as shown in figure 3.9c is the optimum periodic value for the higher Q this design. This shows that in order to obtain a high Q-factor from A-SRRs structure a value of 0.4  $\mu\text{m}$  (40%) should be added to twice the diameter size of the ring resonator as used by Lahiri et al [5]. The optimum periodic value produced Q-factor more than twice the factor produced by reference [5]. Here at the shorter and longer wavelengths of (3.41 and 4.75)  $\mu\text{m}$ , Q-factors of 21 and 16 were obtained by using periodic value 2.4  $\mu\text{m}$ . The result is much higher than the value estimated infrared region by Fedotov et al [20].

### **Variation of the gold thickness**

It is has been reported that the thickness of conductive layer is important for reducing losses and increasing the quality factor which support the FOM of a device [33-35]. Chettiar et al stated that electromagnetic shielding that is caused by thick metal can suppress the performance of the magnetic resonator [33]. They proposed that the problem can be rectified by using a dielectric substrate such as fused silica to form semi-continuous metal films. Through the optimization process of the A-SRR a high quality factor was produced by varying the gold thickness. First, thin film Au thickness of (10 to 70) nm was used for modelling 100 nm arc width A-SRRs of 0.48 outer radius. Numerical simulation of the designs were performed which produced the reflectance spectra as shown in figure 3.10.

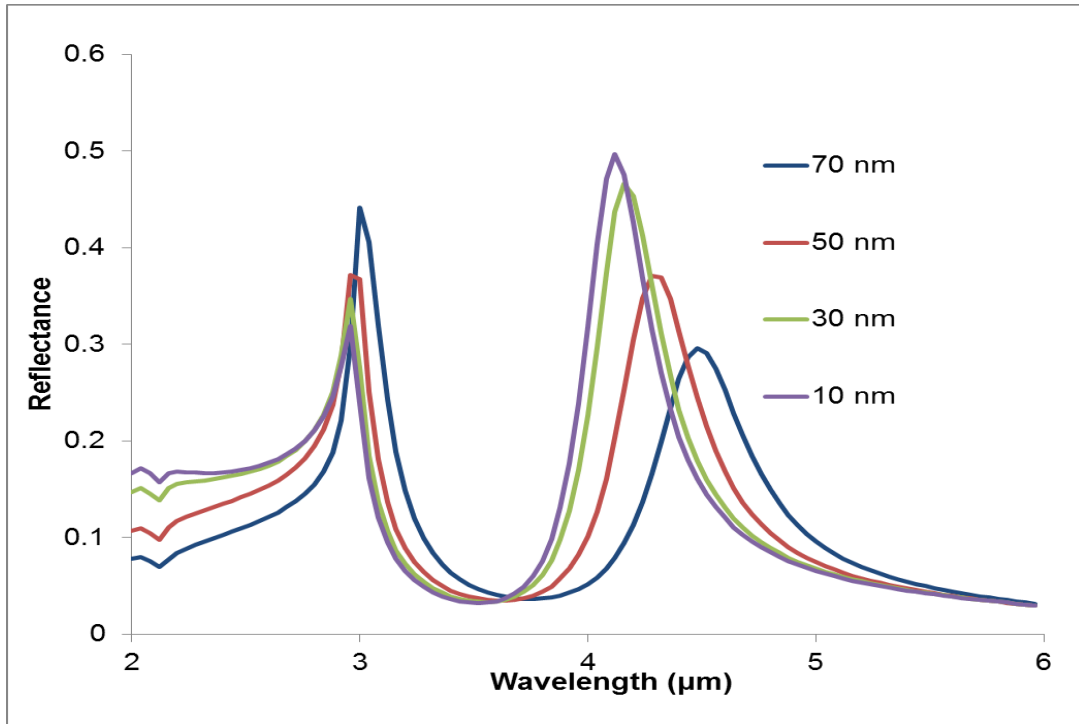


**Figure 3.10** Reflectance spectra from the FDTD numerical simulation of  $0.48 \mu\text{m}$  radius of A-SRRs for 10 nm to 70 nm Au thicknesses showing double plasmonic peaks with artefacts at  $2.2 \mu\text{m}$  arising from grating order due to periodic boundary conditions.

The resonance amplitude at the shorter wavelength increases as the thickness increases while the peaks at the longer wavelength reduce as the thickness increases. There is a small red-shift of both resonance peaks as the thickness increases due to the higher refractive index of the metal. Using the Lumerical script analysis for calculating the low Q-factor as in reference [36] additional numerical simulations were performed for the 70 nm to 100 nm Au thicknesses.

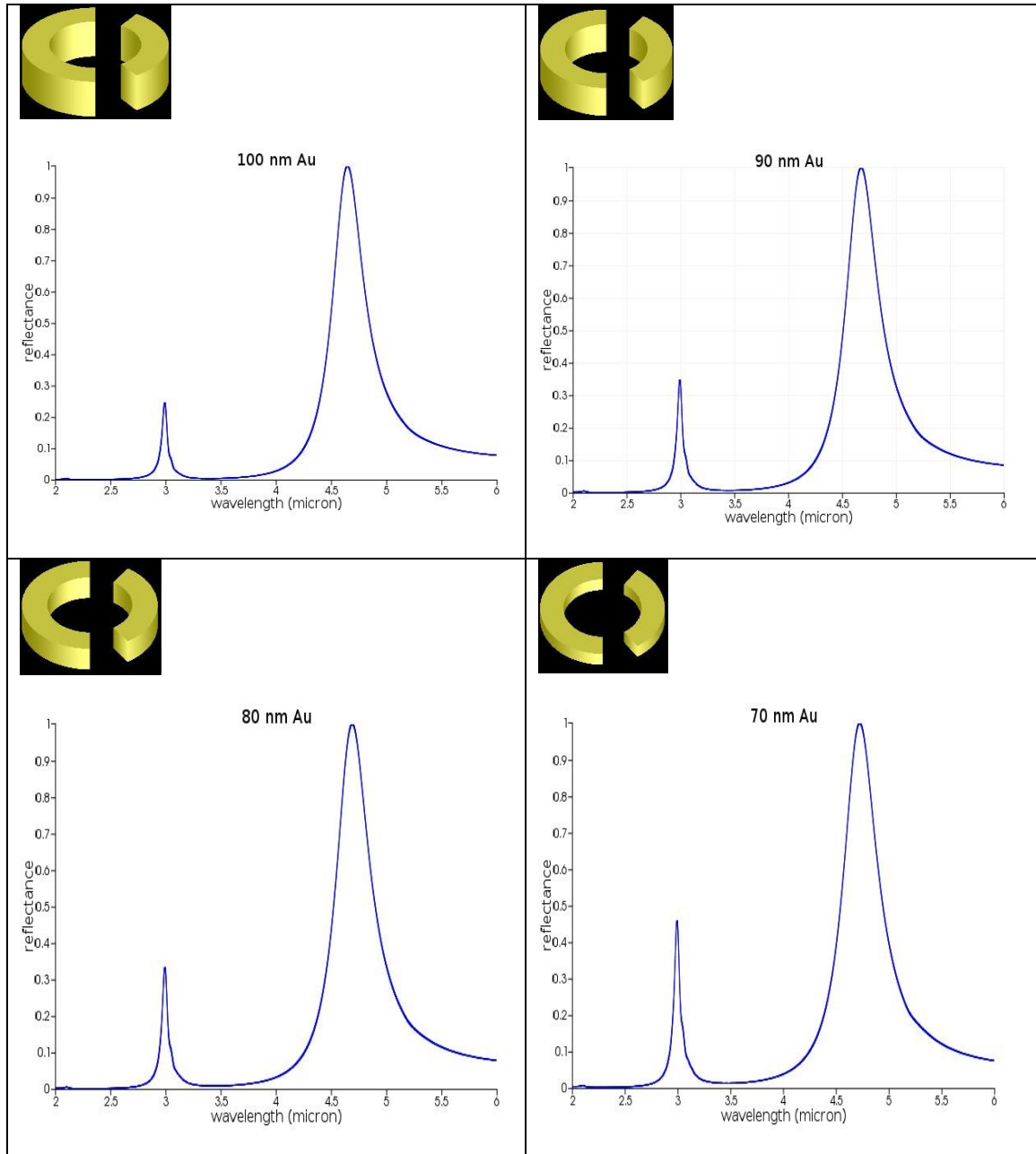


**Figure 3.11:** Reflectance plots for A-SRR thickness comparison.

Output from the analysis script contains a command that produce the resonance wavelength position and their corresponding Q-factor [36]. The analysis script of the monitor produces a plot from the two dimensional low quality factor analysis simulations as shown in figure 3.11. The plots in figure 3.11 show the location and relative amplitude of the resonance peaks shown in figure 3.12 which was used for calculation of the Q-factor values. The Q-factor of

the A-SRRs resonance wavelength of the signal in the plot was calculated by measuring the full width half maximum (FWHM) of the resonant peak at the shorter wavelength for the 100 nm Au thickness using the expression:  $Q = \lambda_p / \Delta\lambda$ .

The FWHM ( $\Delta\lambda$ ) for  $\lambda_1$  and  $\lambda_2$  is 0.06 (3.01- 2.95)  $\mu\text{m}$  and the resonance peak ( $\lambda_p$ ) is at 3  $\mu\text{m}$ . The quality factor of 50 obtained at mid-infrared region from simulations is more than twice the values as compared to other published related articles [5, 20, 24-28].

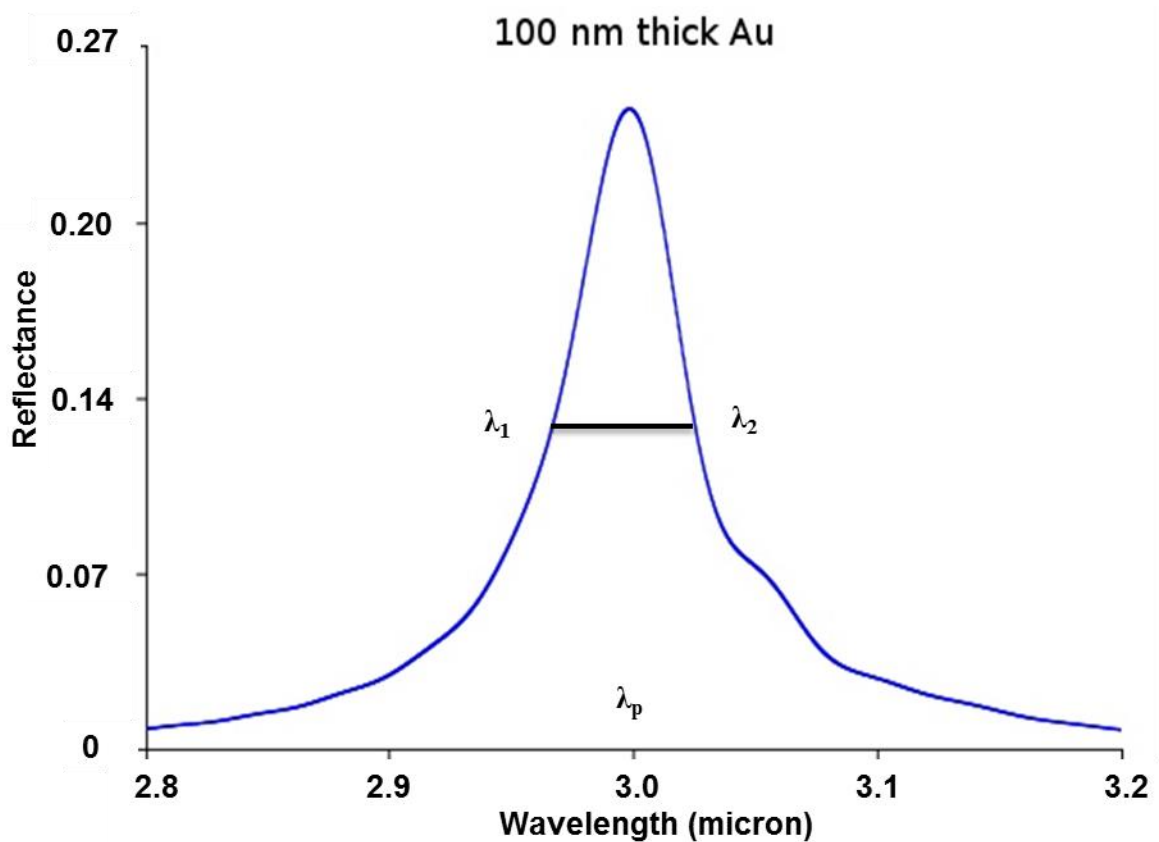


**Figure 3.12:** Zoomed image of the resonance peak shorter wavelength from the simulation of 100 nm Au thickness.

Table 3.4 contains the calculated quality factors with the corresponding Au thickness obtained by using the command from the script analysis [36]. The numerical simulation of the various Au thicknesses and the resultant Q-factors were compared as shown in the figure 3.13.

**Table 3.4:** Comparing gold thickness for the 960 nm diameter A-SRRs pattern

Thickness (nm)	10	20	30	40	50	60	70	80	90	100
Q-factor	4.53	13.01	21.43	30.67	38.64	43.00	46.02	48.58	48.93	49.90

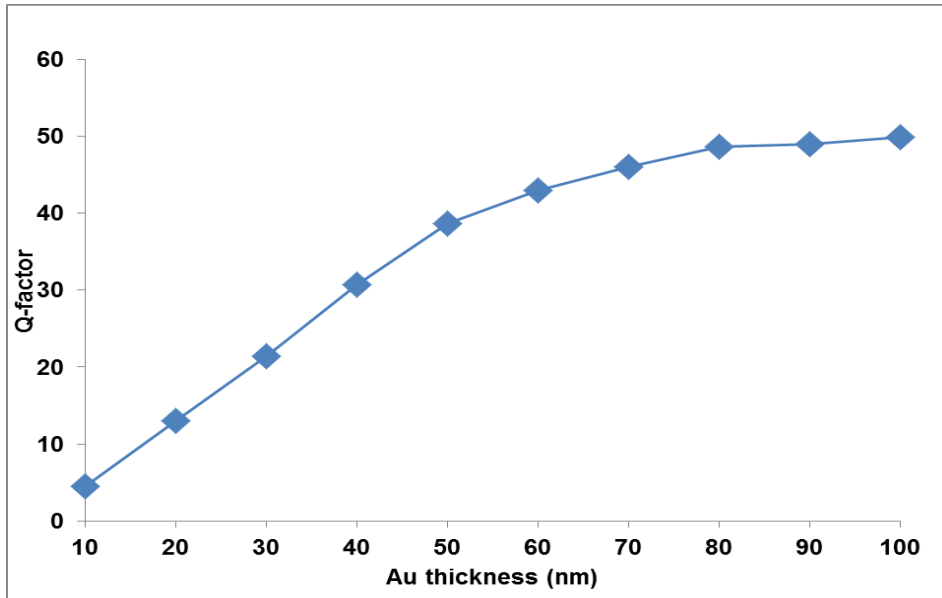


**Figure 3.13:** Comparing gold thickness for the 960 nm diameter A-SRRs pattern

There is a continuous increase of the Q-factor as the Au thickness as increased as show in figure 3.13. From thickness above 80 nm for the A-SRRs pattern the Q-factor values exhibits very little change. So in this work 100 nm Au was the thickness used for every design and fabrication since it produced the highest Q-factors from simulation. Though there is a potential increase for thickness above 100 nm but this quantity is considerable for fabrication in terms of cost.

### 3.5 Dipole structures

The architecture for this structure involves a conventional Au dipole nanoantenna comprising of two asymmetric arms separated by a gap. The asymmetric modelling suggests employing radiative and sub-radiant (dark mode) plasmonic elements that are strongly coupled by being closely placed and appropriately oriented [35-36]. The arms are tuned to produce plasmonic resonances peaks within mid-infrared therefore having a close proximity like the arcs of the A-SRRs discussed in the section 3.4.

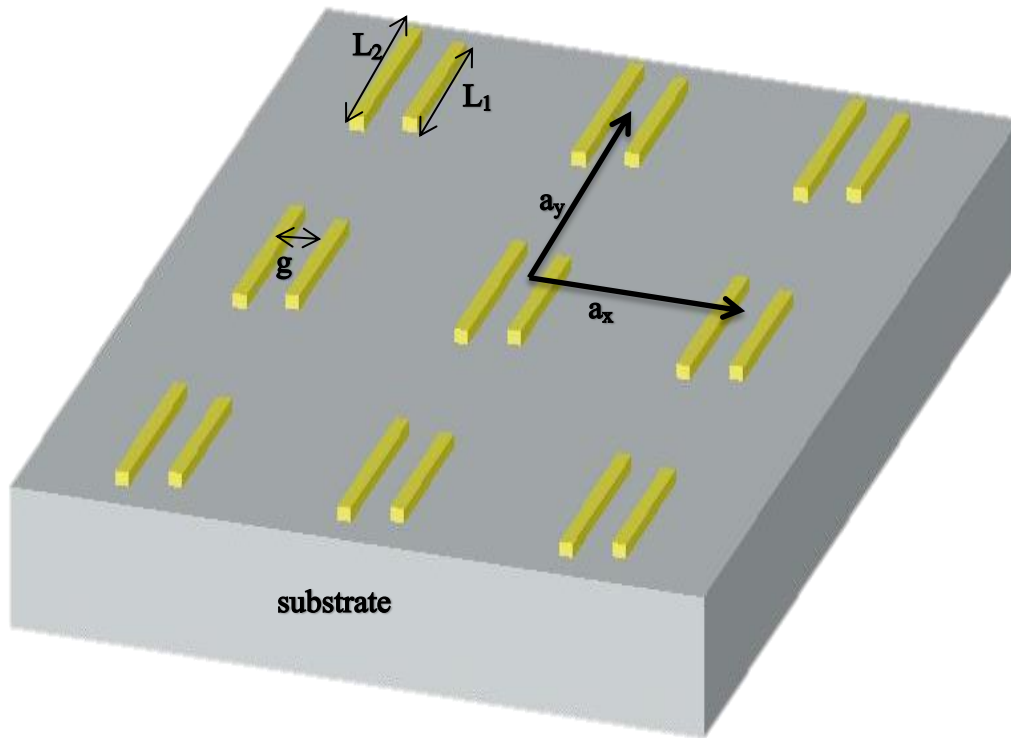


*Figure 3.14: Arrays of asymmetric dipole structures on fused silica substrate.*

The lengths ( $L_1$  and  $L_2$ ) for small and large arms were modelled to be (0.9 and 1.1)  $\mu\text{m}$  respectively. The gap between the two asymmetric arm's length is 0.25  $\mu\text{m}$ . The periodic parameter ( $a_{xy}$ ) for the design was also varied as shown in figure 3.14 to investigate the effect on reflectance peaks.

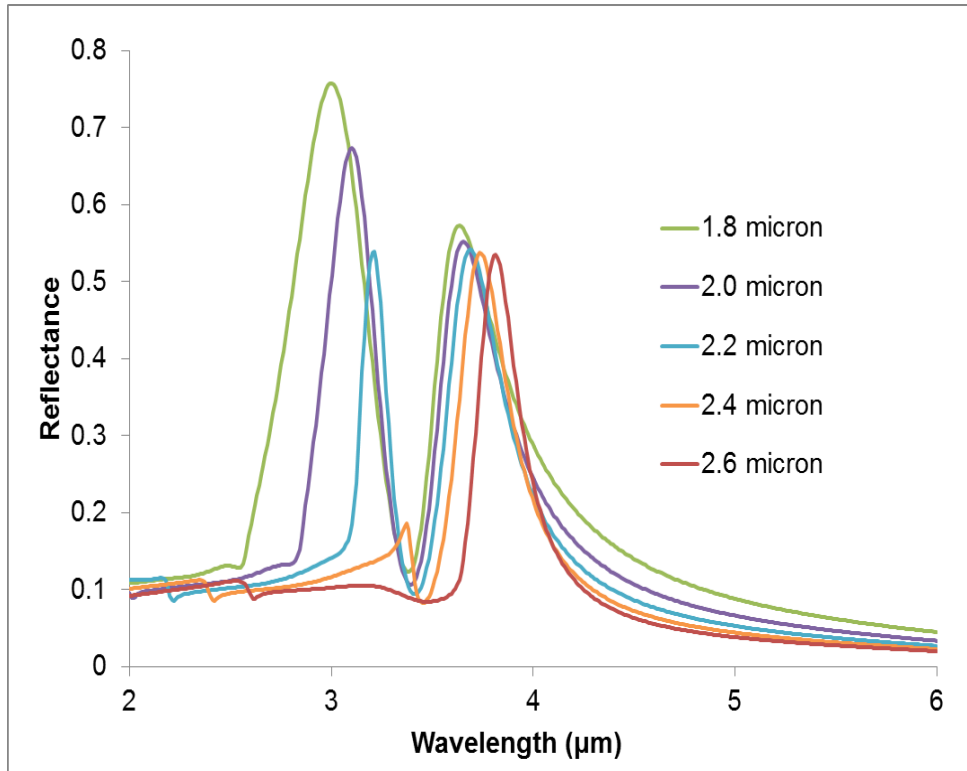


**Figure 3.15:** Reflectance plots from numerical simulation of 100 nm Au thick for dipole with asymmetric arm's length of (1.1 and 0.9)  $\mu\text{m}$  at different periodicity.

Figure 3.15 shows the periodic effect on the reflectance peaks of the designed dipole. The reflectance peaks are being narrowed as the periodicity increase. This result corresponds to the periodic effect of reflectance peaks produced from A-SRRs design as discussed earlier. The periodic value of 2.2  $\mu\text{m}$  is the optimum periodicity for this design because of the well-developed double peaks as shown in figure 3.15. Here, the coupling from the asymmetric arms that form the dipole were placed in line as shown in figure 3.15 compared to design arrangements in references [37-39]. The dipole design ideas from these references were combined with the dipole designed in this work to produce a new structure asymmetric split H-shape structure (ASHs).

### 3.6 Asymmetric split H-shape (ASHs)

The architecture for ASH structure also involves a conventional Au dipole nanoantenna comprising of two asymmetric arms separated by gap but with a cross-bar placed at the centre of the asymmetric arm separated by a slit. Arrays of the structure are schematically shown in figure 3.16. This structure was introduced because of the nanoscale parts referred to as “hot spots” [58] arising from the sharp edges and narrow slit. The ASH structure shown in this thesis exhibits both a nanoscale gap and multiple sharp edges and with proper optimisation of the geometry the structure it can produce a highly sensitive plasmonic sensor [18, 41-46] as detailed in chapter six.

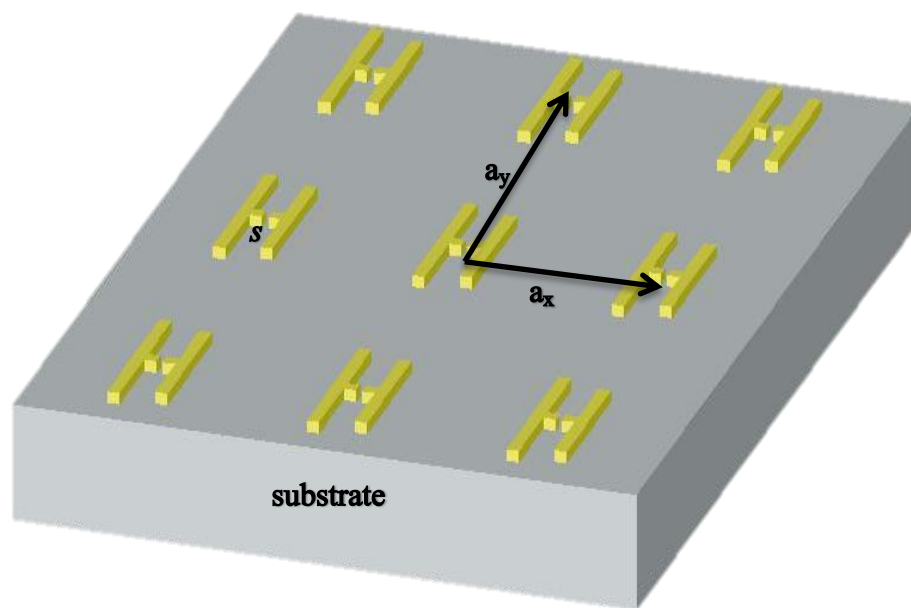


**Figure 3.16:** Schematic diagram of ASHs Au pattern on a fused silica substrate showing an array of split-H structures.

The stated ASH features support high E-field enhancement while the asymmetric nature of the structure increases the sensitivity. These features of the ASHs structure produce a larger shift in the resonance peaks and amplify the vibrational resonance of C-H resonance band [18, 47] as utilized in chapter six.

In this section, different asymmetric arms of the ASHs structures were modelled to tune plasmonic resonance peaks within mid-infrared region of EM spectrum as shown in figure 3.17a. The small arm ( $L_1$ ) dimension ranges from  $(0.7 - 1.5) \mu\text{m}$  while the large arm ( $L_2$ ) is from  $(0.9 - 1.7) \mu\text{m}$  making the arm's length to differs by  $0.2 \mu\text{m}$ . Cross-bars of  $(100 \text{ by } 100) \text{ nm}$  separated by a slit of  $50 \text{ nm}$  were place at centre of the asymmetric arms. Numerical simulation of the design produces double peaks separated with a dip as shown in the reflectance figure of 3.17a. The peaks at shorter and longer wavelengths correspond to the small and large arms respectively as shown in the figure.

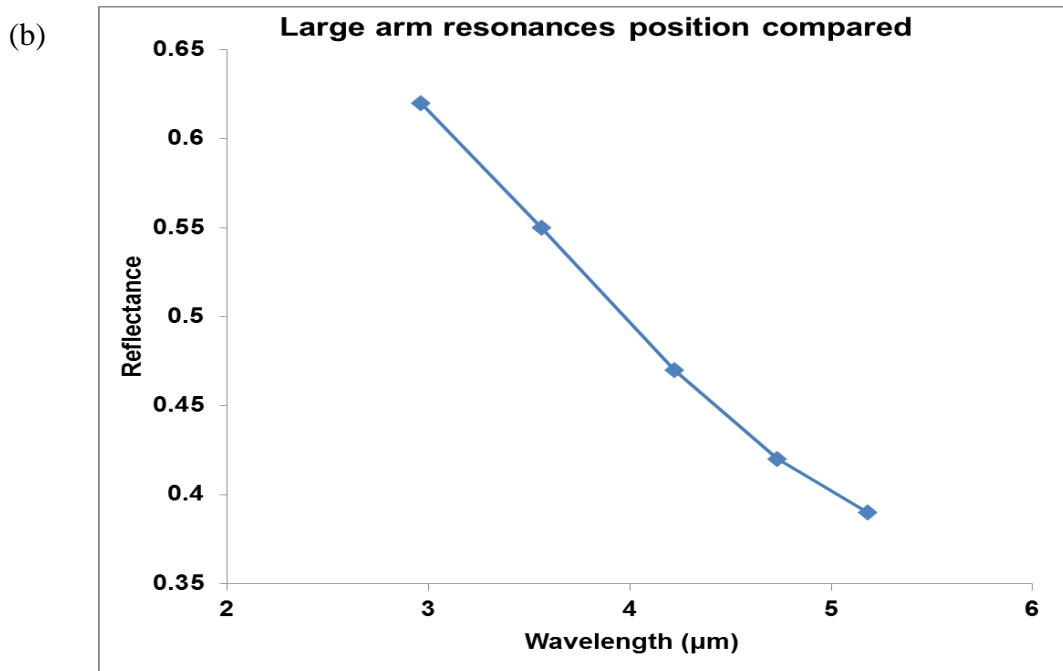
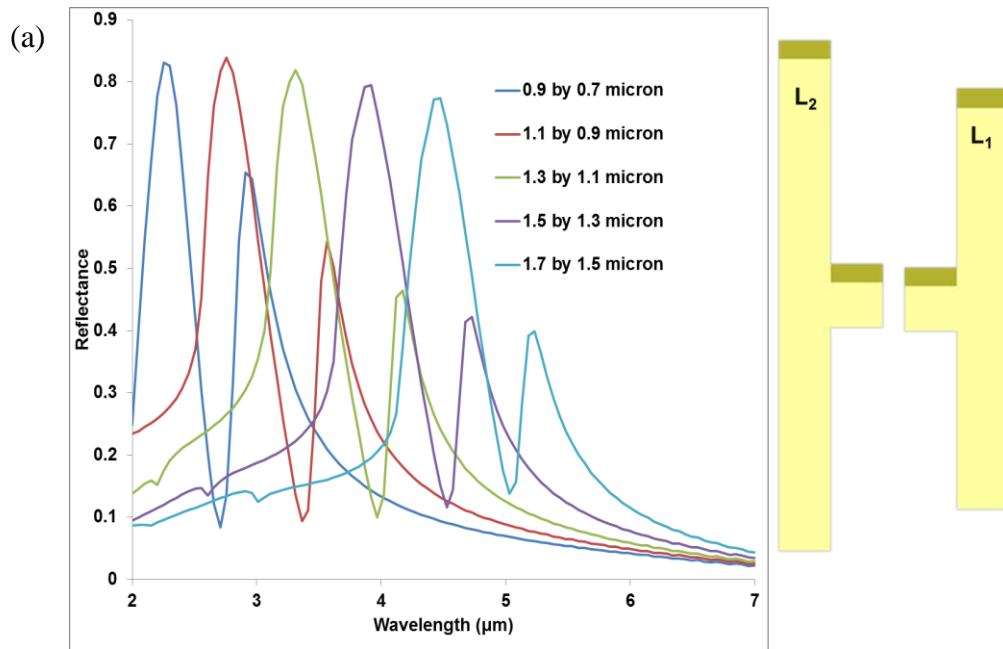


**Figure 3.17:** FDTD numerical simulation of 100 nm Au thick for (a) plasmonic resonance peaks tuned within (2 to 7)  $\mu\text{m}$  by varying the asymmetric arm's length of ASHs structure (b) comparison of the resonance peak position of the large arm.

As expected, the reflectance peaks shift to longer wavelengths as the arms get larger as shown in figure 3.17a. Also, the imaginary index for the modelled material (gold and fused silica) increases from shorter to longer wavelength affects the intensity of the peaks. Figure 3.17b shows the reduction in the peak intensity of the large arm as the resonance is tuned from 2.96  $\mu\text{m}$  to 5.18  $\mu\text{m}$  wavelength which corresponds to dark and light blue plots of figure

3.17a. The analysis of the reflectance resonance enables the choice of suitable dimensions for the targeted sensing application in this region.

Numerical simulations of ASH structures were performed to investigate effect of periodicity on the resultant plasmonic resonances. The dimensions chosen for the structures were based on the targeted wavelength position, within the mid infrared spectrum to match with the sensors region of interest. The reflectance spectra due to the periodic variations produced from the designed structure are shown in figure 3.18a.

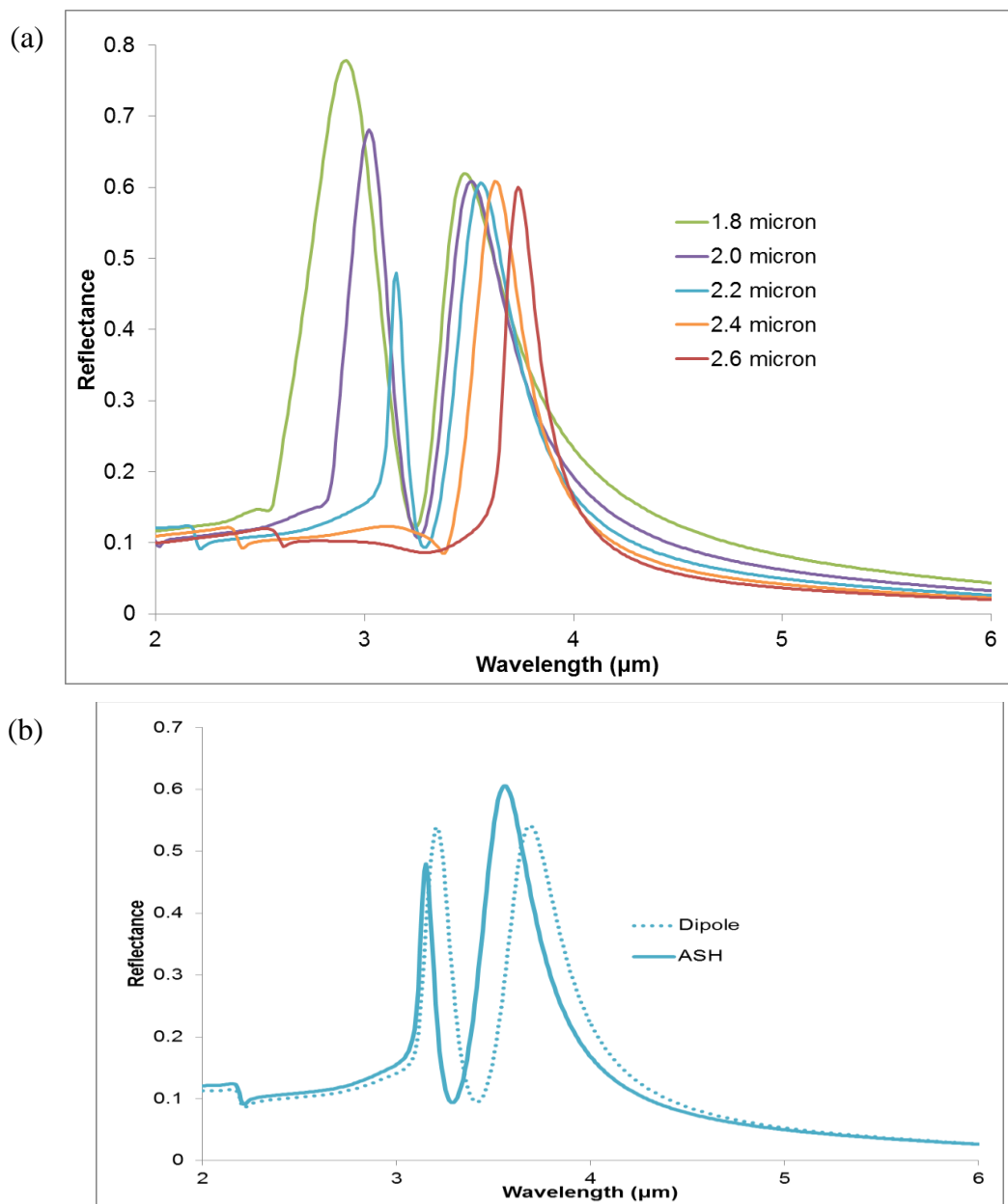


**Figure 3.18:** Reflectance spectra from the numerical simulations of (a) ASHs periodicity (b) Periodic of 2.2 μm for asymmetric dipole and ASH structures.

A comparison of sharpest peak from ASHs and asymmetric dipole as discussed in section 3.5 is shown in figure 3.18b. Increasing the quality factor of plasmonic resonance is a challenge in the design of metallic metamaterial. MMs with high Q-factor value as high as 97, in the visible region [48] and 227 values in the Terahertz [49] regions of the electromagnetic spectrum have been reported. The high Q-factor value of 97 in the visible region was attributed to the effects of hybridization of two distinct resonant elements coupled together [48]. Within the mid-infrared region, researchers [4, 18] have used a different approach to minimize the ohmic losses that are unavoidable in the metal patterns, resulting in Q-factors greater than 100 i.e. for purely dielectric structures. Results previously reported for the metallic metamaterial in the mid-infrared region are typically Q-factors of less than 10[5, 29].

To calculate the Q-factor of the plasmonic resonances for dipole and ASH as shown in figure 3.18b using the expression in 3.1 this involves the full width half maximum (FWHM) of the resonance peak. In figure 3.18b, the FWHM ( $\Delta\lambda$ ) of  $\lambda_p$  (resonance peaks) at (3.20 and 3.15)  $\mu\text{m}$  is 0.14 and 0.08 for the dipole and ASH respectively. The quality factors from the peaks at shorter wavelength is  $Q_{\text{dipole}} = 23$  and  $Q_{\text{ASH}} = 39$  for the structures. The ASH shows a narrower resonance peaks possibly because of the split crossbar between the arms which is the only change between the two designs. The split bar of the H-shape structure involves stronger coupling between the dipole arms of the asymmetric H-shape structure. Reference [50] has also recommended ability of H-shape to produce high Q-factors.

The reflectance spectra from the periodic variation of both structures (asymmetric dipole and ASH) showed blue shift as the periodicity decreases. Also the magnitude of the reflectance increase as the periodic value decreases as observed in figure 3.18a. These results satisfy the blue shift of the resonance peaks at decreasing periodicity [29, 51] with the same effect observed in the experimental section of this work.

Numerical simulation results correspond to the experimental results in chapter five showed that split asymmetric H-shaped (ASH-shaped) structures can produce narrower reflection resonance peaks compared to dipoles of a similar design. The Q-factors calculated from the simulation plots showed Q values produced by ASH structures to be 26% higher than the

corresponding asymmetric dipoles' and the Q-factor generated is more than two times greater than previously achieved values obtained in the mid-infrared [5, 29, 52].

Further exploration of the new structure shows its dual polarization ability. Dual transverse electric waves can be applicable in ASH structure to produce plasmonic resonance tuned by the arms dimension. Figure 3.19 shows the wave polarization with respect to the ASH, where the TE is parallel to the vertical asymmetric arm and across the horizontal gap created by two symmetric cross bars.

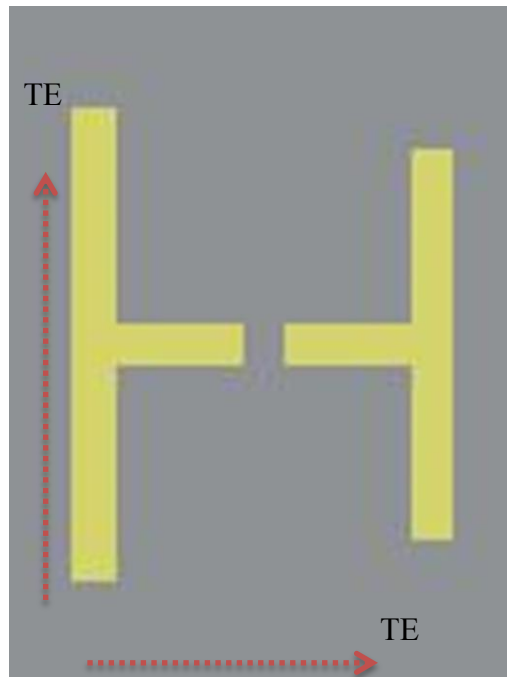


**Figure 3.19:** Schematic diagram showing the directions of the wave on the ASH.

The dimensions of the arms are (1.1 and 0.9)  $\mu\text{m}$  which corresponds to the (large and small) arms respectively. The large and small arms tune the resonance peaks to (4.6 and 3.0)  $\mu\text{m}$  respectively when TE source is applied as shown in figure 3.20a. When the TE polarization is across the small gap between the cross bar of ASH and this produces a single plasmonic peak at 3.9  $\mu\text{m}$  because the bars are symmetric as shown in figure 3.20a. Figure 3.20b shows electric field for the simulated ASH structure using Lumerical. The field plots were generated at the wavelength corresponding to the wavelength position of the plasmonic peaks.

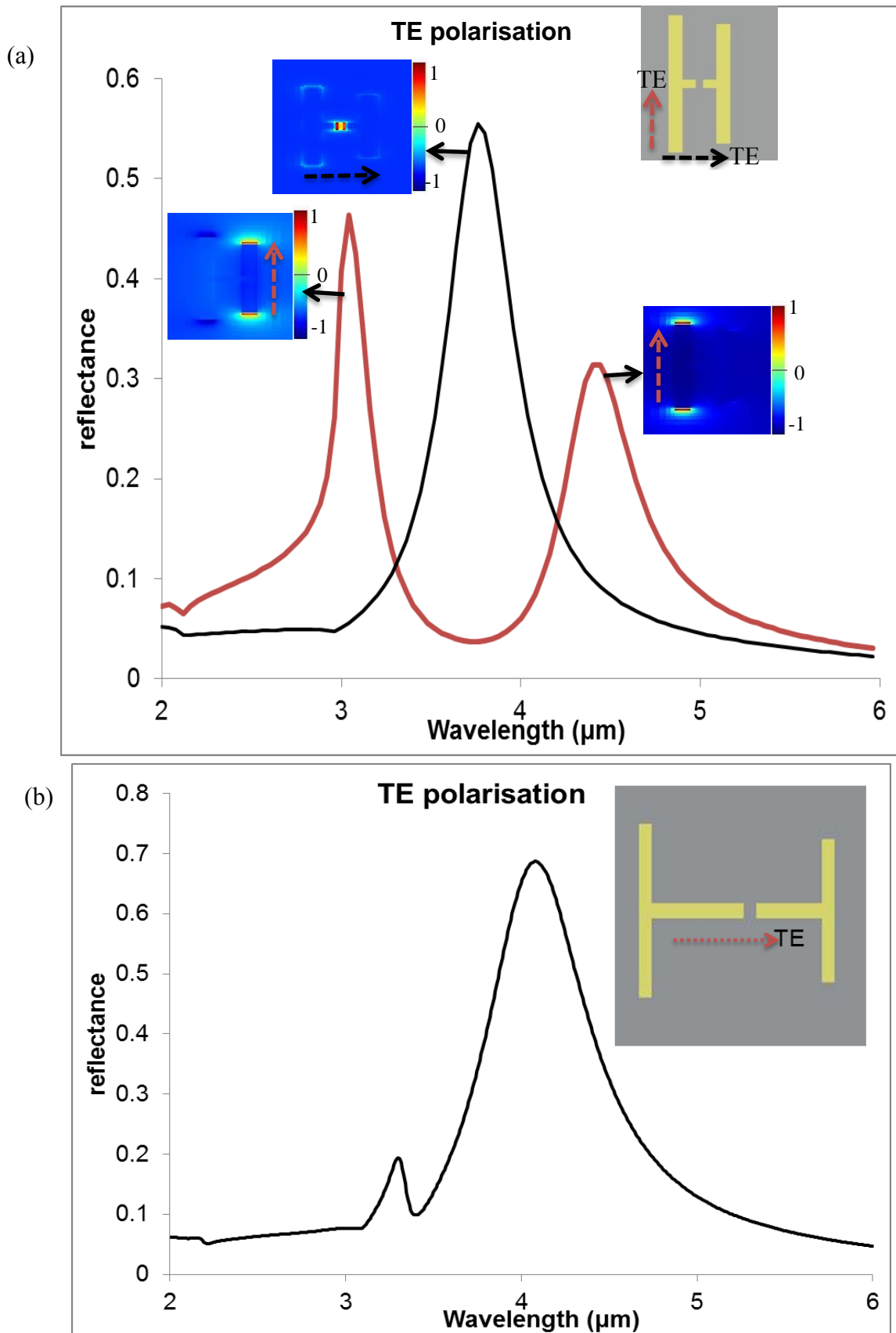


**Figure 3.20:** Reflectance spectra of ASH plasmonic resonances for (a) two TE polarisation sources across the gap and parallel to the arms showing the resultant E-field plots, inset (b) a TE polarisation along asymmetric cross bars of ASH, inset.

The dark blue colour shows the minimum E-field intensity while dark red shows the maximum E-field intensity. The insets E-field plots correspond to the plasmonic peaks at wavelength of (3.0, 3.9 and 4.6)  $\mu\text{m}$  as shown in figure 3.20a. The maximum E-field observed at these wavelengths are shown with the reflectance spectra of figure 3.20a. Inset of figure 3.20b shows transverse TE source across the small gap formed by asymmetric cross bar. This produces double plasmonic resonance peaks as shown with the reflectance spectra in figure 3.20b. The dimensions of the asymmetric cross bars are (0.7 and 0.65)  $\mu\text{m}$  with their corresponding peaks at (4.1 and 3.3)  $\mu\text{m}$  respectively. These reflectance spectra are used to show the ability of the new structure, ASHs to work in orthogonal polarisations.

### **3.7 Discussions and Conclusion**

The 3D simulation tool used to model and design the different photonic structures has been described and the results obtained for different metallic metamaterial devices designed have been analysed and compared. The 3D approach used in the simulations gives good and consistent results from the characteristics of the designed structures. Though the 3D simulations are time consuming but the results produced from this approach are sufficient and easy to compare with the experimental work.

A logical sequence has been followed and used in designing and improving the metallic metamaterial device structures. Beginning with the optimization of the A-SRRs for a narrower reflectance resonance peak which produce high quality factors the amplitude of the resonances is subsequently optimised for the photonic devices is for their use in sensing applications.

A new device was also presented following the idea of asymmetric dipole. The ASH structure designed from dipole was optimized and compared with the dipole structures which showed better characteristics in the reflectance resonance than the dipoles. Also there is the opportunity to use plasmonic resonance peaks from ASH structure when the polarization of the source is orthogonal. This is a scenario is not obtainable with dipole and A-SRR structures.

In conclusion, three different metallic metamaterial structures have been presented, with promising simulation results. The parameters of the structures such as the dimension and periodicity have been described and optimized. Again, the use of the two basic different materials fused silica and gold has been appropriately modelled understanding the effect of their refractive index and variation with wavelength. All devices presented in this chapter can proceed to fabrication and measurement.

### 3.8 References

1. A. Papakostas, A. Potts, D. M. Bagnall, S. L. Prosvirnin, H. J. Coles, and N. I. Zheludev, "Optical Manifestations of Planar Chirality," *Phys. Rev. Lett.* 90, 107404, 2003.
2. D. P. Fromm, A. Sundaramurthy, P. J. Schuck, G. Kino, and W. E. Moerne, "Gap-Dependent Optical Coupling of Single Bowtie Nanoantennas Resonant in the Visible," *Nano Letters* 4, 957-961, 2004.
3. H. Aouani, H. Šípová, M. Rahmani, M. Navarro-Cia, K. Hegnerová, J. Homola, M. Hong, and S. A. Maier, "Ultrasensitive Broadband Probing of Molecular Vibrational Modes with Multifrequency Optical Antennas," *ACS Nano* 7, 669–675, 2013.
4. S. Linden, C. Enkrich, M. Wegener, J. Zhou, T. Koschny, and C. M. Soukoulis, "Magnetic Response of Metamaterials at 100 Terahertz," *Science* 306, 1351-1353, 2004.
5. B. Lahiri, A. Z. Khokhar, R. M. De La Rue, S. G. McMeekin, and N. P. Johnson, "Asymmetric split ring resonators for optical sensing of organic materials," *Optics Express*, 17, 1107-1115, 2009.
6. C. Sabah, "Multi-resonant metamaterial design based on concentric V-shaped magnetic resonators," *J. Electromagn. Waves Appl.* 26, 1105–1115, 2012.
7. H. E. Bennett and J. M. Bennett, "Validity of the Drude theory -for silver, gold and aluminum in the infrared," in *Optical Properties and Electronic Structure of Metals and Alloys*, F. Abeles, ed., North-Holland Amsterdam, 1966.
8. F. A. Modine and D. Y. Smith, "Approximate formulas for the amplitude and the phase of the infrared reflectance of a conductor," *Journal of the Optical Society of America A*, 1, 1171-1174, 1984.
9. V. G. Veselago, "The electrodynamics of substances with simultaneously negative values of permittivity and permeability," *Soviet Physics Uspekhi*, 10, 509-514, 1968.
10. Kane Yee, "Numerical solution of initial boundary value problems involving Maxwell's equations in isotropic media," *IEEE Transactions on Antennas and Propagation*, 14, 302–307, 1966.
11. E. D. Palik, "Handbook of Optical Constants of Solids," Vol 1-3, ISBN: 978-0-12-544415-6, 1997.

12. J-P. Berenger, "A Perfectly Matched Layer for the Absorption of Electromagnetic Waves," *Journal of Computational physics* 114, 185-200, 1994.
13. [www.lumerical.com/fdtd](http://www.lumerical.com/fdtd).
14. Z. Wang, S. Pan, T. D. Krauss, H. Du, and L. J. Rothberg, "The structural basis for giant enhancement enabling single-molecule Raman scattering," *PNAS*, 100, 8638-8643, 2003.
15. Li, K. Stockman, M. I. Bergman, D. J., "Self-Similar Chain of Metal Nanospheres as an Efficient Nanolens," *Phys. Rev. Lett.*, 91, 227402, 2003.
16. J.-H. Tian, B. Liu, X. Li, Z.-L. Yang, B. Ren, S.-T. Wu, N. Tao, and Z.-Q. J. Tian, "Chemical Fabrication of Heterometallic Nanogaps for Molecular Transport Junctions," *Am. Chem. Soc.*, 128, 14748-14749, 2006.
17. D. R. Ward, N. K. Grady, C. S. Levin, N. J. Halas, Y. Wu, P. Nordlander, and D. Natelson, "Electromigrated Nanoscale Gaps for Surface-Enhanced Raman Spectroscopy," *Nano Lett.*, 7, 1396–1400, 2007.
18. I. M. Pryce, Y.A. Kelaita, K. Aydin, and H.A. Atwater, "Compliant Metamaterials for Resonantly Enhanced Infrared Absorption Spectroscopy and Refractive Index Sensing," *Nano*, 5, 8167– 8174, 2011.
19. B. Yuan, W. Zhou and J. Wang, "Novel H-shaped plasmon nanoresonators for efficient dual-band SERS and optical sensing applications," *J. Opt.*, 16, 105013, 2014.
20. V. A. Fedotov, M. Rose, S.L. Prosvirnin, N. Papasimakis and N. I. Zheludev, "Sharp trapped-mode resonances in planar metamaterials with a broken structural symmetry," *Phys Rev Lett.*, 99, 147401, 2007.
21. P. Ding, E. J. Liang, W. Q. Hu, G. W. Cai, and Q. Z. Xue, "Tunable plasmonic properties and giant field enhancement in asymmetric double split ring arrays," *Photon. Nanostructures*, 9, 42–48, 2011.
22. P. Gay-Balmaz, and Olivier J. F. Martin, "Electromagnetic resonances in individual and coupled split-ring resonators," *J. Appl. Phys.*, 92, 2929-2936, 2002.
23. J. D. Baena, J. Bonache, F. Martin, R. M. Sillero, F. Falcone, T. Lopetegi, M. A. G. Laso, and J. Garcia-Garcia, "Equivalent-circuit models for split-ring resonators and complementary split-ring resonators coupled to planar transmission lines" *IEEE Transactions on Microwave Theory and Techniques*, 53, 1451-1461, 2005.
24. N. I. Zheludev, S. L. Prosvirnin, N. Papasimakis, and V. A. Fedotov, "Lasing spaser," *nature photonics*, 2, 351-353, 2008.

25. R. Adato, Yanik, A. A., Wu, C., Shvets, G. and H. Altug, "Radiative engineering of plasmon lifetimes in embedded nanoantenna arrays," *Opt. Express* 18, 4526-4537, 2010.
26. V. A. Fedotov, T. Uchino, and J. Y. Ou, "Low-loss plasmonic metamaterial based on epitaxial gold monocrystal film," *Optics Express*, 20, 9545-9550, 2012.
27. K. Aydin<sup>1</sup>, I. M. Pryce, and H. A. Atwater, "Symmetry breaking and strong coupling in planar optical metamaterials," *Optics Express*, 18, 13407-13417, 2010.
28. T. Koschny, P. Markoš, D. R. Smith, and C. M. Soukoulis, "Resonant and antiresonant frequency dependence of the effective parameters of metamaterials," *Phys. Rev. E*, 68, 065602, 2003.
29. A. Boltasseva, and H. A. Atwater, "Low-Loss Plasmonic Metamaterials," *Science*, 331, 289-291, 2011.
30. N. I. Zheludev, S. L. Prosvirnin, N. Papasimakis, and V. A. Fedotov, "Lasing spaser," *nature photonics*, 2, 351-353, 2008.
31. I. Sersic, M. Frimmer, E. Verhagen, and A. F. Koenderink, "Electric and Magnetic Dipole Coupling in Near-Infrared Split-Ring Metamaterial Arrays," *Phys. Rev. Lett.*, 103, 213902-4, 2009.
32. N. Liu, H. Liu, S. N. Zhu and H. Giessen, "Stereometamaterials," *Nat. Photon.* 3, 157-162, 2009.
33. U. K. Chettiar, A. V. Kildishev, T. A. Klar, and V. M. Shalaev, "Negative index metamaterial combining magnetic resonators with metal films," *Opt. Express*, 14, 7872-7877, 2006.
34. V. M. Shalaev, "Optical negative-index metamaterials," *Nature Photonics*, 1, 41-48, 2007.
35. P. Ding, E. J. Liang, Q. Zhou, L. Zhang, Y. X. Yuan, and Q. Z. Xue, "Influence of metal-layer thickness on the losses in fishnet metamaterial," *Metamaterial international conference, Nanjig*, 4723573, 2008.
36. [http://docs.lumerical.com/en/diffractive\\_optics\\_cavity\\_q\\_calculation.html](http://docs.lumerical.com/en/diffractive_optics_cavity_q_calculation.html)
37. O. L. Muskens, V. Giannini, J. A. Sánchez-Gil and Jaime Gómez Rivas, "Strong Enhancement of the Radiative Decay Rate of Emitters by Single Plasmonic Nanoantennas," *Nano Letters* 7, 2871-2875, 2007.
38. P. Mühlischlegel, H.-J. Eisler, O. J. F. Martin, B. Hecht and D. W. Pohl, "Resonant Optical Antennas," *Science*, 308, 1607-1609, 2005.

39. X-J He, L Wang, J-M Wang, X-H Tian, J-X Jiang and Z-X Geng, "Electromagnetically induced transparency in planar complementary metamaterial for refractive index sensing applications," *J. Phys. D: Appl. Phys.*, 46, 365302, 2013.
40. Mark I. Stockman; Sergey V. Faleev; David J. Bergman, "Localization versus Delocalization of Surface Plasmons in Nanosystems: Can One State Have Both Characteristics," *Phys. Rev. Lett.*, 87, 167401-167404, 2001.
41. W. Kubo and S. Fujikawa, "Au Double Nanopillars with Nanogap for Plasmonic Sensor," *Nano Lett.*, 11, 8–15, 2011.
42. D. R. Ward, N.K. Grady, C.S. Levin, N.J. Halas, Y. Wu, P. Nordlander and D. Natelson, "Electromigrated nanoscale gaps for surface-enhanced Raman spectroscopy," *Nano Lett.*, 7, 1396-1400, 2007.
43. Zi-Q. Cheng, F. Nan, D-J. Yang, Y-T. Zhong, L. Ma, Z-H. Hao, L.Zhou and Q-Q. Wang, "Plasmonic nanorod arrays of a two-segment dimer and a coaxial cable with 1 nm gap for large field confinement and enhancement," *Nanoscale*, 7, 1463-1470, 2015.
44. P. Pavaskar, J. Theiss, and S. B. Cronin, "Plasmonic hot spots: nanogap enhancement vs. focusing effects from surrounding nanoparticles," *Opt. Express* 20(13), 14656-14662, 2012.
45. C-K. Chen, M-H. Chang, H-T. Wu, Y-C. Lee and T-J. Yen, "Enhanced vibrational spectroscopy, intracellular refractive indexing for label-free biosensing and bioimaging by multiband plasmonic-antenna array," *Biosens Bioelectron.*, 60, 343–350, 2014.
46. R. F. Peters, L. Gutierrez-Rivera, S. K. Dew and M. Stepanova, "Surface Enhanced Raman Spectroscopy Detection of Biomolecules Using EBL Fabricated Nanostructured Substrates," *J. Vis. Exp.*, 97, 52712, 2015.
47. H. Aouani, H. Šípová, M. Rahmani, M. Navarro-Cia , K. Hegnerová , J. Homola, M. Hong and S. A. Maier, "Ultrasensitive Broadband Probing of Molecular Vibrational Modes with Multifrequency Optical Antennas," *Nano Lett.*, 7, 669-675, 2013.
48. J. Q. Wang, B. H. Yuan, C. Z. Fan, J. N. He, P. Ding, Q. Z. Xue and E. Liang, "A novel planar metamaterial design for electromagnetically induced transparency and slow light," *Opt. Express* 21, 25159–66, 2013.
49. W. Cao, R. Singh, I. A. Al-Naib, M. He, A. J. Taylor and W. Zhang, "Low-loss ultra-high-Q dark mode plasmonic Fano metamaterials," *Optics Letters* 16, 37(2012).

50. B. Yuan, W. Zhou and J. Wang, "Novel H-shaped plasmon nanoresonators for efficient dual-band SERS and optical sensing applications," *J. Opt.* 16, 105013, 2014.
51. I. Sersic, M. Frimmer, E. Verhagen and A. F. Koenderink, "Electric and Magnetic Dipole Coupling in Near-Infrared Split-Ring Metamaterial Arrays," *PhysRevLett.* 103, 213902-4, 2009.
52. I. G. Mbomson, S.G. McMeekin, B. Lahiri, R.M. De La Rue and N.P. Johnson, "Gold asymmetric split ring resonators (A-SRRs) for nano sensing of estradiol," *Proc. SPIE.* 9125, Metamaterial IX, 912510, 2014.

# Chapter 4

## Fabrication of Metamaterial Devices

### 4.1 Introduction

The fabrication of the design devices was performed on fused silica ( $\text{SiO}_2$ ) by following sequential stages. The initial process consists of transferring a computer aided design (CAD) pattern on to the surface of the substrate by using electron-beam lithography (EBL) tool at James Watt nanofabrication centre (JWNC) cleanroom. Other stages are pattern development which is followed by metallization and then acetone lift-off for the production of the metallic metamaterial (MM) structures are also carried out in the cleanroom. These processes involve a series of separate stages, with each one being important for the fabrication of a functional device.

This chapter is divided into sub sections: the CAD design process, pattern transfer using electron-beam lithography, pattern development and metallization. The material and equipment used are also presented. Three dimensional simulation results particularly where the angles that formed the gaps were scaled in terms of the arc length were compared in order to understand the effects of fabrication tolerances. Lastly, the discussion and conclusions are presented.

### 4.2 Fabrication technique

During fabrication all the listed tools were utilized at different stages by strictly following sequential procedures as shown in the flow chart of figure 4.1 until a specific designed pattern was achieved. The flow chart is as explained in the subsequent section.

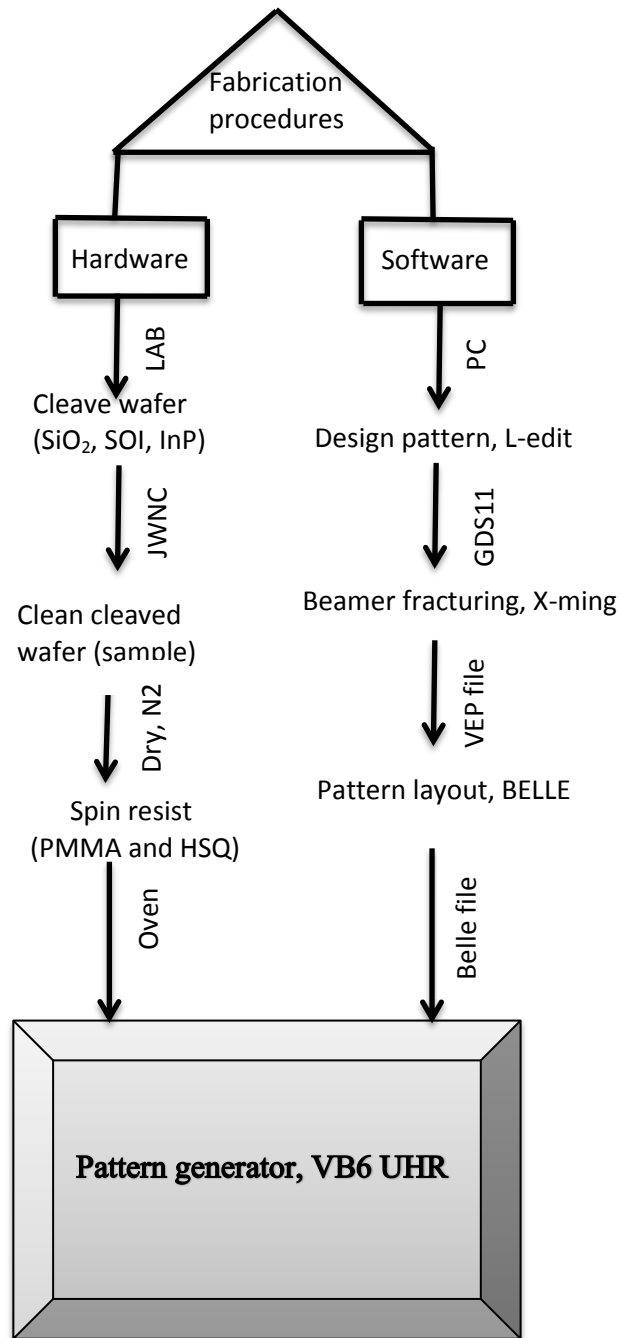


**Figure 4.1:** Flow chart of fabrication process for electron beam lithography writing.

### 4.2.1 CAD design and Substrate preparation

The commercial CAD package, used for initial design of the different patterns is called L-Edit. L-Edit is a layout editor from Tanner EDA, used to design MM and other devices with several layers [1]. The software is useful tool for the micro and nano-fabrication because it enables design hierarchy.

All the parameters set in the L-Edit need to be optimised in accordance with other software use for the EBL [2]. For example, to optimise the total pattern writing times it is important to be able to distinguish between pattern areas written by different spot sizes. Again, patterns designed with different colours or layers can be separated out into separate pattern writing files, allowing the EBL tool to write the layers with different spot size. The large spots expose large areas of the pattern faster than the small spots. The areas are distinguished by assigning layer name and number.

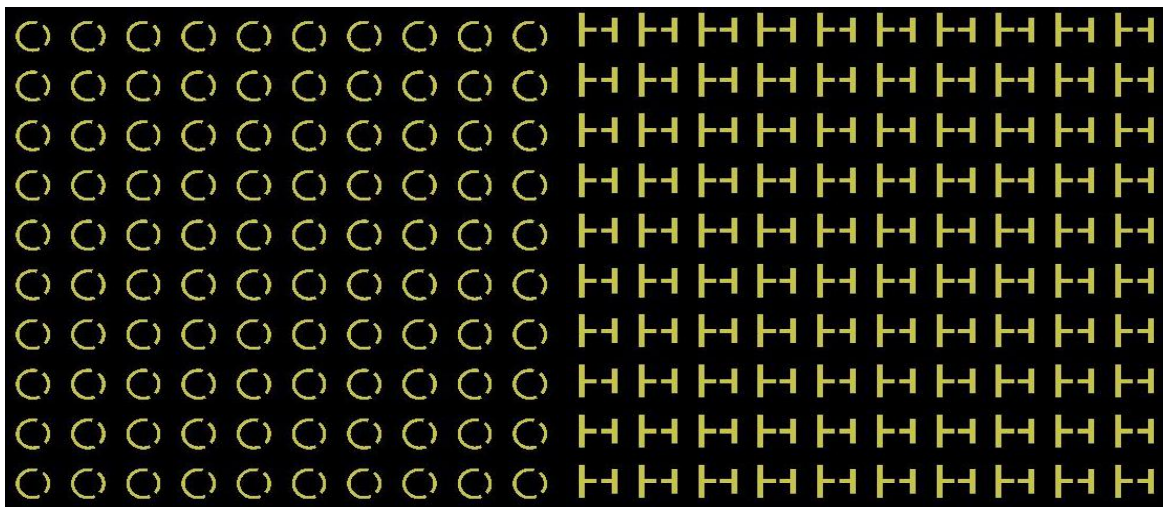


*Figure 4.2: Arrays of metallic metamaterial (A-SRRs and ASHs) pattern design.*

Figure 4.2 displays arrays of the designed MMs structures patterns before the EBL writing is carried out. The gold colour used for the L-Edit design as shown for the arrays of asymmetric split ring resonators (A-SRRs), asymmetric split H-shaped (ASH) are layers of the metallic patterns. These create the gold arcs and arms patterned on the substrate on completion of the fabrication process. The black background shows the spacing i.e. the periodicity of the

pattern. The use of a pattern array as shown in figure 4.2 in a cell saves time in the L-Edit design.

Layers which are represented with different colours in L-Edit software are an important feature during the initial design stage of fabrication process. By considering this feature various patterns were designed to match the corresponding spots sizes and dose required for the pattern creation with electron beam lithography.

The patterns designed on this software can involve creation of different layers and careful positioning of the various shapes with a clear distinction between shapes which should have different doses. The different doses for various patterns of this work have been distinguished with colours that represent different layers in the L-edit. The completed pattern design is saved in a standard graphic database system (GDSII file or .gds) format, an industry-standard file in binary form for transferring two dimensional graphical design data. The generated GDSII files are sent via the computer network to a pattern fracturing software. The pattern fracturing software (Beamer) allows different pattern layers to be converted into separate pattern writing files for writing on the VB6 lithography tool [3]. Beamer software is being run on a Linux server (Scotty) through an Xming window connection. Xming is a display server programme for Microsoft windows. The idea of using different layers (colours) in the software design is to help in recognising different parts of the device, with different writing factors and then identify parts with different resolution when the GDSII file is imported. Once a series of commands and parameters are provided along with the input GDSII file, beamer fractures the designed pattern. After considering the maximum field size, blocks, subfield and resolution grid, an output file (.VEP file) is then produced and exported to a job layout directory and beamwriter exposure layout for lithographic engineers (BELLE) through the beamwriter control computer.

BELLE is the third software programme shown in figure 4.1 flow chart, for the designed pattern preparation before the job is written with the VB6. This is where the substrate size and type are defined. BELLE includes settings for various parameters such as beam or spot size and variable resolution unit (VRU), range of doses, text identifier and patterns arrays

over a specified substrate size. VRU is ratio of the beam step size (BSS) and resolution. This is where the beam is stepped to each location in sequence. Overall, the three stated EBL software products have a graphic interface that allow users to visually observe the pattern design which permit a faster modification of parameters, if necessary.

Finally, the job layout from BELLE is transferred to the control computer together with the design file for VB6 job pattern transfer. Moreover as the software fabrication process is carried out the material process is done in parallel. The wafer used for patterning was first cleaved in a semi-clean room environment to dimensions of (6 by 6) mm sample. In the clean room the samples were thoroughly cleaned with acetone, methanol and lastly with isopropyl alcohol (IPA) then blow dried with nitrogen gas. Positive electron beam resist, polymethacrylate (PMMA) was spun on the substrates for the fabrication of the MM structures. After the resist was spun and baked in an oven or hot plate depending on the substrate and resist type the sample was then submitted for the electron beam lithography job writing by the JWNC technicians.

#### **4.2.2 Electron beam Lithography**

The aim is to create a designed pattern on a surface covered with sensitive film resist that can subsequently be transferred to the material substrate. Electron beam lithography (e-beam) can create nanoscale pattern with less than 10 nm resolution in a thin film electron resist only state of the art photolithography with complex masks can offer similar resolution where the photolithography available at Glasgow is limited to micro-structures.

The e-beam lithography was used to fabricate the designs presented in this thesis. A major feature of the e-beam nano-technology is its ability to obtain a very high resolution within units of 10s of nanometres. Also this technique offers great flexibility when there is need for change in the design because it does not require pre-fabricated masks and it can be applied to different types of materials.

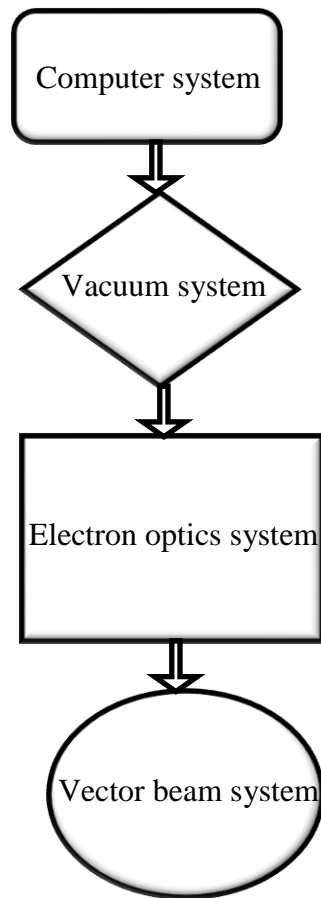


**Figure 4.3:** Flow chart of the fundamental systems of electron beam lithography, VB6 in the JWNC.

For this work, fabrication of multiple arrays of the patterns on a substrate using the Leica vector-beam series (VB6) systems is as shown in figure 4.3. The VB6 is a twenty bit tool with the field size as its primary parameter defined a design file. The VB6 is examined in detail in the subsequent sub-sections.

### **Computer system**

There are three levels of computer systems used with VB6 which are connected via Ethernet (scotty.eng.gla.ac.uk). These include the pattern data preparation computer, the operator terminal and the computer controlled subsystems [4]. The pattern data preparation computer is a PC, running Linux where pattern fracturing software, Beamer operates. The *vep file*, which is the output file, is downloaded through the *Scotty* to the operator or JWNC

technicians' terminal. Almost all control of the vector-beam system is accessed through this computer.

### **Vacuum system**

Ultra high vacuum (UHV) is needed in the gun to avoid damage to the cathode and in the column and chamber to minimise the risk of electrons with residual gas molecules. The airlock enables the technician to load and unload substrates; it also facilitates fast exchange by maintaining vacuum in the chambers, gun, main and column. For evacuation of atmospheric pressure to the UHV mechanical pre-vacuum (rotary), turbo-molecular and ion-getter pumps are provided [4]. These three pumps are used on the gun emission chamber.

### **Electron optics system**

The electron optics system provides an electron beam of suitable energy of an appropriate diameter and scans the beam in a precise pattern to the substrate. It uses a thermal field emission cathode with configurations of high and ultra-high resolution lens [4]. Through the cathode emission process the electron beam for the writing are generated. During pattern writing the information is read from the operator terminal disk and processed by the pattern generator unit which generates the analogue drive signals that drive the main and subfield deflectors. The spots formation occur when the e-beam emerges from gun and passes through two sets of magnetic deflection coils, which tilt and shift the beam to align it to the electron optical axis of the lenses.

### **Vector-beam series system**

The vector-beam (VB) system is used to expose integrated circuit pattern data on an electronic substrate. The substrates are usually spun with an electron-beam sensitive resist which is exposed with the pattern and then developed. A moveable stage supports the substrate that enables exposure to be made as the focused beam of electrons is used to write the patterns. This is done by deflecting over a certain area of the substrate known as the main field. Some specialised detector systems are used to control this process including sensors for substrate position (x, y, and z), beam position and current. After the beam has been

formed and focused, it is then scanned over the substrate using the two basic beam writing techniques, the raster and vector scanning e-beam lithography [4]. In the vector scanning the beam is scanned only over the pattern area requiring exposure composing the pattern from a list of the design structures such as A-SRRs (ring shape), Dipole (rectangular) while with the raster techniques the beam is scanned over the entire substrate. The JWNC VB6 system which is operated by only the JWNC technicians uses the vector technique to generate patterns for development.

### **4.2.3 Pattern development**

After the generated pattern is transferred to the resist through exposure in the e-beam writer, the sample is subjected to development. In this work, lift-off process was employed for the A-SRRs, asymmetric dipoles and ASHs patterns. A bilayer of PMMA positive resist of 2010 and 2041 (designated numbers for PMMA users in the JWNC), with the developer which is a mixture of methyl isobutyl ketone (MIBK) and isopropyl alcohol with an average processing time and temperature of 45 seconds and 23°C respectively were used. The PMMA resist of 2041 is always spun on top because of its higher sensitivity compared to the 2010 resist. The sample was immersed in IPA and then lastly placed in an oxygen barrel (Asher) to etch away any resist remaining after development. The Plasmafab 505 Asher is also used to ensure a clear undercut of the pattern before using the Plassys for thin film metal deposition i.e. metallization.

### **4.2.4 Metallization**

Metallization is process of depositing a thin film of metal on the developed pattern. Different Plassys systems are used to sputter, evaporate and for metal deposition process. The Plassys equipment used for this work facilitates multi-layer deposition of up to eight metal materials. The substrate can be temperature controlled and deposition can be at any angle. Here, titanium (Ti) was deposited before gold for resist adhesion purpose [5-8]. Titanium has been shown [8-10] as the most common adhesive thin-film metal material used to attach gold on to a semiconductor or dielectric substrate. The Plassys have two main parts the load lock and chamber. When the load lock is vented the equipment lid is open and the developed sample is

clamped on the sample holder and the lid is closed and load lock pumped down. When the deposition run is complete the load lock automatically vents and the sample is retrieved.

Lift-off is the immediate process that follows metallization for the production of the metallic metamaterial of this work. The sample is placed in a beaker containing acetone and left in a hot bath for several minutes depending on the designed pattern as will be discussed subsequently. When the metal deposit has lifted off the sample leaving arrays of patterns, it is then brought out of the beaker and blown dried with nitrogen gas.

### 4.3 Fabrication on Fused Silica ( $\text{SiO}_2$ )

The thermal and optical properties of fused silica are superior to those of other types of glass due to its purity. Applications of the material mostly exploit its wide transparency range within electromagnetic spectrum, including ultraviolet, optical and infrared regions. Fused silica produces a strong absorption within mid-infrared between (8 to 10)  $\mu\text{m}$ .

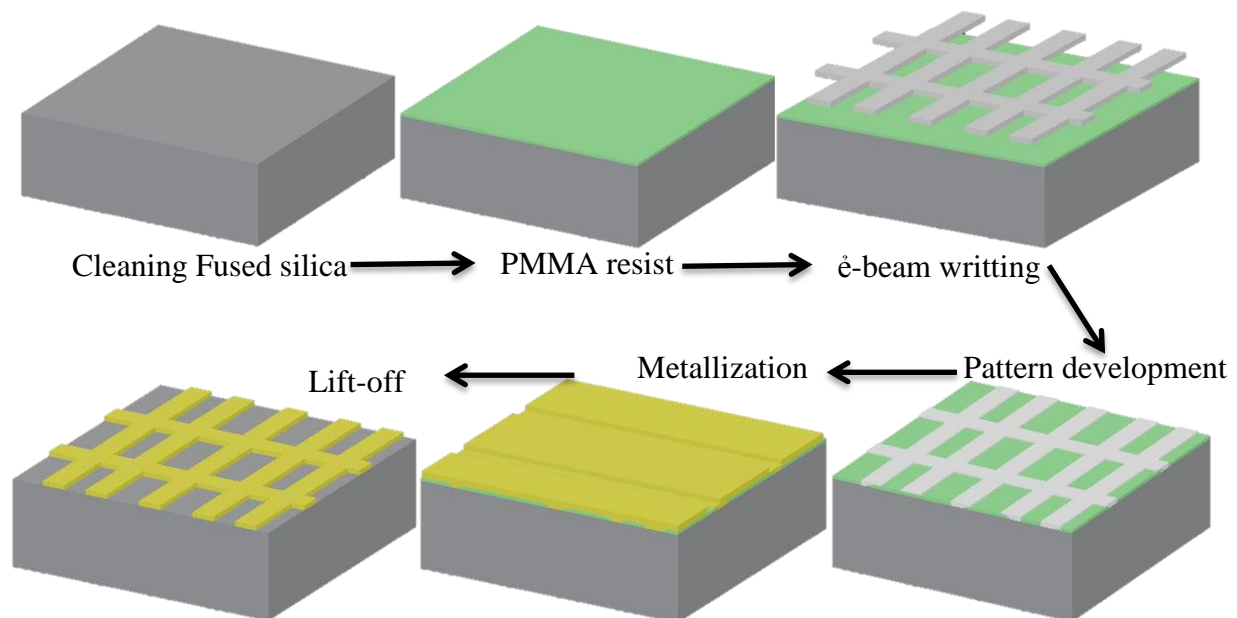


**Figure 4.4:** Flow chart (clockwise) of fabrication process on a fused silica substrate and resist spinning for metallic metamaterial patterns.

Thorough cleaning of the fused silica with acetone, methanol and IPA was performed, and then bilayer of PMMA 4% 2010 and 4% 2041 was spun at the speed of 5000 rpm leaving

approximately 200 nm thickness of the resist. The sample was placed in an oven set at a temperature of 180<sup>0</sup> and left for 40 minutes after the first PMMA spinning and for 120 minutes after the second spinning before submitting for exposure to e-beam pattern transfer. The transferred pattern was developed with 2.5:1 solution of isopropyl alcohol (IPA) and methyl isobutyl ketone (MIBK) and then rinsed with IPA for a period of 60 seconds. This was followed by evaporation of 10 nm Ti for adhesion and 100 nm Au. Acetone was used for the lift off which leaves gold patterns (yellow) on a fused silica, as shown in figure 4.4.

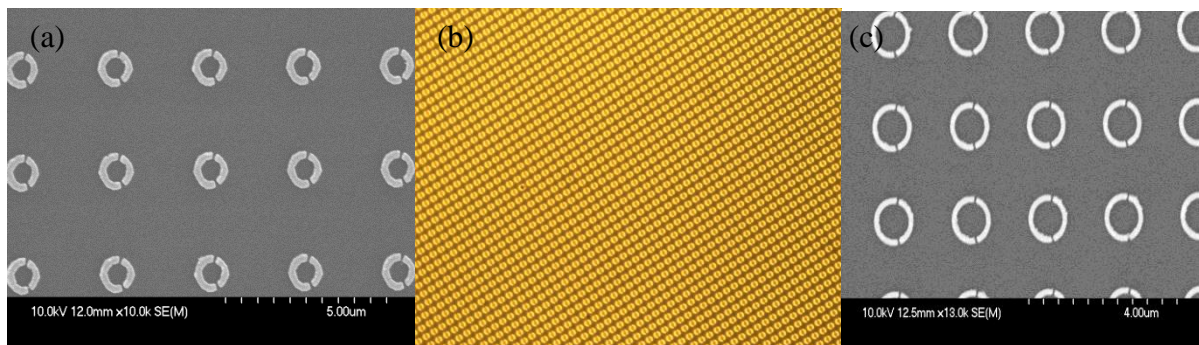


**Figure 4.5:** Fabrication on fused silica (a) Scanning electronic microscopic (SEM) image of A-SRRs arrays showing irregular arcs due to inadequate design resolution (b) optical microscope image of A-SRRs arrays showing a high density of structure (c) Properly designed SEM image of A-SRRs, with less dense and smooth arcs.

In this work, arrays of A-SRRs metamaterials were first designed with L-edit software as shown in figure 4.2a. In the setup design tool bar of L-Edit it is important to note that the mouse grid for the cursor type was set to smooth in order to avoid arcs shown in the figure 4.5a but produce smooth arcs, as shown in figure 4.5c. The periodicity varied as shown in figures 4.5 and has been described in references [11-14].

The *gds.file* of the 100 nm arc width (*w*) with 500 nm outer radius of A-SRRs array design in L-Edit were imported in beamer for fracturing. The *vep.file* from the beamer was then exported to BELLE as a *bel.file* for pattern layout and clearing and base doses ( $\mu\text{C cm}^{-2}$ ) suitable for the e-beam lithography were assigned.

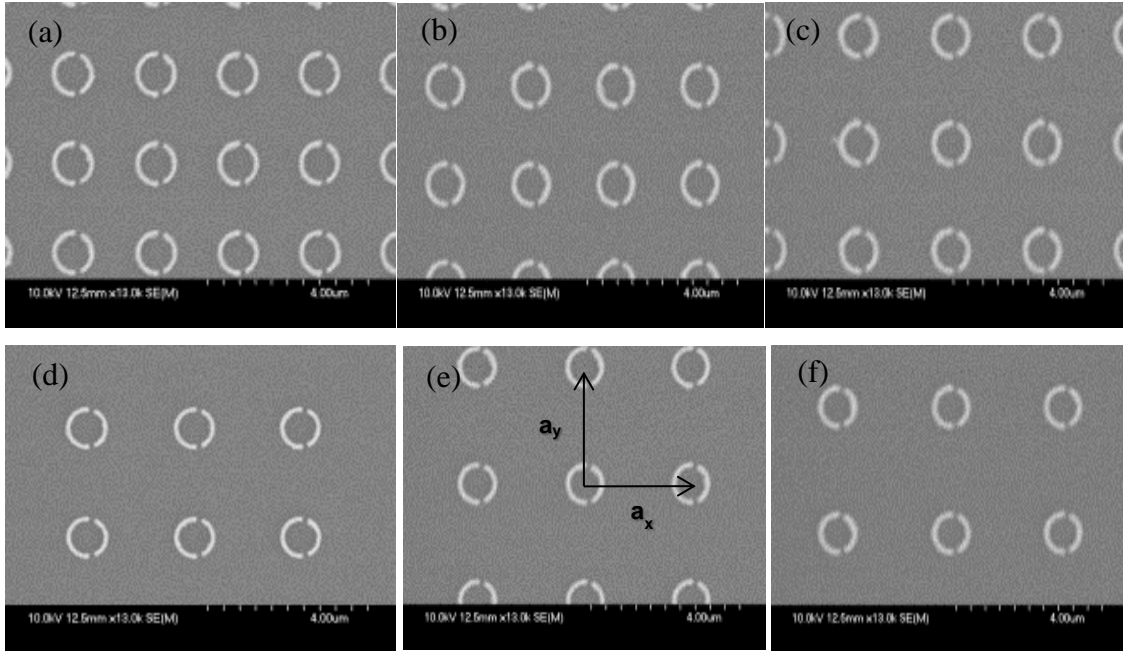


**Figure 4.6:** SEM image of different periodicity (a) of A-SRRs arrays fabricated on fused silica (a)  $a = 4r$  (b)  $a = 4r + 2$  (c)  $a = 4r + 4$  (d)  $a = 4r + 6$  (e)  $a = 4r + 8$  (f)  $a = 4r + 10$ .

In previous work [10, 15], the A-SRRs arrays were only designed with periodicity to be four times the radius of the outer arcs, meaning  $a = 4r$  ( $2 \mu\text{m}$ ) as shown in figure 4.6a. In this work, improving the reflectance resonances towards producing high quality factor led to variation of the periodicity as shown in figures 4.6 (a-f) in order to investigate the periodic effect on the resonance peaks. The gap between the two asymmetric arcs such as observing the effect the parallel and wedge gaps as shown in the figures 4.7 (a & b) respectively was also investigated.

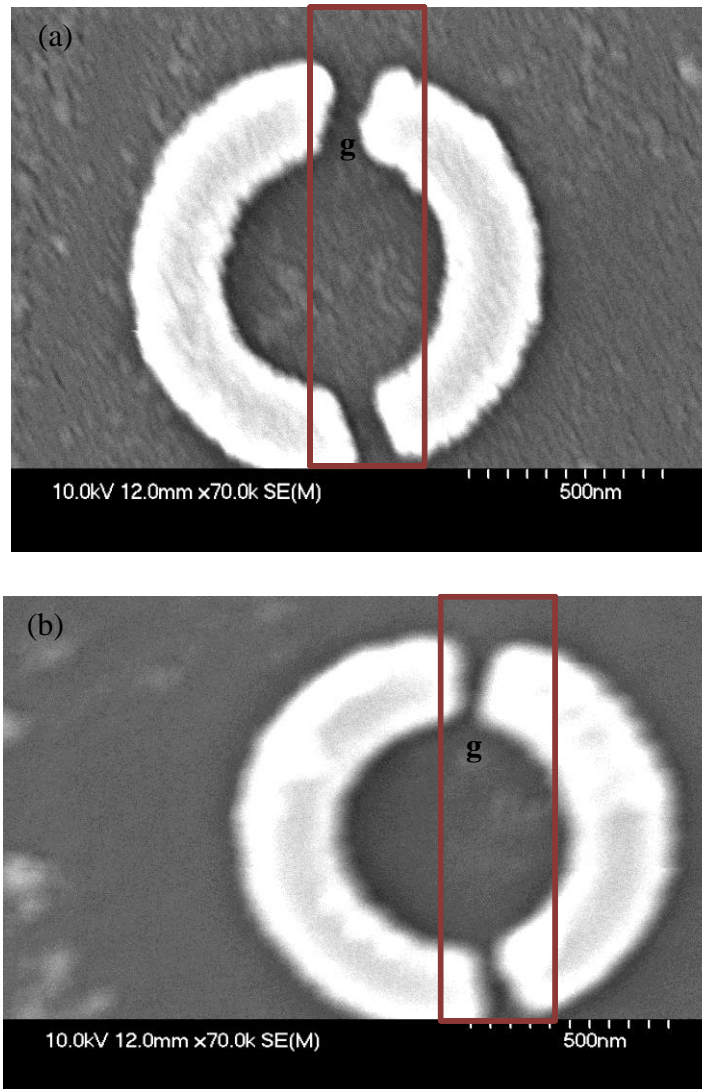


**Figure 4.7:** Fabrication of two different gaps (parallel and wedge) between the asymmetric arcs.

A small change was observed in the reflectance resonance peaks from the two different gaps fabricated as included in chapter five. The gaps between the arcs are varied and fabricated between 55 nm to 175 nm as shown in figure 4.8. This was used to study the effect of narrower gap on resonance peaks produced from A-SRRs structure. The same design process was followed but a higher clearing dose was assigned in the BELLE because of the nanoscale feature size of the gaps and arc edges involved.

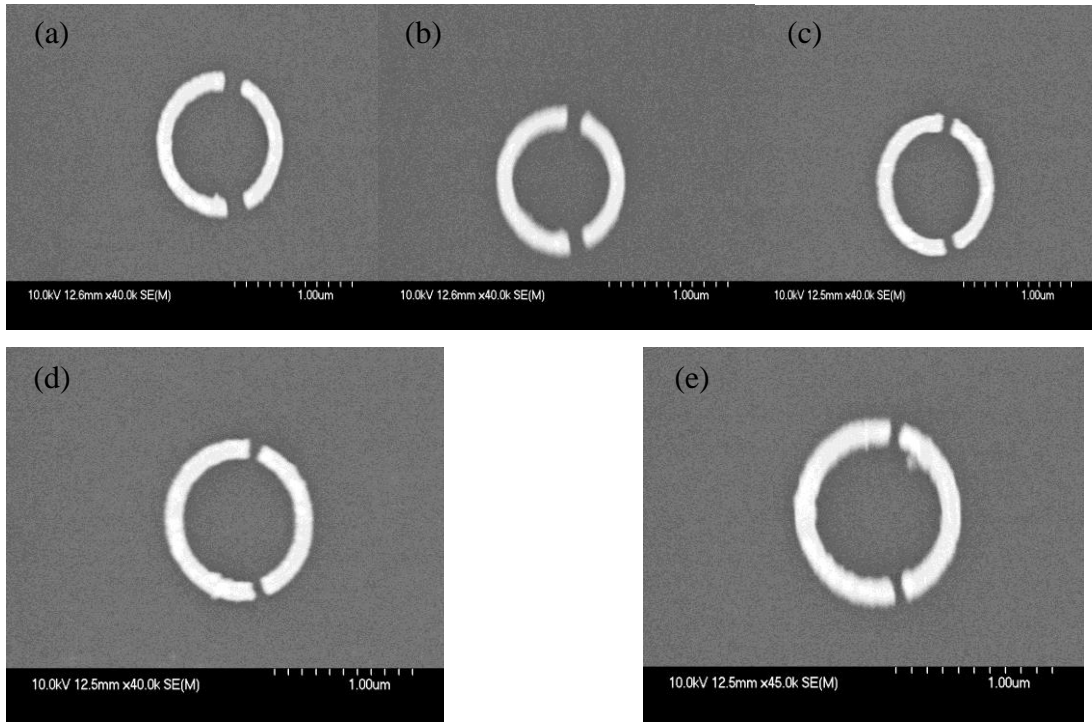


**Figure 4.8:** Variation of the nanoscale gap between the asymmetric arcs (a) 175 nm (b) 145 nm (c) 115 nm (d) 85 nm (e) 55 nm.

It is important to note that the SEM images on the fused silica substrate were produced by evaporating 5 nm film thin of aluminium (Al) for electron charge dispositions during imaging. This added process due to the nonconductive substrate in the case of fused silica sometimes disrupted production of a high resolution image as shown in figure 4.7 which can be obtained easily with other substrates such as silicon, shown in figure 4.9. The thin film Al of 30 nm thickness is also evaporated on the fused silica substrate after baking the resist in the oven before exposure to dissipate charge during the electron writing process.

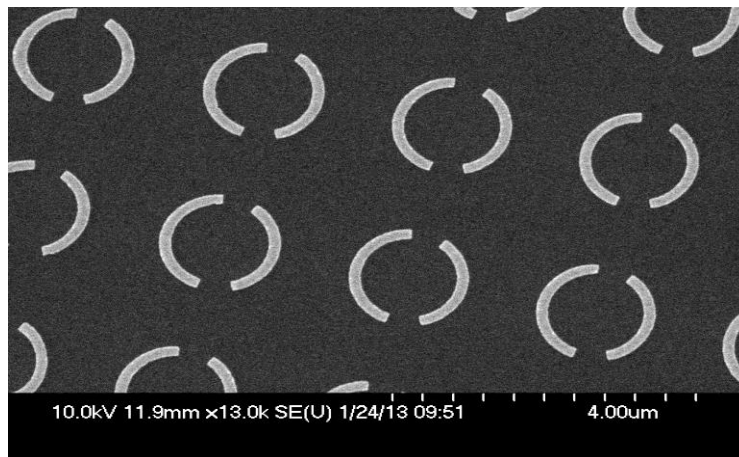


**Figure 4.9:** SEM image of A-SRRs arrays on a different substrates silicon

Virtually the same process that produced array of A-SRRs on fused silica substrate was followed to fabricate the dipole structures as shown in figure 4.10 that led to producing an asymmetric split H-shape (ASH) structure shown in the figure 4.11. The only difference is during the L-Edit design of the structures and doses assigned in the BELLE. The same flow chart in the figure 4.4 produced the SEM results in figures (4.10 - 4.12).

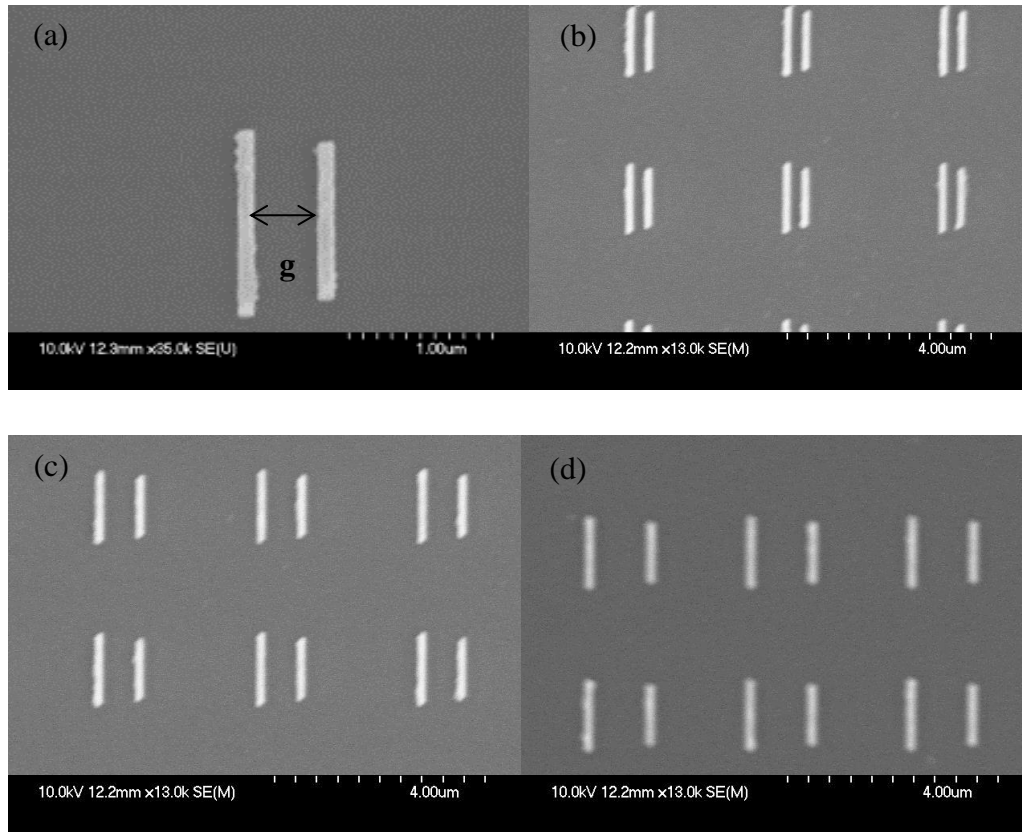


**Figure 4.10:** SEM image of the dipole structure at different gap ( $g$ ) (a) Single dipole  $g = 400$  nm (b)  $g = 200$  nm (c)  $g = 450$  nm (d)  $g = 650$  nm.

Arrays of dipoles were also fabricated on a fused silica substrate. The dipoles were designed to be two asymmetric arms of  $1.1 \mu\text{m}$  and  $0.9 \mu\text{m}$  placed vertically and parallel to each other with gap ( $g$ ) separating them. This is different from most of the existing dipole metamaterial. For the mostly published articles [16-18] the arms are placed horizontal, to be adjacent to each other and separated with a small gap. The structures shown in figures 4.10 were used to investigate and compare the effect of the dipole structure with close dimensions to A-SRRs.

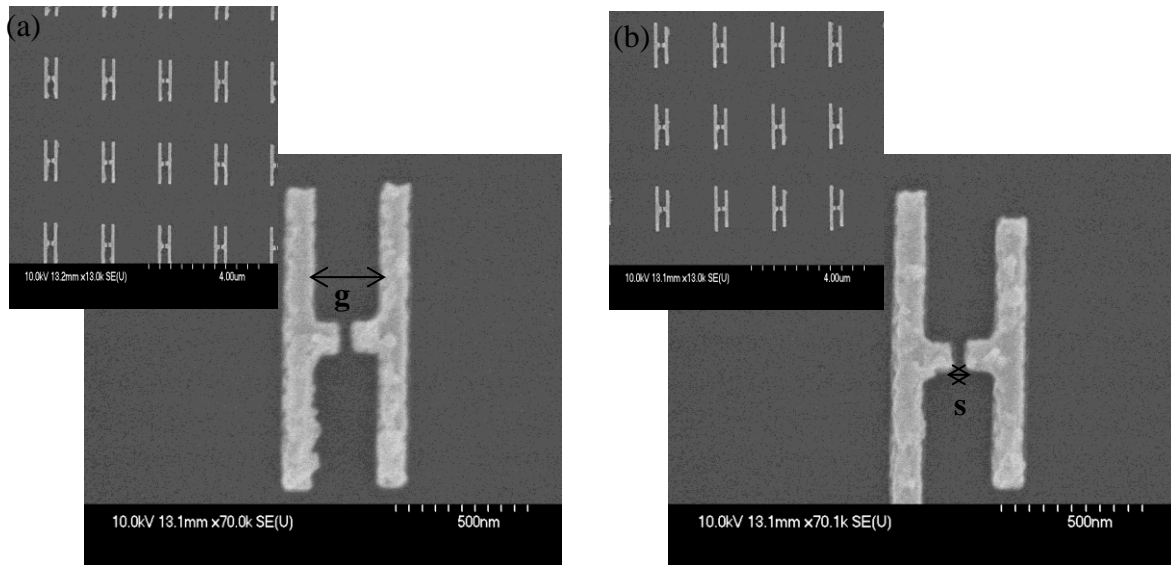


**Figure 4.11:** SEM image of (a) symmetric and (b) asymmetric ASHs showing the gap ( $g$ ) and space ( $s$ ) in the structure.

The idea of the horizontal and vertical arms was combined to produce a novel structure, asymmetric split H-shape (ASHs) as shown in figure 4.11. The structure was fabricated on fused silica substrate following the same procedure as of dipole but with a horizontal crossbar of (100 by 100) nm attached to each of the vertical arms as shown in the figures. Fabrication of symmetric split H-shape (SSH) was also performed which was used for sensitivity comparison in chapter six. Figures of 4.11 (a & b) show dimension of the arms for SSH is 1  $\mu\text{m}$  and that of ASH are (1.1 and 0.9)  $\mu\text{m}$  the respectively. These designed dimensions produce reflectance resonance peaks between 2  $\mu\text{m}$  to 6  $\mu\text{m}$ . For the purpose of achieving an optimized reflectance resonance peak, the gap and split between the arms and cross bar of the ASH structure was also varied respectively as shown in figure 4.12 and the effect was observed as detailed in chapter five.

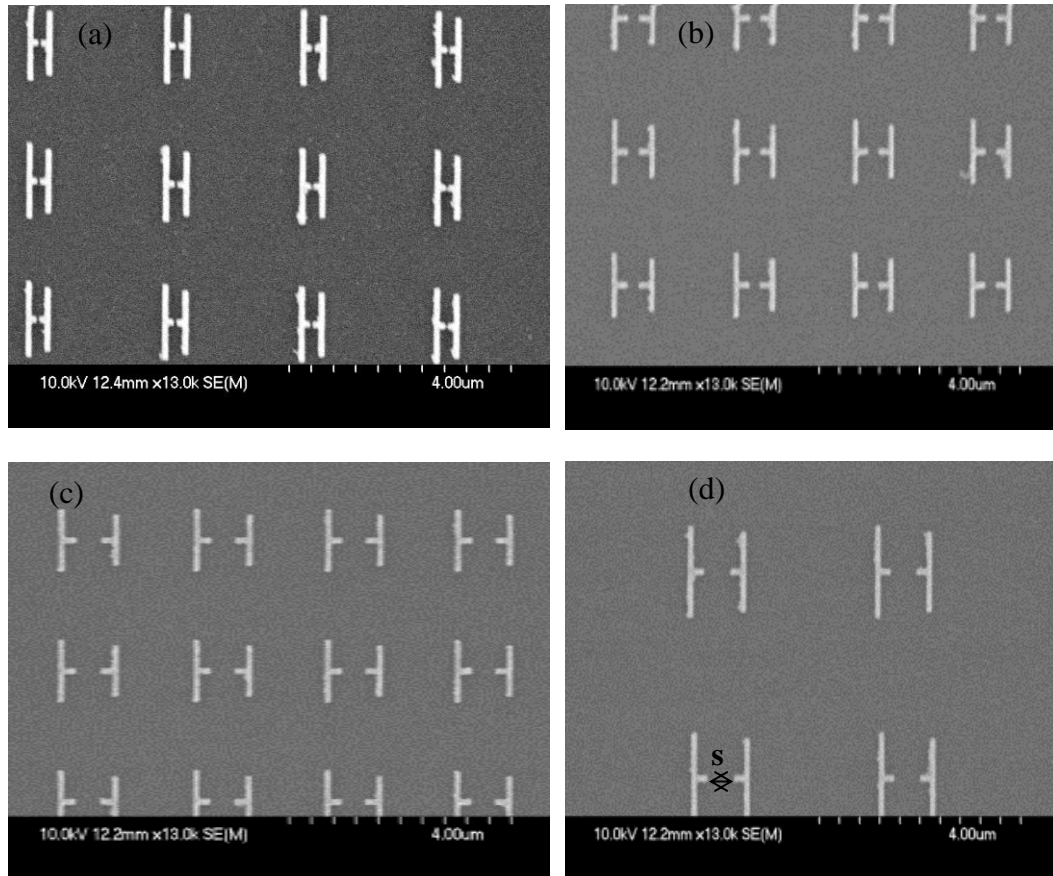


**Figure 4.12:** SEM image of ASHs at different slit ( $s$ ) between arms with cross (a)  $s = 50 \text{ nm}$  (b)  $s = 150 \text{ nm}$  (c)  $s = 250 \text{ nm}$  (d)  $s = 350 \text{ nm}$ .

From all the metallic metamaterials such as A-SRRs, dipoles and ASHs fabricated of this work the dipole was easiest to design and fabricate followed by ASH structure. The measurement results from the three structures show a higher quality and enhancement factor can easily be produced from the ASH structure than the other two. Therefore in chapters six, the ASH was mostly used as a sensor device for the application part of this work. A promising result can be achieved with ASH because of the structure dual polarization ability.

## 4.4 Discussions and Conclusion

In this chapter, methods involved in the fabrication of metallic metamaterial such as A-SRRs, dipoles and ASHs have been presented. Pattern creation using electron beam lithography has been a big challenge in the course of this work due to small features and wide variation of dimension involved which led to reconstruction of some design to accommodate the fabrication tolerances.

The use of dose test and re-designs of some structural size were the solutions adopted to achieve regular and well-written patterns. Other major problems in the pattern transfer were stitching, alignment and over-lay error. The misalignment was corrected in the fracturing software, (Beamer) by making sure that the entire designed patterns on a sample maintained the same origin or a start point from L-Edit to BELLE software. To produce a smooth curves or arcs from the initial stage of L-Edit should involve a smooth cursor grid to avoid irregular curve as shown in the fabrication results. The over-lay error was reduced by changing the method of the clamped sample submitted to the ebeamwriter.

The fabricated gaps within the structures were not easy to achieve. As shown in some of the figures of this chapter, there is a wide variation of the aspect ratio between the pattern and gap dimensions for some of the structures. This took much writing time by creating many arrays of pattern to find the right clearing dose by performing dose tests. The problem was rectified and job writing time is reduced to less than half an hour.

Using the developed recipe in the Plassys for metallisation such as evaporating the titanium and gold on the pattern sometimes evaporates more than the requested amount of metals. Suggestion was made to use less quantity than as stated in the recipe or design which is more likely to produce the desired amount. Again recommendation to perform metallisation using the newer version of the Plassys equipment in the cleanroom where the user has the authority to specify the quantity needed. From the initial experience of the dose test in the e-beam job writing a suitable clearing dose that is needed for a pattern or structure with features of a very

wide aspect ratio was determined. A good calculation for proportionality relationship between pattern dimensions and resist thickness is recommended for fabrication process in the BELLE in order to produce design.

In conclusion, the various designed devices presented in chapter 3 of this thesis were successfully fabricated on a fused silica substrate. The three designed patterns have been transferred to the cleaved samples and there has been initial evaporation of titanium for gold adhesion which is not involved in the modelling or design of the metallic metamaterial. However, small thickness of Ti will not significantly affect the performance of the devices.

## 4.5 References

1. <http://www.tanner.com/EDA/company/>
2. D. Macintyre and S. Thoms, "Electron Beam Lithography Course" Lecture notes, University of Glasgow, 2012.
3. [http://jwnc.eng.gla.ac.uk/pages/Ebeam\\_Docs/LB\\_tutorial.pdf](http://jwnc.eng.gla.ac.uk/pages/Ebeam_Docs/LB_tutorial.pdf)
4. [http://jwnc.eng.gla.ac.uk/vb6docs/operators\\_manual.pdf](http://jwnc.eng.gla.ac.uk/vb6docs/operators_manual.pdf)
5. B. E. Roberts, C. M. Dalton, J. C. Black and N. C. Durham, "multiple layer tungsten/titanium/titanium nitride adhesion/diffusion barrier layer structure for gold\_base microcircuit interconnection," Patent number 4,753,851, 1988.
6. K. W. Vogt, P. A. Kohl, W. B. Carter, R. A. Bell and L. A. Bottomley, "Characterization of thin titanium oxide adhesion layers on gold: resistivity, morphology, and composition," *Surface Science*, 93, 0039-6028, 1993.
7. D. S. Macintyre, I. Young, A. Glidle, X. Cao, J.M.R. Weaver, S. Thom, "High resolution e-beam lithography using a thin titanium layer to promote resist adhesion." *Microelectronic engineering* 83.4, 1128-1131, 2006.
8. B. Lahiri, R. Dylewicz, R. M. De La Rue, and N. P. Johnson, "Impact of titanium adhesion layers on the response of arrays of metallic split-ring resonators (SRRs)," *Optics Express* 18,11202-11208, 2010.
9. B. Lahiri, S. G. McMeekin, R. M. De La Rue, and N. P. Johnson, "Enhanced Fano resonance of organic material films deposited on arrays of asymmetric split-ring resonators (A-SRRs)," *Optics Express* 21, 9343-9352, 2013.
10. I. G. Mbomson, S. McMeekin, Basudev Lahiri, R. De La Rue, and N. P. Johnson, "Gold asymmetric split ring resonators (A-SRRs) for nano sensing of estradiol," *Proc. SPIE* 9125, *Metamaterials IX*, 91251O, 2014.
11. R. Adato, Yanik, A. A., Wu, C., Shvets, G. and H. Altug, "Radiative engineering of plasmon lifetimes in embedded nanoantenna arrays," *Opt. Express* 18, 4526-4537(2010).
12. N. I. Zheludev, S. L. Prosvirnin, N. Papasimakis, and V. A. Fedotov, "Lasing spaser," *nature photonics*, 2, 351-353, 2008.
13. I. Sersic, M. Frimmer, E. Verhagen, and A. F. Koenderink, "Electric and Magnetic Dipole Coupling in Near-Infrared Split-Ring Metamaterial Arrays," *Phys. Rev. Lett.*, 103, 213902-4, 2009.

14. N. Liu, H. Liu, S. N. Zhu and H. Giessen, "Stereometamaterials," *Nat. Photon.* 3, 157-162, 2009.
15. B. Lahiri, A. Z. Khokhar, R. M. De La Rue, S. G. McMeekin, and N. P. Johnson, "Asymmetric split ring resonators for optical sensing of organic materials," *Optics Express*, 17, 1107-1115, 2009.
16. P. Mhlschlegel, H.-J. Eisler, O. J. F. Martin, B. Hecht, and D. W. Pohl, "Resonant optical antennas," *Science* 308, 1607–1609, 2005.
17. V. Giannini, A. Berrier, S. A. Maier, J. A. Sánchez-Gil, and J. G. Rivas, "Scattering efficiency and near field enhancement of active semiconductor plasmonic antennas at terahertz frequencies," *OSA*, 18, 2797-2807, 2010.
18. X. Ren, W.E. I. Sh, and W. C. H. Choy, "Tuning optical responses of metallic dipole nanoantenna using grapheme," *OSA*, 21, 1530–1534, 2013.

# Chapter 5

## Experimental Results

### 5.1 Introduction

The experimental results concern measurements of the reflectance spectra of all the metallic metamaterials (MMs). The asymmetric split ring resonators, asymmetric dipoles and H-shape structures were measured in order to characterize the fabricated MM devices designed to operate in the mid-infrared region. The measurements were performed using a Fourier transform infrared (FTIR) apparatus set-up as described in the first part of this chapter and analyses of some common factors that are associated with poor spectra from the devices are also presented.

The results presented involve measurements of MM devices fabricated on fused silica ( $\text{SiO}_2$ ) substrates. The characteristic reflectance spectra of the devices are plotted as alongside simulations of the resonances originally shown in chapter three. This was followed by a detail analysis of the three metamaterial structures at different parameter developed towards improving the reflectance spectra. Lastly, comparison of the reflectance spectra and other features of the three metallic metamaterial structures are presented. The discussion and conclusions section close the chapter.

## 5.2 Measurement Setup

The reflectance of light from the fabricated metamaterial devices as a function of wavelength is used to characterize the photonic properties of the designed and fabricated patterns. The Fourier Transform Infrared Spectrometer (FTIR) as shown in the figure 5.1 was used.

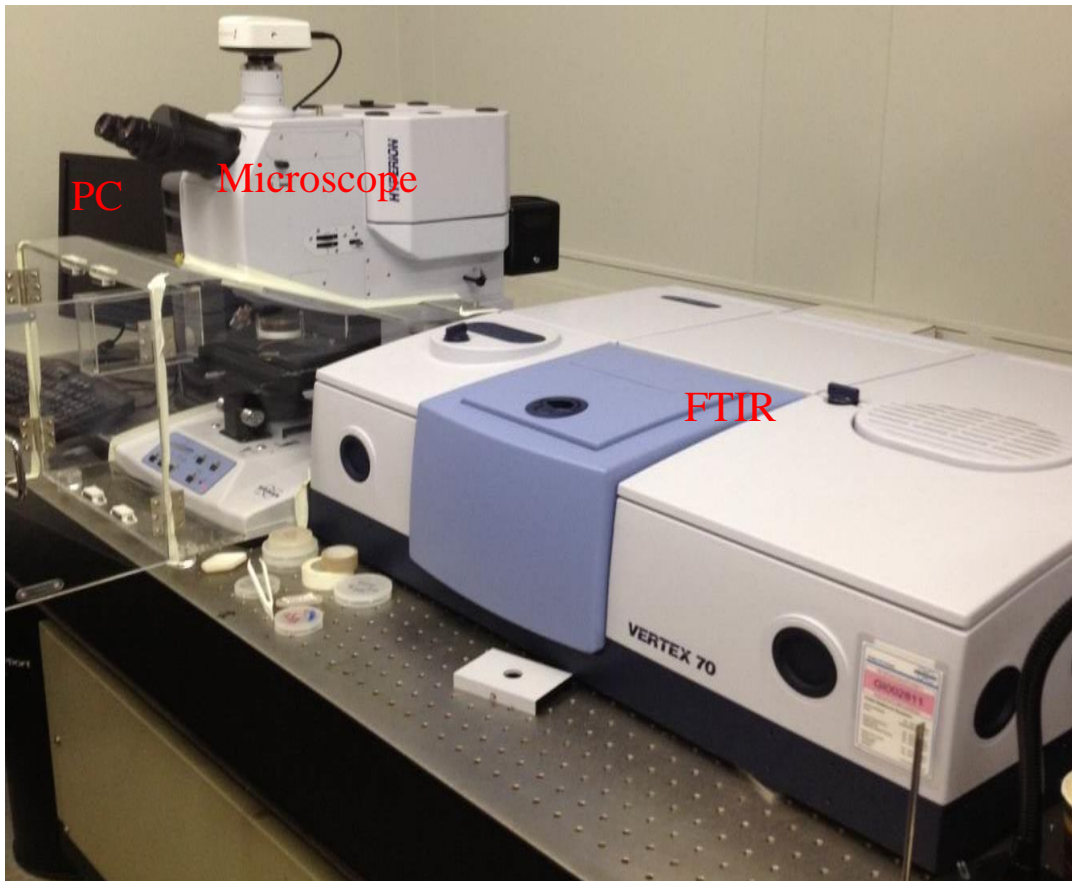


*Figure 5.1: Pictorial image of the measurement setup in the FTIR Lab*

The general measurement setup is as shown in figure 5.1, showing a Hyperion microscope coupled to a Bruker FTIR spectrometer. The microscope allows optimal sample visualization as well as quick and accurate infrared spectroscopic measurements of the nanoscale patterns at a small micro scale sample area. This was also used for the examination of inhomogeneity in samples. There is a purge gas inlet at the rear side of the microscope that enables purging the system with nitrogen gas.

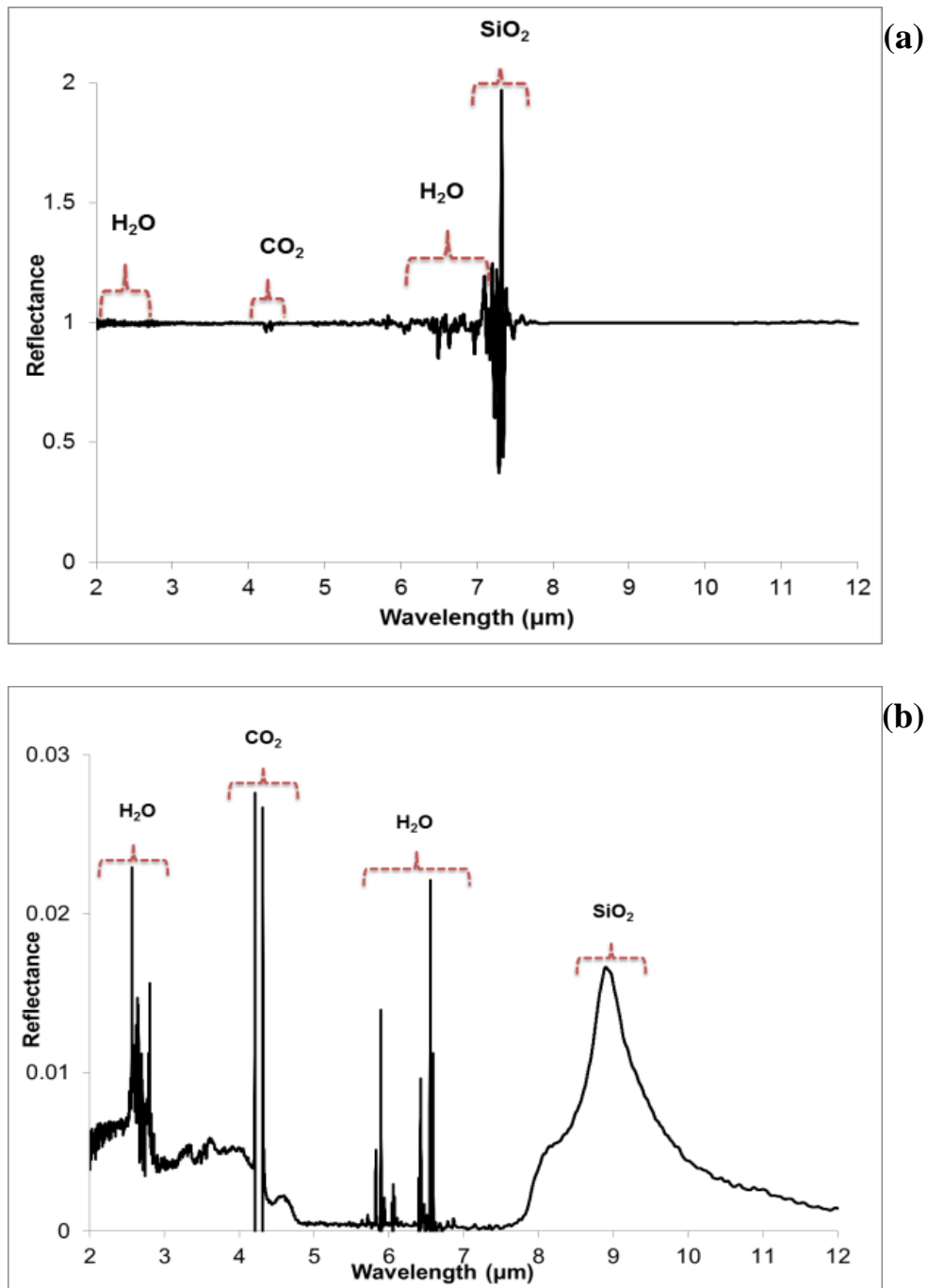


**Figure 5.2:** FTIR measurements on fused silica using (a) the fused silica sample and (b) gold mirror for background measurement which show the atmospheric interference and spectra from the silica substrate at points pointed with red markers.

Purging the system is sometimes necessary because of unwanted atmospheric interference such as water vapour ( $\text{H}_2\text{O}$ ) and carbon dioxide ( $\text{CO}_2$ ). The absorption of the atmosphere can mask weak spectral features of the sample [1]. The  $\text{H}_2\text{O}$  vapour appears at approximately

2.85  $\mu\text{m}$  and 6.6  $\mu\text{m}$  while the atmospheric  $\text{CO}_2$  is at 4.2  $\mu\text{m}$  as shown in figure 5.2. A background spectrum can compensate for the atmospheric features but may change over the course of several measurements.

The installed OPUS software is used for processing and evaluating the measured infrared spectra data. The software offers an extensive set of spectral processing routines such as the spectrum calculator, absorbance-to-transmission conversion, automatic baseline correction, peak picking and many others. When loading a file all the spectra and interferograms included in data file are displayed on the spectrum overview window in 2D data format. All the functions are set up in window such that the multiple spectra from measurements can be manipulated at the same time. The default settings for the spectral range are from 1.25  $\mu\text{m}$  to 16  $\mu\text{m}$  and from 0 to 1.5 extinction units. However, in this work the spectra range is mostly scaled from 2  $\mu\text{m}$  to 6  $\mu\text{m}$  where the switching for the spectra range positions is controlled from the software.

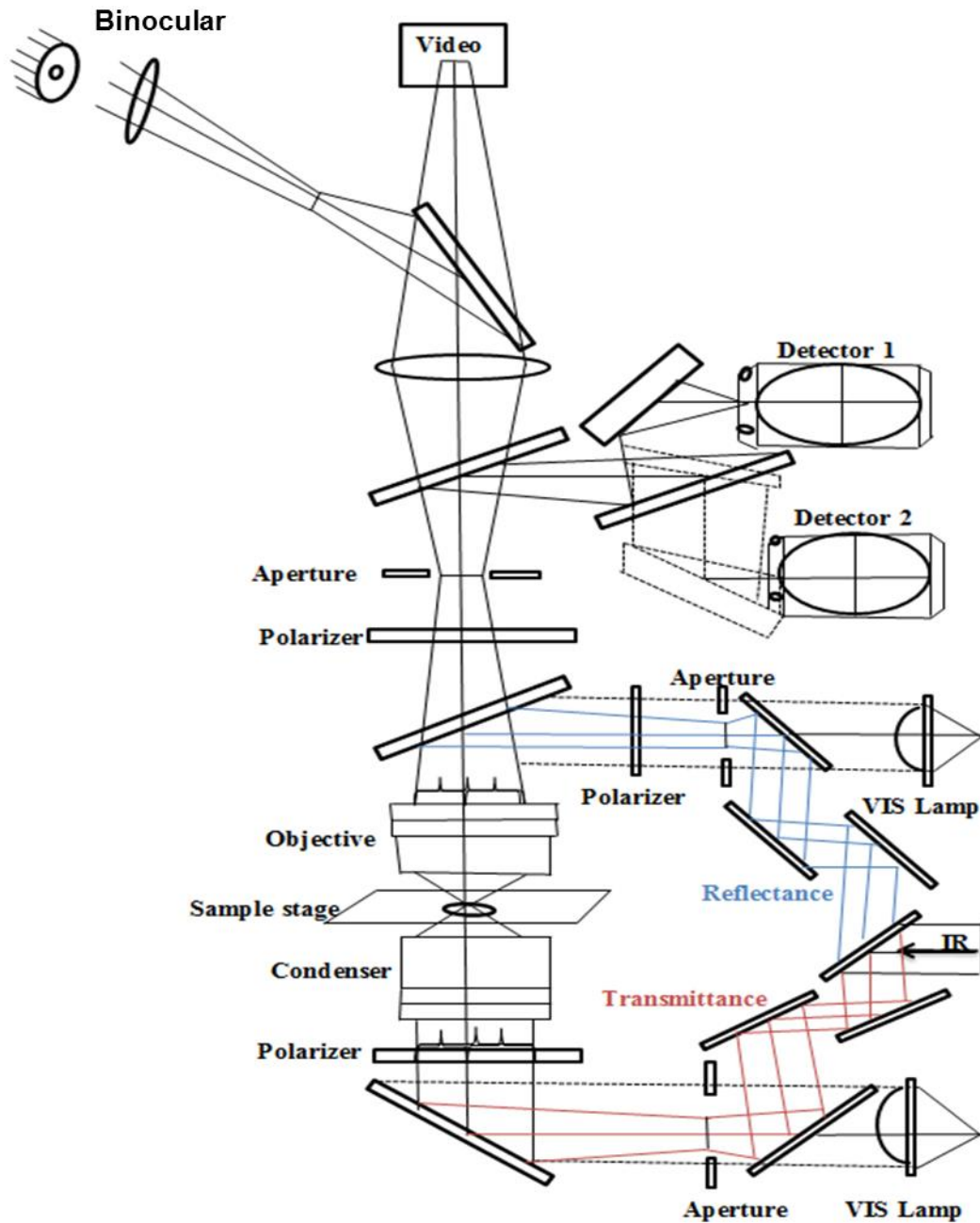


*Figure 5.3: Schematic diagram of an optical beam-path showing both reflectance and transmittance path [2].*

Figure 5.3 is a schematic diagram of an optical beam-path that shows a condenser and the transmittance polariser beneath the stage. A reflectance polariser is placed in front of the aperture adjacent to the objective. The condenser is used to correct the vertical displacement of the focus caused by the specimen slide. Before analysing the sample by FTIR microscopy the pattern area was mapped out with the aperture while viewing through the binocular eyepiece.

The sample is then illuminated by the visible light source or lamp (VLS) and the spectrometer is coupled from the infrared (IR) beam inlet port. Both detectors as shown in figure 5.3 are single-element detectors where the infrared detector, mercury cadmium telluride (MCT or HgCdTe) was used for all the measurements which are in the MIR spectral region. The reflectance spectra of the fabricated MM structures were measured at normal incident light using a 15 x IR objective lens with of 0.4 numerical aperture (NA) obtained from Bruker manual. This arrangement produced a maximum angle of approximately  $23.6^\circ$  which was calculated from NA expression:  $NA = n \sin \theta$ . The refractive index (n) of air was used to determine the angle. The working distance between sample and objective is 24 mm.

In this work, the initial step followed for the measurements once the equipment passed the operational qualification test (OQ) was to cool the MCT detector with the liquid nitrogen and then check the signal intensity. The reflectance measurements of the fabricated patterns were then performed by activating the IR mode. Samples were placed on the stage and positioned in the optical path as shown in figure 5.3. The interference occurring from differences in the optical path are process through Fourier transform function to produce a wavelength dependent transmission spectrum. After the sample area was defined by an aperture, an uncontaminated gold mirror was mostly used for the reference measurement before the actual measurements of the different fabricated patterns as detailed in the subsequent sections.

### **5.3 Asymmetric split ring resonators (A-SRRs)**

There are several measurements performed during this work for the different fabricated A-SRRs pattern. The aim is to produce an optimum A-SRRs device for the plasmonic sensing applications. Sensitivity and quality factor of MM devices is one of the important factors discussed in this work. The asymmetric structure was used because it has been demonstrated to produce higher sensitivity and Q-factor than the symmetric structure due to presence of trapped mode [3-6]. A trapped or closed mode [3, 6] introduce by asymmetric structures occur due to the excitation of non-symmetric current [6] mode that weakly couples with free space. Researchers have achieved very sharp resonances [3] and double reflectance peaks [5] in the presence of trapped mode.

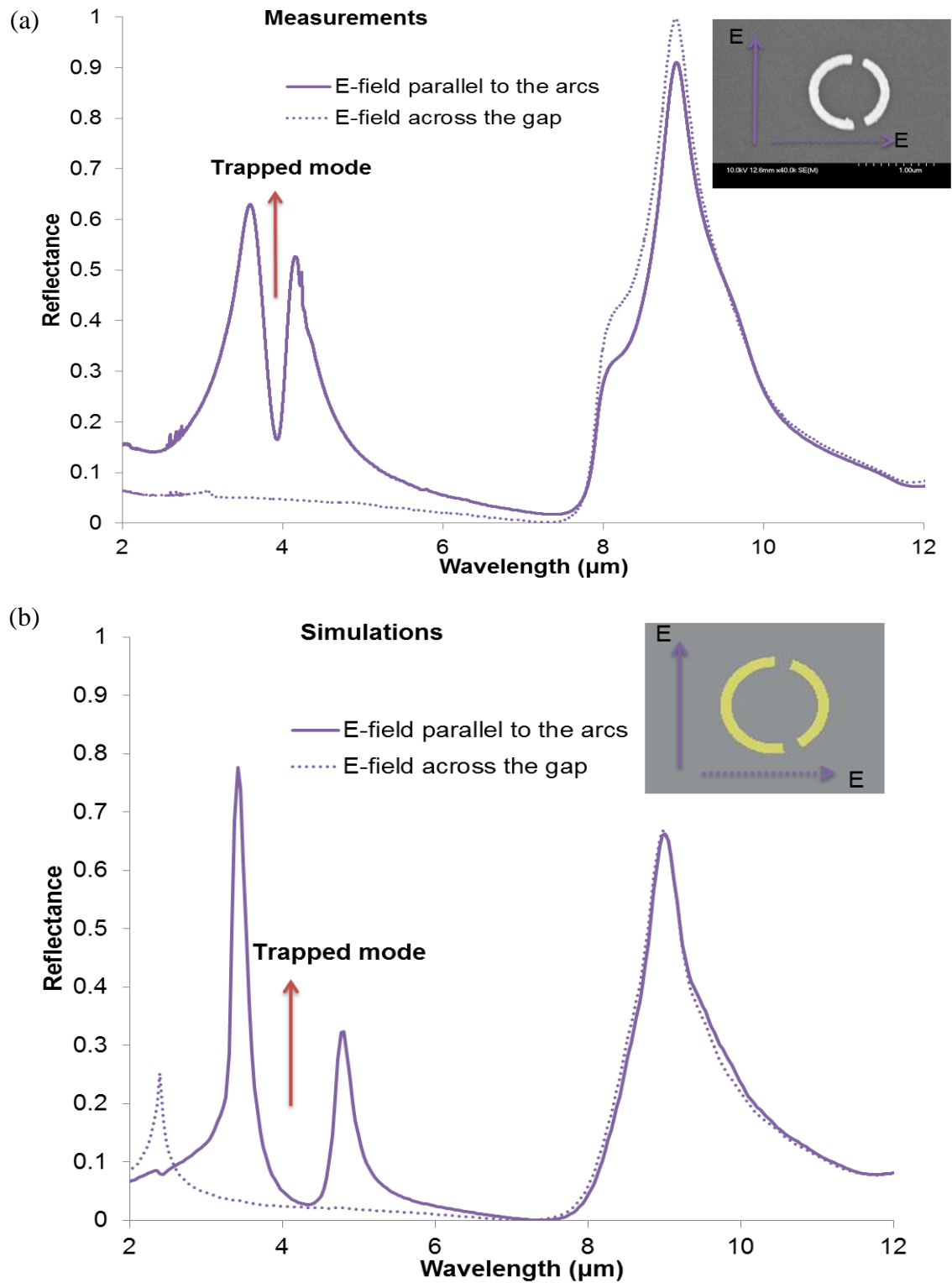


**Figure 5.4:** Reflectance spectra in mid-infrared for E-field polarizations showing the trapped mode separating the double plasmonic peaks of A-SRRs, and vibrational spectrum from fused silica at  $9.1 \mu\text{m}$  (a) FTIR measurement with  $\text{H}_2\text{O}$  vapour ripples at  $2.85 \mu\text{m}$  (b) Simulation with grating order artefact at  $2.4 \mu\text{m}$ .

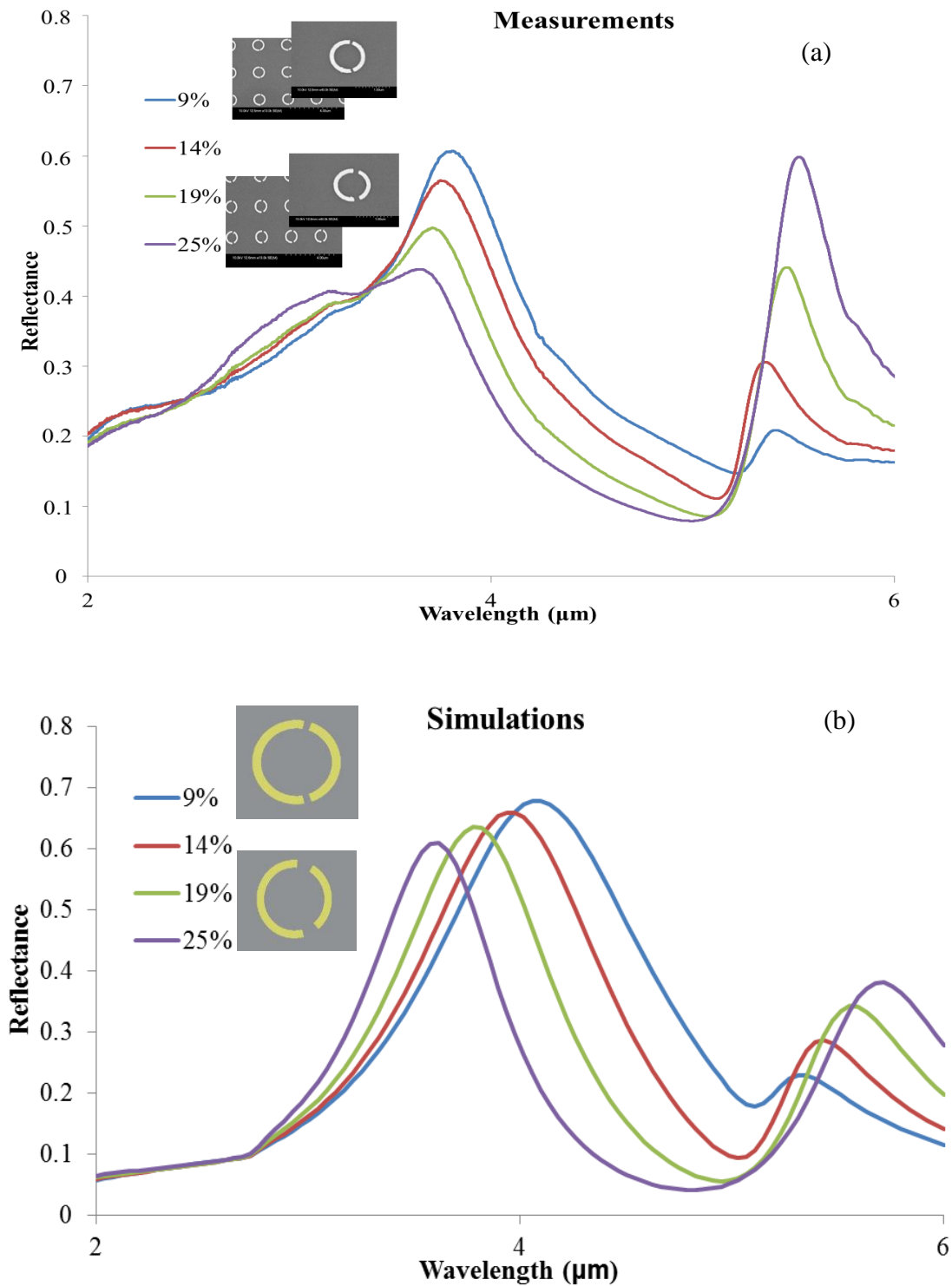
The trapped mode is present in asymmetric structure as shown in figure 5.4 when the E-field is parallel to the arcs of the A-SRRs. The correct polarization as explained in chapter two is important to achieve the correct excitation. In this work setting the polarizer to  $90^\circ$  corresponds to the E-field being parallel to the arcs produces the plasmonic resonance peaks when the sample is viewed as shown in figure 5.4.

Figure 5.4a shows two sets of reflectance plots where E-field across the gap ( $0^\circ$  polarizations) represent coupling of wave through the gap of the A-SRRs structure which produces only the magnetic resonance at much longer wavelength. The measurement requires a careful alignment of the sample orientation in order to correspond with the modelling results as shown in figure 5.4b. The difference observed in the results of figures 5.4 (a & b) can be attributed to some factors such as incident angle, beam collimation, line edge roughness (LER) in the fabrication and numerical artefact from grating order transmission which may affect experimental or simulation process. The measurement was performed using a gold mirror for background check which shows the vibrational spectrum [7] of fused silica at  $9.1 \mu\text{m}$  ( $1100 \text{ cm}^{-1}$ ). The gold mirror normalizes the spectra strength of reflectance to (0 to 1) while using the fused silica as the background or reference measurement can produce some spectra with reflectance higher than unity shown in figure 5.2a as compared with figure 5.2b. This is because silica has very much lower reflectance than gold.

### **Arc length of A-SRRs**

The intensity and spectral position of the double plasmonic resonance peaks produced from the A-SRRs can be altered by changing asymmetric arcs length. The arc lengths affects the reflectance magnitude as explained in chapter three are as shown in figure 5.5 (a & b). The measurement and simulation plots of the spectra are close match. The plots demonstrated the double plasmonic peaks at approximately  $(3.8 \text{ and } 5.8) \mu\text{m}$  corresponding to (small and large) arcs respectively of A-SRRs. The changes in the reflectance magnitude and position are due to the arcs variation represented in percentage, from (9 to 25) % as shown in the figures. These reflectance spectra show the percentage difference of the asymmetric arc length. The blue plot represents the less asymmetric A-SRR that is with only 9% different between the

arcs while the purple is more asymmetric with the large arc being 25% larger than the small arc. The images showed the nature of the arc variations.

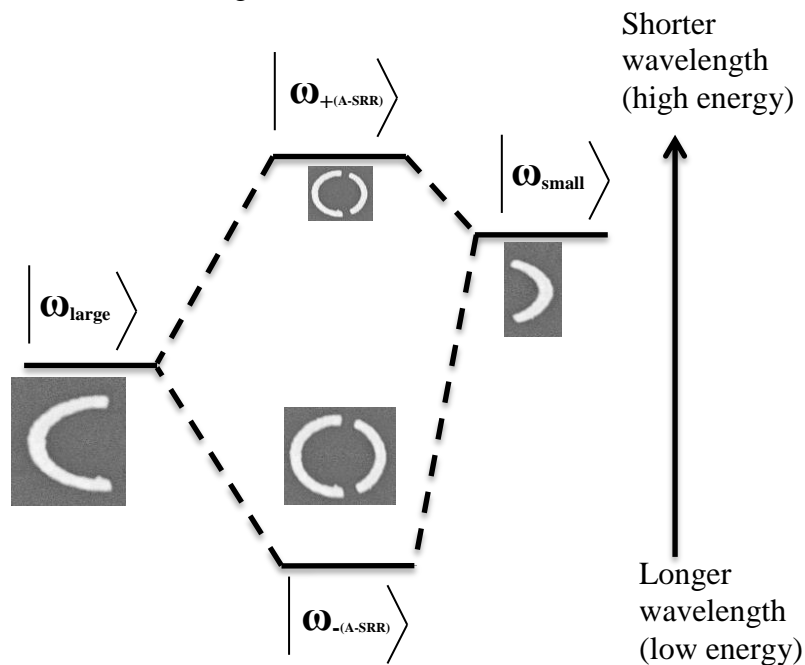


**Figure 5.5:** Reflectance spectra showing double plasmonic peaks from A-SRRs for the asymmetric arcs variation in percentage (a) FTIR measurements (b) Lumerical Simulation.

The magnitude of the peak at shorter wavelength decreases as shown in figures 5.5 from blue to purple plots due to reduction in the small arc and there is a shift to longer wavelength with the peaks corresponding to the large arc. Subsequently, the large and small arcs of A-SRR which produce single plasmonic resonance have been investigated. Understanding the characteristics of the individual arcs in relation with their corresponding resonance peaks helped to the description of resonance hybridization.

### Resonance hybridization of A-SRRs

References [8-12] described hybridized plasmon modes using the coupling between individual elements of different asymmetric metallic metamaterial structures. An A-SRR structure was used in this work to study the resonance hybridization from the individual arcs as shown in figure 5.6. The structure which comprises of two asymmetric arcs (large and small) as designed was measured. A finite-difference time-domain (FDTD) simulation was also used to simulate the resonant response of the arcs for a direct comparison of the reflectance plots. The individual arcs produce a mode which is the single plasmonic resonance [11] as shown in figures 5.7 and 5.8.



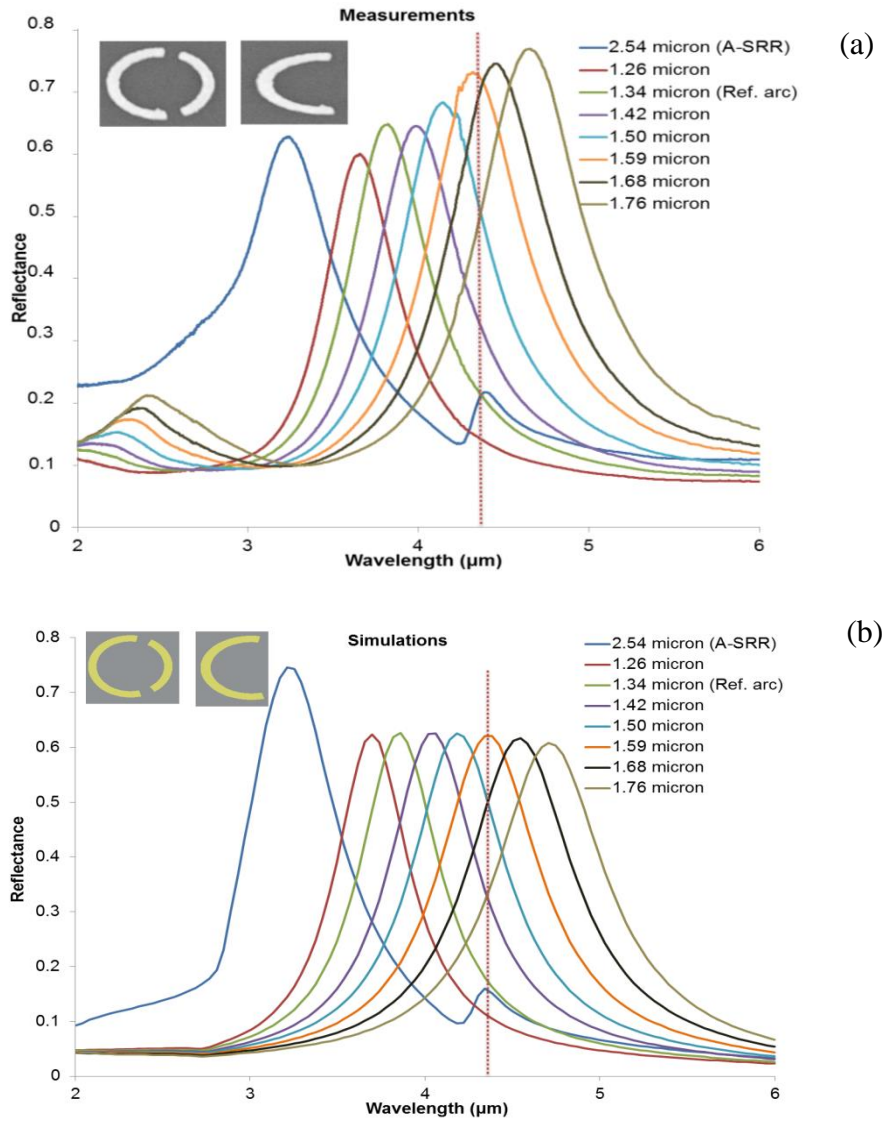
**Figure 5.6** Energy correlation diagrams that describe A-SRR plasmonic hybridization from the large and small arcs.

Figure 5.6 shows positions of the reactive elements (large and small) arcs and A-SRR in the energy diagram. The diagram represents energy level derived from the spectra plots from the measurements and simulations. There is a contribution from the individual arcs to the energy coupled to the A-SRR spectra position.

In the diagram the small arc is positioned towards the shorter wavelength (i.e. high energy level) while the large arc is close to the longer wavelength (i.e. low energy level). These positions of the arcs represent the plasmonic peaks produced from A-SRRs as shown with dark blue plot in figures 5.7 and 5.8 as distributed on EM spectrum. The peaks at (3.2 and 4.3)  $\mu\text{m}$  of the dark blue plot corresponds to (small and large) arcs of the A-SRR respectively. This shows the small arc at shorter wavelength is at high energy than the large arc at longer wavelength which means low energy. With the initial or reference (ref.arc) arcs length of (1.2 and 1.34)  $\mu\text{m}$  i.e. totally length of 3.02  $\mu\text{m}$  calculated from an A-SRR of 0.96  $\mu\text{m}$  diameter. The high ( $\omega_{+(A-SRR)}$ ) and low ( $\omega_{-(A-SRR)}$ ) energy levels are taken from the A-SRR spectral position. Small arcs tuned the resonance to high frequency  $\omega_{+(A-SRR)}$  i.e. high energy while large arcs tunes the resonance to low frequency  $\omega_{-(A-SRR)}$  equivalent to low energy. Tables 5.1(a & b) contain the calculated values for the arcs length that produce reflectance plots of figures 5.7 and 5.8.

Table 5.1a      Table for the large arc length

Degree ( $^{\circ}$ )	150	160	170	180	190	200	210
Micron ( $\mu\text{m}$ )	1.26	1.34	1.42	1.50	1.59	1.68	1.76



**Figure 5.7:** Reflectance spectra of 0.96 μm A-SRR diameters showing the double and single plasmonic peaks from A-SRR and different arcs (large) length (a) FTIR measurements showing measurement artefacts at 2.5 μm (b) Lumerical simulations.

The green plot which is the reference arc (1.34) μm and other plots in figure 5.7 were produced from measurements and simulations of a single arc (large). The reference plot shifts to shorter wavelength 3.8 μm i.e. blue shift (blue light of EM spectrum) when compared with the A-SRR peak at 4.3 μm (marked with dotted red line). There are blue shifts for the large arcs length of (1.26, 1.42 and 1.50) μm while red shifts occur for (1.68 and 1.76) μm compared with the A-SRR peak at 4.3 μm. This shows that for a red shift to occur the altered arcs length have to be at least 25 % (when calculated percentage difference) greater than the reference arc.

Table 5.1b Table for the small arc length

Degree ( $^{\circ}$ )	170	160	150	140	130	120	110
Micron ( $\mu\text{m}$ )	1.42	1.34	1.26	1.17	1.09	1.00	0.92

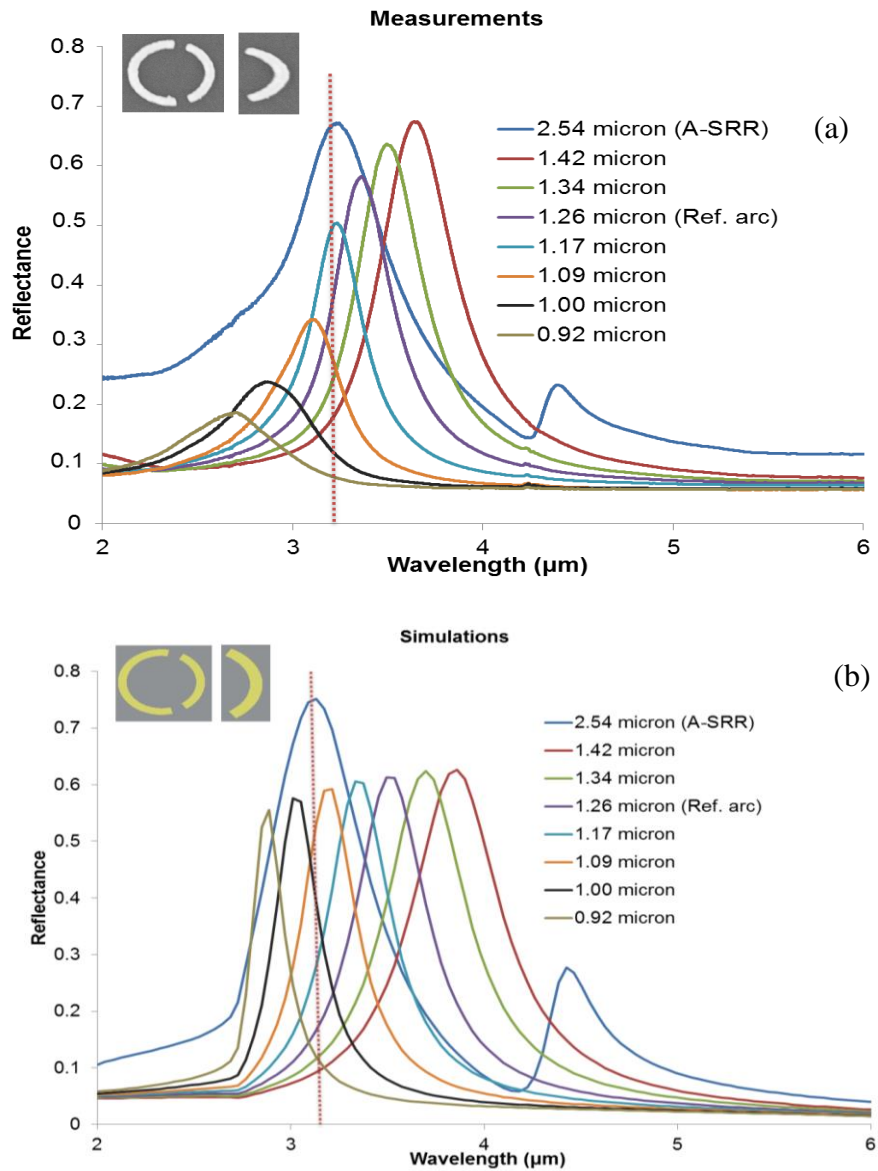


**Figure 5.8:** Reflectance plots of 0.96  $\mu\text{m}$  A-SRR diameters showing the double and single plasmonic peaks from A-SRR and different arcs (small) length (a) FTIR measurements (b) Lumerical simulations.

In figure 5.8 the reference arc (1.26)  $\mu\text{m}$  and altered (small) arcs length of (1.42, 1.34 and 1.17)  $\mu\text{m}$  were red shifted when compared with the A-SRR peak at 3.2  $\mu\text{m}$  (marked with

dotted red line) while the lengths of (1.00 and 0.92)  $\mu\text{m}$  were blue shifted. This shows that for a red shift to occur the altered arcs (small) length have to be at least 8 % greater than the reference arc. Blue shift begins when the reference arc is 26 % greater the altered arc. The study showed that the single resonances from the reference arcs (large and small) are (blue and red) shifted respectively in comparison to their hybridised resonance. This study was compared with the work of references [10-11].

### **Periodicity of A-SRRs**

The plasmonic resonance peaks from the A-SRRs are continually tuned between 2  $\mu\text{m}$  to 6  $\mu\text{m}$  of the electromagnetic spectrum since the targeted analyte of this work has its bond in the mid-infrared region. The A-SRRs outer diameter of 1  $\mu\text{m}$  with an arc width of 100 nm produces the resonance peaks as shown in figures 5.9. The gaps ( $\theta$ ) between the asymmetric arcs, background measurement and the periodicity also affect the position of the resonance peaks. For example, figures 5.9 showed the effect of using a constant gap for the 1  $\mu\text{m}$  diameter while varying the periodicity as measured from the fabricated arrays of A-SRRs. A gold mirror was used for the background measurement which normalizes the magnitude of the reflectance resonance to unity.

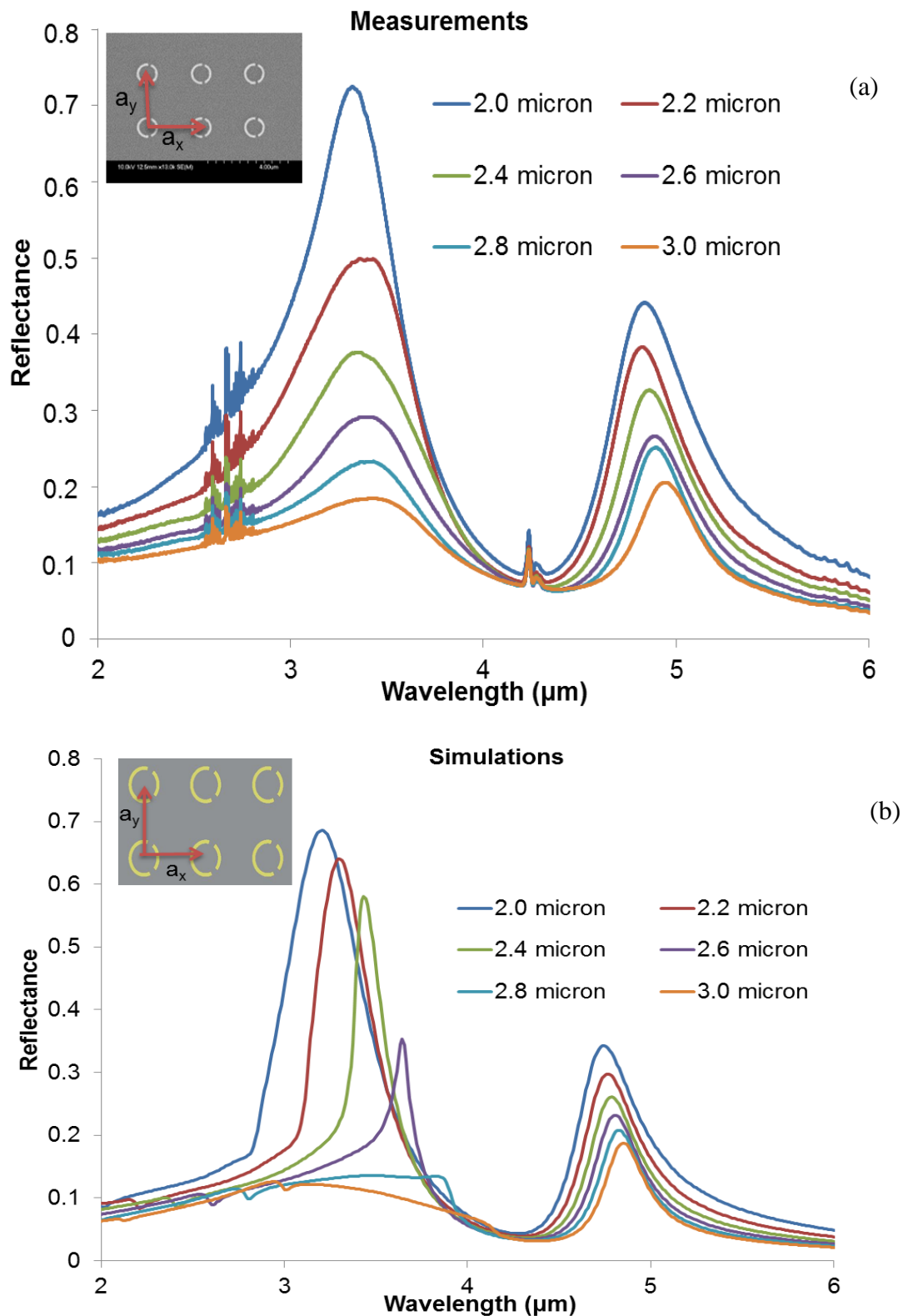


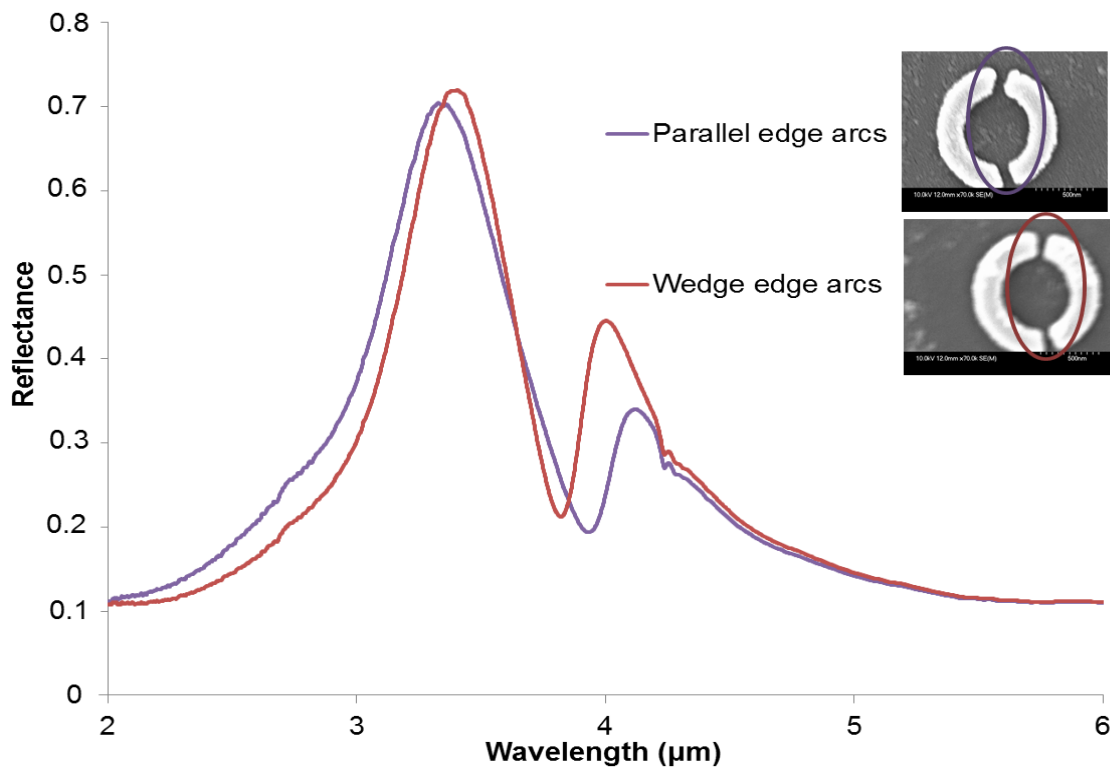
**Figure 5.9:** Reflectance spectra showing double plasmonic peaks from A-SRR for the periodicity variation (a) FTIR measurements with water vapour ripples at 2.85 and  $\text{CO}_2$  at 4.2 (b) Lumerical Simulation with grating order artefacts due to periodic boundary condition corresponding to the varied periods.

Periodicity is one of the fundamental parameters considered in the design of the array structures. The variations in the periodicity of fabricated arrays of A-SRRs in chapter four was measured to give reflectance spectra in figure 5.9a which broadly follow the simulation results as shown in figure 5.9b. The experimental and simulation results validate the effect produced by other research by varying periodicity [13-15]. There is a blue shift showing of the resonances, as the periodicity is decreased from (3 to 2)  $\mu\text{m}$ . The 2  $\mu\text{m}$  periodicity is twice the diameter (i.e. 1 $\mu\text{m}$ ) of the designed A-SRRs structures. The lower spacing gives a higher density for the A-SRRs which leads to higher reflection intensity because of the greater quantity of gold present. The variation in A-SRRs array periodicity helps in this work to achieve the optimum density which is periodicity of 2.4  $\mu\text{m}$  for this particular design. The measurement and simulations have shown that narrow plasmonic resonance peaks can be produce with periodicity greater than twice the larger metallic element of a MM design. In the simulation results the amplitude at the shorter wavelength diminishes faster and shifts the peaks position are more pronounced. The discrepancy in the figures can be attributed to the substrate thickness and experimental defects.

Figure 5.9a shows water vapour ripple at wavelength of 2.8  $\mu\text{m}$  and carbon dioxide peaks at 4.2  $\mu\text{m}$ . Tuning of resonance peak to a desired wavelength does not occur with variation of the metamaterial (A-SRR) dimensions only. For example, the resonance peaks in figures 5.9 (a & b) have been produced from A-SRR of the same diameter, but wavelength position of the peaks changed a little due to periodic variation.

## Gaps of A-SRRs

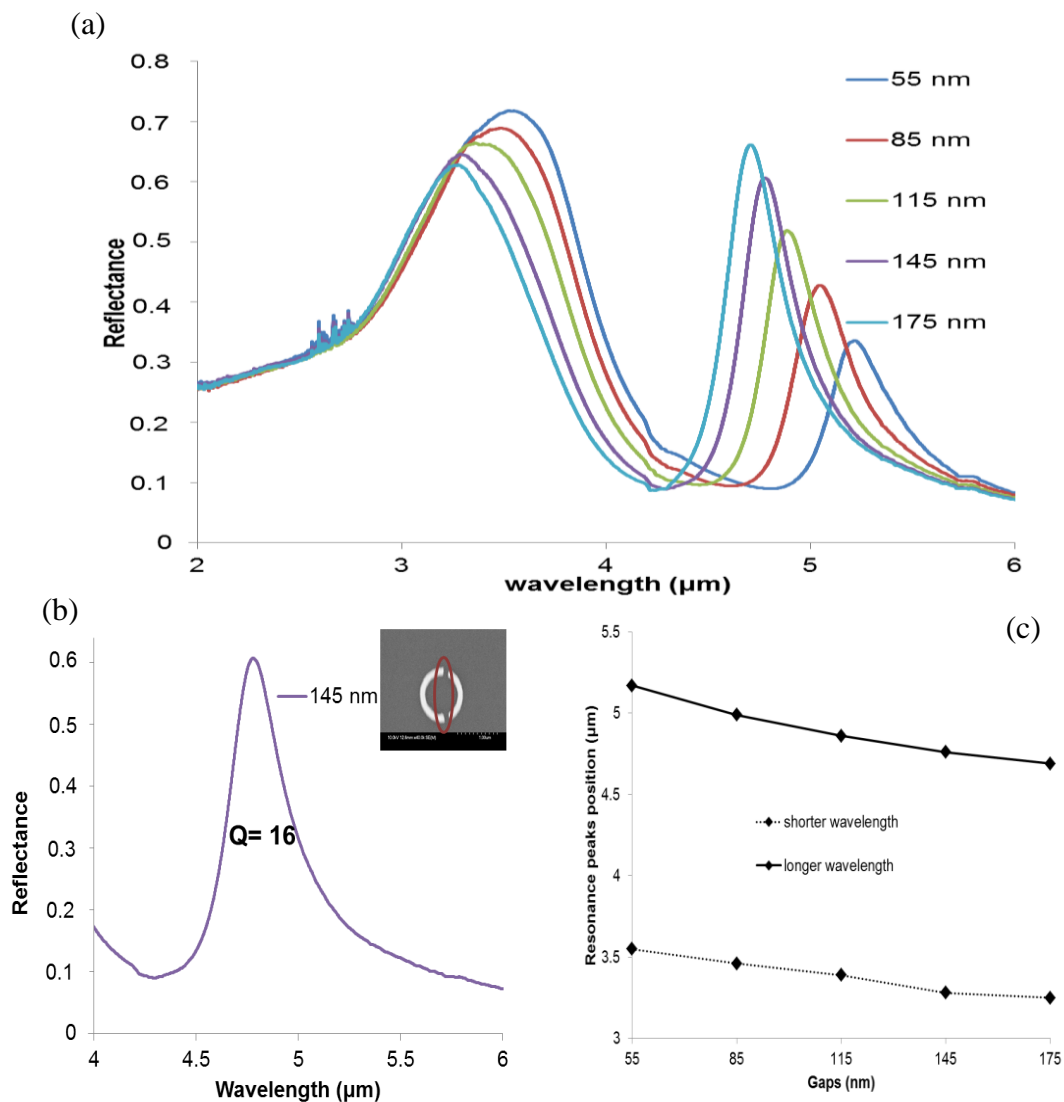
The arcs length of A-SRRs which mostly tune the resonance were adjusted to design an optimum gap to maximise Q for the structure as shown in figure 5.10.



**Figure 5.10:** Reflectance spectra from FTIR measurements of A-SRRs with parallel and wedge arc edges that form gap

Simulation result for A-SRRs structures with a parallel nanoscale gap has been demonstrated by Ding et al [16]. In this work, measurements of the fabrication A-SRR with parallel and wedge-shaped arcs at both ends as shown in figure 5.10 were performed. The comparison did not show much improvement to the reflectance resonance peaks as desired. Quality factor of the resonance peaks were calculated using the expression:  $Q = \lambda_p / \Delta\lambda$ . The FWHM ( $\Delta\lambda$ ) for the wavelength at 3.36 and 4.00 for wedge edge arc is 0.464 and 0.297 given the Q-factor of 7.24 and 13.47, respectively. For the parallel edge, Q-factor of 6.00 and 18.59 was calculated from  $\Delta\lambda$  of 0.55 and 0.22 at wavelength position of 3.30 and 4.09, respectively. Average Q-factor from figure 5.10 resonances for the wedge and parallel edges is approximately 10 and 12, respectively.

The reflectance magnitude of the wedge edge arc (red plot) was higher because there is more reflectivity material (gold) in the pattern than in parallel edge arc (purple plot). Again, researchers have designed equal [5] and unequal gaps [17] between the asymmetric arcs. The parameters they have used to denote and differentiate between the gaps (angle  $\theta$ ) are  $\beta$  for equal, then  $\alpha$  and  $\beta$  for unequal gap. In this section FTIR measurements were performed for equal gaps ( $\theta$ ) to understand the effect of different gap size towards improving the reflectance resonance peaks as shown in figure 5.11.



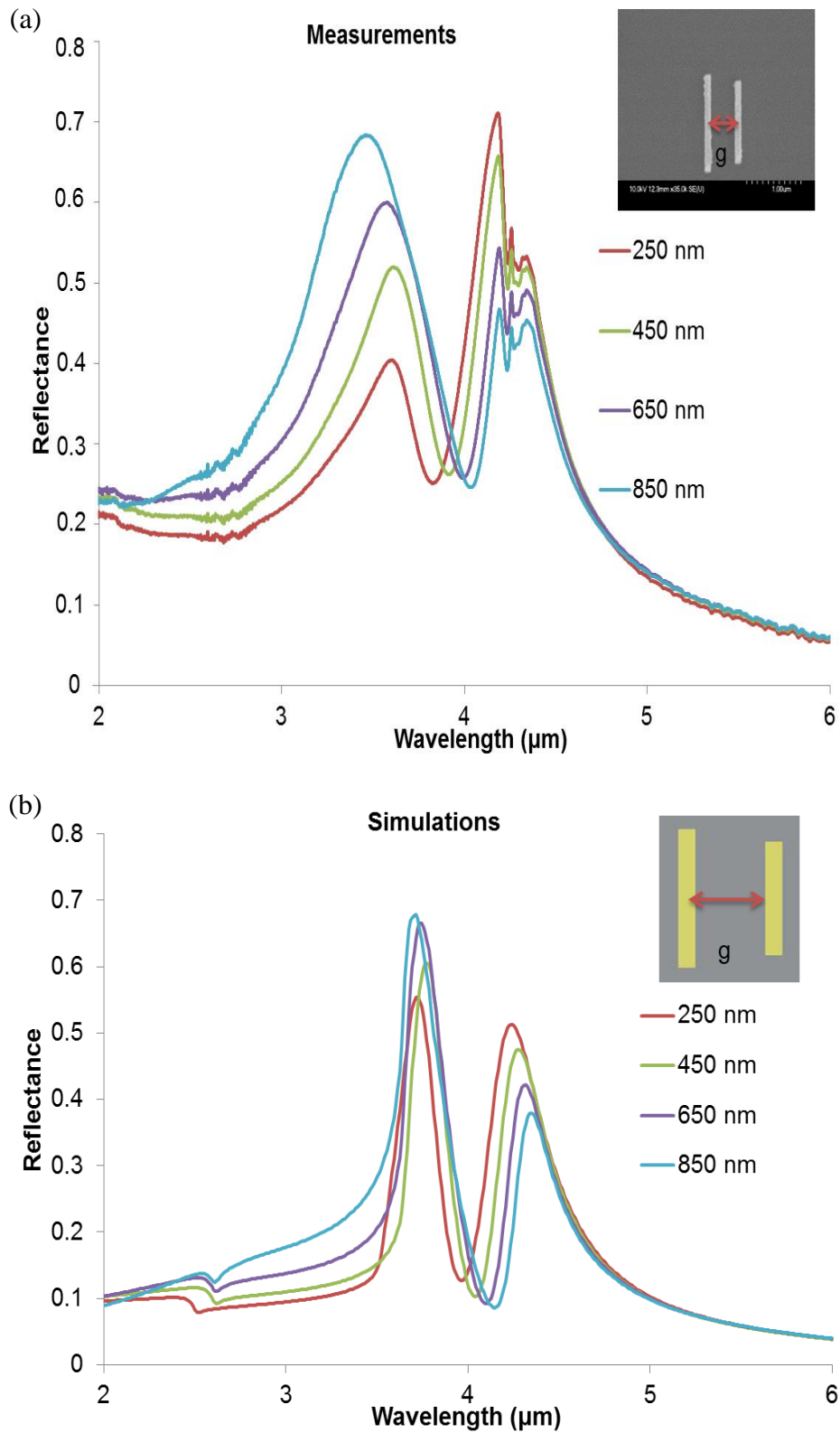
**Figure 5.11:** FTIR measurement (a) for the variations of two equal nanoscale gaps between asymmetric arcs of A-SRRs (b) Gap of 145nm showing peak with the highest  $Q$  (c) comparison of the resonance peaks position due to gap.

Figure 5.11a shows reflectance plots for different gaps of A-SRR with diameter of 1  $\mu\text{m}$ . The gaps between the arcs as shown in the inset of figure 5.11b was reduced by 30 nm from (175 to 55) nm. The gap sizes were achieved by increasing the two asymmetric arcs simultaneously. This produced the resonance peaks which shift to longer wavelength as the gap reduces as shown in figure 5.11a. The gap variations also affect the reflectance magnitude of the peaks. The asymmetric arcs produce double plasmonic peaks in figure 5.11a while the ripple at 2.8  $\mu\text{m}$  is from water vapour. From the figure, a quality factor for 145 nm gap was calculated.

In figure 5.11b, the FWHM ( $\Delta\lambda$ ) is 0.3 from  $\lambda_1$  and  $\lambda_2$  (4.95- 4.65)  $\mu\text{m}$  and the  $\lambda_p$  (resonance peak) is at 4.75  $\mu\text{m}$ . The quality factor of approximately 16 shown in the figure was obtained at mid-infrared region from the experimental results of the A-SRRs. This result is greater than any other Q-factor that has been published in the related articles [5-6, 12-13, 17-20]. The concept of optimum periodicity and gap variations for the A-SRRs to achieve high Q values were applied to the fabricated dipole patterns.

## 5.4 Dipole structures

Experimental measurements were also carried out for the fabricated dipole structures. Arrays of fabricated vertical gold rod on fused silica substrate were measured with the FTIR. The dipole pattern was designed in the way that the reflectance resonance peak is tuned to mid-infrared. The dimension of the asymmetric arms of the dipole that produced the resonance peaks in figures 5.12 is 1.1  $\mu\text{m}$  and 0.9  $\mu\text{m}$  for the large and small arms respectively.



**Figure 5.12:** Reflectance spectra for dipole structure at different gap ( $g$ ) between the asymmetric arms (a) FTIR measurements (b) Lumerical simulations.

The gap between the arms as shown figure 5.12 was varied to investigate the effect on the reflectance resonance peaks. Reflectance plots of the figure show the effect of the gap variation. This demonstrated how the magnitude of the peak changes with the gap, the peak at shorter wavelength decreases at closer gap between the arms as shown with 250 nm gap while the longer wavelength peak decreases with increasing gap. The measurement results of the gap variation correspond to the simulation result as shown in figure 5.12b of the dipole. In the both results, the resonance peaks at the shorter wavelength is narrowed as the gap is reduced while at longer wavelength peak is broaden. The ripples and small peaks at 2.8  $\mu\text{m}$  and 4.2  $\mu\text{m}$  are from water vapour and  $\text{CO}_2$  respectively as shown in figure 5.12a. Figure 5.12b contains grating order effect at 2.5  $\mu\text{m}$  due to periodic boundary condition.

## **5.5 Asymmetric Split H-shape structure**

Shapes of different types have been experimentally studied by many research groups in the field of nanoantennas or metamaterials. The most common fabricated structure in this field is circular or U-shaped split ring resonator, V-shape, chiral and dipole nanoantenna [21-27]. Recently, B.Yuan et al completed a study with asymmetric H-shape structures but there is no slit between the cross bar of the H-shape [28]. The article also emphasized improving the resonance peak through the smaller gap as shown with dipole structure. In this work, 50 nm split (s) between the crossbars of symmetric (SSH) and asymmetric (ASH) split H-shape structures were fabricated and the experimental results are shown in figure 5.13. The split is the distance between the horizontal crossbars on the H-shape structure.

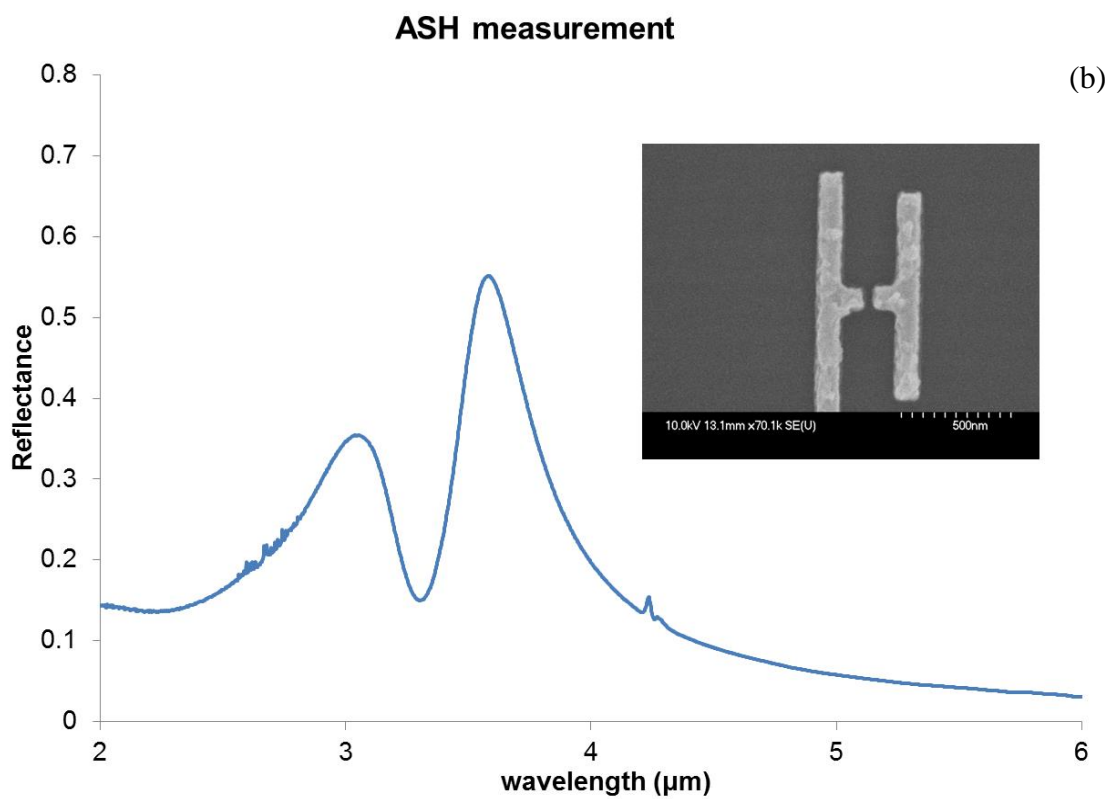
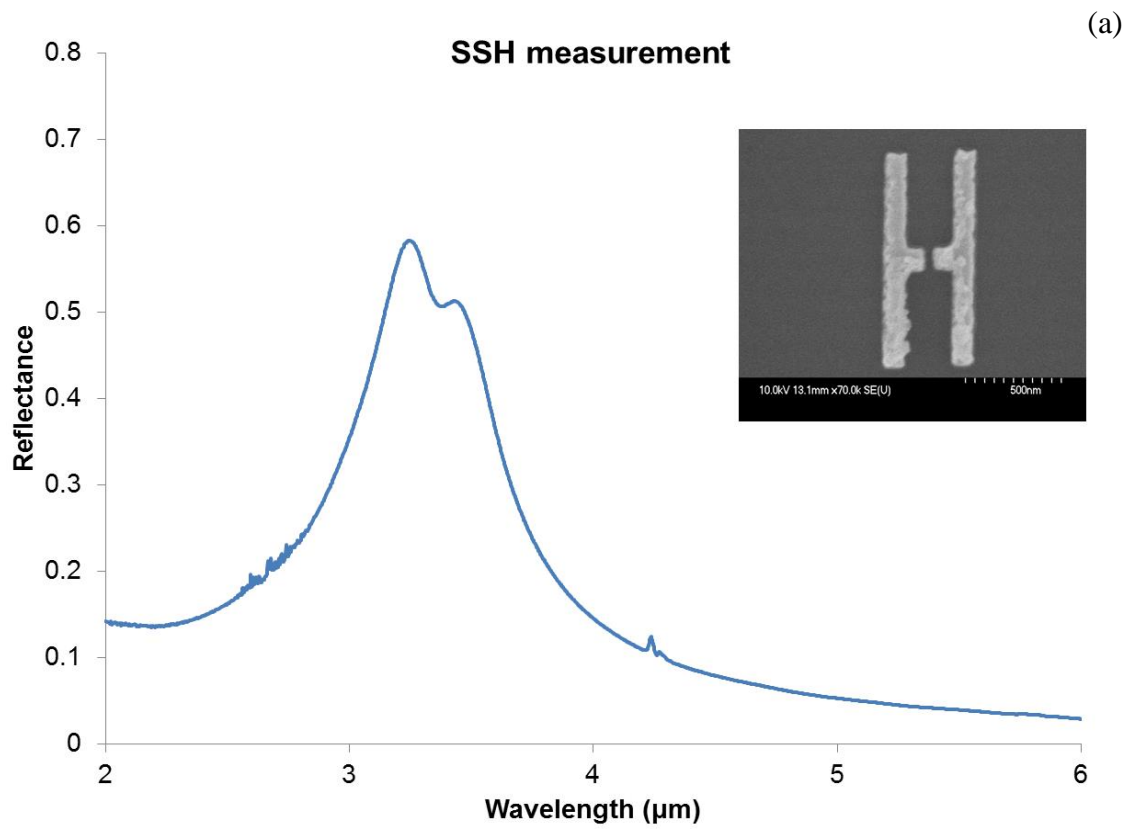


*Figure 5.13: FTIR measurements for reflectance spectra showing plasmonic resonance peak of (a) symmetric split H-shape (b) asymmetric split H-shape.*

The dimension of the arms for the SSH are  $1 \mu\text{m}$  while  $(1.1 \text{ and } 0.9) \mu\text{m}$  were used for the ASH arms. The dimension of the crossbars on the arm is  $(100 \text{ by } 100) \text{ nm}$  as shown in the SEM image of figure 5.13. In the figure 5.13, the  $\text{H}_2\text{O}$  ripples,  $\text{CO}_2$  and the vibrational resonance from the fused silica is shown on the plot. The SSH experiment shows a single plasmonic peak with a shoulder on the peak due to slightly unequal arm lengths from imperfection in fabrication. The ASH has double plasmonic peaks with the peak at shorter and longer wavelengths corresponding to the small and long arms respectively.

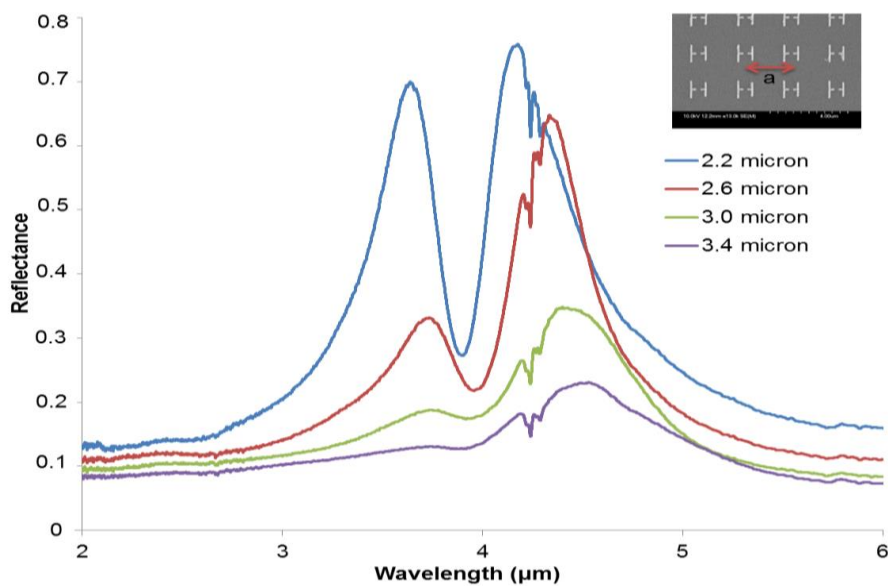


**Figure 5.14:** FTIR measurement of ASH at different periodicity.

The periodicity was also investigated with the ASHs structure. The experimental results of figure 5.14 have a similar as the periodicity variation performed for other structures. The  $2.2 \mu\text{m}$  periodicity exhibit the highest reflectance magnitude because of the high density of the gold pattern. With all these parameter variations a narrow reflectance resonance has been achieve which produced a high  $Q$  factors within the mid-infrared measurements for metallic metamaterial.

## 5.6 Discussions and conclusion

The three different metallic metamaterial structures fabricated on a fused silica were measured. The results presented are those that give the most important information concerning the characteristic and optimized structures process for the metallic metamaterial.

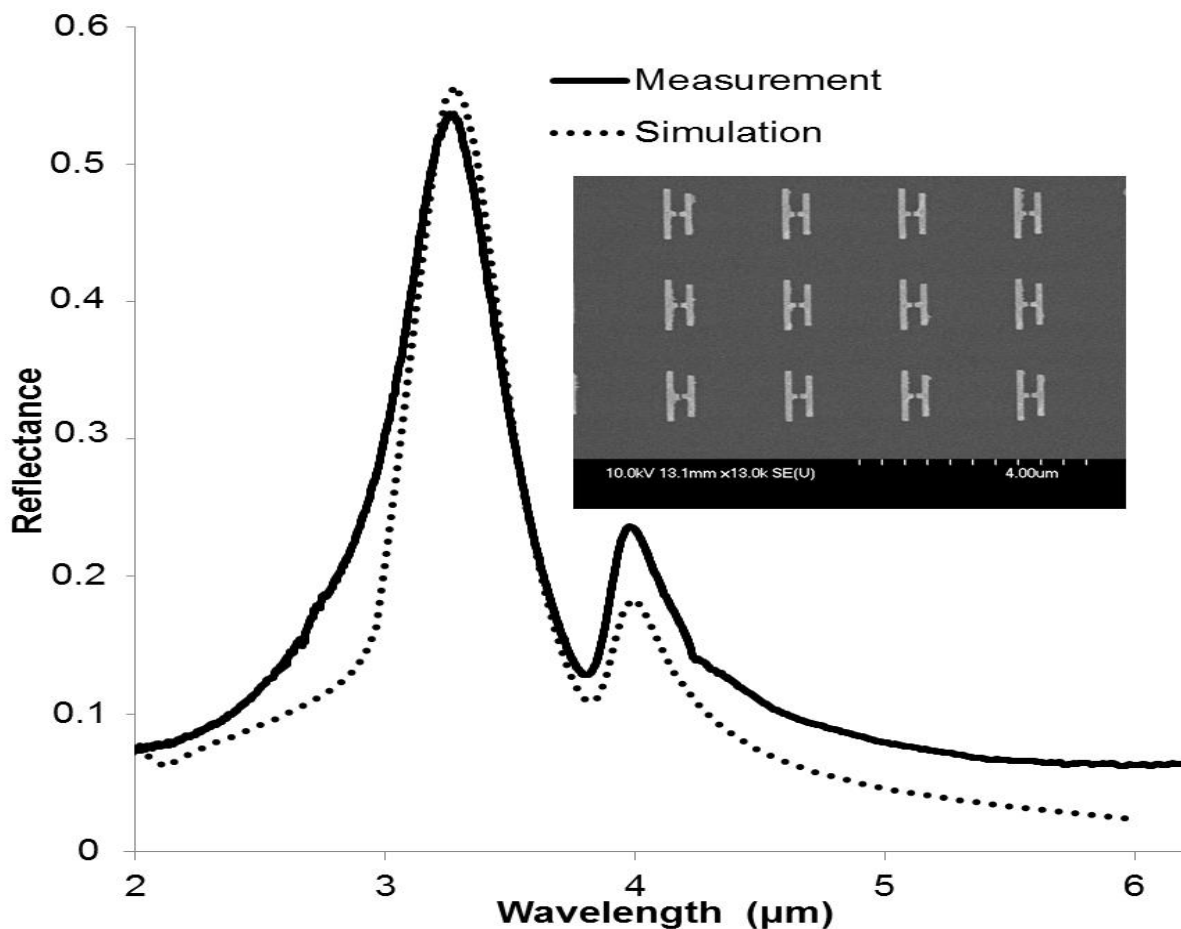


**Figure 5.15:** Matching reflectance from experiment and simulation for asymmetric split H-shape structure of metallic metamaterial.

The experimental results generally closely match the results from the numerical simulations as compared and also shown in figure 5.15. However, slight differences can be observed in some of the investigated parameters such as the devices gap and periodicity in comparison of the two results (simulations and measurements). These changes can be attributed to fabrication tolerances errors, thickness of the substrate, ripples from water vapour and CO<sub>2</sub>. The use of a gold mirror for the background measurement in order to match the resonance

intensity obtained by simulation was considered. The measurements were normalized to gold mirror due to high reflectivity of gold material. Also the effective refractive index distribution used in the simulations is only an estimation of the refractive index distribution of the materials taken from literature as measured data.

The hybridized resonance from asymmetric arcs was used to study the energy levels. Figures 5.16 (a & b) show the reflectance spectra from measurements and simulations of A-SRR and the individual arcs.

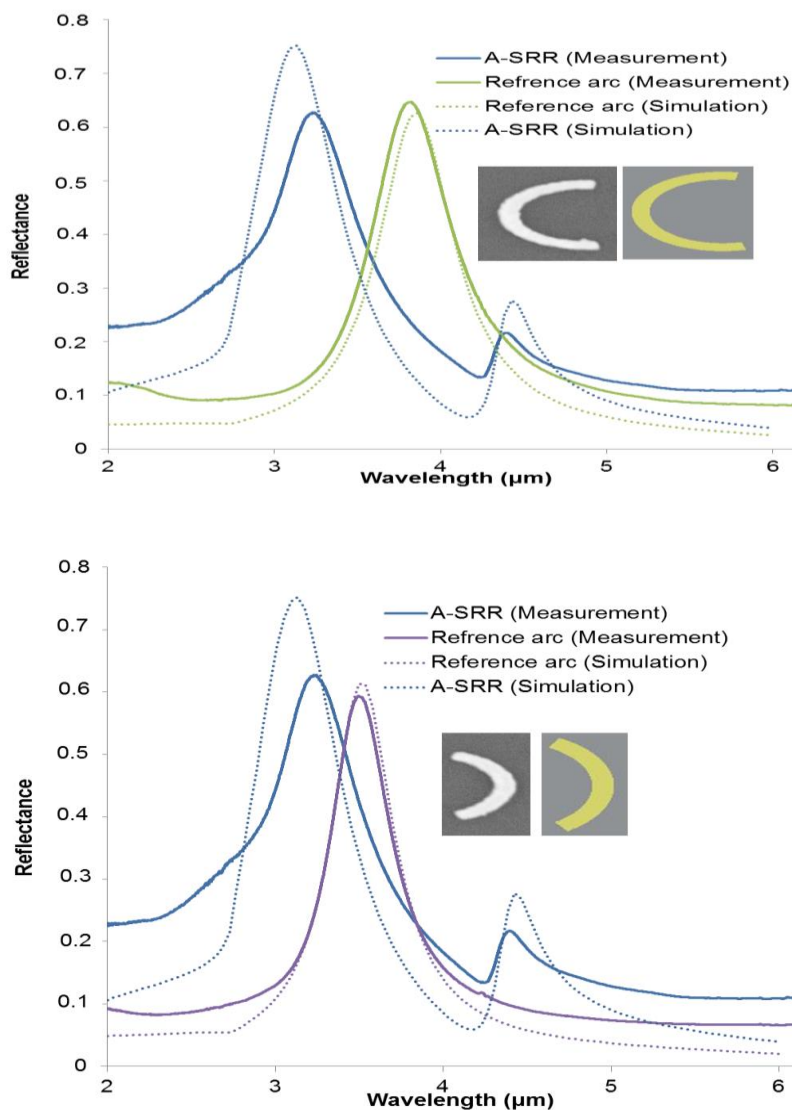


**Figure 5.16:** Reflectance spectra from experiment and simulation for hybridized resonance of A-SRR structure (a) A-SRR and Large arm (b) A-SRR and small arm.

The figures show double and single plasmonic from A-SRR and the individual arc as explained. This also concludes what was stated earlier in the chapter that the hybridized resonance of A-SRR exhibit both blue and red shift when compared with the individual coupled arcs. Again the little variations in the measured resonance peaks from simulation are because of experimental problems.

All of the results presented here can be compared with the results presented in the relevant references cited throughout the thesis. The asymmetric dipole result was also used to confirm the periodicity effect on resonance peaks as suggested in the literature [13-14] and this prompted the idea to develop the ASH structure which was mostly optimised and used for the assay of analyte,  $17\beta$ -estradiol.

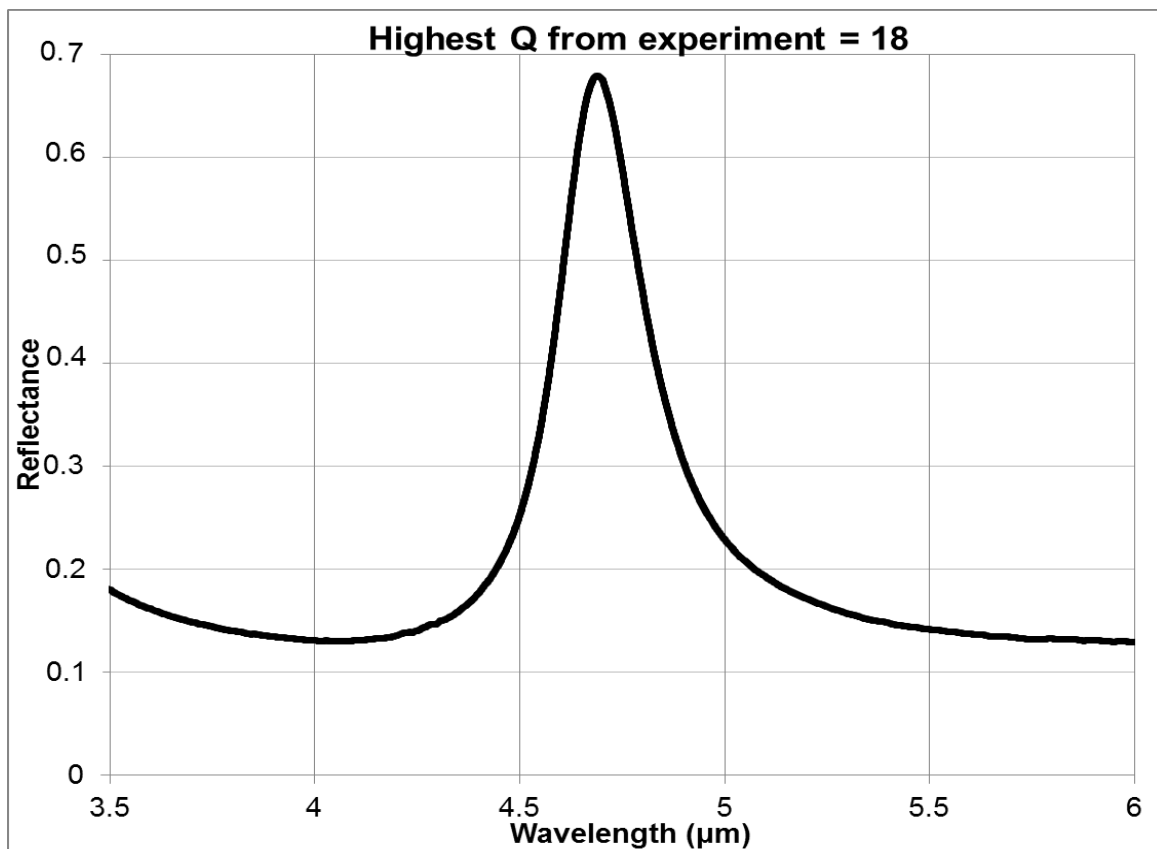


**Figure 5.17:** Reflectance resonance peak that produced the highest  $Q$  factor from the experimental results.

The main devices of the thesis, A-SRRs and ASH show excellent results which could become a promising platform for new developments in metallic metamaterial based sensors. Among reported related articles for metallic metamaterial that produces resonance peaks within mid-infrared, an approximate value of 18 as shown in figure 5.17 which to date is the highest quality factor in mid IR region from experimental work [5-6, 12-13, 17-21, 29-30] achieved. For a similar MM design a higher Q-factor of 50 is obtained from the numerical simulation than 18 from experiment. The variation in the produced value can be attributed to some limiting factors in relation to the two processes. In the experiment a maximum incident angle of  $23.6^\circ$  has been applied which is not the case in simulation where a plane wave source was used. Some other factors such as incident angle, beam collimation, line edge roughness in the fabrication and numerical artefact from grating order transmission of a periodic structure can affect the experimental or simulation process. In conclusion, the designed, fabricated and measured devices are quite complex structures and some useful experimental results have come from imperfectly fabricated devices.

## 5.7 References

1. C. N. Banwell, and E. M. McCash, "Fundamentals of Molecular Spectroscopy" 4th edition, 1994.
2. Hyperion, Bruker optics, user manual, 2<sup>nd</sup> updated edition, 2007.
3. V. A. Fedetov, M. Rose, S. L. Prosvirnin, N. Papasimakis, and N. I. Zheludev, "Sharp Trapped-Mode Resonances in Planar Metamaterials with a Broken Structural Symmetry," *Phys Rev Lett.*, vol 99, 147401, 2007.
4. C. Debus and P. H. Bolivar, "Frequency selective surfaces for high sensitivity terahertz sensing," *Appl Phys Lett.*, vol. 91, 184102, 2007.
5. B. Lahiri, A. Z. Khokhar, R. M. De La Rue, S. G. McMeekin, and N. P. Johnson, "Asymmetric split ring resonators for optical sensing of organic materials," *Opt. Express*, vol. 17, 1107, 2009.
6. S. Prosvirnin and S. Zouhdi, in *Advances in Electromagnetics of Complex Media and Metamaterials*, Kluwer Academic Publishers, The Netherlands, 281–290, 2003.
7. E. R. Lippincott, A. V. Valkenburg, C. E. Weir and E. N. Bunting, "Infrared Studies on Polymorphs of Silicon Dioxide and Germanium Dioxide," *Journal of Research of the National Bureau of Standards*, 61, 61-70, 1958.
8. A. Christ, T. Zentgraf, S. G. Tikhodeev, N. A. Gippius, J. Kuhl and H. Giesse, "Controlling the interaction between localized and delocalized surface plasmon modes: Experiment and numerical calculations," *PHYSICAL REVIEW B* 74, 155435-155443, 2006.
9. H. Guo, N. Liu, L. Fu, T. P. Meyrath, T. Zentgraf, H. Schweizer, and H. Giessen, "Resonance hybridization in double split-ring resonator metamaterials," *Opt. Express* 15, 12095, 2007.
10. N. Liu, H. Guo, L. Fu, H. Schweizer, S. Kaiser, and H. Giessen, "Plasmon Hybridization in Stacked Cut-Wire Metamaterials," *Phys. Status Solidi*, 244, 1251 2007.
11. Basudev Lahiri, Scott G. McMeekin, Richard M. De La Rue, and Nigel P. Johnson, "Resonance hybridization in nanoantenna arrays based on asymmetric split-ring resonators," *Appl. Phys. Lett.*, 98, 153116, 2011.
12. K. Aydin<sup>1</sup>, I. M. Pryce, and H. A. Atwater, "Symmetry breaking and strong coupling in planar optical metamaterials," *Optics Express*, 18, 13407-13417, 2010.

13. R. Adato, Yanik, A. A., Wu, C., Shvets, G. and H. Altug, "Radiative engineering of plasmon lifetimes in embedded nanoantenna arrays," *Opt. Express* 18, 4526-4537, 2010.
14. I. Sersic, M. Frimmer, E. Verhagen, and A. F. Koenderink, "Electric and Magnetic Dipole Coupling in Near-Infrared Split-Ring Metamaterial Arrays," *Phys. Rev. Lett.*, 103, 213902-4, 2009.
15. N. Liu, H. Liu, S. N. Zhu and H. Giessen, "Stereometamaterials," *Nat. Photon.* 3, 157-162, 2009.
16. P. Ding, E. J. Liang, W. Q. Hu, G. W. Cai, and Q. Z. Xue, "Tunable plasmonic properties and giant field enhancement in asymmetric double split ring arrays," *Photon. Nanostructures*, 9, 42-48, 2011.
17. V. A. Fedotov, M. Rose, S. L. Prosvirnin, N. Papasimakis, and N. I. Zheludev, "Sharp Trapped-Mode Resonances in Planar Metamaterials with a Broken Structural Symmetry," *Phys Rev Lett.* 99, 147401, 2007.
18. J. Chae, B. Lahiri and A. Centrone, "Engineering Near-Field SEIRA Enhancements in Plasmonic Resonators," *ACS Photonics*, 3, 87-95, 2016.
19. T. Koschny, P. Markoš, D. R. Smith, and C. M. Soukoulis, "Resonant and antiresonant frequency dependence of the effective parameters of metamaterials," *Phys. Rev. E*, 68, 065602, 2003.
20. V. A. Fedotov, T. Uchino, and J. Y. Ou, "Low-loss plasmonic metamaterial based on epitaxial gold monocrystal film," *Optics Express*, 20, 9545-9550, 2012.
21. S. Linden, C. Enkrich, M. Wegener, J. Zhou, T. Koschny, and C. M. Soukoulis, "Magnetic Response of Metamaterials at 100 THz," *Science*, 306, 1351-1361 2004.
22. B. Lahiri, S. G. McMeekin, A. Z. Khokhar, R. M. De La Rue and N.P. Johnson, "Magnetic response of split ring resonators (SRRs) at visible frequencies," *Optics Express* , 18, 3210-3218, 2010.
23. R. Singh, C. Rockstuh, C. Menze, T. P. Meyrath, M. He, H. Giessen, F. Lederer, and W. Zhang, "Spiral-type terahertz antennas and the manifestation of the Mushiake principle," *Opt. Express*, 17, 9971-9980, 2009.
24. H. Nornikman , B. H. Ahmad, M. Z. A. Abd Aziz and A. R. Othman, "Rhombic Split Ring Resonator (R-SRR) Structure on Rectangular Patch Antenna Design," *International Journal of Electronics and Computer Science Engineering*, 322-330, 2013.

25. C. R. Bridges, P. M. DiCarmino and D. S. Seferos, "Gold Nanotubes as Sensitive, Solution-Suspendable Refractive Index Reporters," *Chem.Mater.*, 24, 963–965, 2012.
26. H. Aouani, H. Šípová, M. Rahmani, M. Navarro-Cia , K. Hegnerová , J. Homola, M. Hong and S. A. Maier, "Ultrasensitive Broadband Probing of Molecular Vibrational Modes with Multifrequency Optical Antennas," *Nano Lett.*, 7, 669-675, 2013.
27. B. Wang, J. Zhou, T. Koschny, M. Kafesaki and C. M Soukoulis, "Chiral metamaterials: simulations and experiments," *J. Opt. A: Pure Appl. Opt.*, 11, 114003, 2009.
28. B. Yuan, W. Zhou and J. Wang, "Novel H-shaped plasmon nanoresonators for efficient dual-band SERS and optical sensing applications," *J. Opt.*, 16, 105013, 2014.
29. I. M. Pryce, Y. A. Kelaita, K. Aydin and H. A. Atwater, "Compliant metamaterials for resonantly enhanced infrared absorption spectroscopy and refractive index sensing," *Acs Nano*, 5, 8167– 8174, 2011.
30. C-K. Chena, M-H. Changa, H-T. Wua, Y-C. Leeb and T-J. Yena, "Enhanced vibrational spectroscopy, intracellular refractive indexing for label-free biosensing and bioimaging by multiband plasmonic-antenna array," *Biosens Bioelectron*, 60, 343–350, 2014.

# Chapter 6

## Detection of 17 $\beta$ -Estradiol

### 6.1 Introduction

17 $\beta$ -estradiol usually referred to as E2 is a type of human hormone with a molar mass of 272.382g/mol. E2 is mostly responsible for the development of human sex organs [1] and its 2D molecular structure is as shown in figure 6.1. The hormone can also be found naturally in the environment through human excreta or by anthropogenic activities [2]. High demand of the E2 for clinical analysis in monitoring the performance of the human biological system [1, 3-4] and in water treatment motivates researchers at an interdisciplinary level to investigate and report their various detection or sensing techniques [2, 5-12].

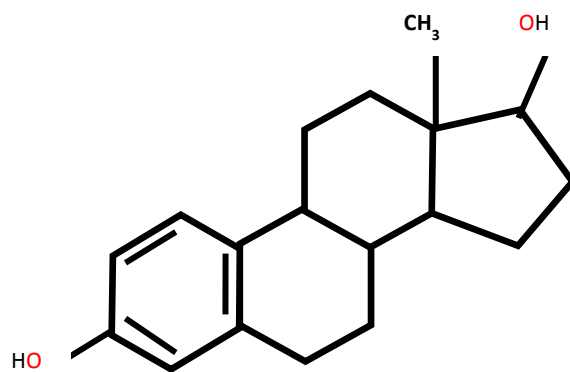


*Figure 6.1: Molecular structure of 17 $\beta$ -estradiol.*

17 $\beta$ -estradiol exhibits vibrational resonances due to the existence of molecular bonds such as C=C and C-H bonds in the analyte. These two molecular bonds have vibrational bonds within the (2 to 8)  $\mu\text{m}$  mid-infrared region of EM spectrum. The C-H bond has very strong vibrational resonances that range from (3.31 to 3.55)  $\mu\text{m}$  [13-19] while the much weaker stretching of C=C is at approximately 6.20  $\mu\text{m}$  [17, 20]. Williams et al [15] have stated that

the double bond C=C vibrational resonance which is at longer wavelength than the single bonding of C-H is due to the attached low mass of hydrogen atoms that place the stretching vibration of the alkenyl group at shorter wavelength even though the double bond is stronger. The aromatic stretching frequency C-H occurs below 3.33 $\mu\text{m}$  while the unsaturated frequency is above 3.33 $\mu\text{m}$  [15]. The presence of two different bands of frequency stretching are associated to the double peaks of the C-H as observed in this work and other references [13-19].

The significant characteristics for identifying the absorption band source of the molecular bonds are through vibrational intensity, shape and spectral position [19]. In this chapter, the designed and fabricated metallic metamaterial has been used to detect the significant characteristics of C-H that the E2 analyte exhibits. Work on the vibrational characteristics of C=C bond from the analyte is given in reference [17].

## **6.2 Sensing technique**

Over the years, there have been several sensing techniques employed by different research groups in order to assay 17 $\beta$ -estradiol [2, 5-12, 21]. These methods such as screen-printed carbon electrochemistry (SPCE) [5], gas chromatography-mass spectrometry (GC-MS) [6], gold electrode surface via under-potential deposition (UDP) [7] and aptamer-based optical fibre [8, 21], give a modest limit of detection (LOD) with complex laboratory experiments. Recent development of the surface enhanced infrared absorption (SEIRA) method by using plasmonic resonances from metallic metamaterial has been shown to provide a rapid and simple specific assay of 17 $\beta$ -estradiol [22-24]. The SEIRA method applied by some groups [8, 22-28] for the detection of 17 $\beta$ -estradiol did not evaluate the vibrational resonance or significant characteristic signature present in the mid-infrared region that the analyte exhibits.

In this work surface enhanced infrared absorption is the technique used for the E2 detection. The fabricated metallic metamaterial, such as asymmetric split ring resonators (ASRRs) and asymmetric split H-shape (ASH) which produces plasmonic resonance were applied to

evaluate C-H vibrational resonances present in E2. References [13-14, 29-32] have evaluated and reported the vibrational resonances of C-H with other types of analyte such as polydimethylsiloxane (PDMS), 1-octadecanethiol (ODT) and poly-methyl-methacrylate (PMMA). These analytes reveal other molecular bonds in the mid-infrared region. Here, 17 $\beta$ -estradiol has been analyzed through numerical simulations and experimental work to evaluate C-H bond within (2 to 6)  $\mu\text{m}$  of EM spectrum.

### 6.3 Modelling and Simulation

The modelling and design of all the material data used for the sensing was performed with commercial software (Lumerical) which employs the finite difference time domain (FDTD) method. A Schematic diagram of the analyte material 17 $\beta$ -estradiol and the ASH structure on a substrate are as shown in figure 6.2.

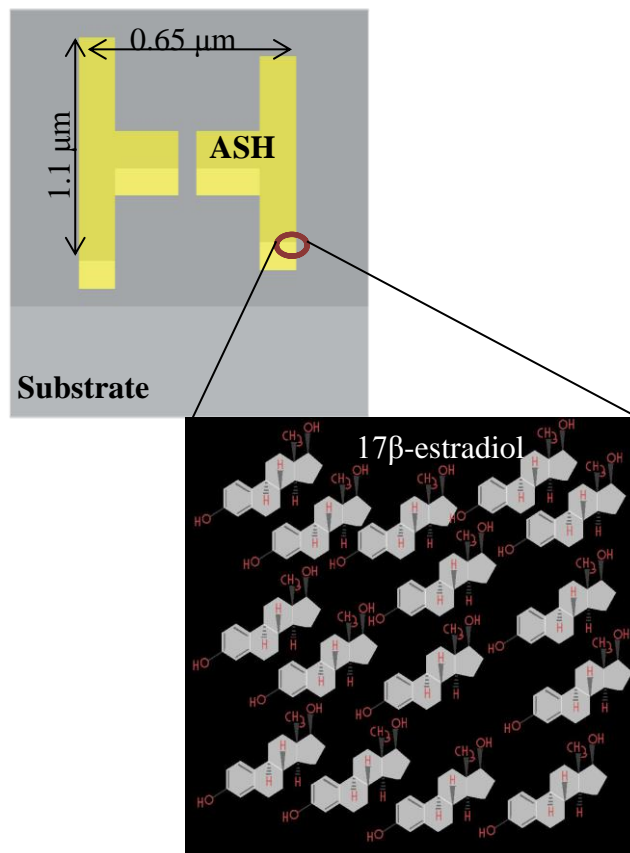


**Figure 6.2:** Systematic diagram of arrays of molecular formula of 17 $\beta$ -estradiol mapped to a sharp edge of an asymmetric split H-shape metamaterial.

The design for material data was performed using the experimental data from Palik [33] as contained in Lumerical. Similar procedures for modelling and fabricating metallic metamaterial (MM) as in chapters three and four were used to produce the sensor device. The dimensions of the MM devices are designed to tune the plasmonic resonance peak from (2 to 6)  $\mu\text{m}$  of EM spectrum.

The 17 $\beta$ -estradiol layer was modelled as a Lorentz oscillator material in which the background relative permittivity of the E2 analyte modifies the standard Lorentz resonance to produce a Fano type resonance as defined in the equation 6.1 [32].

$$\varepsilon(f) = \varepsilon + \frac{\varepsilon_L \omega_L^2}{\omega_L^2 - 2i \delta_L \omega - \omega^2} \quad (6.1)$$

In this work, the background relative permittivity ( $\varepsilon$ ) of the analyte E2 is 2.13 obtained from the expression  $\varepsilon = (n_{E2})^2$ , where n (1.46) is used as the refractive index of the analyte. The Lorentz permittivity ( $\varepsilon_L$ ) 0.0012 was used. Lorentz linewidth ( $\delta_L$ ) was used to provide resonance peak of a close match with the experimental measurements. Omega ( $\omega$ ) is the angular frequency and it is expressed as  $2\pi/\lambda$ . The double resonance peaks produced by C-H bond have been modelled with Lorentz resonance frequency ( $\omega_L$ ) of (5.51 and 5.4)  $10^{14}$  rad/s which corresponds to ( $\lambda_1 = 3.42$  and  $\lambda_2 = 3.49$ )  $\mu\text{m}$  as shown in figure 6.3. A three dimensional square block with the height or thickness in hundreds of nanometre in correspondence to the experiments was applied for modelling the E2.

These numerical models lead to Fano type resonance as associated with the E2 analyte. This is formed by superimposition of the Lorentz resonance on a slowly varying dielectric background to produce the negative and positive changes in the refractive index of the E2 layer. This also produces a wavelength dependent absorption coefficient. The plots of the real refractive index (n) and the absorption coefficient (k) for the E2 that result to Fano type resonance calculated from equation in 6.1 is as shown in figure 6.3.

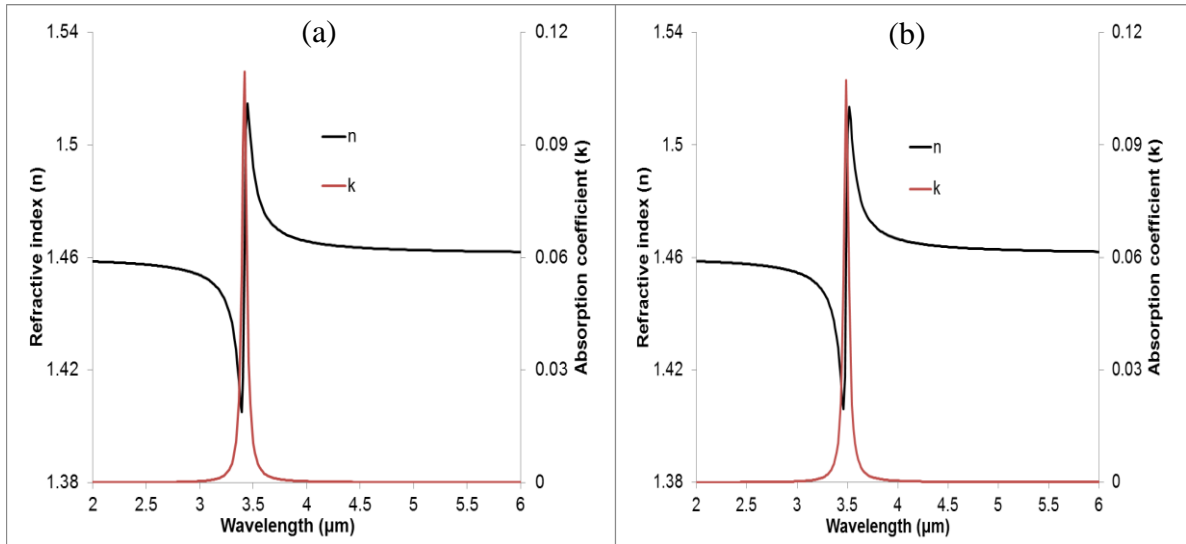


**Figure 6.3:** Refractive index and absorption coefficient of the analyte E2 with a Fano type resonance of the C-H bond at (a)  $\lambda_1 = 3.42 \mu\text{m}$  (b)  $\lambda_2 = 3.49 \mu\text{m}$  calculated from equation 6.1

The resonances that represent the Fano type in the refractive index of the analyte E2 at wavelengths of  $\lambda_1 = 3.42$  and  $\lambda_2 = 3.49 \mu\text{m}$  usually produce a red-shift to the plasmonic resonance peaks of the asymmetric structures. This occurs as a result of change in the refractive index of the analyte which replaces the low background index of air. Consequently in comparison with sensor's surroundings, the high index shifts the resonance to longer wavelength (red-shift) of EM spectrum while the low index will result in shorter wavelength (blue-shift) of the EM. Different refractive index values ranging from  $n = 1, 1.2, 1.4$  and  $1.6$  with their equivalent values of  $\epsilon$  were applied in equation 6.1 to model the Fano type resonance as shown in figure 6.4.

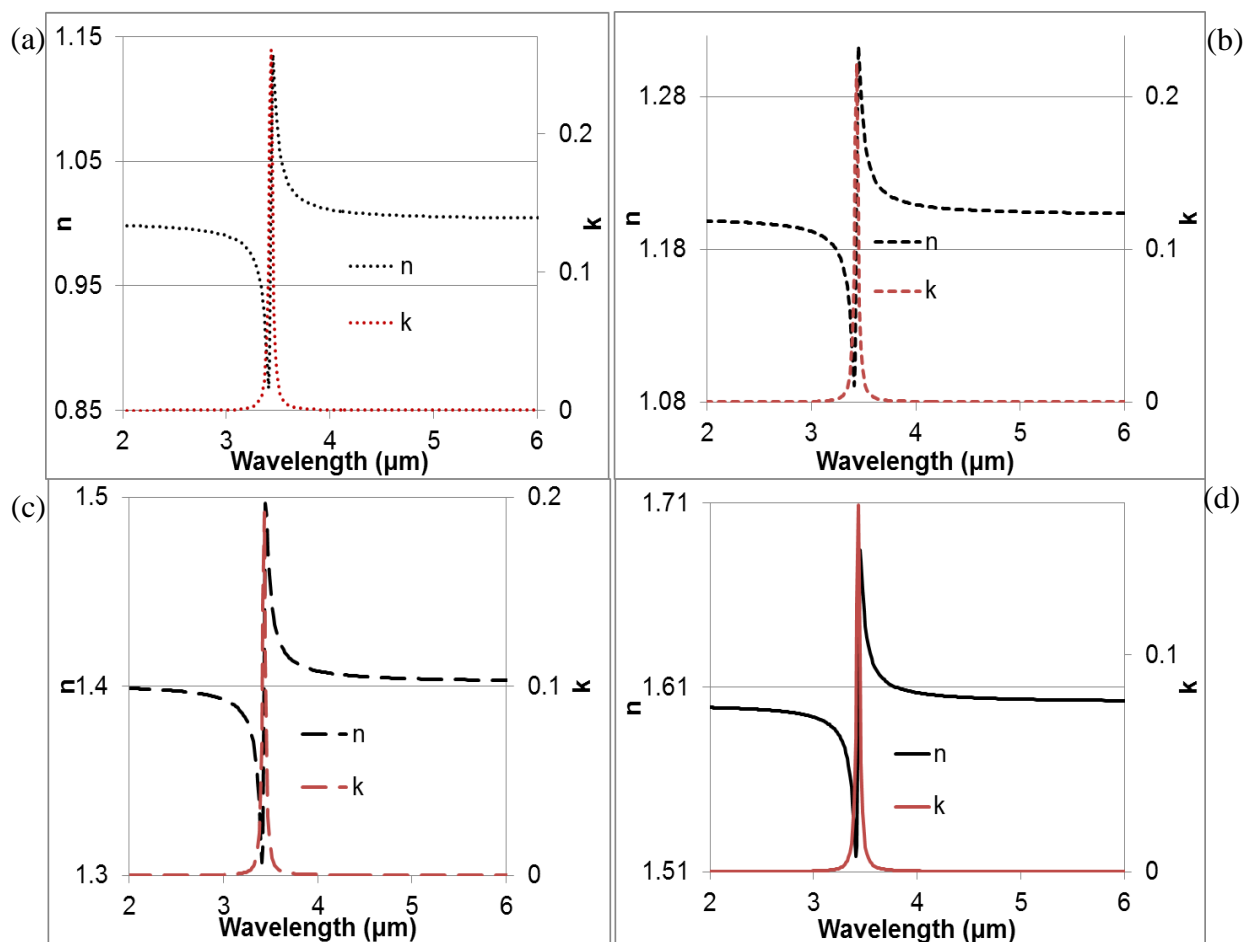


**Figure 6.4:** Fano type resonance plots for different refractive indexes (a)  $n_a = 1$  (b)  $n_b = 1.2$  (c)  $n_c = 1.4$  (d)  $n_d = 1.6$  of the sensors surrounding analyte.

The indexes variation affects the magnitude of the resonance plots as compared in figures 6.5 (a-c). The figure shows that low index has a greater magnitude than the high index values as expected and shown in figure 6.5c. This comparison is important towards understanding changes in the modelled molecular resonance. Reference [15] states that the significant characteristics for identifying absorption band source for molecular bonds are known through vibrational magnitude, shape and spectral position.

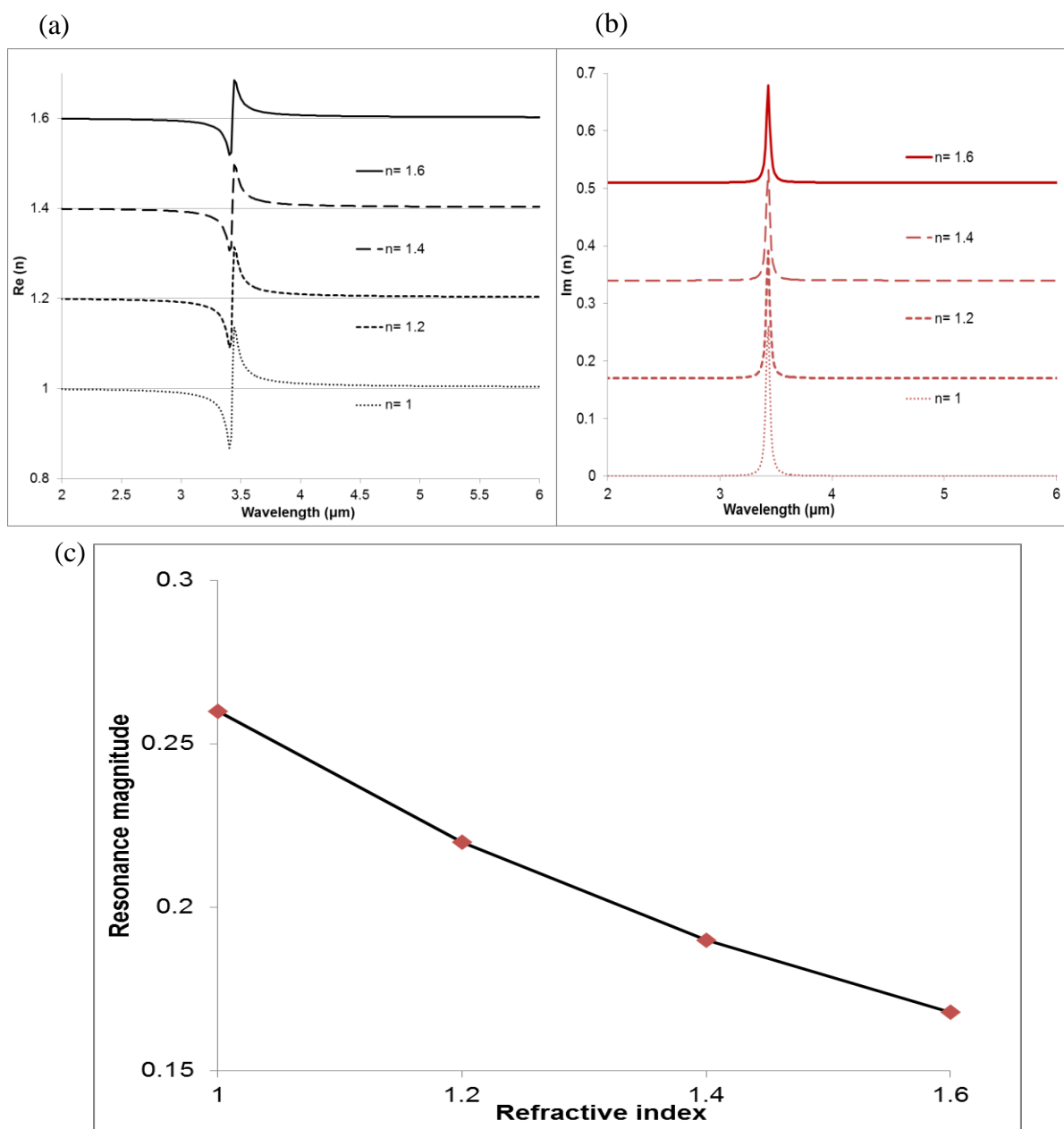


**Figure 6.5:** Comparison of the resonance magnitude for the indexes.

The indexes from 1 to 1.6 are compared because the targeted analyte E2 is a low index molecular substance but greater than the index of air. In this work, index of 1.46 has been applied to model Fano type resonance which produced a close match to the vibrational resonance of C-H bond observed on the plasmonic resonance peaks. A refractive index ( $n_{E2}$ ) value was selected due to the absence of a fixed  $n$  value for the analyte in the targeted wavelength region, at the time of this thesis. The vibrational resonance modelling results for C-H bond oscillation on the plasmonic resonance peaks are as explained in this chapter.

## 6.4 Experimental Process

The experimental procedures followed for detection of the  $17\beta$ -estradiol analyte with the metamaterial based sensor devices for this work involved measurement of square ( $150 \times 150$ )  $\mu\text{m}$  arrays of A-SRRs and ASHs fabricated patterns on a clean fused silica substrate. The dimensions for the asymmetric structures used are lengths ( $L_1$  and  $L_2$ ) of (0.9 and 1.1)  $\mu\text{m}$  respectively with pattern thickness ( $t$ ) of 100 nm. The fabrication of the sensor devices are explained in chapter four.

The bio-reagent white powder  $17\beta$ -estradiol ( $\text{C}_{18}\text{H}_{24}\text{O}_2$ ) of molecular weight 272.382 g/mole was purchased from Sigma-Aldrich. The solvent used to dissolve the solute E2, was absolute ethanol from VWR which formed a clear solution after a thorough shaking of the mixture.

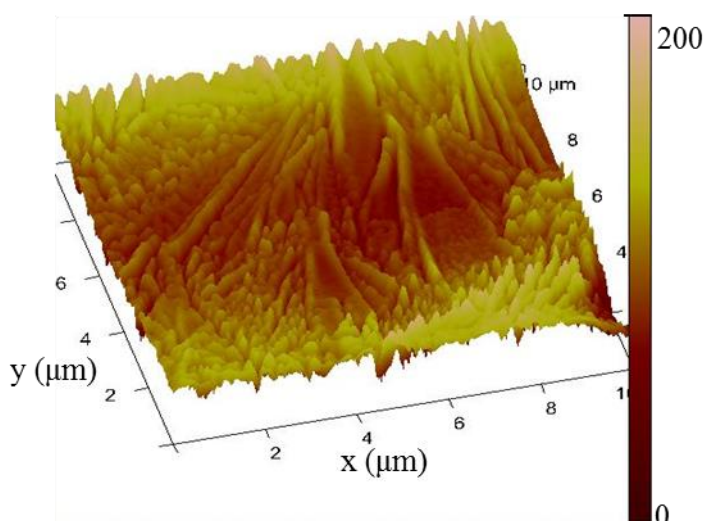


**Figure 6.6:** Atomic force microscopy (AFM) for surface measurement of the  $17\beta$ -estradiol was allowed to evaporate on substrate; the scanning height was set from 0 nm to 200 nm.

The clear solution formed was deposited on a substrate using the pipette. The solvent was allowed to evaporate leaving a thin film of the solute E2 on the surface. The surface roughness was checked using the AFM image as shown figure 6.6. Figure 6.6 showed what was expected from a non-uniform mixture, where the smooth part is concentrated at the centre and the rough at the edge even when clear solution has been formed. The assay of all the material used is  $> 98\%$  as stated by Sigma-Aldrich.

## 6.5 Experiment and Simulation results

The experimental results concern FTIR measurements of the reflectance spectra for the 17 $\beta$ -estradiol evaporated on a substrate with the fabricated metallic metamaterials of A-SRRs and ASHs. Initial reflectance measurement on a plain fused silica were performed as shown with the plots of figure 6.7 with no C-H vibrational resonance between 3.3  $\mu\text{m}$  and 3.6  $\mu\text{m}$  which was clearly absent in the zoomed spectra. Three measurements (a, b & c) of figure 6.7 were performed on two different cleaned fused silica substrates at different times and there was no molecular resonance observed at the targeted region.

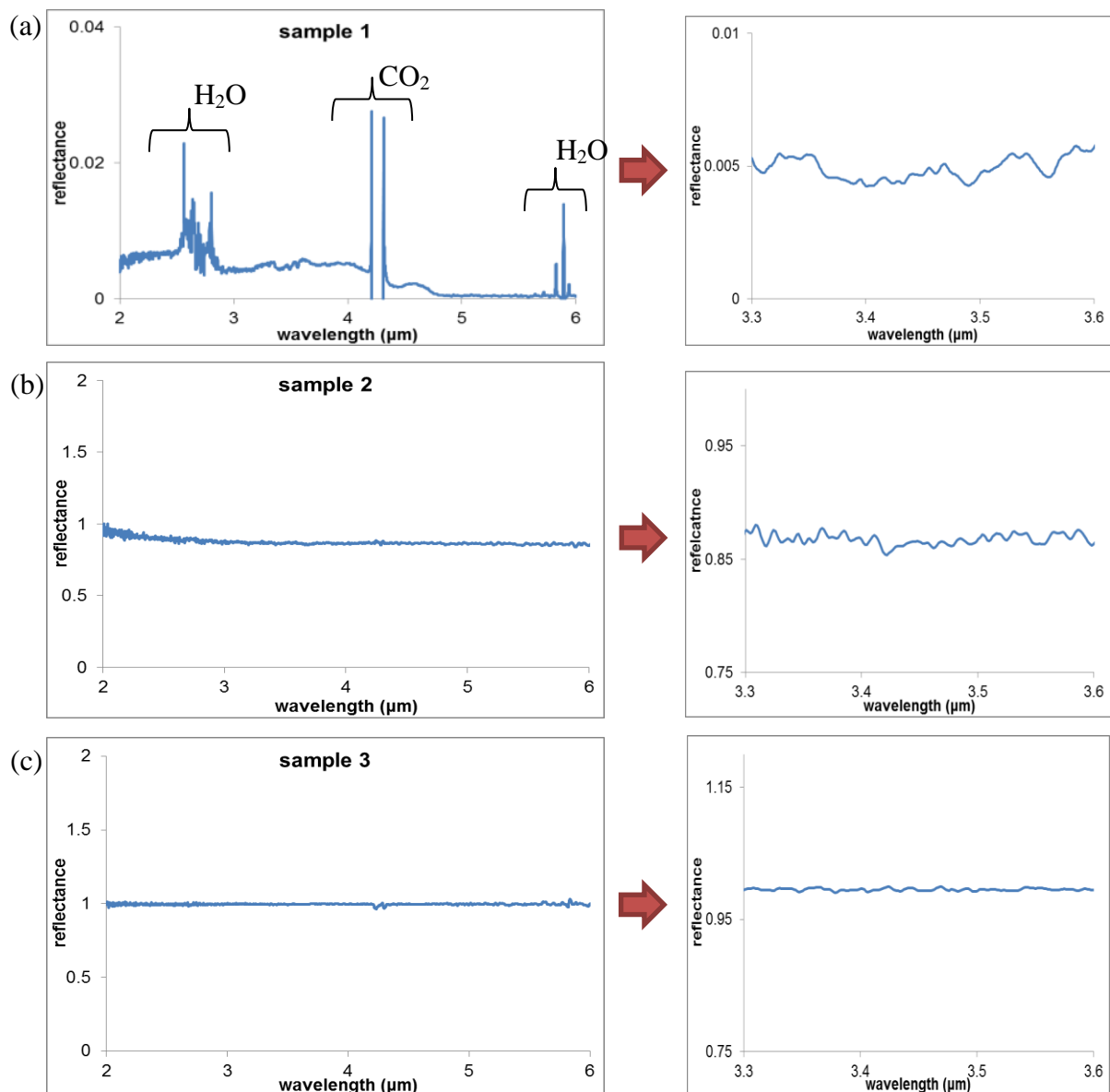


**Figure 6.7:** Reflectance spectra from two different fused silica substrates using FTIR: (a & b) 1 mm thickness of fused silica substrate, normalised to gold and to the substrate respectively (c) 0.5 mm thickness of fused silica, normalised to the substrate.

The three measured samples (fused silica) are of two different thicknesses of approximately 1 mm for samples (a & b) then sample (c) is 0.5 mm. Sample (a) was measured by normalizing the normal incidence source on a gold mirror shown in figure 6.7a while samples (b & c) as shown in figure 6.7 the source was normalized on a fused silica substrate. Normalization on the gold mirror is of higher reflectance than on the fused silica because of high reflectivity of gold. The fused silica normalization obtained values greater than unity while gold produced values from 0-1 as shown in figure 6.7.

On completing the initial measurements with three different samples which produced the reflectance results as shown in figure 6.7, the experimental detection of E2 was then performed. The reflectance spectra of the cleaned sample shown in blue is included on figure 6.8a for a closer comparison with the other two (green and red) plots which exhibit the C-H vibrational resonance from E2. The observed vibrational resonance on the green and red plots is C-H bond stretches at approximately (3.3 to 3.6)  $\mu\text{m}$  as shown in figure 6.8c. The signature of the bond has also been observed in other analyte as reported in references [13-14, 29-31].

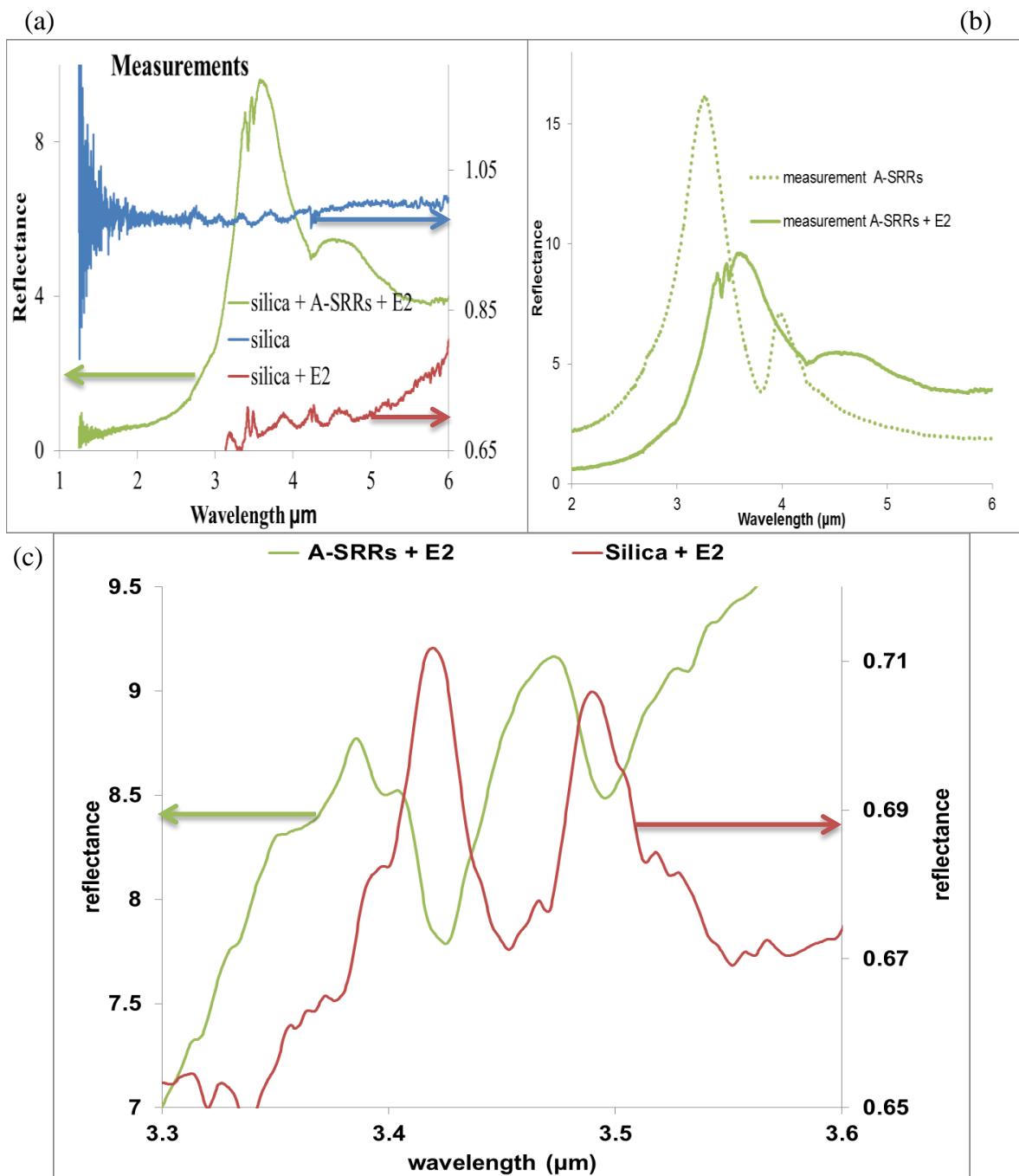


**Figure 6.8:** Experimental measurements for the sensor work using FTIR without normalization of the reflectance spectra (a) reflectance spectra from fused silica substrate, A-SRR and E2 (b) reflectance resonance peaks of A-SRRs alone and with E2 (c) Vibrational resonance of C-H on fused silica substrate and on A-SRRs.

The green plot in figures 6.8 (a & b) show the double plasmonic resonance peaks produced from A-SRRs sensor of 960 nm diameter as explained in chapter five. The dotted green plot in figure 6.8b was measured without the E2 analyte while the solid plot in the figure was

measured with E2. A redshift (shift to longer wavelength of EM spectrum) as shown in figure 6.8b was observed due to higher index from E2 analyte at the sensor surrounding which replaces the initial refractive index from air. Hence a shift obtained by the initial position of the plasmonic resonance from 3.33  $\mu\text{m}$  to 3.63  $\mu\text{m}$  and 4.04  $\mu\text{m}$  to 4.50  $\mu\text{m}$  for the peaks at shorter and longer wavelength respectively as shown in the figure. Figure 6.8 (c) is a zoomed plot to show clearly the double vibrational resonance shown in figure 6.8a from the C-H bond stretch.

In this work in order to understand the sensing and enhancement ability of the fabricated metamaterial based sensor devices experiments were performed for detection of four different quantities of 17 $\beta$ -estradiol mixed with ethanol as solvent. The quantity dissolved in 1 ml of ethanol were (0.0001, 0.001, 0.01 and 0.1) grams of E2 which respectively correspond to molarity of (0.37, 3.7, 36 and 334)  $\mu\text{mole/ ml}$ . The molarity was calculated based on the molar mass of E2 and calculation procedure is included in appendix C. These were pipetted on the fused silica substrate that contains fabricated arrays of ASHs (fabrication as described in chapter four). The mixture was allowed to evaporate for few minutes leaving a thin film of E2. The FTIR microscope was used for the reflectance spectra measurements by shining light normally first on the arrays of fabricated ASH nanostructure and next upon deposited E2. The reflectance spectra showing red-shift of the resonance peaks at presence are shown in figure 6.9. For these plots the E-field is polarized parallel to the arms of ASHs for both simulations and experiments to produce the plasmonic resonance peaks i.e. the black plots in figure 6.9.

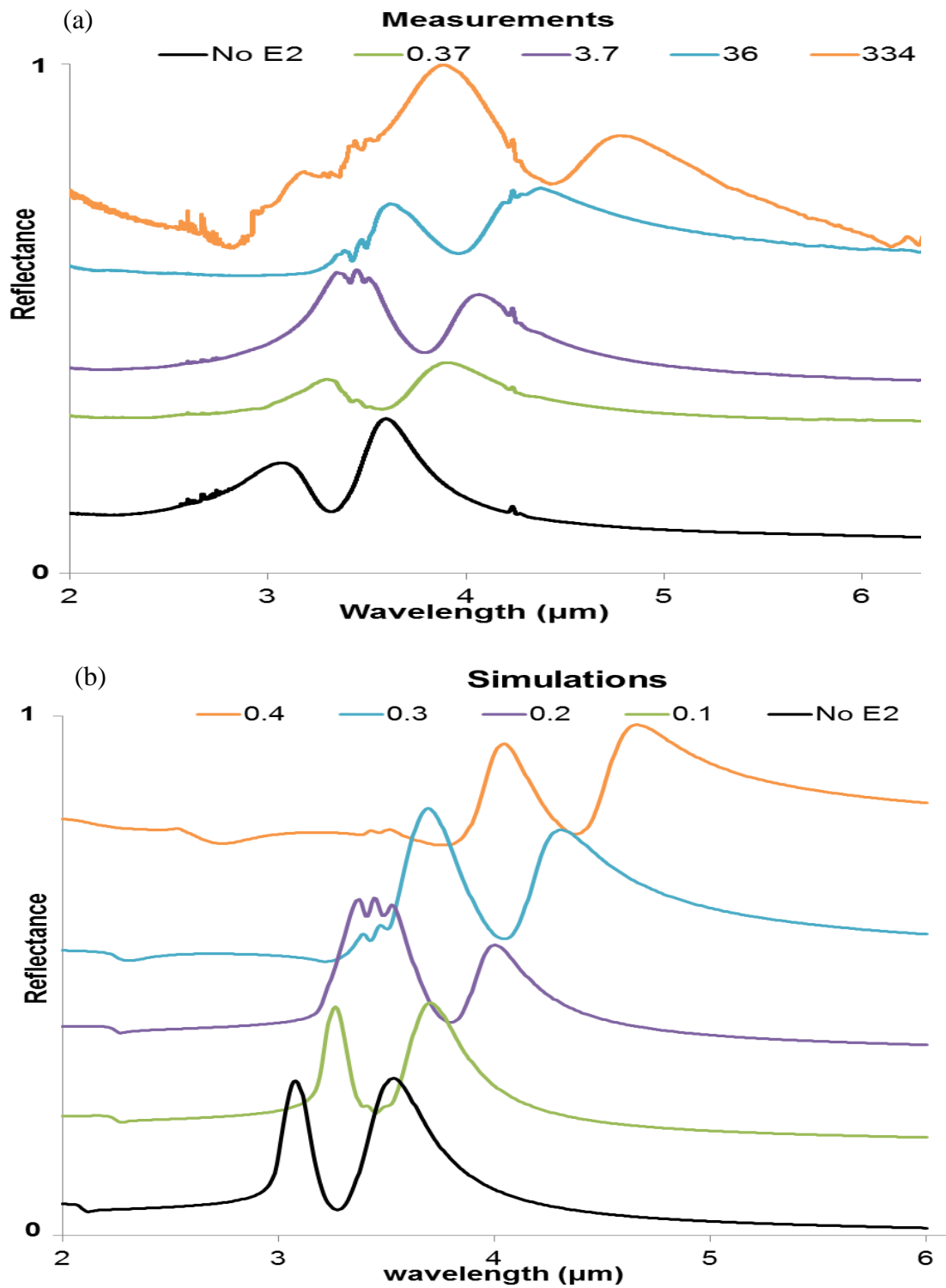


**Figure 6.9:** Vertically offset plots of reflectance spectra of the red-shifted resonance peaks due to refractive index change in the ASH surroundings (a) FTIR measurements for different molarity; ripples from H<sub>2</sub>O vapour at 2.8 μm, C-H vibrational resonance bond stretch from 3.31 μm to 3.55 μm and CO<sub>2</sub> at 4.2 μm (b) Lumerical simulations for different thickness from zero to 0.4 μm thick.

Figure 6.9a shows red-shifted (a shift to longer wavelength of EM spectrum) resonance peaks at different E2 molarity of (0.37, 3.7, 36 and 334)  $\mu\text{mole/ml}$  when compared with the no E2 plot. The measurements were normalized to the reflectivity of a gold coated mirror and the figure shows an offset of the spectra to avoid plot clustering. Normalization to the Au mirror enables clearer analyses of the enhancement factor for the C-H vibrational resonance. Figure 6.9b also show red-shift plasmonic resonance peaks when different modelled E2 thicknesses of (0.1, 0.2, 0.3 and 0.4)  $\mu\text{m}$  were simulated. Figure 6.9 is a general result used to evaluate the sensitivity and enhancement factor for the four experiment performed as subsequently explained. Enhancement factor is one of the basic features to characterise the ability of the metamaterial sensor devices [14, 17, 30]. In this section, metamaterial structure such as ASHs can produce a high enhancement and sensitive plasmonic sensors [18, 30, 34-37]. The ASHs features support high enhancement as shown in figures (6.10 - 6.12) while the asymmetric nature of the structure facilitates sensitivity by clear red-shifted resonance peaks shown in figure 6.9. The sensitivity produced here is high compared with works of these references [13-14, 30]. Figure 6.10 shows the general overview of using plasmonic resonance peaks from ASH metamaterial as a sensor based device. In the figure, black plot shows the reflectance measurement of E2 on the fused silica substrate, the red plot is the plasmonic resonance peaks from the ASH while the green, purple, blue and yellow plots demonstrates the red-shift and enhanced vibrational resonance with the plasmonic resonance with the presence of E2.

To demonstrate the sensing ability of the ASHs nanostructure without any surface functionalization steps, the sensitivity produced from redshift resonance peaks due to refractive index changes of the surroundings was calculated. The experiments were performed using the four different E2 molarity of (0.37, 3.7, 36 and 334)  $\mu\text{mole/ml}$ . A homogenous thin film layer was assumed for the analyte, E2 that covered the arrays of fabricated ASHs on a fused silica substrate in a square area of (150 by 150)  $\mu\text{m}$ . The sensitivity of the reflectance resonance for the four experiments was calculated using the expression [38]:  $s = \Delta\lambda / \Delta n$  (nm/ RIU). Where  $\Delta\lambda$  and  $\Delta n$  are changes in the resonance peak position and refractive index respectively. Values used for the calculations were obtained from the resonance peak at longer wavelength change ( $\Delta\lambda$ ) in position as shown in figure 6.10.

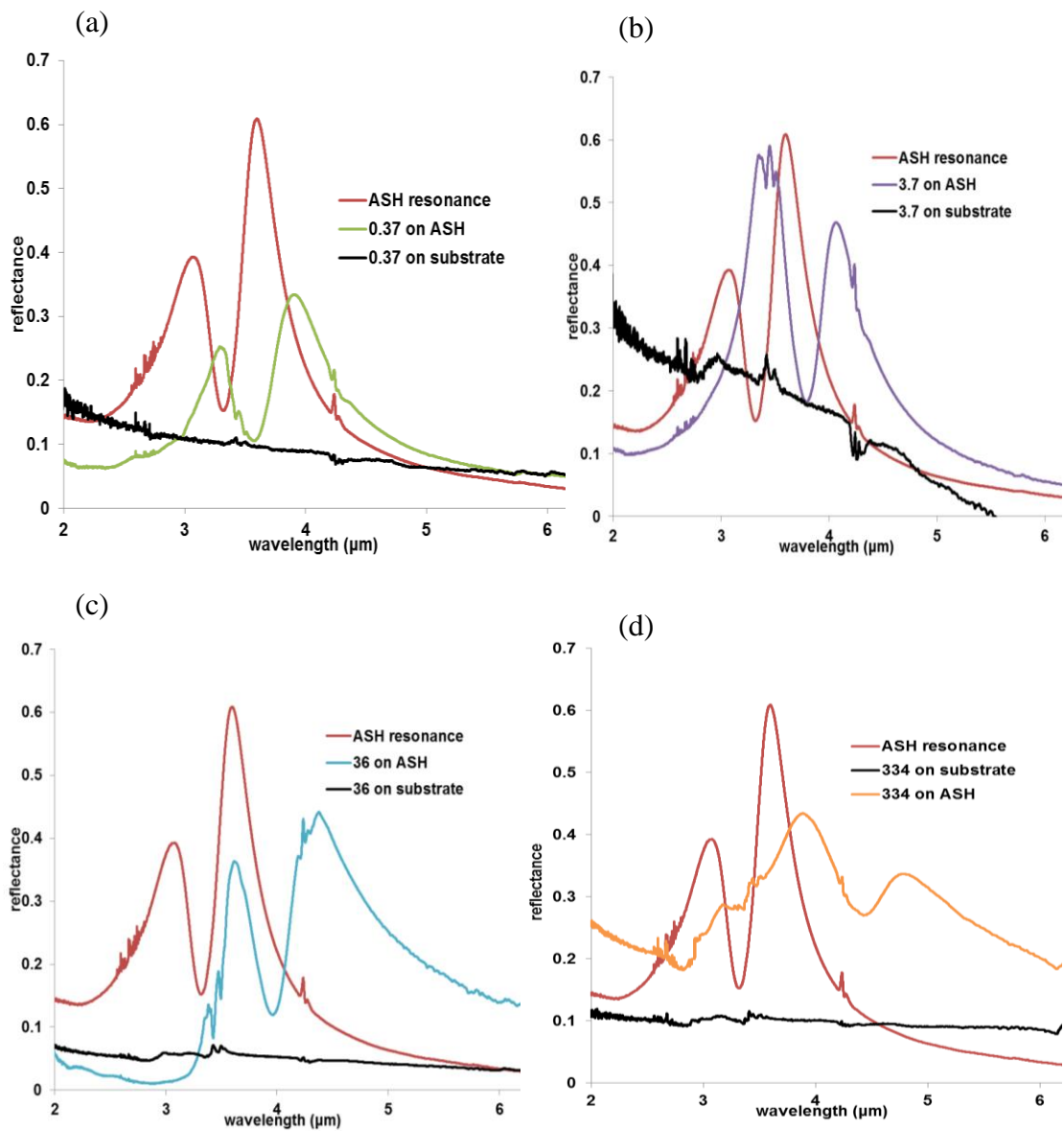


**Figure 6.10:** FTIR reflectance spectra of the red-shifted resonance peaks due to refractive index change in the ASH surroundings for the four different molarities in  $\mu\text{mole/ml}$  (a) 0.37 (b) 3.7 (c) 36 (d) 334; ripples from  $\text{H}_2\text{O}$  vapor at  $2.8 \mu\text{m}$ , C-H vibrational resonance bond stretch from  $3.31\mu\text{m}$  to  $3.55\mu\text{m}$  and  $\text{CO}_2$  at  $4.2 \mu\text{m}$ .

The plasmonic reflectance peak is red-shifted from the longer resonance peak position of  $3.59 \mu\text{m}$  to ( $3.87 \mu\text{m}$ ,  $4.06 \mu\text{m}$ ,  $4.38 \mu\text{m}$  and  $4.87 \mu\text{m}$ ) as shown in the measurements results of figures 6.9(a-d). The  $\Delta n$  of 0.46 was calculated from  $n_{E2} = 1.46$  and  $n_{air} = 1$ . The results achieved from the experiments give sensitivities of (622, 1020, 1726, 2791) nm / RIU for the four different E2 molarities of (0.37, 3.7, 36 and 334)  $\mu\text{mole/ml}$  respectively. The sensitivity

calculation is detailed in appendix C1. The high sensitivity value is attributed to asymmetric nature of the MM structure which introduces a dip in reflectance spectra between the double plasmonic peaks compared. Thus, the full width half maximum (FWHM) of 320 nm calculated from the resonance wavelength position at 3.59  $\mu\text{m}$  from red plot of figure 6.10. The FWHM value was used with the sensitivity of 2791 nm / RIU in the expression [30]: figure of merit (FOM) = sensitivity/ FWHM which produced FOM of approximately 9.

The enhancement factor which can be define as increase in intensity of the molecular resonance for adsorbates on particular surface occurs because of an enhancement in the electric field provided by the surfaces was calculated for the measurements shown in figure 6.10. In this work, the enhancement factor ( $E_f$ ) was calculated using expression of reference [30] and it is defined as follows:

$$E_f = \frac{\Delta V_2 / N_2}{\Delta V_1 / N_1} \quad (6.2)$$

Where N is total number of molecules and  $\Delta V$  is change in the amplitude of the molecular resonance.  $N_1$  &  $\Delta V_1$  is measurement without ASH pattern while  $N_2$  &  $\Delta V_2$  is with ASH. Generally, surface-enhanced Raman spectroscopy (SERS) and surface enhanced infrared absorption (SEIRA) are two plasmonic sensor techniques. SERS has produced higher enhancement factors from the E-field of the EM signal because of its second order nature than the first order use for SEIRA [30, 36]. SEIRA method was applied in this work as the target is in mid-infrared region. This method was based upon plasmonic resonance peaks produced from the ASHs structure. The absolute  $E_f$  values per unit area of  $10^4$  to  $10^5$  for the assay of E2 were achieved. The relative  $E_f$  value was also calculated to compare with the absolute values as included in appendix C2. The experiments were performed using the four different E2 molarities of (0.37, 3.7, 36 and 334)  $\mu\text{mole/ml}$  as explained in the previous paragraph. A homogenous thin film layer of the analyte (E2) that covered an array of fabricated ASHs on a fused silica substrate in a square area of (150 x 150)  $\mu\text{m}$  was assumed.

For the E2 experiments the number of molecules ( $10.027 \times 10^8$ ,  $10.027 \times 10^9$ ,  $9.756 \times 10^{10}$  and  $9.033 \times 10^{11}$ ) was calculated from an approximate measurement of 200 nm thickness of E2. These are the initial values of number ( $N_1$ ) of molecules which correspond to the thickness contributing to the intensity of the vibrational resonances. The  $N_2$  ( $10.027 \times 10^4$ ,  $10.027 \times 10^5$ ,  $9.756 \times 10^6$  and  $9.033 \times 10^7$ ) is defined by both the number of molecules of E2 interacting with the total number of (5625) ASHs in the measured area of (150 x 150)  $\mu\text{m}$ . An estimated molecular density of  $1 \text{ gm/cm}^3$  for the E2 was also used for  $E_f$  calculation as detailed in appendix C2.

The maximum E-field occurs at the four sharp edges of the ASH structure as indicated with white dotted circle in figure 6.11(a) (field plot was explained in chapter 3). This is the most effective resonance area explained as hot spots in reference [39] where 10 nm is the dimension of the hot spot upper-limit. In this work, the enhancement factors calculations of the hot spots area used was the (10 by 10)  $\text{nm}^2$  as detailed in appendix C2. The plasmonic resonance peaks is produced when the electric field (E-field) is parallel to the arms of the ASH as shown in figure 6.11(b). The field plot was obtained from ASHs simulation resonance peak wavelength at 3.31  $\mu\text{m}$  which corresponds to the peak at shorter wavelength as shown in purple colour plots of figure 6.9b.

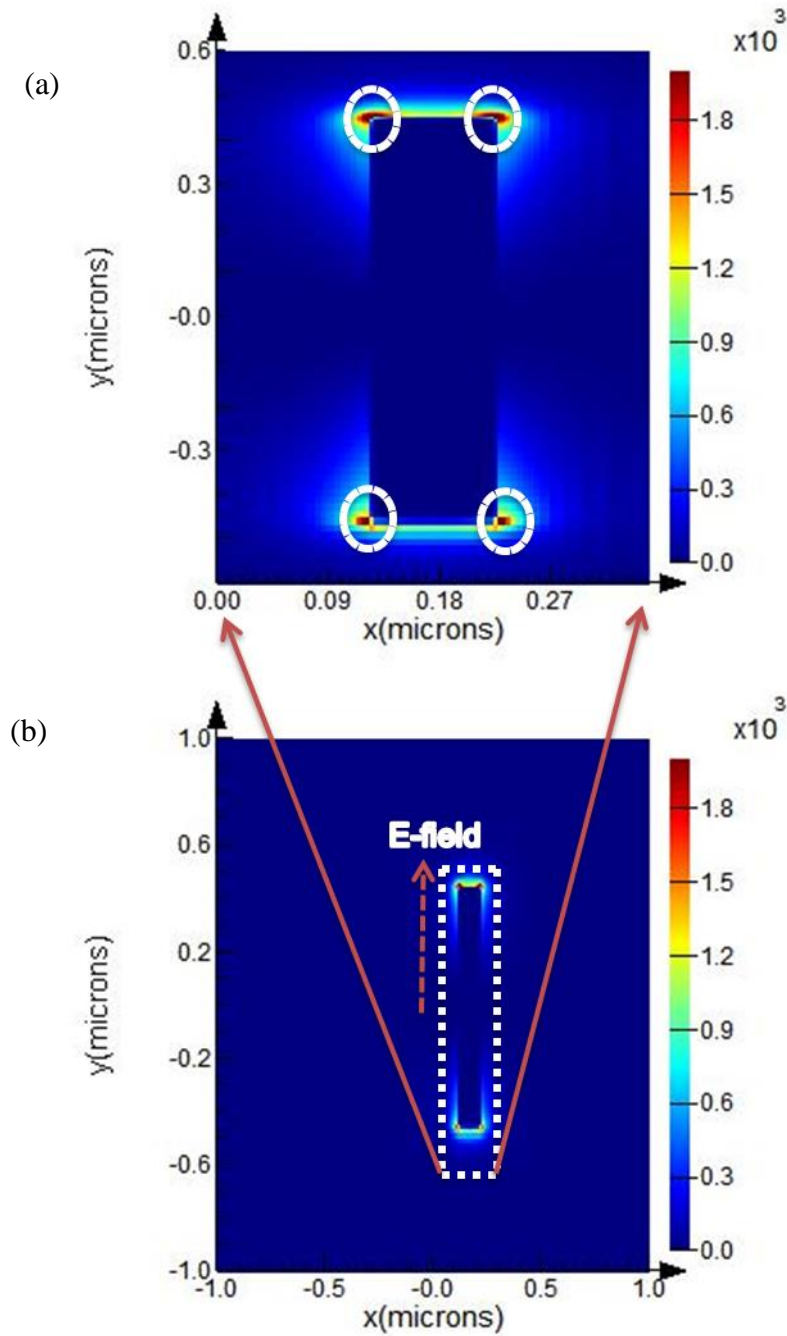


**Figure 6.11:** (a) Expanded view of (b) the absolute magnitude of the E-field from the design simulated for x-y axis with the dark red and dark blue colour showing the maximum and minimum value respectively with E-field parallel to arms of ASH for the resonance peak at wavelength  $3.31 \mu\text{m}$ .

The resonance peak at wavelength of  $3.31 \mu\text{m}$  for the purple colour plots in figures (6.9 & 6.10) was used because produced the highest enhancement factor from the calculations as detailed in appendix C2. The change in vibrational resonance ( $\Delta V$ ) intensity produced from

the vibrational resonance without ASH ( $\Delta V_1$ ) at 3.42  $\mu\text{m}$  and 3.45  $\mu\text{m}$  for the E2 evaporated on a clean fused silica substrate as shown in figures 6.12 (a-d) and vibrational resonance with ASH ( $\Delta V_2$ ) produced when the E2 is on the arrays of ASH nanoantennas for the four experiments performed are:  $\Delta V_1$  (0.0013, 0.00237, 0.0081 and 0.0180) which corresponds to  $V_2$  (0.0110, 0.0623, 0.1060 and 0.0270) respectively.

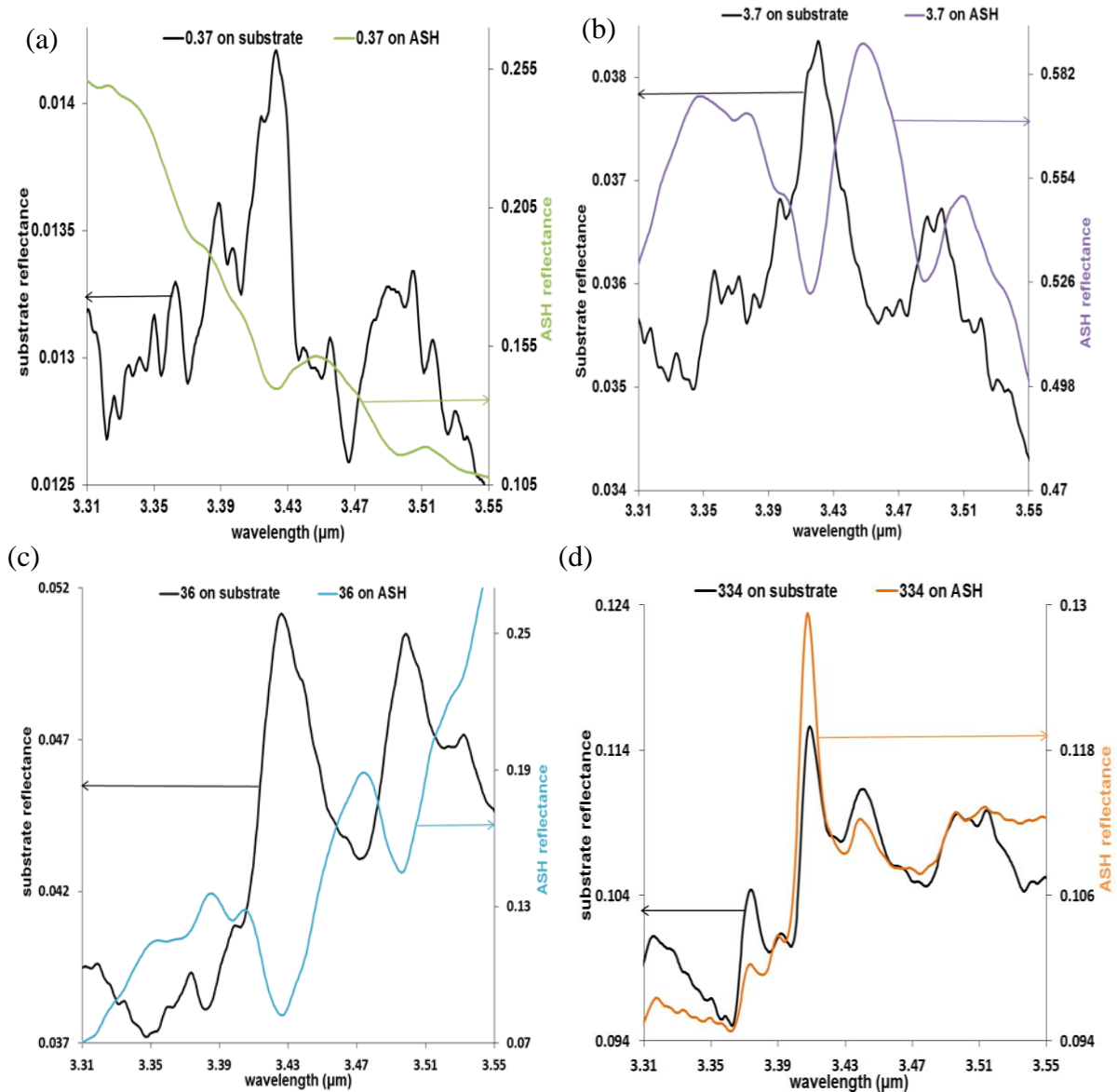


**Figure 6.12:** FTIR reflectance spectra of the enhanced C-H bond stretching from 3.31  $\mu\text{m}$  to 3.55  $\mu\text{m}$  vibrational resonance peaks by the ASH plasmon resonances zoomed plots of figure 6.9 (a)  $E_f$  of  $8.5 \times 10^4$  (b)  $E_f$  of  $2.6 \times 10^5$  (c)  $E_f$  of  $1.3 \times 10^5$  (d)  $E_f$  is  $1.5 \times 10^4$  for the different molarities of E2.

By substituting the values as defined in expression 6.2, enhancement factors of ( $8.5 \times 10^4$ ,  $2.6 \times 10^5$ ,  $1.3 \times 10^5$  and  $1.5 \times 10^4$ ) for the four experimental measurements shown in figure 6.12 were achieved. Detail of the enhancement calculation is included in the appendix C2. The enhancement factor did not increase uniformly with the increase in molarity of the E2. From the result the enhancement is greatest when the molecular resonance is on the apex of the resonance peak i.e. the case of the second experiment as shown in figures (6.10b & 6.12b).

Figure 6.13 was used for plasmonic resonance sensitivity comparison between the symmetric and asymmetric H-shape (SSHs and ASHs) for the concentration of  $37 \mu\text{mole/ml}$  of E2 analyte. The values used for the calculations were obtained from the resonance peak position shift for the ASHs at wavelengths of (3.57 to 3.94)  $\mu\text{m}$  which gives  $\Delta\lambda$  as 370 nm and for SSHs the resonance position shift at wavelengths of (3.23 to 3.37)  $\mu\text{m}$  gives  $\Delta\lambda$  as 140 nm shown in figure 6.13. The  $\Delta n$  of 0.46 was calculated from  $n_{\text{E2}} = 1.46$  and  $n_{\text{air}} = 1$ .

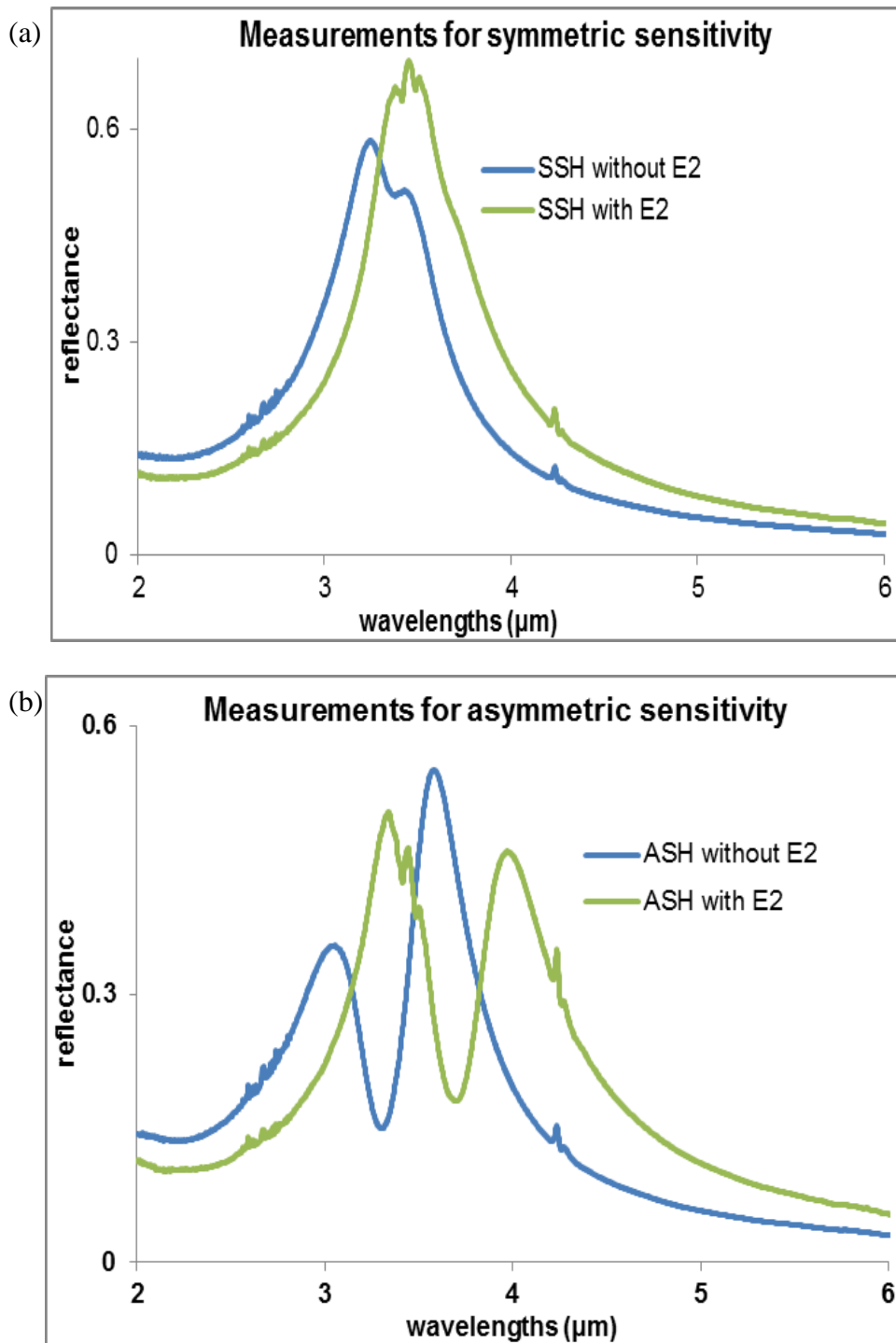


**Figure 6.13:** FTIR measurements for reflectance spectra showing the redshift in the resonance peaks from an initial wavelength of (a) 3.23  $\mu\text{m}$  for SSHs and (b) 3.05  $\mu\text{m}$  and 3.57  $\mu\text{m}$  for two peaks of ASHs. Other spectral features are water vapour at 2.85  $\mu\text{m}$ ,  $\text{CO}_2$  at 4.20  $\mu\text{m}$  and the C-H resonance stretch at 3.31  $\mu\text{m}$ . Note: Small dip on the blue plot of (a) at 3.2  $\mu\text{m}$  is due to imperfections in fabrication.

From these values, the sensitivity of 340 nm/ RIU and 804 nm/ RIU were calculated for the SSHs and ASHs metamaterial based sensor respectively. In comparison the sensitivity from

asymmetric structure is approximately 41% greater than symmetric. These results show that an optimized metallic metamaterial design such as ASH structure has promising features for a high sensitive bio-sensor device as demonstrated in this work.

The E2 thin film layer was modeled as explained in section 6.3 using a Lorentz oscillator which produces Fano type resonance as shown in figures 6.14 (a-c). Different refractive index values of 1, 1.2, 1.4 and 1.6 were applied to the Lorentz model. A match at  $n = 1.46$  was achieved from our various numerical simulations as shown in figure 6.14b for a thickness of 200 nm of E2. The absolute and relative  $E_f$  (space) per unit cell for the 200 nm modelled E2 placed on fused silica substrate, plain gold and ASHs structures were calculated. The details of  $E_f$  calculations are included in the appendix C2. The matched index was then applied to modeled different thicknesses (10, 200, 300 and 400) nm of E2 which produced shifts in the resonance peaks as shown in Figure 6.14c. From the figure, a calculated E2 quantity of 0.15 femtomoles per ASH for the 10 nm thickness produces sensitivity of 104 nm/RIU (corresponding to a red-shift of 47.84 nm) as shown in figure 6.14c. Detail of the femtomole calculation is included in the appendix C3. The 0.15 femtomole is a smallest quantity of E2 detected by the ASHs as shown in figure 6.14c. This limit of detection for the structure highlights the high sensing potential with application of SEIRA method [12, 22-25]. The degree of sensitivity based on the refractive index change as well as the thickness was observed and compared as shown figure 6.14d.

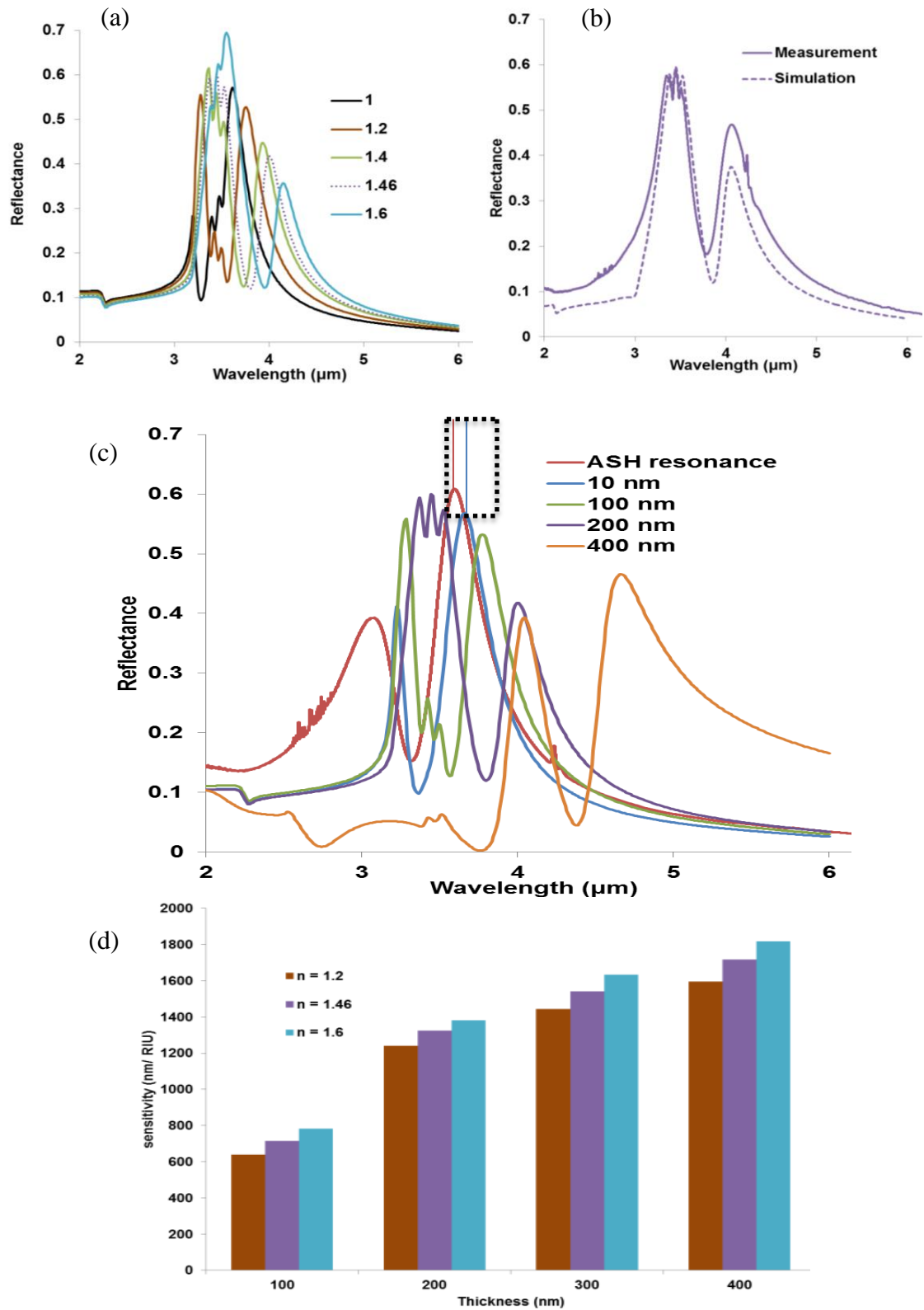


**Figure 6.14:** Simulations results (a) Reflectance plots for 200 nm thickness of E2 at various indexes (b) Matching results of experiment and simulation for reflectance molecular resonances of the E2 (c) simulations of the red-shift in the position of the resonance peaks for E2 thickness of (10, 100, 200, & 400) nm (d) Comparison of sensitivity of the ASH due to refractive index changes and thickness of E2.

The results enable a direct comparison of the sensitivity due to thickness of analyte and refractive index change. A sensitivity of 1818 nm/ RIU from the numerical simulation of 400 nm thickness modeled E2 was achieved with the ASHs nanoantennas as shown in figure 6.14d. The sensitivity was calculated using expression:  $s = \Delta\lambda / \Delta n$  (nm/ RIU). Lumerical which employs the FDTD method was used for the numerical simulations. As explained earlier Lorentz model [32] was used to model the Fano type resonance for the E2 which corresponds to the molecular resonance of experiments performed.

## 6.6 Discussions and conclusion

Two metamaterial sensors A-SRRs and ASHs have been used experimentally and with numerical simulations in order to assay E2 analyte. In this chapter, the presence of the C-H bond in 17 $\beta$ -estradiol was evaluated as shown with measurement and simulation reflectance spectra of figure 6.15. The figure summarizes the work of this chapter by showing the detection in a way of plasmonic peaks red-shift due to change in refractive index. The C-H stretch vibrational resonance enhancement is achieved by using the method of SEIRA with optimised metamaterial sensor structures or nanoantenna which produces the plasmonic resonance.

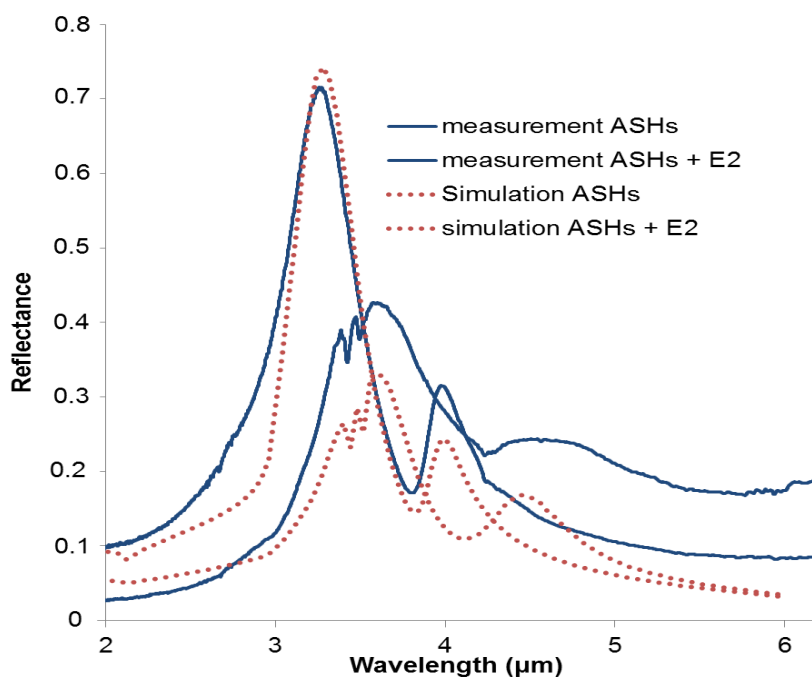


**Figure 6.15:** FTIR measurements and simulations of Reflectance spectra from ASHs and E2.

The characterization process of the sensors that produced high sensitivity was explained. For example, the ability of ASH arrays to produce higher sensitivity in detecting E2 analyte than the SSH structure, is because of the trapped mode which narrows the resonance peaks of the asymmetric structures there by producing a high quality factor device.

Table 6.1 summarizes the calculated values for the enhancement factors and sensitivities for the four experiments performed.

Table 6.1: Values for  $E_f$  and sensitivity for the four experiments

Experiment	Enhancement factor ( $E_f$ )	Sensitivity (nm/RIU)
a	$8.5 \times 10^4$	622
b	$2.6 \times 10^5$	1020
c	$1.2 \times 10^5$	1726
d	$1.5 \times 10^4$	2791

In conclusion a new metallic metamaterial structure with multiple sharp edges and a narrow gap that allows assay of E2 has been developed. Plasmon resonances produced from the ASHs arrays enhance the vibrational resonances of C-H bond by a factor of  $2.62 \times 10^5$ . From simulations limit of detection is 0.15 femtomole was obtained. A high sensitivity biosensor has been achieved with calculated value greater than 2700 nm/RIU at  $3.59 \mu\text{m}$  and figure of merit (FOM) of 9.

The vibrational resonance of the C-H bond stretch using Lorentzian modelling was almost perfectly matched to the experiment by varying the refractive index close to 1.46 which is close to the predicted index of E2 [40]. The plasmonic sensors are less complex in the detection of analyte such as  $17\beta$ -estradiol which is in high demand for biomedical and water treatment assays.

## 6.7 References

1. S. R. Staden, A. L. Gugoasa, B. Calenic and J. Legler, "Pattern recognition of estradiol, testosterone and dihydrotestosterone in children's saliva samples using stochastic microsensors," *Scientific Reports*, 4, 5579, 2014.
2. Y. Zhang, J. L. Zhou and B. Ning, "Photodegradation of estrone and 17 $\beta$ -estradiol in water," *Science Direct*, 1, 19-26, 2007.
3. L. M. Brown, L. Gent, K. Davis and D. J. Clegg, "Metabolic impact of sex hormones on obesity," *Brain Res.*, 1350, 77-85, 2010.
4. Y.S. Kim, H. S. Jung, T. Matsuura, H. Y. Lee, T. Kawai and M. B. Gu, "Electrochemical detection of 17 $\beta$ -estradiol using DNA aptamer immobilized gold electrode chip," *Biosens. Bioelectron.*, 22, 2525-2531, 2007.
5. R. M. Pemberton, T. T. Mottram and J. P. Hart, "Development of a screen-printed carbon electrochemical immunosensor for picomolar concentrations of estradiol in human serum extracts," *J. Biochem. Biophys. Methods*, 63, 201–212, 2005.
6. P-T. Katalin, B. Darius and P. Laszlo, "Simultaneous Measurement of 17 $\beta$ -Estradiol, 17 $\alpha$ -Estradiol and Estrone by GC–Isotope Dilution MS–MS," *Chromatographia.*, 71, 311–315, 2010.
7. X.Q. Liu, X. H. Wang, J. M. Zhang, H. Q. Feng, X. H. Liu and D. K. Y. Wong, "Detection of estradiol at an electrochemical immunosensor with a Cu UPD vertical bar DTBP-Protein G scaffold," *Biosens Bioelectron.*, 35, 56-62, 2012.
8. N. Yildirim, F. Long, C. Gao, M. He, H-Cg. Shi and A. Z. Gu, "Aptamer-Based Optical Biosensor For Rapid and Sensitive Detection of 17 $\beta$ -Estradiol In Water Samples," *Environ. Sci. Technol.*, 46, 3288–3294, 2012.
9. L. Zhao, J-M. Lin, Z. Li and X. Ying, *Anal. Chim. Acta*, "Development of a highly sensitive, second antibody format chemiluminescence enzyme immunoassay for the determination of 17 $\beta$ -estradiol in wastewater," 558, 290-295, 2006.
10. S. Zhu, Q. Zhang, L-H. Guo, "Part-per-trillion level detection of estradiol by competitive fluorescence immunoassay using DNA/dye conjugate as antibody multiple labels," *Anal. Chim. Acta*, 624, 141–146, 2008.

11. Y. Yang and E. P. C. Lai, "Optimization of Molecularly Imprinted Polymer Method for Rapid Screening of 17 $\beta$ -Estradiol in Water by Fluorescence Quenching," *Int J Anal Chem*, 214747, 1-8, 2011.
12. C. Desbrow, E.J. Routledge, G. C. Brighty, J.P. Sumpter, M. Waldox , "Identification of estrogenic chemicals in STW effluent. 1. Chemical fractionation and in vitro biological screening," *Environ Sci Technol*, 32, 1549-1558, 1998.
13. E. Cubukcu, S. Zhang, Y-S. Park, G. Bartal and X. Zhang, "Split ring resonator sensors for infrared detection of single molecular monolayers," *Appl. Phys. Lett.*, 95, 043113, 2009.
14. C-K. Chen, M-H. Chang, H-T. Wu, Y-C. Lee and T-J. Yen, "Enhanced vibrational spectroscopy, intracellular refractive indexing for label-free biosensing and bioimaging by multiband plasmonic-antenna array," *Biosens Bioelectron.*, 60, 343–350, 2014.
15. D. H. Williams, and I. Flemming, *Spectroscopic Methods in Organic Chemistry*; McGraw-Hill: UK, 1973.
16. I. G. Mbomson, S. McMeekin, Basudev Lahiri, R. De La Rue, and N. P. Johnson, "Gold asymmetric split ring resonators (A-SRRs) for nano sensing of estradiol," *Proc. SPIE 9125, Metamaterials IX*, 91251O, 2014.
17. I. G. Mbomson, S. McMeekin, R. De La Rue, and N. P. Johnson, "Matching plasmon resonances to the C=C and C-H bonds in estradiol," *Proc. SPIE 9340, Plasmonics in Biology and Medicine XII*, 93400G, 2015
18. R. F. Peters, L. Gutierrez-Rivera, S. K. Dew and M. Stepanova, "Surface Enhanced Raman Spectroscopy Detection of Biomolecules Using EBL Fabricated Nanostructured Substrates," *J. Vis. Exp.*, 97, 52712, 2015.
19. D. Enders and A. Pucci, "Surface enhanced infrared absorption of octadecanethiol on wet-chemically prepared Au nanoparticle films," *A. Appl. Phys. Lett.* , 88, 184104, 2006.
20. B. Stuart, [*Infrared spectroscopy: Fundamentals and Applications*], John Wiley & Sons, UK, 45-70, 2004.
21. J. Liu, W. Bai, S. Niu, C. Zhu, S. Yang and A. Chen, "Highly sensitive colorimetric detection of 17 $\beta$ -estradiol using split DNA aptamers immobilized on unmodified gold nanoparticles," *Scientific Reports* , 4, 7571, 2014.
22. Q. Zhang, Y. Wang, A. Mateescu, K. Sergelen, A. Kibrom, U. Jonas, T. Wei and J. Dostalek, "Biosensor based on hydrogel optical waveguide spectroscopy for the detection of 17 $\beta$ -estradiol," *Talanta*, 104, 149-154, 2013.

23. M. Miyashita, T. Shimada, H. Miyagawa, M. Akamatsu, "Surface plasmon resonance-based immunoassay for 17 beta-estradiol and its application to the measurement of estrogen receptor-binding activity," *Anal. Bioanal. Chem.*, 381,667–673, 2005.
24. W-W. Zhang, Y-C. Chen, Z-F. Luo, J-Y. Wang and D-Y. Ma, "Analysis of 17 beta-estradiol from sewage in coastal marine environment by surface plasmon resonance technique," *Chem. Res. Chin.*, 404–407, 2007.
25. U. Latif, J. Qian, S. Can and F. L. Dickert, "Biomimetic receptors for bioanalyte detection by quartz crystal microbalances - from molecules to cells," *Sensors*, 12, 23419–23438, 2014.
26. J. Liu, W. Bai, S. Niu, C. Zhu, S. Yang and A. Chen, "Highly sensitive colorimetric detection of 17 $\beta$ -estradiol using split DNA aptamers immobilized on unmodified gold nanoparticles," *Scientific Reports*, 4, 7571, 2014.
27. H. Ou, Z. Luo, H. Jiang, H. Zhou, X. Wang and C. Song, "Indirect Inhibitive Immunoassay for Estradiol Using Surface Plasmon Resonance Coupled to Online In-Tube SPME," *Analytical Letters*, 42, 2758-2773, 2009.
28. E. D. Son, J. Y. Lee, S. Lee, M. S. Kim, B. G. Lee, I. S. Chang and J. H. Chung, "Topical application of 17beta-estradiol increases extracellular matrix protein synthesis by stimulating TGF-beta signalling in aged human skin in vivo *Journal of Investigative Dermatology*, 124, 1149-1161, 2005.
29. B. Lahiri, A. Z. Khokhar, R. M. De La Rue, S. G. McMeekin, and N. P. Johnson, "Asymmetric split ring resonators for optical sensing of organic materials," *Optics Express*, 17, 1107-1115, 2009.
30. I. M. Pryce, Y. A. Kelaita, K. Aydin and H. A. Atwater, "Compliant metamaterials for resonantly enhanced infrared absorption spectroscopy and refractive index sensing," *ACS Nano*, 5, 8167– 8174, 2011.
31. H. T. Flakus and B. Hachula, "Effect of the resonance of the C–H and O–H bond stretching vibrations on the IR spectra of the hydrogen bond in formic and acetic acid," *Spectrochimica Acta Part A: Molecular and Biomolecular Spectroscopy*, 79, 1276–1284, 2011.
32. B. Lahiri, S. G. McMeekin, R. M. De La Rue, and N. P. Johnson, "Enhanced Fano resonance of organic material films deposited on arrays of asymmetric split-ring resonators (A-SRRs)," *Optics Express* 21, 9343-9352, 2013.
33. Palik, E. D. *Handbook of Optical Constants of Solids*; Academic Press: San Diego, CA, 1985.

34. W. Kubo and S. Fujikawa, "Au Double Nanopillars with Nanogap for Plasmonic Sensor," *Nano Lett.*, 11, 8–15, 2011.
35. D.R. Ward, N.K. Grady, C.S. Levin, N.J. Halas, Y. Wu, P. Nordlander and D. Natelson, "Electromigrated nanoscale gaps for surface-enhanced Raman spectroscopy," *Nano Lett.*, 7, 1396-1400, 2007.
36. H. Aouani, H. Šípová, M. Rahmani, M. Navarro-Cia , K. Hegnerová , J. Homola, M. Hong and S. A. Maier, "Ultrasensitive Broadband Probing of Molecular Vibrational Modes with Multifrequency Optical Antennas," *Nano Lett.*, 7, 669-675, 2013.
37. S. Lal, N. K. Grady, J. Kundu, C. S. Levin, J. B. Lassiter and N. J. Halas, "Tailoring plasmonic substrates for surface enhanced spectroscopies," *Chem. Soc. Rev.* 37, 898-911, 2008.
38. P. S. Nunes, N. A. Mortensen, J. P. Kutter and K. B. Mogensen, "Photonic crystal resonator integrated in a microfluidic system," *Opt. Lett.*, 33, 1623–1625, 2008.
39. M. I. Stockman, "Nanoplasmonics: The physics behind the applications," *Physics Today*, 39-44, 2011.
40. Santa Cruz Biotechnology. <http://www.scbt.com/datasheet-204431-b-estradiol>, 2015.

# Chapter 7

## Future work and Conclusions

### 7.1 Introduction

Other work performed that may form the basis for future projects is now described. Two different devices, A-SRRs and ASH on waveguide were also designed and fabricated using electron beam lithography. The patterns were design with a different substrate, silicon on insulator (SOI) as detailed in the following sub-sections. The summary of the entire work closes the thesis.

### 7.2 Future work

Although, the results presented in this thesis have demonstrated the effectiveness of the optimized plasmonic resonance peaks in the mid-infrared region of EM spectrum. This work could be further developed in a number of ways as explained in the section.

#### **Fabrication on Silicon-on-Insulator (SOI)**

SOI is a technology where a silicon-insulator-silicon substrate is used to improve electronic device performance by reducing the parasitic device capacitance [1]. This technology offers significant advantages in design, fabrication and application of many semiconductor circuits. SOI also improves prospects for extending silicon devices into the nanoscale region which makes it very useful for integrated electronic, photonic circuit devices and even dielectric metamaterials.

The SOI wafer consists of a film of monocrystalline silicon separated by a layer of SiO<sub>2</sub> from the bulk silicon substrate [2-4]. Silicon on sapphire (SOS) is another version of SOI that is

produced through epitaxial growth but the SOS was found to be of limited utility [1]. SOI diminishes short channel effects in microelectronic devices [5]. More recently, it has been widely used [6-8] for integrated photonic devices. The insulating and topmost silicon layers vary widely with application [9] which makes it useful also for metamaterial based sensor devices.

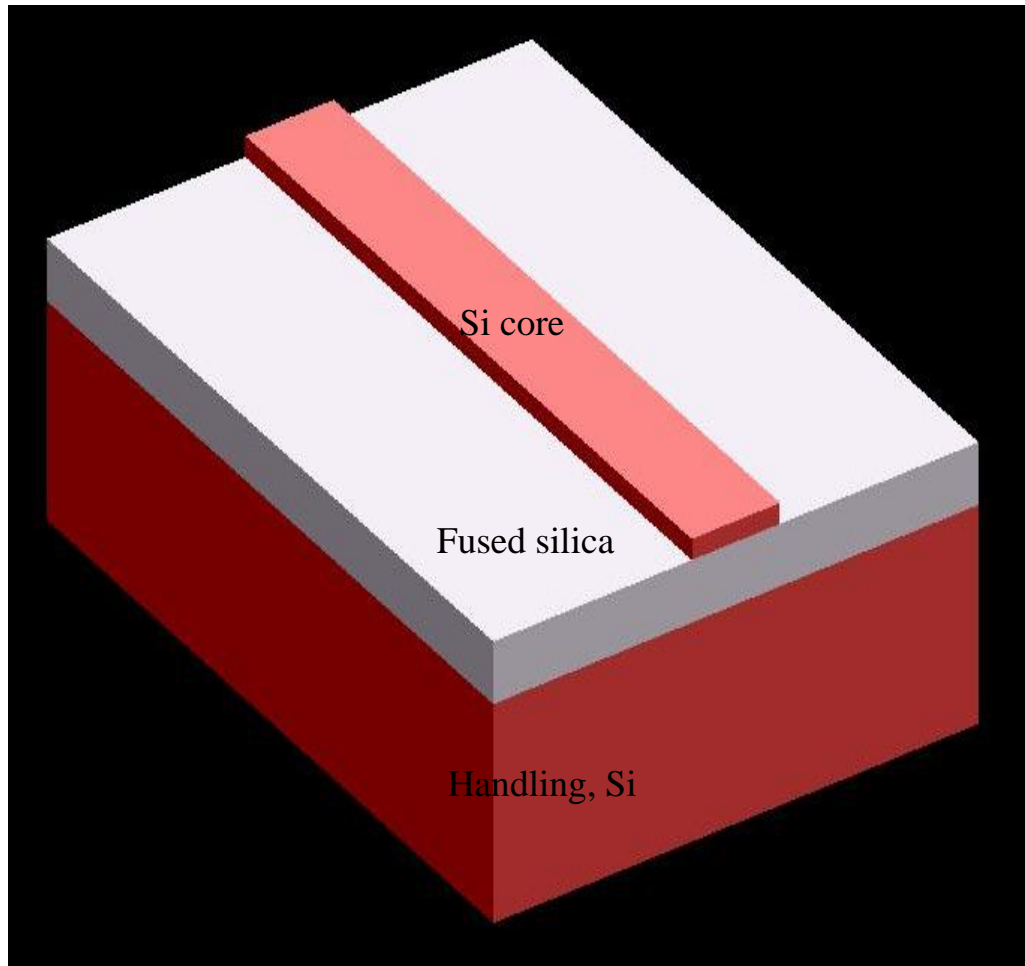


*Figure 7.1: Schematic diagram of Silicon-on-Insulator sample.*

In this work, the SOI wafer used has a  $0.50\ \mu\text{m}$  thick layer of the Si core, a lower cladding layer of  $\text{SiO}_2$  of  $3\ \mu\text{m}$  thick and bulk Si substrate as shown in the figure 7.1. Firstly, the four inch wafer was cleaved into 12 mm by 12 mm samples. The cleaved sample was cleaned using acetone, methanol and IPA, blow dried with nitrogen gas and baked for 60 seconds on a hotplate before the Hydrogen silsesquioxane (HSQ) was spun. Neat HSQ was spun at the

speed of 5000 rpm which leaves thickness of 340 nm on the sample. The sample was baked again at 95<sup>0</sup>C on a hotplate for four minutes and then submitted for writing.

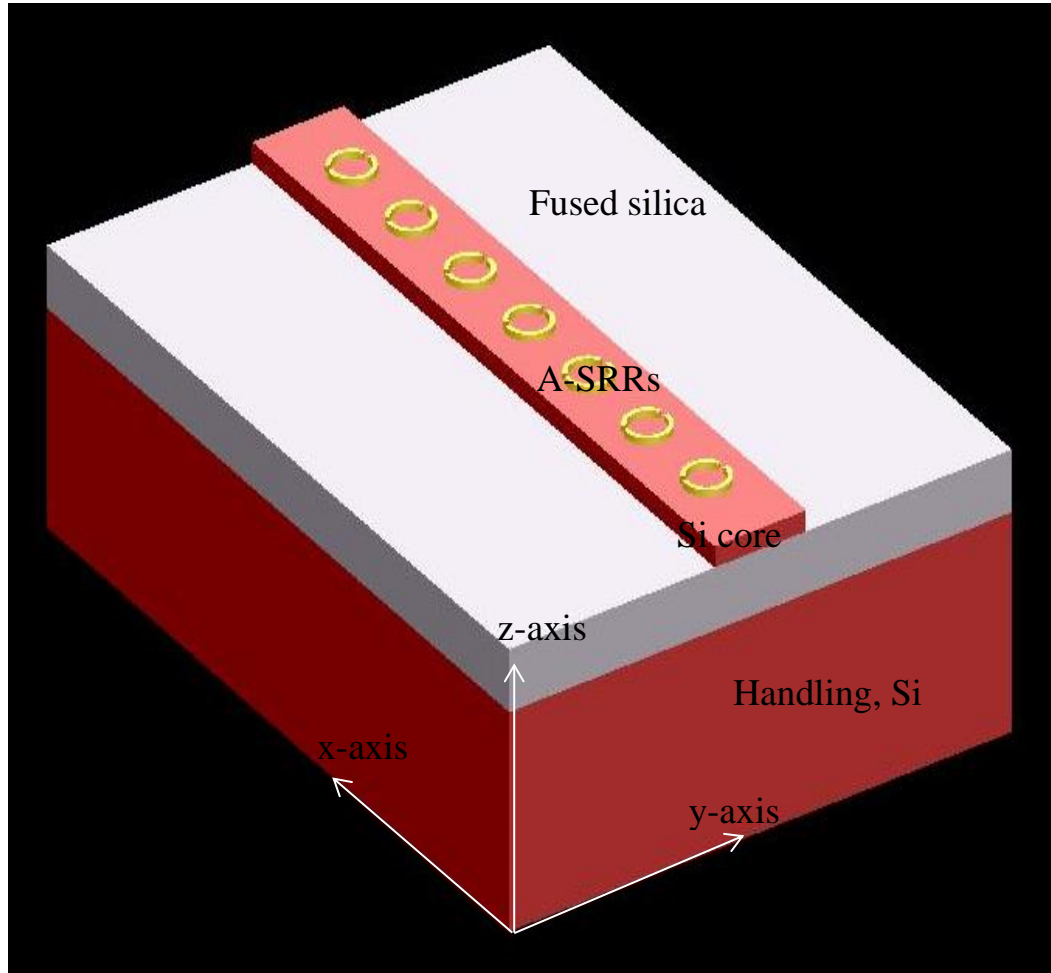


**Figure 7.2:** Sketch gold A-SRRs on waveguide of silicon-on insulator (SOI) substrate.

The device designed has arrays of A-SRRs on top of an SOI waveguide. The design concept is to couple light from the waveguide into the MM structures. The e-beam lithography of this design is complex due the alignment of the A-SRRs structure that has to be at the centre of the waveguide width. The lithography was performed twice with the use of different layers/colours for differentiating the design in L-Edit. Use of global makers which comprises of Au squares and crosses was essential to achieve the designed patterns as shown in figure 7.3a. The substrate cleaning was performed followed by spinning of two different resists. A

PMMA resist was used for creating the markers and A-SRRs on the SOI sample. After development and metallization, the sample was processed again for the second layer of lithography. HSQ resist was spun for the waveguide pattern transfer, baked and submitted for ebeamwriter exposure as explained in the last paragraph.

In the cleanroom, a Surface Technology System (STS) tool was used for the plasma dry etch where high density low pressure (HDLP) method for etching SOI was applied. The HDLP used was generated by excitation of inductively coupled plasma (ICP) on the STS equipment. The major benefit of operating in HDLP plasma mode is the reduction in ion collision probability as the sheath thickness decreases at higher ion density and the ion mean free path increases at lower pressures with improved ion directionality which enhances the control of anisotropy [10]. The present work has been carried out in the STS-ICP system as described in the literature [10, 11]. A reactive ion etch (RIE) employed utilizes the mix etch process, which exhibit no scalloping on etched sidewalls [12]. This process provides vertical sidewall profile with very smooth surface where the etching stops over SiO<sub>2</sub> layer on SOI substrate as shown in figure 7.3. The mixed etch process involves alternating between a Si etch step and a fluoropolymer deposition. The gases used were sulphur hexafluoride (SF<sub>6</sub>) for Si etch step and halocarbon R318 (C<sub>4</sub>F<sub>8</sub>) for deposition. The recipe on the JWNC dry etch processing webpage [12-13] was used as a starting point and changes were made to achieved device shown in figure 7.3.

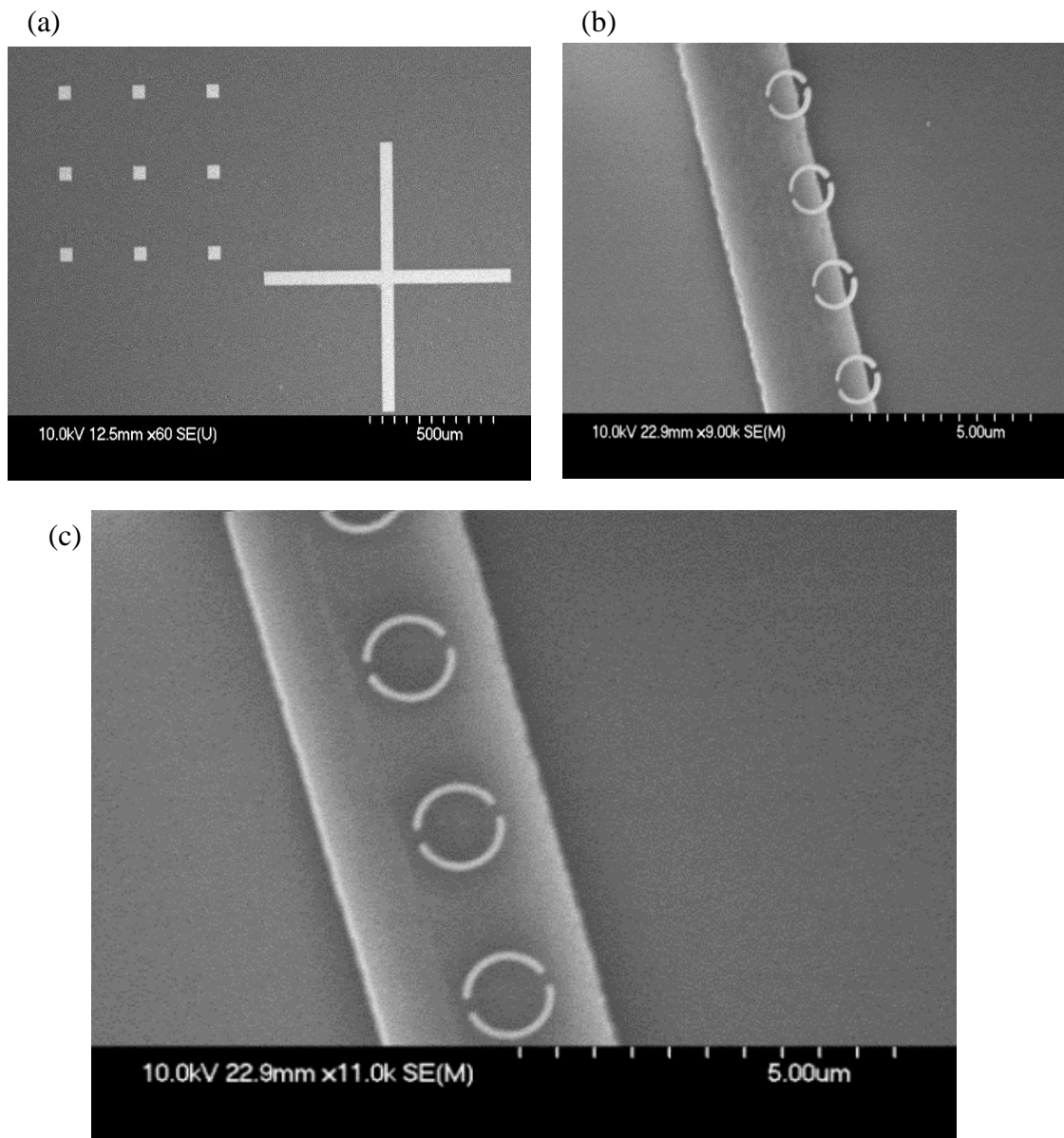


**Figure 7.3:** SEM images of (a) Global makers with cross (b) Misaligned A-SRRs on waveguide (c) Aligned A-SRRs on waveguide.

The etching parameters were set to: a temperature of 23<sup>0</sup>C, etching chamber pressure of 10 mT, flow rate of 30 sccm and RF power level 300 W. The etching time was set to 3.2 minutes, which was sufficient to etch through the 500 nm silicon core layer. The etching time increased here because the core layer of the wafer used here is 500 nm thick with 3 μm layer of SiO<sub>2</sub>. The SEM image in the figure 7.3b showed misaligned patterns which were corrected in the L-Edit and beamer software design by maintaining the central point of the entire pattern design in both software. Figure 7.3c shows SEM image of the aligned A-SRRs on the waveguide corresponding to the schematic diagram.

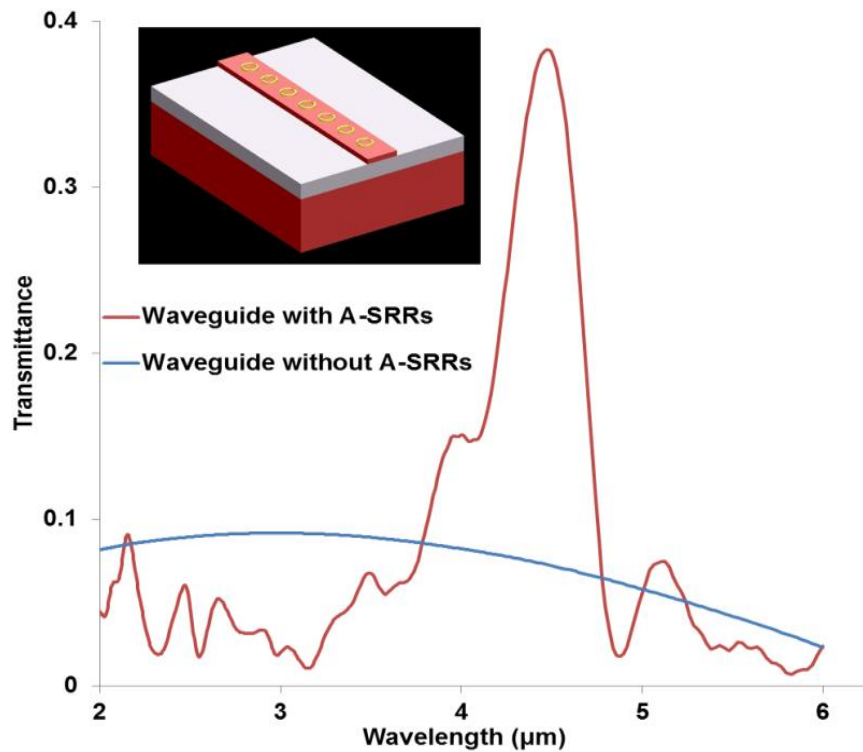
Lumerical software was used to design silicon on insulator (SOI) waveguide on which the A-SRRs was designed on top of the waveguide as shown in figure 7.2. The thickness of the structure was designed based on SOI sample used for fabrications with the silicon core of 500 nm, fused silica of 3  $\mu\text{m}$  and the handling layer of 750  $\mu\text{m}$ .

The effective refractive index ( $n_{\text{eff}}$ ) is an important material property for this type of design. The  $n_{\text{eff}}$  depends on the wavelength and mode (for multimode waveguides) in which the light propagates. This was calculated using Lumerical software for the designed waveguides for the device as shown in figure 7.4. The  $n_{\text{eff}}$  also depends on the whole waveguide design and can be defined as number that quantifies the phase delay per unit length in a waveguide, relative to the phase delay in vacuum or air.

Waveguide width ( $\mu\text{m}$ )	Effective index	Loss (db/cm)	Modal field plots
1	$2.52+3.51 \times 10^{-11}i$	$6.38 \times 10^{-6}$	
2	$2.82+2.29 \times 10^{-11}i$	$4.17 \times 10^{-6}$	
3	$2.87+2.18 \times 10^{-11}i$	$3.97 \times 10^{-6}$	

**Figure 7.4:** Dimension of waveguide width (y-axis), effective index, loss and modal field plots for electric component

The modal field plot included in the table is the fundamental mode refers to as first mode in Lumerical as detailed in appendix D. The colour coding bar where dark red is the maximum and dark blue is the minimum shows the modal field strength. The fundamental mode was generated by propagation of mode source of EM wave through a silicon waveguide with depth of 0.5  $\mu\text{m}$  but at varying widths (1, 2 and 3)  $\mu\text{m}$  as shown in the table. The propagation described by the mode takes place at a fixed frequency. The fixed frequency of the fundamental mode of the device is known as its resonant frequency. The resonant frequency or wavelength for the propagating modes of (2 to 6)  $\mu\text{m}$  as applied here is at wavelength of 3  $\mu\text{m}$  and this wavelength depends on the structure, materials and boundary conditions. The waveguide width of 3  $\mu\text{m}$  which gives the least loss of  $3.97 \times 10^{-6}$  db/cm for the propagating modes was width used for the fabrication. The loss is from the effective index which is shown as a complex quantity. This is produced by the imaginary part of the complex quantity which describes the gain or loss effective refractive index. The loss increases as the width of the waveguide reduces and this corresponds to increase in then imaginary part, as stated in the figure 7.4. Reference [14] also explains the loss as a mode profile mismatch between the mode that actually exists at that wavelength and the mode profile of the centre wavelength that is being injected. The errors will be largest at the minimum and maximum wavelength of the source where the mode mismatch is largest. This investigation will help for future work on simulation validation with preliminary simulations shown in figure 7.5 and measurement of the fabricated A-SRR on waveguide. Advancements with the use of SOI will support the development of portable photonic sensors systems suitable for field work.



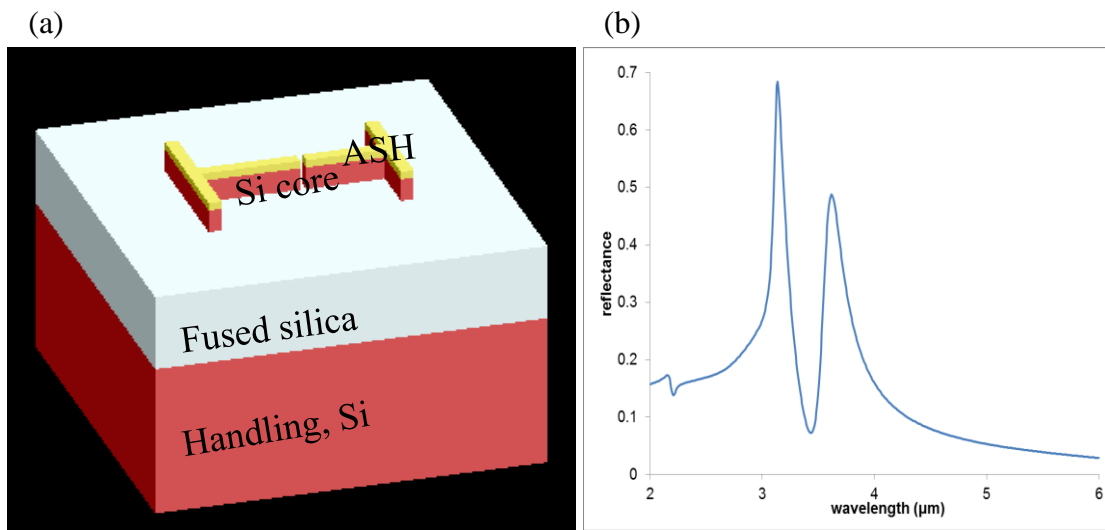
*Figure 7.5: Transmittance spectra showing plasmonic peaks from waveguide with A-SRRs and no resonance from waveguide without A-SRRs with design inset.*

Figure 7.5 shows the transmittance spectra from simulation of the designed A-SRRs on SOI waveguide. There is a production of strong plasmonic resonance peak from the simulation of A-SRRs on waveguide while no resonance appears for waveguide without A-SRRs structure when a mode source was coupled into the waveguide. This result shows the tuning ability of the designed A-SRR dimension that produced plasmonic resonance peaks between (2-6)  $\mu\text{m}$ . The dimension of the A-SRRs is radius of 0.5  $\mu\text{m}$  by 0.4  $\mu\text{m}$  with height of 100 nm. Future work will be on measurement of the fabricated device and validating on the simulation of the design. The work was established based on high Q-factor produced by all-dielectric metamaterial using SOI as presented in reference [15].

### **Simulation of ASH on SOI**

An ASH structure was also modelled on SOI substrate as shown in figure 7.6a. The objective of this modelling is to get a high Q and enhancement factors. Following similar dimension for

the design of ASH on fused silica as explained, the preliminary result from the simulation of the design produced a narrowed resonance peaks as shown in figure 7.6b.



**Figure 7.6:** (a) 3-D schematic diagram of split H-shaped structure on SOI (b) Reflectance spectra showing double plasmonic peaks from ASH simulation for a normal incidence source.

This idea comes from studying the work of reference [15]. In the reference all-dielectric silicon-based metasurface was produce with high Q-factors. Here, metal is included because it is the basis for high enhancement factors which is important factors for this type of sensors. This is an introductory design for future works on MM structures.

## 7.2 Conclusion

In this thesis, photonic sensors based metamaterial devices have been designed, fabricated and applied in detection of a biological analyte 17 $\beta$ -estradiol. In order to produce a high quality factor and sensitive sensor device different features of the two common types of metallic metamaterial, asymmetric split ring resonators (A-SRRs) and Dipoles were characterized. In the course of this work, structures such as the A-SRRs and asymmetric split H-shaped (ASH) have also been investigated. The work on A-SRRs and ASH on waveguide is as part of the optimization process for the design of the metallic metamaterial towards producing a high quality factor sensor device. An asymmetric split H-shaped ASH structure has been introduced as a new metallic metamaterial device. Utilization of dual polarization source has been shown to be possible for the ASH structures. These optimized structures could be useful in sensing and monitoring environment, food, security and biochemical substances. All the devices described in the present work were fabricated using two different material substrates, fused silica (SiO<sub>2</sub>) and Silicon on insulator (SOI).

The devices presented in this thesis were fabricated mostly by using fabrication processes which comprise of electron beam lithography (e-beam), pattern development, metallization and dry etching. Some of the processes applied to produce the patterns were partly modified from the existing process and developed during the course of the project. The process for the SOI material were more challenging and etching quality could not be reproduced regularly simply by using the same conditions. Solutions were adopted to minimize the effects of chamber conditions in the fabrication process by submitting the sample for etching before the busy period and use of an interferometer also helped to produce the correct etch depth. Again alignment of the A-SRR pattern on the silicon waveguide of the SOI material was a major difficulty but was resolved by proper redesign of the device in the software. The process for SOI has been demonstrated to have the potential for good reproducibility with acceptable tolerances in producing waveguide devices. The two gases Halocarbon R318 (C<sub>4</sub>F<sub>8</sub>) and SF<sub>6</sub> used for the dry-etch process for the silicon etchings are stable and capable of repeatable etching rates.

Devices fabricated on fused silica show small imperfections in the final device structure. The roughness of the ring shape was smoothed and the sharp edges of the patterns were produced by using the proximity grid command on the beamer fracturing tool.

Also included in the work is the analysis of the theoretical concepts of the devices based on references [16-17]. The photonic sensor based plasmonic resonance peaks produced from metallic metamaterial device was the basis of this project; the operating principle of the device was described, demonstrating how the resonance peaks can be used to sense changes in the surrounding device environment. The developed sensors device prompts a shift in the resonance peak with respect to the refractive index change.

The numerical simulation tool used to model and design the different photonic structures has been described and the results obtained for different metallic metamaterial device designed have been analysed and compared in various ways. The 3D approach used in the simulations gives good and consistent results of the designed structures as compared with the experimental work. A logical sequence was followed. The optimization of the A-SRRs for a narrower reflectance plasmonic resonance which can produce a high quality factor is an important characteristic of all plasmonic devices useful for sensing applications. In the numerical simulation the artefact from grating order transmission of a periodic structure can affect the resonance peak. The ASH structure designed from the dipoles was optimized and showed improvement in the reflectance resonance compared with the asymmetric dipole structure.

The fabricated devices that could not be measured during the course of this work are because of the lack of suitable measurement set-up and limitations of time. A super-continuous source and grating couplers or end-fire rig could be required for the A-SRRs on SOI waveguide. The recent advancement of designing MM structures using SOI material can minimize losses and it is a good platform for developing a portable photonic sensors system suitable for field work.

In conclusion, three different metallic metamaterial structures have been presented, with promising results from experiment and simulation. The parameters of the structures such as the dimension and periodicity have been described and optimized to produce a high quality device in the mid-infrared region. The A-SRRs and ASH on SOI waveguide were also presented as other work carried out during the period. The numerical simulations of the designed structures and fabrication can form the base of future work. One of the aims of this project is to produce a high quality factor from the metallic metamaterial and demonstrate its ability by using  $17\beta$ -estradiol to analyse a molecular resonance C-H. This has been achieved. Finally, all MM devices presented in this thesis are optimally designed for sensing application in mid-infrared as discussed.

## 7.3 References

1. G. K. Celler, S. Cristoloveanu, "Frontiers of silicon-on-insulator," J Appl Phys, 9, 4955-4978, 2003.
2. G. K. Celler, Silicon-on-Insulator Structures: Fabrication, the Encyclopedia of Advanced Materials ~Pergamon, New York, 1994.
3. S. Cristoloveanu and S. S. Li, Electrical Characterization of Silicon on Insulator Materials and Devices ~Kluwer, Boston, 1995.
4. J.-P. Colinge, Silicon-on-Insulator Technology: Materials to VLSI, 2nd ed. ~Kluwer, Boston 1997.
5. A. Marshall and S. Natarajan, "SOI design: analog, memory and digital techniques," Boston: Kluwer, 2002.
6. S. J. McNab, N. Moll, and Y.A. Vlasov, "Ultra-low loss photonic integrated circuit with membrane-type photonic crystal waveguides," Optics express, 11, 2927-2939, 2003.
7. A. R Md Zain, N. P. Johnson, M. Sorel, R. M De La Rue, "Ultra high quality factor one dimensional photonic crystal/photonic wire micro-cavities in silicon-on-insulator (SOI)," Optics express 16, 12084-12089, 2008.
8. C. V. Poulton, X. Zeng, M. T. Wade, J. M. Shainline, J. S. Orcutt and M. A. Popovic', "Photonic Crystal Microcavities in a Microelectronics 45 nm SOI CMOS Technology," IEEE Photonics Technology Letters, 10, 2014.
9. J.-P. Colinge, "Silicon-on-Insulator Technology: Materials to VLSI," Berlin: Springer Verlag, 1991.
10. J.K. Bhardwaj., H. Ashraf., "Advanced Silicon Etching Using High Density Plasmas" Proc. SPIE Micromachining and Microfabrication Process Technology, 2639, 224-233, 1995.
11. J. Bhardwaj, H. Ashraf, A. McQuarrie, "Dry silicon etching for MEMS," The Symposium on Microstructures and Microfabricated Systems at the Annual Meeting of the Electrochemical Society, 1997.
12. <http://jwnc.eng.gla.ac.uk/index.php?module=dryetch>.
13. M. M. Mirza, "Nanofabrication of silicon nanowires and nanoelectronic transistors," PhD thesis, University of Glasgow, 2015.

14. [https://kb.lumerical.com/en/index.html?ref\\_sim\\_obj\\_mode\\_source\\_-\\_broadband.html](https://kb.lumerical.com/en/index.html?ref_sim_obj_mode_source_-_broadband.html), 2016.
15. Y. Yang, I. I. Kravchenko, D. P. Briggs and J Valentine, "All-dielectric metasurface analogue of electromagnetically induced transparency," *Nature communications*, 5, 2014.
16. J. B. Pendry, A. J. Holden, D. J. Robbins, and W. J. Stewart, "Magnetism from Conductors and Enhanced Nonlinear Phenomena," *IEEE transactions on microwave theory and techniques*, **47**, 2075-2084, 1999.
17. V. G. Veselago, "The electrodynamics of substances with simultaneously negative values of permittivity and permeability," *Soviet Physics Uspekhi*, **10**, 509-514, 1968.

# APPENDIX

## A: Modelling

### A1: Drude model

Drude model is the method employed for the transport properties of electron in the material such as gold [1-3]. For conductors in which inter-band contributions to the optical functions can be largely neglected in the infrared, the simple Drude dielectric function can be used:

$$\epsilon_1 = \epsilon_0 - \frac{\omega_p^2}{[\omega^2 + (1/\tau)^2]}$$

(a)

$$\epsilon_2 = \frac{(1/\tau\omega)\omega_p^2}{\omega^2 + (1/\tau)^2}$$

Here  $\omega_p$  is the plasma frequency,  $\tau$  is the relaxation time, and  $\epsilon_0$  is a background dielectric function, constant in the infrared, which arises from transitions at higher energy.

### A2: Optical properties for fused silica

The optical dispersion of fused silica can be approximated by the following Sellmeier equation [4].

$$\epsilon = n^2 = 1 + \frac{0.70\lambda^2}{\lambda^2 - 0.07^2} + \frac{0.41\lambda^2}{\lambda^2 - 0.12^2} + \frac{0.81\lambda^2}{\lambda^2 - 9.90^2} \quad (b)$$

The wavelength  $\lambda$  is measured in micrometres. This equation is valid between 0.21 and 3.71 micrometres and at 20 °C [6]. Its validity was confirmed for wavelengths up to 6.7  $\mu\text{m}$  [5]. Experimental data for the real (refractive index) and imaginary (absorption index) parts of the complex refractive index of fused quartz reported in the literature over the spectral range from 30 nm to 1000  $\mu\text{m}$  has been reviewed by Kitamura et al [5] and are used for simulations.

## B: FDTD simulations

### B1: A-SRR arcs length variation

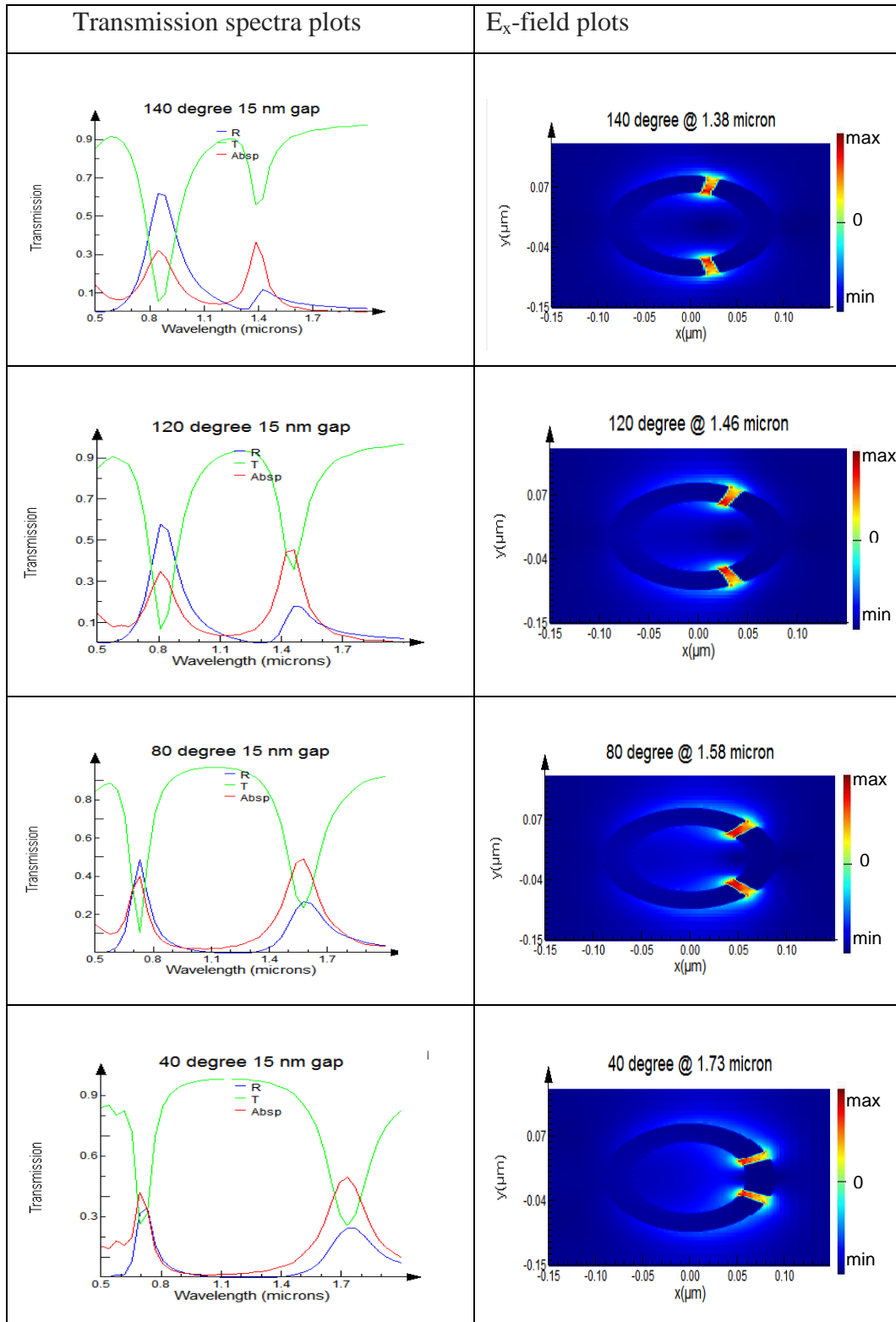


*Figure 1: Transmission spectra plots and  $E_x$ -field plots from more symmetric to less symmetric A-SRRs*

The transmission plots in the first column and first row of figure 1 where R is reflectance, T is transmittance and Absp is absorption, demonstrated the plots in reference [6]. The dip between the two plasmonic peaks broadens or the coupling between the arcs is reduced as they become more asymmetric. In the second column of the figure, electric field plots of the x-component is use to show the confinement of the e-field intensity at the 15 nm gap.

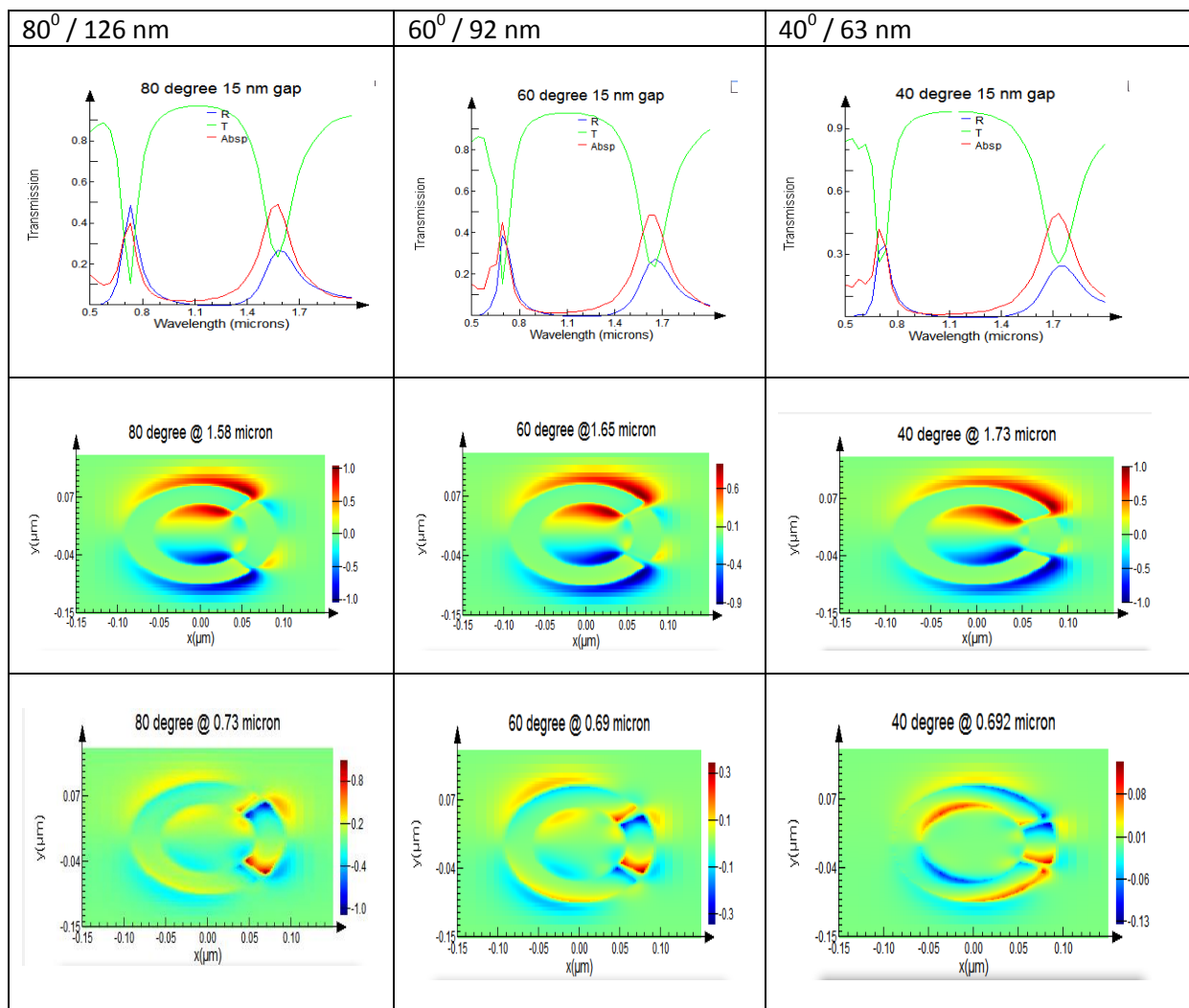


**Figure 2:** Transmission spectra and z-components of the E-field plots from the two peaks

Figure 2 first rows show the transmission plots of the more asymmetric arcs where the small arc is, 40°, 60° and 80° with the corresponding arcs length of 63 nm, 92 nm and 126 nm, respectively. The e-field plots of the z-components are shown in the subsequent rows based

on the resonance peaks from the longer to shorter wavelength as stated on the top of the plots. The plots are in agreement with that in reference [6] where field strength at longer wavelength is greater than that at shorter wavelength. The simulation results are included in appendix because it's on visible to near-infrared region.

### **C: 17 $\beta$ -estradiol experiment and simulation**

Experiment for the four different concentration of E2

A glass experimental bottle with cover of 16 g was used for mixing the E2 and ethanol. Then 1 ml of ethanol was used to dissolve (0.0001, 0.001, 0.01 and 1) g of E2.

Calculation of the molarity of the solution (E2 and ethanol)

Steps:

Molar mass of E2 = 272.382g

272.382g in 1 litre = 1 mole

Convert the 1ml of ethanol to gram, will be 1 g

Experiment (a): E2 = 0.0001g

If 272.382g of E2 = 1 mole

Then 0.0001g = ? mole

$$Ans = \frac{0.0001}{272.382} \sim 3.67 \times 10^{-7} \text{ mole}$$

For 1.0001 mL solution (E2 and ethanol)

$$Molarity = \frac{3.67 \times 10^{-7}}{0.0010001} = 3.67 \times 10^{-4} \text{ mole/litre}$$

Ans  $\sim$  0.37  $\mu$ m/mL

Experiment (b): E2 = 0.001g

If 272.382g of E2 = 1 mole

Then 0.001g = ? mole

$$\text{Ans} = \frac{0.001}{272.382} \sim 3.67 \times 10^{-6} \text{ mole}$$

For 1.001 mL solution (E2 and ethanol)

$$\text{Molarity} = \frac{3.67 \times 10^{-6}}{0.001001} = 3.67 \times 10^{-3} \text{ mole/litre}$$

Ans ~ 3.7  $\mu\text{m}/\text{mL}$

Experiment (c): E2 = 0.01g

If 272.382g of E2 = 1 mole

Then 0.01g = ? mole

$$\text{Ans} = \frac{0.01}{272.382} \sim 3.67 \times 10^{-5} \text{ mole}$$

For 1.01 mL solution (E2 and ethanol)

$$\text{Molarity} = \frac{3.67 \times 10^{-5}}{0.00101} = 3.67 \times 10^{-2} \text{ mole/litre}$$

Ans ~ 36  $\mu\text{m}/\text{mL}$

Experiment (d): E2 = 0.1g

If 272.382g of E2 = 1 mole

Then 0.1g = ? mole

$$\text{Ans} = \frac{0.1}{272.382} \sim 3.67 \times 10^{-4} \text{ mole}$$

For 1.001 mL solution (E2 and ethanol)

$$\text{Molarity} = \frac{3.67 \times 10^{-4}}{0.00101} = 3.336 \times 10^{-1} \text{ mole/litre}$$

Ans ~ 334  $\mu\text{m}/\text{mL}$

## C1 Sensitivity Calculations

The sensitivity for the four experiments was also calculated from figures 6.10 (a-d):

$S = \frac{\Delta\lambda}{\Delta n}$  ( $\text{nm}/\text{RIU}$ ) Where  $\Delta\lambda$  is the plasmonic resonance peak shift and  $\Delta n$  is change in the refractive index of the analyte and air.

Experiment (a): 0.37  $\mu\text{mole}/\text{mL}$

$$s = \frac{3872 - 3586}{1.46 - 1} = 621.7 \sim 622 \text{ nm}/\text{RIU}$$

Experiment (b): 3.7  $\mu\text{mole}/\text{mL}$

$$s = \frac{4055 - 3586}{1.46 - 1} = 1019.6 \sim 1020 \text{ nm}/\text{RIU}$$

Experiment (c): 36  $\mu\text{mole}/\text{mL}$

$$s = \frac{4380 - 3586}{1.46 - 1} = 1726 \text{ nm}/\text{RIU}$$

Experiment (d): 334  $\mu\text{mole}/\text{mL}$

$$s = \frac{4870 - 3586}{1.46 - 1} = 2791 \text{ nm}/\text{RIU}$$

## C2 Enhancement factors Calculations

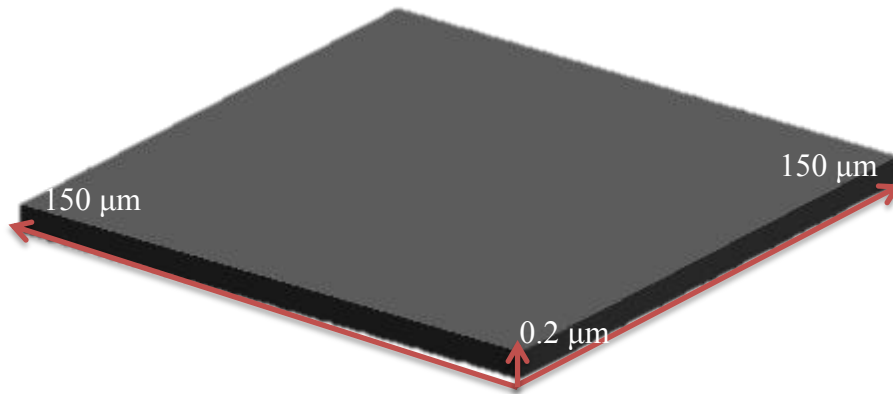


Figure 3: Schematic diagram for volume of (150 by 150 by 0.2)  $\mu\text{m}$  E2 measured

The volume was used to calculate the enhancement factor for the experiments of figures 6.12 (a-d).

$$E_f = \frac{\Delta V_2 / N_2}{\Delta V_1 / N_1}$$

Where  $N$  is total number of molecules and  $\Delta V$  is change in the amplitude of the molecular resonance detailed in chapter 6.  $N_1$  &  $\Delta V_1$  is measurement without ASH pattern while  $N_2$  &  $\Delta V_2$  is with ASH.

$$\text{Volume} = (150 \times 10^{-6} \times 150 \times 10^{-6} \times 200 \times 10^{-9}) \text{ m}^3 = 0.45 \times 10^{-14} \text{ m}^3 = 0.45 \times 10^{-11} \text{ litre}$$

Experiment (a): 0.37  $\mu\text{mole}$ / mL

This means that: 1 L contained  $0.37 \times 10^{-3}$  mole

$$0.45 \times 10^{-11} \text{ L contained } 1.665 \times 10^{-15} \text{ mole}$$

First calculating number of molecules without ASHs ( $N_1$ ):

$N_1$ :

$$1 \text{ mole} = 6.022 \times 10^{23} \text{ (Avogadro number)}$$

$$1.665 \times 10^{-15} \text{ mole} = ?$$

$$= 10.027 \times 10^8 \text{ molecules}$$

Secondly calculating number of molecules with ASHs ( $N_2$ ):

$N_2$ :

There are 5625 ASHs with periodicity of 2  $\mu\text{m}$  in an area of (150 by 150)  $\mu\text{m}$ .

Area of hot-spots is (10 by 10) nm = 100 nm<sup>2</sup> from reference [8].

Total volume of excited molecules at the 4 hot spots as shown in the E-field plots of chapter 6:

$$(100 \times 4) \times 10^{-18} \times 5625 \times 200 \times 10^{-9} = 0.45 \times 10^{-18} \text{ m}^3 \text{ or } 0.45 \times 10^{-15} \text{ L}$$

$$1 \text{ L} \quad \text{contained} \quad 0.37 \times 10^{-3} \text{ mole}$$

$$0.45 \times 10^{-15} \text{ L} \quad \text{contained} \quad 1.665 \times 10^{-19} \text{ mole}$$

Calculating number of molecules:

$N_2$ :

$$1 \text{ mole} = 6.022 \times 10^{23} \text{ (Avogadro number)}$$

$$1.665 \times 10^{-19} \text{ mole} = ?$$

$$10.027 \times 10^4 \text{ molecules}$$

$$(\text{Absolute value per unit area})E_f = \frac{\Delta V_2/N_2}{\Delta V_1/N_1}$$

$\Delta V_1$	$\Delta V_2$	$N_1$	$N_2$
0.0013	0.011	$10.027 \times 10^8$	$10.027 \times 10^4$

$$(\text{Absolute value per unit area})E_f = \frac{\Delta V_2/N_2}{\Delta V_1/N_1} = \frac{1.097 \times 10^{-7}}{1.296 \times 10^{-12}} = 8.464 \times 10^4$$

Experiment (b): 3.7 μmole/ mL

1 L contained  $3.7 \times 10^{-3}$  mole

$0.45 \times 10^{-11}$  L contained  $1.665 \times 10^{-14}$  mole

$N_1$ :

1 mole =  $6.022 \times 10^{23}$  (*Avogadro number*)

$1.665 \times 10^{-14}$  mole =?

=  $10.027 \times 10^9$  molecules

$N_2$ :

1 L contained  $3.7 \times 10^{-3}$  mole

$0.45 \times 10^{-15}$  L contained  $1.665 \times 10^{-18}$  mole

Calculating number of molecules:

1 mole =  $6.022 \times 10^{23}$  (*Avogadro number*)

$1.665 \times 10^{-18}$  mole =?

$10.027 \times 10^5$  molecules

$\Delta V_1$	$\Delta V_2$	$N_1$	$N_2$
0.00237	0.06225	$10.027 \times 10^9$	$10.027 \times 10^5$

$$(\text{Absolute value per unit area})E_f = \frac{\Delta V_2/N_2}{\Delta V_1/N_1} = \frac{6.208 \times 10^{-8}}{2.364 \times 10^{-13}} = 2.626 \times 10^5$$

Experiment (c): 36 μmole/ mL

1 L contained  $36 \times 10^{-3}$  mole

$0.45 \times 10^{-11}$  L contained  $1.62 \times 10^{-13}$  mole

$N_1$ :

1 mole =  $6.022 \times 10^{23}$  (*Avogadro number*)

$1.62 \times 10^{-13}$  mole =?

=  $9.756 \times 10^{10}$  molecules

N<sub>2</sub>:

1 L contained 36 x 10<sup>-3</sup> mole

0.45 x 10<sup>-15</sup> L contained 1.62 x 10<sup>-17</sup> mole

Calculating number of molecules:

1 mole = 6.022 x 10<sup>23</sup> (*Avogadro number*)

1.62 x 10<sup>-17</sup> mole =?

9.756 x 10<sup>6</sup> molecules

$\Delta V_1$	$\Delta V_2$	$N_1$	$N_2$
0.0081	0.106	9.756 x 10 <sup>10</sup>	9.756 x 10 <sup>6</sup>

$$(\text{Absolute value per unit area})E_f = \frac{\Delta V_2/N_2}{\Delta V_1/N_1} = \frac{0.011 \times 10^{-6}}{8.303 \times 10^{-14}} = 1.325 \times 10^5$$

Experiment (d): 334 μmole/ mL

1 L contained 334 x 10<sup>-3</sup> mole

0.45 x 10<sup>-11</sup> L contained 1.5 x 10<sup>-12</sup> mole

N<sub>1</sub>:

1 mole = 6.022 x 10<sup>23</sup> (*Avogadro number*)

1.5 x 10<sup>-12</sup> mole =?

= 9.033 x 10<sup>11</sup> molecules

N<sub>2</sub>:

1 L contained 334 x 10<sup>-3</sup> mole

0.45 x 10<sup>-15</sup> L contained 1.5 x 10<sup>-16</sup> mole

Calculating number of molecules:

1 mole = 6.022 x 10<sup>23</sup> (*Avogadro number*)

$$1.5 \times 10^{-16} \text{ mole} = ?$$

$$9.033 \times 10^7 \text{ molecules}$$

$\Delta V_1$	$\Delta V_2$	$N_1$	$N_2$
0.018	0.027	$9.033 \times 10^{11}$	$9.033 \times 10^7$

$$(\text{Absolute value per unit area})E_f = \frac{\Delta V_2/N_2}{\Delta V_1/N_1} = \frac{2.989 \times 10^{-10}}{1.993 \times 10^{-14}} = 1.50 \times 10^4$$

An estimated density of  $1 \times 10^6 \text{ g/cm}^3$  was used also to calculate the  $E_f$  of experiment (b):

$$\text{Density} = \frac{\text{mass}}{\text{volume}}$$

Experiment (b):  $3.7 \mu\text{mole/mL}$

$$\text{Volume without ASHs} = (150 \times 10^{-6} \times 150 \times 10^{-6} \times 200 \times 10^{-9}) \text{ m}^3 = 0.45 \times 10^{-14} \text{ m}^3$$

$$\text{Volume with ASHs} = (100 \times 4) \times 10^{-18} \times 5625 \times 200 \times 10^{-9} = 0.45 \times 10^{-18} \text{ m}^3$$

$$\begin{aligned} \text{Mass without ASHs} &= \text{Density} \times \text{volume} \\ &= 1 \times 10^6 \text{ g/m}^3 \times 0.45 \times 10^{-14} \text{ m}^3 \\ &= 0.45 \times 10^{-8} \end{aligned}$$

$$\begin{aligned} \text{Mass with ASHs} &= 1 \times 10^6 \text{ g/m}^3 \times 0.45 \times 10^{-18} \text{ m}^3 = \\ &0.45 \times 10^{-12} \end{aligned}$$

$$\text{Number of molecules} = \frac{\text{Mass} \times \text{Avogadro number}}{\text{Molecular weight}}$$

$$N_1 = \frac{0.45 \times 10^{-8} \times 6.022 \times 10^{23}}{272.382} = 9.9489 \times 10^{12}$$

$$N_2 = \frac{0.45 \times 10^{-12} \times 6.022 \times 10^{23}}{272.382} = 9.9489 \times 10^8$$

$\Delta V_1$	$\Delta V_2$	$N_1$	$N_2$
0.00237	0.06225	$9.9489 \times 10^{12}$	$9.9489 \times 10^8$

$$(Absolute\ value\ per\ unit\ area)E_f = \frac{\Delta V_2/N_2}{\Delta V_1/N_1} = 2.626 \times 10^5$$

The relative values for a normalized source to gold mirror give unity i.e. 1

But the unmodulated values for the measurements of ASH ( $V_{02}$ ) and fused silica substrates ( $V_{01}$ ) were taken:

$$(Relative\ value\ per\ unit\ area)E_f = \frac{(\Delta V_2/V_{02})/N_2}{(\Delta V_1/V_{01})/N_1}$$

In this work the relative value per unit area for experiment (b) which showed the highest  $E_f$  from absolute value was calculated.

**Table A:** The tabulated values are obtained from measurements:

Wavelength ( $\mu\text{m}$ )	Fused silica substrate	ASHs structure
3.42026	0.03835	0.52794
3.44801	0.03598	0.59019

- For substrate  $\Delta V_1 = 0.03835 - 0.03598 = 0.00237$
- For ASH  $\Delta V_2 = 0.59019 - 0.52794 = 0.06225$

$\Delta V_1$	$V_{01}$	$\Delta V_2$	$V_{02}$	$N_1$	$N_2$
0.00237	0.03835	0.06225	0.59019	$10.027 \times 10^9$	$10.027 \times 10^5$

$$\frac{\Delta V_2}{V_{02}} = 0.105474$$

$$\frac{\Delta V_1}{V_{01}} = 0.061799$$

$$E_f = \frac{(\Delta V_2/V_{02})/N_2}{(\Delta V_1/V_{01})/N_1} = \frac{0.0105 \times 10^{-5}}{6.1633 \times 10^{-12}} = 1.704 \times 10^4$$

Calculation of enhancement factor per unit cell using simulation result with a close match to the experiment (b).

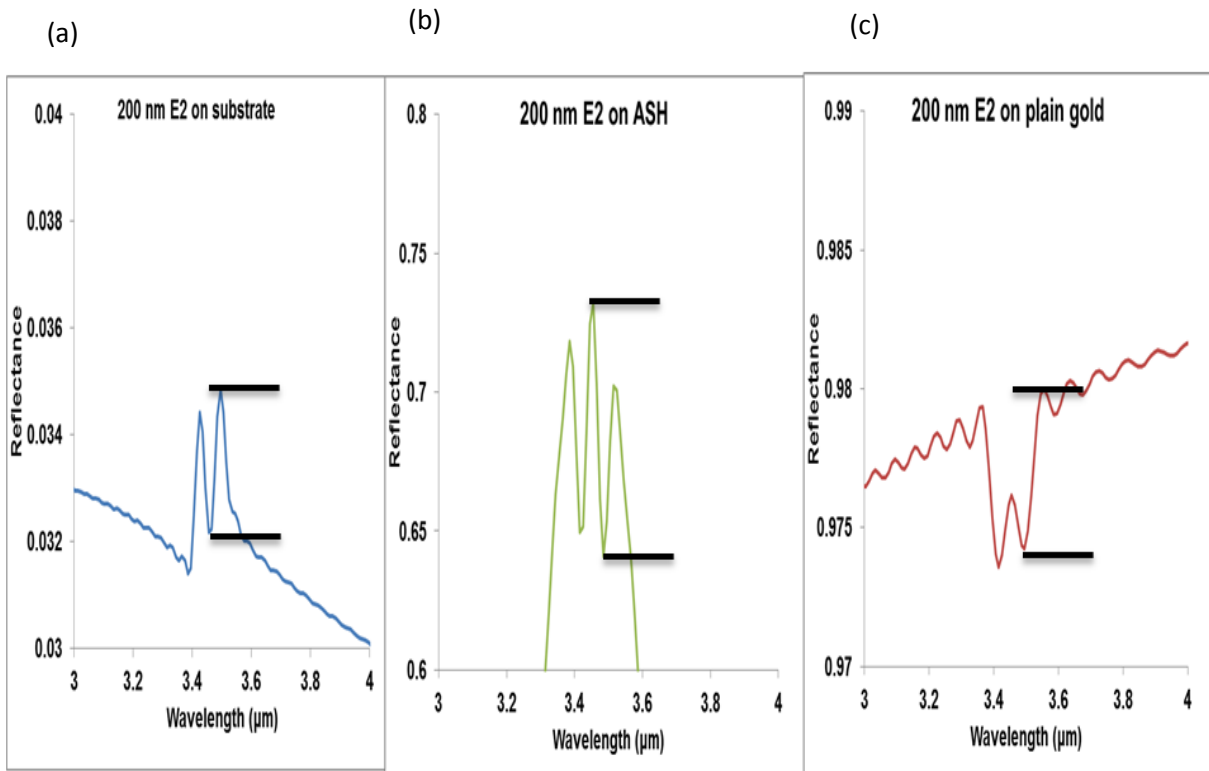


**Figure 4:** Reflectance spectra from simulation of 200 nm E2 thicknesses on (a) Fused silica substrate (b) ASHs structure (c) Plain gold.

Figure 4 shows the vibrational resonance peaks from simulation of E2 with dimensions of (2 x 2 x 0.2) μm. The black lines shows the minimum and maximum position of the reflectance peaks which were used to calculate the change in vibrational resonance for the  $E_f$ .

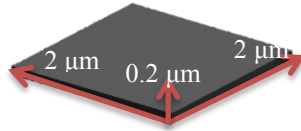


**Figure 5:** Schematic diagram for volume of (2 by 2 by 0.2)  $\mu\text{m}$  E2 simulated

**Table B:** Reflectance values from simulations of 200 nm on fused silica, ASH and gold

Wavelength (microns)	Fused silica substrate	ASH	Gold
3.45491	0.032174	0.732473	0.976155
3.48497	0.034329	0.64094	0.974377
3.54509	-	-	0.979818

a. For substrate  $\Delta V = 0.034329 - 0.032174 = 0.002155$

b. For ASH  $\Delta V = 0.732473 - 0.64094 = 0.091533$

c. For plain gold  $\Delta V = 0.979818 - 0.974377 = 0.036068$

Volume  $(2 \times 10^{-6} \times 2 \times 10^{-6} \times 200 \times 10^{-9}) \text{ m}^3 = 0.8 \times 10^{-18} \text{ m}^3 = 0.8 \times 10^{-15} \text{ litre i.e. } 0.8 \times 10^{-12} \text{ g}$

$$\text{Number of molecule } (N_1) = \frac{\text{mass} \times \text{Avogadro number}}{\text{molecular weight}} = \frac{0.8 \times 10^{-12} \times 6.022 \times 10^{23}}{272.382} =$$

$$1.8 \times 10^9 \text{ Molecules/unit cell}$$

For  $N_2$

$(100 \times 4) 10^{-18} \times 1 \times 200 \times 10^{-9} = 0.8 \times 10^{-22} \text{ m}^3 = 0.8 \times 10^{-19} \text{ litre i.e. } 0.8 \times 10^{-16} \text{ g}$

$$(N_2) = \frac{\text{mass} \times \text{Avogadro number}}{\text{molecular weight}} = \frac{0.8 \times 10^{-16} \times 6.022 \times 10^{23}}{272.382} = 0.0177 \times 10^7 = 1.7 \times$$

$10^5 \text{ Molecules/unit cell}$

$$(\text{Absolute value per unit area})E_f = \frac{\Delta V_2 / N_2}{\Delta V_1 / N_1}$$

For fused silica substrate:

$\Delta V_1$	$\Delta V_2$	$N_1$	$N_2$
0.002155	0.091533	$1.8 \times 10^9$	$1.7 \times 10^5$

$$E_f = \frac{0.054 \times 10^{-5}}{1.20 \times 10^{-12}} = 0.045 \times 10^7 = 4.5 \times 10^5$$

For plain gold:

$\Delta V_1$	$\Delta V_2$	$N_1$	$N_2$
0.036068	0.091533	$1.8 \times 10^9$	$1.7 \times 10^5$

$$E_f = \frac{0.054 \times 10^{-5}}{0.020 \times 10^{-9}} = 2.7 \times 10^4$$

$$(Relative\ value\ per\ unit\ area)E_f = \frac{(\Delta V_2/V_{02})/N_2}{(\Delta V_1/V_{01})/N_1}$$

For fused silica substrate:

$\Delta V_1$	$V_{01}$	$\Delta V_2$	$V_{02}$	$N_1$	$N_2$
0.002155	0.034329	0.091533	0.732473	$1.8 \times 10^9$	$1.7 \times 10^5$

$$E_f = \frac{0.0735 \times 10^{-5}}{0.0349 \times 10^{-9}} = 2.11 \times 10^4$$

For plain gold:

$\Delta V_1$	$V_{01}$	$\Delta V_2$	$V_{02}$	$N_1$	$N_2$
0.036068	0.979818	0.091533	0.732473	$1.8 \times 10^9$	$1.7 \times 10^5$

$$E_f = \frac{0.07351 \times 10^{-5}}{0.02045 \times 10^{-9}} = 3.69 \times 10^4$$

**C3 Limit of Detection (LOD) from modelling**

From the simulations the limit of detection of 0.15 femtomole of E2 was obtain per unit cell of the ASH modelled at periodicity of 2  $\mu\text{m}$ .

a.) 10 nm E2 thick

$$\text{Volume} = (2 \times 10^{-6} \times 2 \times 10^{-6} \times 10 \times 10^{-9}) \text{ m}^3 = 40 \times 10^{-21} \text{ m}^3 = 40 \times 10^{-15} \text{ g}$$

Molarity of E2 for 10 nm thickness:

Molar mass of E2: 272.382 g/mole

$$272.382 \text{ g} \dots\dots\dots 1 \text{ mole}$$

$$40 \times 10^{-15} \text{ g} \dots\dots\dots ? \text{ mole}$$

$$= 1.5 \times 10^{-16} \text{ mole} = 0.15 \text{ femtomole}$$

b.) 100 nm E2 thick

$$\text{Volume} = (2 \times 10^{-6} \times 2 \times 10^{-6} \times 100 \times 10^{-9}) \text{ m}^3 = 400 \times 10^{-21} \text{ m}^3 = 400 \times 10^{-15} \text{ g}$$

Molarity of E2 for 10 nm thickness:

Molar mass of E2: 272.382 g/mole

$$272.382 \text{ g} \dots\dots\dots 1 \text{ mole}$$

$$400 \times 10^{-15} \text{ g} \dots\dots\dots ? \text{ mole}$$

$$= 1.5 \times 10^{-15} \text{ mole} = 1.5 \text{ femtomole}$$

c.) 200 nm E2 thick

$$\text{Volume} = (2 \times 10^{-6} \times 2 \times 10^{-6} \times 200 \times 10^{-9}) \text{ m}^3 = 800 \times 10^{-21} \text{ m}^3 = 800 \times 10^{-15} \text{ g}$$

Molarity of E2 for 10 nm thickness:

Molar mass of E2: 272.382 g/mole

272.382 g ..... 1 mole

$800 \times 10^{-15}$  g ..... ? mole

$$= 2.9 \times 10^{-15} \text{ mole} = 3 \text{ femtomole}$$

d.) 400 nm E2 thick

$$\text{Volume} = (2 \times 10^{-6} \times 2 \times 10^{-6} \times 400 \times 10^{-9}) \text{ m}^3 = 1600 \times 10^{-21} \text{ m}^3 = 1600 \times 10^{-15} \text{ g}$$

Molarity of E2 for 10 nm thickness:

Molar mass of E2: 272.382 g/mole

272.382 g ..... 1 mole

$1600 \times 10^{-15}$  g ..... ? mole

$$= 5.9 \times 10^{-15} \text{ mole} = 6 \text{ femtomole}$$

## **D: Lumerical mode calculation**

Mode source operates in a broadband time-domain simulations [9]. The mode solver of the source uses a frequency or wavelength domain technique to calculate the modes of the waveguide structure. The technique is inherently single frequency but in this work broadband simulations are need for wavelength between (2-6)  $\mu\text{m}$ . For the broadband simulations, the mode solver calculates the modes at the centre wavelength i.e 3.5  $\mu\text{m}$  of the source. The selected mode profile as shown in figure 6 is injected over the entire frequency range of the source.

Figure 6 shows the modal field plot for the electric intensity and material index plot for the waveguide width of 3  $\mu\text{m}$  as explained in reference [9].

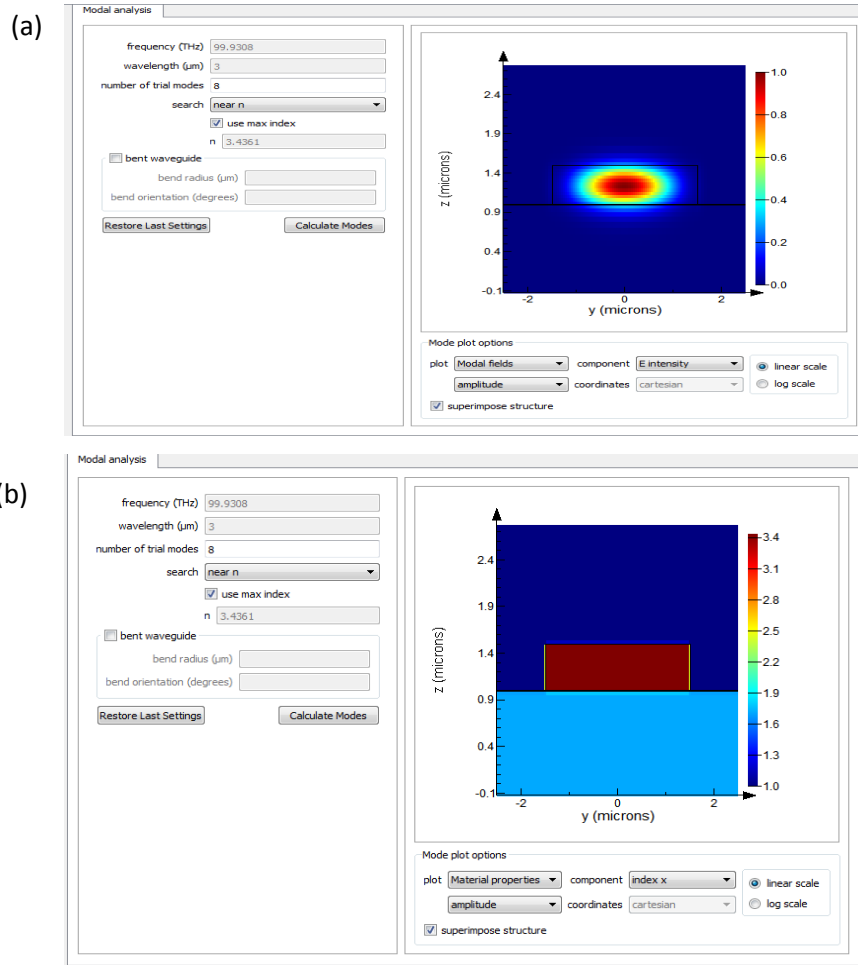


**Figure 6:** Screen shot of Lumerical solution mode source showing the (a) mode field (b) material properties.

In this simulation there are eight trial modes and the basic mode which is with lowest loss is selected for simulation of A-SRRs on SOI waveguide as described. The waveguide is  $3 \mu\text{m}$  wide and thickness is  $0.5 \mu\text{m}$  as shown in figure 6b.

## E: References

1. H. E. Bennett and J. M. Bennett, "Validity of the Drude theory -for silver, gold and aluminum in the infrared," in *Optical Properties and Electronic Structure of Metals and Alloys*, F. Abeles, ed., North-Holland Amsterdam, 1966.
2. F. A. Modine and D. Y. Smith, "Approximate formulas for the amplitude and the phase of the infrared reflectance of a conductor," *Journal of the Optical Society of America A*, 1, 1171-1174, 1984.
3. E. D. Palik, "Handbook of Optical Constants of Solids," Vol 1-3, ISBN: 978-0-12-544415-6 (1997).
4. P. Ding, E. J. Liang, W. Q. Hu, G. W. Cai, and Q. Z. Xue, "Tunable plasmonic properties and giant field enhancement in asymmetric double split ring arrays," *Photon. Nanostructures*, 9, 42–48, 2011.
5. I. H. Malitson, "Interspecimen Comparison of the Refractive Index of Fused Silica," *Journal of the Optical Society of America* 55, 1205–1209, 1965.
6. R. Kitamura, L. Pilon, M. Jonasz, "Optical Constants of Silica Glass From Extreme Ultraviolet to Far Infrared at Near Room Temperatures," *Applied Optics* 46, 8118–8133, 2007.
7. I. M. Pryce, Y. A. Kelaita, K. Aydin and H. A. Atwater, "Compliant metamaterials for resonantly enhanced infrared absorption spectroscopy and refractive index sensing," *ACS Nano*, 5, 8167– 8174, 2011.
8. M. I. Stockman, "Nanoplasmonics: The physics behind the applications," *Physics Today*, 39-44, 2011.
9. [https://kb.lumerical.com/en/index.html?ref\\_sim\\_obj\\_mode\\_source\\_broadband.html](https://kb.lumerical.com/en/index.html?ref_sim_obj_mode_source_broadband.html), 2016.